UNIVERSITY OF BIRMINGHAM

Upgrading of Bio-Oil Model Compounds and a Sewage Sludge Oil via Hydrodeoxygenation Using Non-Noble Transition Metal-Based Catalysts

By

MUSTAPHA YUSUF

A Thesis Submitted to the

SCHOOL OF CHEMICAL ENGINEERING, UNIVERSITY OF BIRMINGHAM, UK

For the Degree of

DOCTOR OF PHILOSOPHY

SEPTEMBER 2023

Abstract

The realisation of biofuels and chemicals requires the development of highly active and selective catalysts. In this research work, the catalytic hydrodeoxygenation (HDO) of bio-oil model compounds; anisole and benzoic acid, and sewage sludge oil have been investigated. Different catalysts were prepared via the impregnations of Ni and Zn on microporous zeolite (mic-ZSM-5), mesoporous zeolite (hie-ZSM-5), and mesoporous silica (SiO_2) supports. The catalysts were characterised, and the reactions were performed over a range of temperatures. The hie-Ni/ZSM-5 catalyst shows the highest acid site concentration, the best metal dispersion, and hence the highest catalytic activity. When treated separately, the HDO of anisole showed a 100% conversion in 2 h at 200 °C, while benzoic acid yields a conversion of 97% in 6 h at 340 °C. However, a decrease in activity was seen during the HDO of a blend of the two model compounds. Conversion was 37% (anisole) and 75% (benzoic acid) in 6 h at 340 °C. This was attributed to the competitive adsorption of the reactants on the catalytic active sites. Interestingly, both the catalysts from the highly acidic support (ZSM-5) and the nearly neutral support (SiO_2) showed a high degree of hydrodeoxygenation. While the Ni/SiO_2 produced toluene, the zeolite-base catalysts generated a significant amount of benzene and cyclohexane. This implies a synergy between the support acidity and metal sites in promoting C-C cleavage and hydrodearomatization reactions. A kinetic study carried out with the hie-Ni/ZSM-5 catalyst produced activation energy values of 53.3 kJ mol^{-1} (anisole) and 137.2 kJ mol^{-1} (benzoic acid). A comparative analysis of the prepared catalyst with a commercial hydrotreating catalyst in the HDO of sewage sludge oil revealed a promising result. The outstanding performance of the Ni/SiO_2 catalyst shows the combined effects of mesoporosity and metal sites. It is obvious that the metal sites, support mesoporosity, and acidity are critical design principles in the development of catalysts for real bio-oil HDO.

Dedication

This research work is gladly dedicated to my late parents, Alhaji Shitu Sani and Hajiya Rukayya Sani. May their gentle souls continue to rest in perfect peace, amen.

Acknowledgement

I thank Allah Almighty, Who, in His infinite mercy, favoured me in life, among which is seeing me through this noble course and making my dream a reality. I remain highly indebted to my late parents, for whatever I achieve in life is the progeny of what you planted in me. I will live with happy memories of your immeasurable support and always be grateful for your role in my life. Thank you! May Allah reward you with paradise. My profound gratitude also goes to the Petroleum Technology Development Fund (PTDF) under the Overseas Scholarship Scheme (OSS) grant, PTDF/ED/OSS/PHD/MY/1554/19, for funding the research. Words are certainly not enough to heartily express my thanks to my supervisor, Prof. Joseph Wood, for providing valuable information and tireless support. His advice and constructive criticism made this work a great success. Warmly, I want to acknowledge the immense contribution of the co-supervisor, Prof. Gary Leeke. To both, I say your valuable support is genuinely appreciated. Special thanks to Dr. Miloud Quadi, Dr. Marcin Sajdak, Dr. Abarasi Hart, Dr. Helen Vahey, June Callison, Lisa Allen, Sining Chen, Prof. B. Y. Jibril, and Prof. M. S. Waziri for their intellectual contributions. A word of thanks to Chyntol Kanhimbe, Jonathan Goldfinch, Zoe Simon for their technical support. I'm deeply grateful to all members of the catalysis and reaction research group. To the entire staff in the School of Chemical Engineering, I say thank you. Finally, it is not only pertinent but a must to duly acknowledge and thank my beloved wife (Rabi'atu) and my lovely kids, Abdullahi (son) and Rukayyah (daughter), for their patience, understanding, and prayers. My entire family and friends, whose unending support I could not possibly express in this space or time, are highly appreciated.

Table of Contents

List of Figures

List of Tables

Lists of Abbreviations, Symbols, and their Definitions

Abbreviation	Definition
AHFS	Ammonium Hexa-Fluorosilicate
BA	Benzoic Acid
BET	Brunauer-Emmett-Teller
BTX	Benzene-Toluene-Xylene
CTAB	Cetyl Trimethyl Ammonium Bromide
DDO	Direct Deoxygenation
DOE	Design of Experiment
FID	Flame Ionisation Detector
FTIR	Fourier Transform Infrared Spectroscopy
GC-MS	Gas Chromatography–Mass Spectrometry
H_2-TPR	Hydrogen temperature-programmed reduction, ii
HDN	Hydrodenitrogenation
HDO	Hydrodeoxygenation
HDS	Hydrodesulfurization
HHV	High Heating Value
hie-ZSM-5	Hierarchical ZSM-5
HTL	Hydrothermal Liquefaction
HYD	Hydrogenation
ICP	Inductively Coupled Plasma
IRENA	International Renewable Energy Agency
IUPAC	International Union of Pure and Applied Chemistry
JMP	John's Macintosh Project

LHHW	Langmuir Hinshelwood-Hougen Watson
MAP	Microwave-Assisted Pyrolysis
MFI	Mobil-type Five
mic-ZSM-5	Microporous ZSM-5
NH_3-TPD	Ammonium Temperature-Programmed Desorption
NIST	National Institute of Standards and Technology
OSS	Overseas Scholarship Scheme
PFO	Pseudo-First-Order
PSO	Pseudo-Second-Order
PTDF	Petroleum Technology Development Fund
Py-IR	Pyridine-adsorption Infrared-spectroscopy
QGA	Quantitative Gas Analysis
Q-TOF MS	Quadrupole-technologies-Time-of-Flight Mass Spectroscopy
REmap	Renewable Energy Roadmap
RSS	Residual Sum of Squares
RTFO	Renewable Transport Fuels Obligation
SEM-EDX	Scanning Electron Microscopy with Energy Dispersive X-ray
TCR	Thermochemical Reforming
TEM	Transmission Electron Microscopy
TGA	Thermogravimetric Analysis
TPAOH	Tetrapropylammonium Hydroxide
TPOAC	Octadecyl-(3-Trimethoxysilylpropyl)- Ammonium Chloride
XRD	X-ray Diffraction
ZSM-5	Zeolite Socony Mobil–5

Symbol/Notation	Definition
A	Arrhenius constant, s^{-1}
C	BET constant, dimensionless
C_C	Impeller clearance, m
C_A	Concentration of anisole, mol L^{-1}
C_{A0}	Initial concentration of anisole, mol L^{-1}
C_{BA}	Concentration of benzoic acid, mol L^{-1}
C_{BA0}	Initial concentration of benzoic acid, mol L^{-1}
C_e	Anisole concentration after adsorption, mg L^{-1}
C_{H2}	Concentration of hydrogen, mg L^{-1}
C_{mb}	Carbon mass balance, mass percent
C_o	Initial anisole concentration before adsorption, mg L^{-1}
$(D_{ei})_T$	Diffusion coefficient of reactant i at a temperature T, $cm^2\ s^{-1}$
$(D_{ei})_{T=25\ ^\circ C}$	Diffusion coefficient at 25 °C, $cm^2\ s^{-1}$
D_{cat}	Catalyst particle diameter, m
D_{imp}	Impeller diameter, m
d_p	Catalyst particle size, m
E_a	Activation energy, J mol^{-1}
g	Gravitational constant, m s^{-2}
H	Liquid level in the reactor, m
k	Reaction rate constant, s^{-1}
K_{ac}	Apparent equilibrium constant, L g^{-1}
k_{ads}	Adsorption equilibrium constant, L mol^{-1}
K_{BA}	Benzoic acid equilibrium constant, L mol^{-1}

K_F	Freundlich constan, (mg g^1)(L mg^{-1})$^{1/n}$
K_{H2}	Hydrogen equilibrium constant, L mol^{-1}
K_L	Langmuir isotherm constant, mg g^{-1}
k_S	Surface reaction rate constant, kmol $kgcat^{-1}mim^{-1}$
L	Length of a spherical catalyst particle, m
m	Mass of the dry adsorbent, g
m_s	Mass of the sample, g
M_{H2}	Molar mass of hydrogen, g mol^{-1}
M_s	Molar mass of solvent, g mol^{-1}
N	Avogadro's number, molecules mol^{-1}
NAR_j	Number of aromatic rings in *j*, dimensionless
n_{iF}	Number of moles of *i* in the feed, moles
n_{iR}	Number of moles of *i* reacted, moles
n_{jP}	Number of moles of *j* in the products, moles
Njs	Critical impeller speed, rpm
NOA_j	Number of oxygen atoms in *j*, dimensionless
p	Equilibrium pressure of adsorbate, kPa
p_0	Saturation pressure of adsorbate, kPa
q_e	Equilibrium adsorption capacity, mg g^{-1}
q_m	Maximum monolayer adsorption capacity, mg g^{-1}
q_t	Adsorption capacity at time *t*, mg g^{-1}
R	Gas constant, J K^{-1} mol^{-1}
r_0	Initial rate of reaction, mol L^{-1} min^{-1}
r_{Exp}	Experimental reaction rate, mol L^{-1} min^{-1}
r_{Mean}	Average experimental reaction rate, mol L^{-1} min^{-1}

r_{Mod}	Modeled reaction rate, mol L^{-1} min^{-1}
s	Cross-sectional area of adsorbed gas molecule, cm^2 $molecules^{-1}$
S_Z	Zwietering correlation parameter, dimensionless
S_{BET}	Specific surface area, BET, m^2 g^{-1}
S_j	Selectivity of product *j*, mole percent
S_{meso}	Mesoporous surface area, m^2 g^{-1}
S_t	Total surface area of the sample, m^2 g^{-1}
T	Temperature, ℃
Td	Reactor diameter, m
TMC_{DP}	Total mass of carbon atoms of detectable products, g
TMC_{FC}	Total mass of carbon atoms of *i* in the feed, g
v	Kinematic viscosity of the solvent, m^2 s^{-1}
V_M	Molar volume of adsorbed gas, cm^3 mol^{-1}
V	Volume of solution, L
V_A	Molar volume of solvent at normal boiling temperature, cm^3 $gmol^{-1}$
v_{ads}	Volume of the adsorbed gas, cm^3
V_i	Molar volume of reactant at the normal boiling point temperature, cm^3 $gmol^{-1}$
v_m	Monolayer adsorption gas volume, cm^3
V_{meso}	Mesoporous Volume, m^3 g^{-1}
V_{micro}	Microporous Volume, m^3 g^{-1}
x_{H2}	Mole fraction of hydrogen in liquid phase, dimensionless

X_{HDA}	Degree of hydrodearomatisation, percentage
X_{HDO}	Degree of hydrodeoxygenation, percentage
X_i	Conversion of reactant *i*, mole percent
X_w	Weight percent of the solid, percentage
y_{H2}	Mole fraction of hydrogen in gas phase, dimensionless
Y_j	Yield of product *j*, mole percent
ΔG	Gibbs free energy change, kJ mol^{-1}
ΔH	Enthalpy change, kJ mol^{-1}
ΔS	Entropy change, J $mol^{-1}K^{-1}$
η	Effectiveness factor, dimensionless
ρ_{cat}	Density of the catalyst, kg m^{-3}
φ	Thiele modulus, dimensionless
ω	Catalyst loading, kg m^{-3}
ρ_s	Density of solvent, g L^{-1}
μ_A	Viscosity of solvent, cP

CHAPTER 1

1.1 Background

Energy is an essential component of any functioning society (Madurai Elavarasan et al., 2023). Demand for energy, however, is rising as a result of the world's population growth and industrialization (Qu et al., 2021). Fossil fuels remain the major global energy source, accounting for about 88% of the total world's energy supply (Bhoi et al., 2020; Cheng et al., 2016; Deshmukh et al., 2023; Neto et al., 2019). A total consumption of 4.362 billion metric tonnes of oil was reported worldwide in 2015 (Wang et al., 2017). Consumption has been projected to increase by 48% between 2012 and 2040 (Bhoi et al., 2020). Petroleum reserves, which are thought to have peaked and are currently declining, provide a significant share of the world's liquid transportation fuels (Höök, 2009). In addition to the depletion of fossil fuel reserves, carbon dioxide is one of the principal greenhouse gases produced primarily by the combustion of the fuels (Muhammad, 2018; Xu et al., 2015). This poses a great environmental concern (Zhang et al., 2023).

To meet up with future energy demands as well as to avert global warming and other forms of environmental deterioration caused by the use of fossil fuels, there is a need for alternative, sustainable, and green energy sources (Yusuf et al., 2022; Zhou and Hu, 2020). Figure 1.1 presents a global source of renewable energy (Tursi and Olivito, 2021). These include biomass (72.3%), hydro (16.8%), wind (4.4%), geothermal (3.4%) solar (1.9%), and others (1.2%). Apart from being the one with the greatest potential compared to the other renewable energy resources, biomass is the only source of sustainable liquid fuels, which are essential for transportation (Madurai Elavarasan et al., 2023; Tu et al. 2019). Consequently, research on biomass and biomass-based fuels and chemicals has drawn a lot of interest.

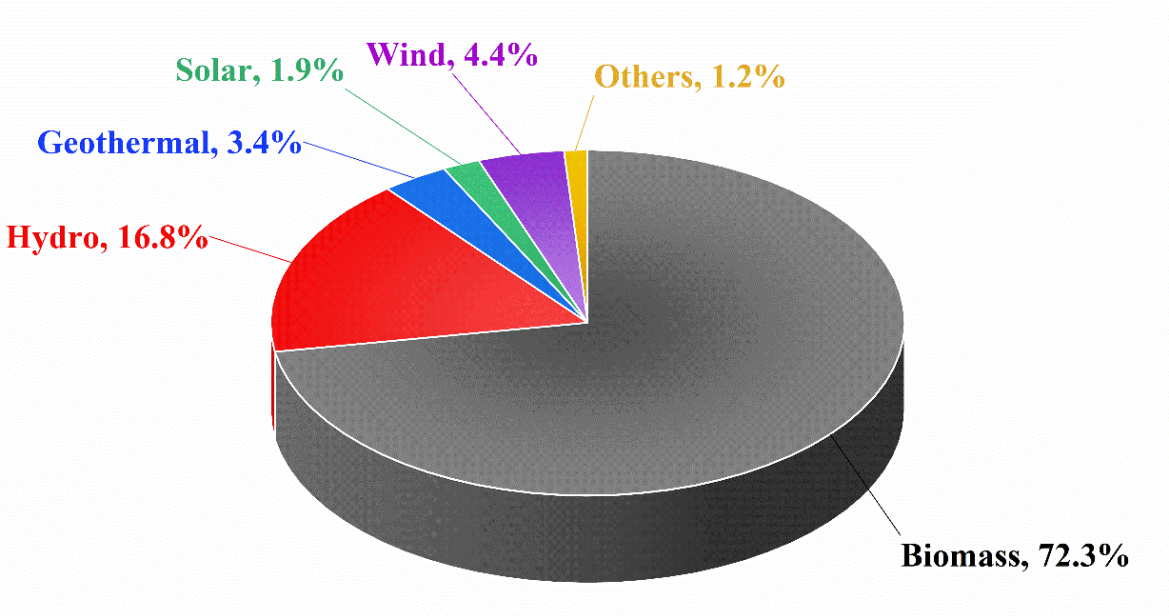

Figure 1.1: *Global sources for renewable energy (Tursi and Olivito, 2021).*

A proposal by the European Commission entitled "The Energy Strategy 2020" strongly recommended the utilisation of plant and animal-derived resources (biomass) as alternative sources of energy. Similarly, the International Renewable Energy Agency (IRENA) introduced a programme called "Renewable Energy Roadmap (REmap 2030)" to strategize and boost the developmental capacities of biomass energy (Jin et al., 2019). In addition, a UK legislation known as the Renewable Transport Fuels Obligation (RTFO) is designed to reduce greenhouse gas emissions from fuel used for transportation. This is to be realised by promoting the provision of renewable fuels, which, by extension, would support the government's ultimate goal of attaining net zero by 2050. It is predicted that bioenergy will make up 25–33% of the world's energy supply by 2050 (Salmi, 2023).

1.1.1 Biomass and conversion technologies

Biomass refers to organic matter use for biofuels production (Li et al., 2023). It comprises of agricultural residues (edible plant-based, also known as first generation biomass), by-products from forest resources and other forms of organic waste (second generation biomass),

and a highly diverse macro- and microalgae (third generation biomass), (Neto et al., 2019; Shi et al., 2017; Wang et al., 2017). Figure 1.2 presents the different types of biomass generations, from first to third. Unlike fossil fuels that take millions of years to form, biomass can be continuously produced through sustainable agricultural practices. It constitutes a wide range of alternative feedstocks that can be used for the production of a valuable variety of platform chemicals. Apart from being less expensive, biomass is the only renewable source of liquid fuels and chemicals (Hansen et al., 2020; Niu et al., 2019; Ravanchi and Sahebdelfar, 2019; Sankaranarayanan et al., 2018).

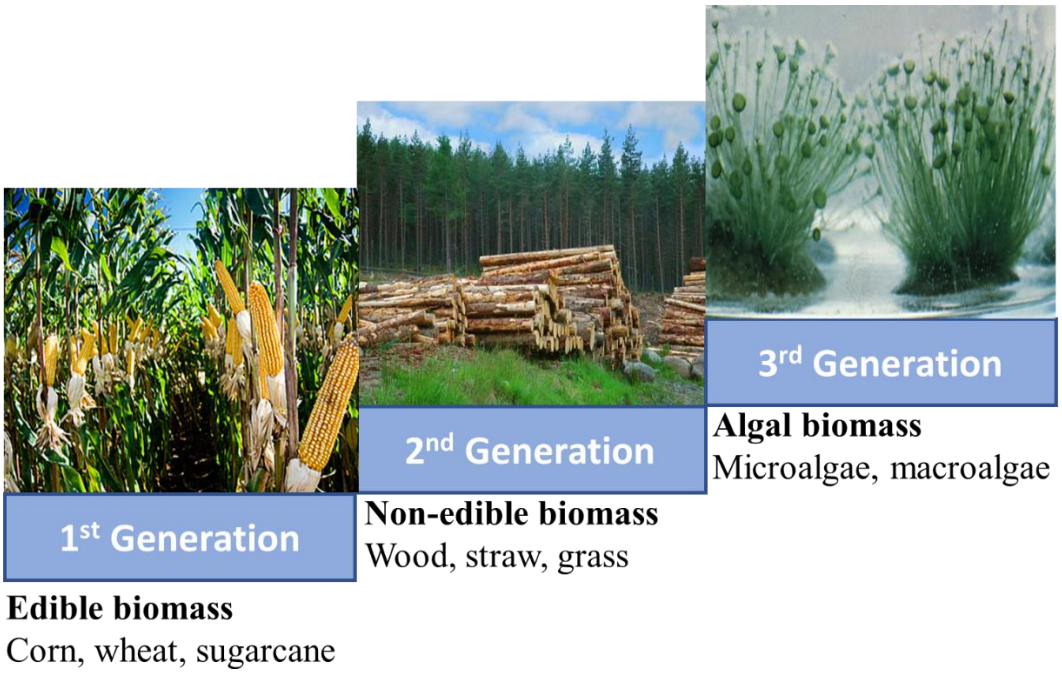

Figure 1.2: *The generations of biomass (Alalwan et al., 2019).*

A number of processes, including thermal, biochemical, and physicochemical processes, can be used to convert biomass into various forms of fuels or chemicals (Chaihad et al., 2019). Figure 1.3 shows the main technologies involved. In thermochemical conversion, chemical

reactions that take place at moderate to high temperatures convert biomass into useful forms of energy (Neto et al., 2019). The biochemical conversion is certainly the most well-known and employed method of biomass transformation, even at the industrial level (Tursi and Olivito, 2021). The two main biochemical conversion methods are anaerobic digestion and fermentation. In anaerobic digestion, microorganisms are employed to break down organic matter using cellular respiration that occurs in the absence of oxygen. During the fermentation process, biomass with a high sugar content is transformed into bioethanol via a series of microorganism-induced chemical reactions. Where raw materials such as animal fat and vegetable oil are involved as raw materials, transesterification, a physicochemical conversion process, is used to produce biofuels (Alalwan et al., 2019; Elavarasan et al., 2023).

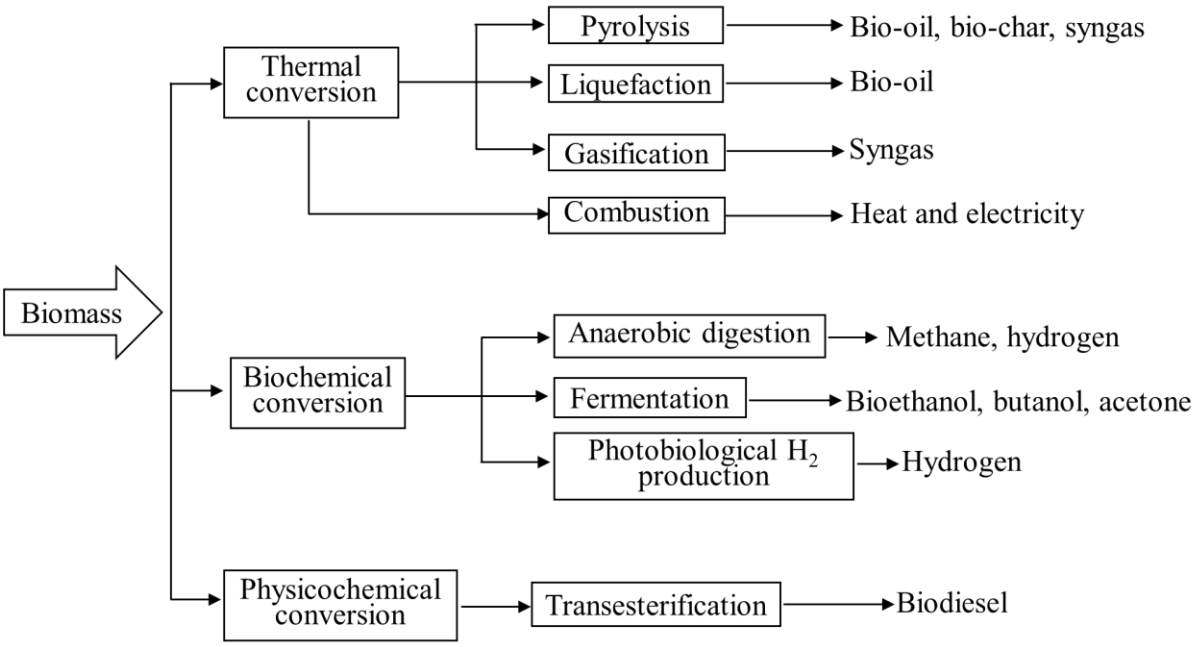

Figure 1.3: *Schematic diagram of the biomass conversion processes (Neto et al., 2019).*

Among all the aforementioned technologies, pyrolysis, a thermochemical process, received great attention due to its high yield of liquid fuels (Song et al., 2010; Wang et al., 2017). The process is carried out in the absence of oxygen at a temperature between 300 ℃ to 700 ℃, producing bio-oil, bio-char, and syngas (Tursi and Olivito, 2021). In some special circumstances, a low stoichiometric amount of oxygen is used to promote partial oxidation and facilitate heat generation during the process (Fu et al., 2022; Pocha et al., 2023).

1.1.2 Bio-oil and its constituents

Bio-oil, a dark brown liquid commonly referred to as biomass oil or biocrude, has been recognised as a promising renewable energy source that can be used in various applications in energy and industries (Haghighat et al., 2020). It is derived from the pyrolysis of various biomass resources, such as agricultural waste, wood chips, and algae. The unique chemical composition of bio-oil makes it an attractive alternative to conventional fossil fuels. Bio-oil contains high amounts of oxygenated compounds such as acids, aldehydes, ketones, and phenols, which make it highly reactive and prone to spontaneous combustion. This property makes bio-oil a suitable feedstock to produce fuels and chemicals such as adhesives, resins, and solvents used in industries like paints, coatings, and pharmaceuticals (Li et al., 2017).

Different types of biomass yield different constituents in bio-oil (Tursi and Olivito, 2021). For instance, lignocellulosic biomass, such as wood and agricultural residues, produces bio-oil with a high content of oxygenated compounds like acetic acid, furans, phenols, and levoglucosan. These compounds are responsible for the acidic nature and high viscosity of lignocellulosic bio-oils (Yang et al., 2023). On the other hand, algae-based biomass produces bio-oils with a higher concentration of lipids and some nitrogen-containing compounds. These lipids can be further processed into biodiesel, making algae-based bio-oils suitable for

transportation fuel applications (Zhou and Hu, 2020). Bio-oil from municipal solid waste, such as sewage sludge, contains a wide range of organic compounds, including aldehydes, ketones, acids, esters, phenols, and furans. These compounds contribute to its unique chemical composition and properties (Heracleous et al., 2022). In addition, the moisture content of the biomass also affects the composition of bio-oil produced from it. Unlike dry biomass, which yields higher amounts of volatile organic compounds such as phenols and furans, wet or fresh biomass tends to produce more water-soluble compounds like sugars and organic acids. By adjusting the feedstock choices and processing conditions, researchers can modify the composition to improve desirable qualities like stability, energy density, and compatibility with current infrastructure (Tursi and Olivito, 2021).

1.1.3 The concept of catalysis

Catalysis is a fundamental process in engineering that plays a crucial role in various industries. It involves the use of catalysts to accelerate chemical reactions, thereby increasing efficiency and reducing costs (Fogler, 2019). The application of catalysts in engineering processes has revolutionised many fields, including petroleum refining, pharmaceutical production, and environmental protection (Elahi et al., 2019). The two main types of catalytic processes are homogeneous and heterogeneous catalysis. While both types involve the use of catalysts to accelerate reactions, they differ in terms of their composition and mechanism. In homogeneous catalysis, a catalyst is present in the same phase as the reactants. In this case, the catalyst and reactants are usually dissolved in a solvent, forming a homogeneous mixture. The catalyst interacts with the reactants, forming an intermediate complex that lowers the activation energy required for the reaction to occur. Homogeneous catalysis offers several advantages over other types of catalytic systems. For instance, it enables precise control over reaction conditions such as temperature and pressure.

Furthermore, the activity and selectivity of homogeneous catalysts may be easily altered by changing the ligands or substituents on the catalysts. However, one major drawback is the separation of the catalyst from the product after the reaction. This often requires additional steps and can be energy-intensive, limiting its practical applications (Regalbuto, 2007).

On the other hand, heterogeneous catalysis involves the use of catalysts that are present in a different phase from the reactants, typically solid catalysts in contact with gaseous or liquid reactants. This type of catalysis plays a crucial role in various industrial processes and has been extensively studied for its potential applications. Some of the key advantages of heterogeneous catalysis are its ability to be easily separated from the reactants and products. This allows for the catalyst to be reused multiple times, making it economically viable and environmentally friendly (Fogler, 2019; Regalbuto, 2007). Additionally, heterogeneous catalysts can be tailored to specific reactions by modifying their surface properties or incorporating different active sites (Ruddy et al., 2014). This versatility makes them highly efficient and selective in promoting desired reactions. The mechanism behind heterogeneous catalysis involves the adsorption of reactants onto the catalyst surface, followed by transformation into products through various chemical reactions. Here, the surface structure and composition of the catalyst play a crucial role in determining its activity and selectivity for specific reactions. Despite its numerous advantages, heterogeneous catalysis also presents some challenges. For instance, mass transport limitations can occur when reactants cannot easily diffuse to active sites on the catalyst surface. Furthermore, deactivation of the catalyst can occur due to poisoning or fouling caused by impurities present in the reaction mixture ((Tu et al., 2019; Gao et al., 2014).

1.1.4 Catalytic upgrading of bio-oil

One of the challenges in the utilization of bio-oil is its high oxygen content, which can lead to instability and reduced energy density of the oil. This results in low-quality fuel and incompatibility with existing industrial facilities and current transportation infrastructure, hence the need for upgrading (Hansen et al., 2020; Song et al., 2010; Witsuthammakul and Sooknoi, 2015). Upgrading processes such as hydrotreating or hydrocracking can convert bio-oil into more stable products with lower acidity and a higher calorific value, making it suitable for use in diesel engines. Of the various hydrotreating processes, catalytic hydrodeoxygenation (HDO) has been identified as the most promising approach for upgrading bio-oil. In this method, oxygen-containing functional groups are removed through hydrogenation reactions in the presence of a solid catalyst, and subsequently, valuable products such as gasoline or diesel fuel are produced.

1.2 Research Significance and Knowledge Gap

The development of technologies for bio-oil upgrading process is a crucial step towards achieving sustainable energy production. Hydrodeoxygenation (HDO) has proven to be an efficient method for improving the quality of bio-oil by removing impurities and increasing its stability. The process provides economic benefits by increasing market value and creating new opportunities in the renewable energy sector. Different catalysts have been prepared and used for bio-oil upgrading (Guvenc et al., 2023; Kim et al., 2022; Niu et al., 2019), including traditional hydrodesulphurization/hydrogeneration catalysts (Chen et al., 2019), noble and transition metal catalysts (Gutiérrez-Rubio et al., 2019). However, these catalysts are highly susceptible to coke formation (Keav et al., 2010), which hinders their utilization at large-scale (Niu et al., 2019). Since catalytic HDO of bio-oil progresses through hydrogenation and deoxygenation, there is need for a good catalyst support to promote these reactions. Hence,

the focus of recent research works has been to identify better solid-support candidates (Zhang et al., 2023; Zhang et al., 2020). In comparison to metal-microporous support catalysts, metal-mesoporous support catalysts showed remarkable performance in the HDO of bio-oil (Li, et al., 2020; Niu et al., 2019). Additionally, solvent compositions could affect the distribution of catalyst and reactant in the reacting mixture and the adsorption of the reactant onto the catalyst active sites during hydrodeoxygenation reaction. This may further affect catalytic activity and product distribution (Kim et al., 2022).

Researchers studied catalytic HDO mechanisms using model compounds rather than bio-oils because of the complexity of bio-oil components. It is believed that the study of model compounds could be an important step towards further developing effective methods to produce and upgrade bio-oil (Jin et al., 2019; Si et al., 2017). For this research work, anisole has been selected as one of the model compounds for the catalytic test. It's a phenolic ether, which is typical of lignin depolymerization fractions present in pyrolysis bio-oils derived from lignocellulosic biomass. Phenolic compounds are highly reactive; their presence contributes significantly to the undesirable properties of pyrolysis bio-oil (Shafaghat et al., 2015). Among the acidic model compounds studied is the HDO of acetic acid and palmitic acid (Lawal et al., 2019; Liu et al., 2021; Song et al., 2010; Wang et al., 2017). Both compounds and the carboxylic acid substitutes have substantially simpler aliphatic hydrocarbon chains than their benzoic acid counterparts, which have more intricate benzene-ring structures. In addition, different model compounds have different adsorption coefficients and reactivity (Guvenc et al., 2023; Kristensen et al., 2022). However, information is limited in the literature on how catalytic activity is affected by the competitive adsorption of a blend of model compounds onto the catalyst's available active sites during the HDO process (Chen et al., 2020; Sankaranarayanan et al., 2018). Hence, many more relevant

bio-oil model compounds as well as their mixtures have to be explored. As the world strives towards a sustainable future with reduced reliance on fossil fuels, investing in bio-oil upgrading research is essential for achieving energy security and environmental preservation. While remarkable progress has been made in this direction, there is still more to be done to ensure the realisation of this goal. Consequently, after a comprehensive survey of the literature, the following research gaps have been identified:

- Insufficient information on the effect of supports on the performance of Ni-based catalysts during the HDO of anisole as a bio-oil model compound.
- There is a need to investigate the influence of solvent during the HDO of anisole.
- Limited data exist on the catalytic HDO of benzoic acid as a bio-oil model compound.
- Lack of sufficient data for the HDO kinetics of benzoic acid.
- Limited information on the HDO of mixtures of bio-oil model compounds exists.
- Specifically, there is no data on the HDO of a mixture of anisole and benzoic acid.
- The HDO of real bio-oil requires further investigation.

In general, further research is needed to optimize catalyst design and reaction conditions for efficient bio-oil upgrading processes.

1.3 Aim and Objectives

1.3.1 Aim of the research

The aim of this research work is to develop catalysts with high metal dispersion and stability for the hydrodeoxygenation (HDO) of anisole, benzoic acid, a binary mixture of anisole and benzoic acid, and sewage sludge oil.

1.3.2 Specific objectives of the research

i. Design new catalysts using a 'top-down' approach to produce a mesoporous support, followed by the incipient wetness impregnation to incorporate the active metals, nickel and zinc (5 wt.% loading of each metal onto different supports and a combination of nickel-zinc, 3 wt.% and 2 wt.%, on a support).

ii. Carry out a comparative assessment of the HDO of single model compounds (anisole and benzoic acid) and a mixture of the two model compounds on a Parr reactor.

iii. Investigate the role of diffusion and surface reaction as well as evaluate the influence of different solvents on the extent of HDO of anisole and product distribution.

iv. Perform kinetic studies for the HDO of anisole and HDO of benzoic acid over the mesoporous nickel-based catalyst, develop a kinetic model to describe the reaction, and determine kinetic parameters, which are required for the process equipment design and scaling up.

v. Upgrade a real bio-oil obtained from the thermo-chemical reforming of sewage sludge using the prepared catalysts and a commercial hydrotreating catalyst, NiMo-Al_2O_3 (TK-341).

vi. Carry out a comprehensive catalyst characterisation using XRD, BET, TEM, SEM-EDX, H_2-TPR, TGA, and NH_3-TPD techniques and link the catalysts' properties to their activities.

vii. Use GC and GC-MS for the analysis of the liquid products.

1.4 Thesis Layout

In accordance with the aim and objectives of the study as listed above, this research work is presented in eight chapters. Chapter one provides a background on global energy sources and resources, biomass and conversion technologies, the concept of catalysis, catalytic upgrading

of bio-oil, and the significance of the study. It identifies research gaps, defines the aim and objectives of the research work, and the format in which the entire thesis is reported. Chapter two gives a comprehensive literature survey in the area covering the HDO of different bio-oil model compounds, the HDO of real bio-oil, the type of reactors used for the upgrading operation, the most widely used active metal for the HDO catalyst preparation, catalyst support materials, the preparation of mesoporous catalyst supports, catalyst deactivation, and kinetic analysis. Chapter three provides a complete list of all the materials used in the research work, describes experimental procedures for catalyst preparation, discusses techniques for catalyst characterization, provides background information on the working principles of some of the major tools used for the catalyst's characterization, the reactor configuration for catalytic activity tests, and techniques used for product analysis. Chapter four discusses the result of the catalyst characterization. Chapter five reports the effects of catalyst support properties and solvent during the HDO of anisole. The chapter also presents a kinetic study of anisole HDO over the hie-Ni/ZSM-5 catalyst. Chapter six provides the reaction mechanism and kinetics of benzoic acid HDO over the prepared nickel-based catalysts. Chapter seven presents the HDO of a binary mixture of bio-oil model compounds (anisole and benzoic acid) and a real bio-oil obtained from sewage sludge. Finally, Chapter eight presents conclusions and makes some recommendations on areas that require further research.

1.5 Summary of the Chapter

This chapter introduces the research topic. It commences by highlighting the world's increasing demand for energy, the need to carry out more research on the available renewable liquid fuel sources, and the upgrading processes. The significance of the study is outlined,

including the areas that need further study. The aim and objectives of the research are clearly stated. The next chapter (Chapter 2) provides a detailed literature survey in the research area.

CHAPTER 2

Literature Review

2.1 Introduction

This chapter presents a review of literature, covering in Section 2.2, biomass as a renewable energy source, whilst pyrolysis of biomass is discussed in Section 2.3. Bio-oil and its potential as an alternative energy source are discussed in Section 2.4. Challenges in implementing bio-oil for energy are presented in Section 2.5. In Section 2.6, bio-oil upgrading is discussed. Catalytic hydrodeoxygenation is highlighted in Section 2.7. The most widely used active metals for bio-oil HDO are presented in Section 2.8. Catalyst support materials are discussed in Section 2.9. Hydrodeoxygenation of bio-oil model compounds is presented in Section 2.10. The influence of process parameters on HDO efficiency is presented in Section 2.11. Catalyst stability, poisoning, and deactivation are discussed in Section 2.12. And finally, the kinetics study is discussed in Section 2.13.

2.2 Biomass as a Renewable Energy Source

Biomass energy, a renewable energy source derived from organic matter, presents significant environmental benefits (Kristensen et al., 2022). One of the primary advantages of biomass apart from being a sustainable source of energy, is its ability to reduce greenhouse gas emissions (Lee, et al., 2016). The main reason for this is that the carbon absorbed during growth of the biomass is offset by their conversion to fuels and burning. As biomass materials decompose naturally, they release carbon dioxide into the atmosphere. However, by converting these materials into energy through processes like combustion or anaerobic digestion, the amount of carbon dioxide released during combustion is equivalent to the amount absorbed during plant growth. Consequently, biomass energy significantly reduces

net carbon emissions compared to fossil fuels (Pierobon et al., 2018). In addition, biomass energy contributes to waste management by utilizing organic waste materials that would otherwise end up in landfills or be left to decompose in an uncontrolled manner. Methane is a potent greenhouse gas with a 25 times higher global warming potential than carbon dioxide over a 100-year period (Alalwan et al., 2019). By diverting these waste materials towards energy production, biomass facilities not only generate energy but also minimize methane emissions from decaying organic matter in landfill (Ighalo and Adeniyi, 2020). The utilization of agricultural residues such as straw and corn stover also reduces the need for open-field burning, an activity that contributes to air pollution (Sakka et al., 2023). Additionally, if carbon capture and storage, or utilisation is connected to the combustion process, it could potentially be made carbon-negative (Alalwan et al., 2019).

A number of processes, including thermal, biochemical, and physicochemical processes, can be used to convert biomass into various forms of energy or bio-based chemicals (Chaihad et al., 2019). However, pyrolysis, a thermochemical process, received great attention due to its high yield of liquid fuels (Song et al., 2010; Wang et al., 2017). Its applications in industrial processes have proven invaluable for waste management and energy generation while contributing to sustainable practices.

2.3 Pyrolysis of Biomass

Pyrolysis is a transformative process that occurs when organic materials are subjected to intense heat in the absence of oxygen (Roy et al., 2023). This thermal decomposition leads to the breakdown of complex molecules into simpler compounds such as gases, liquids, and solid residues. It has been a subject of interest for scientists and engineers for centuries. This technique has proven to be exceptionally efficient, yielding higher quantities of bio-oil while

minimising waste materials (Garba et al., 2018). Figure 2.1 presents a schematic diagram of pyrolysis. The process can effectively convert various types of waste materials into bio-oil, syngas, and carbon black. Bio-oil obtained from pyrolysis, after upgrading, possesses similar properties to conventional fossil fuels and can be used as a renewable energy source or as a precursor for bio-based chemicals. Syngas, on the other hand, is a mixture of hydrogen and carbon monoxide that can be utilised for heat and power generation (Sartipi et al., 2014). Carbon black can serve as an essential raw material for manufacturing products like tyres (Adhikari et al., 2018).

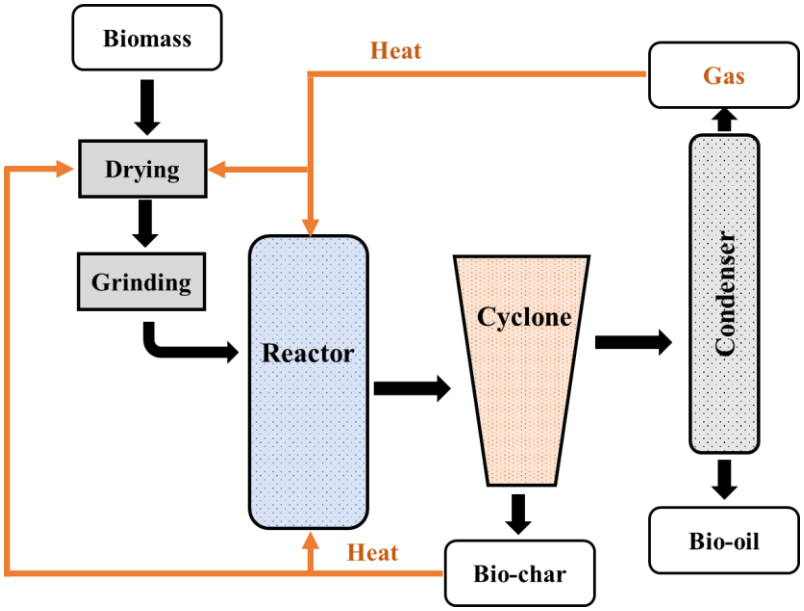

Figure 2.1: *Schematic diagram of biomass pyrolysis process (Khitab et al., 2021).*

By utilizing this technology, industries can potentially contribute to a greener future while simultaneously meeting their production needs. Although pyrolysis still produces liquid fuels for combustion, they are potentially more carbon neutral than exploiting fossil fuels. The versatility and effectiveness of pyrolysis make it a promising avenue for addressing multiple challenges faced by various sectors (Che et al., 2019). For example, marine, haulage and aviation, which may otherwise be difficult to decarbonise or are not suitable for electrification (Muhammad et al., 2018).

2.3.1 Types of biomass pyrolysis

The choice of which type of pyrolysis to use depends on factors such as feedstock composition, desired product yields, energy requirements, and economic considerations (Ghashghaee et al., 2019). Table 2.1 presents some basic operating conditions for different types of pyrolysis. Slow pyrolysis is the oldest and most traditional form of pyrolysis. As the name suggests, it involves a slow heating rate and a long residence time at relatively low temperatures. Typically, slow pyrolysis occurs between 300 ℃ to 700 ℃ with a residence time ranging from several minutes to hours (Cheah et al., 2023).

Table 2.1: Major operating conditions for different types of pyrolysis (Singh et al., 2022).

Method	Temperature (℃)	Heating rate (℃ s^{-1})	Residence time (s)
Slow pyrolysis	300–700	0.1–1	450–550
Fast pyrolysis	600–1000	10–200	0.5–10
Flash pyrolysis	800–1000	>1000	<0.5

This type of pyrolysis is commonly used for the production of biochar or charcoal (Adhikari et al., 2018). Fast pyrolysis, on the other hand, involves rapid heating rates and shorter residence times compared to slow pyrolysis (Sangnikul et al., 2019). The temperature range for fast pyrolysis is normally between 600 ℃ to 1000 ℃ with residence times ranging from seconds to minutes. This type of pyrolysis produces higher yields of liquid products known as bio-oil or biomass oil (Tran et al., 2014). Flash pyrolysis in the other hand is a variation of fast pyrolysis that involves extremely rapid heating rates and very short residence times. The temperature range for flash pyrolysis usually exceeds 800 ℃, and the residence time is on the

order of milliseconds. This type of pyrolysis is primarily used for the production of gases such as syngas or synthesis gas (Mortensen et al., 2011).

2.3.2 Mechanism of biomass pyrolysis

Generally, as the temperature rises within the pyrolysis chamber, bonds holding the organic molecules together begin to weaken, indicating the beginning of a series of reactions and transformation. The first step in the process is known as depolymerization (Pocha et al., 2023). Here, long chains of polymers are cleaved into smaller fragments through homolytic or heterolytic bond scission. These fragments engage in various reactions such as cracking, cyclization, rearrangement, and condensation. Cracking reactions serve as gateways to simpler compounds by breaking large molecules into smaller ones through thermal decomposition (Khitab et al., 2021). In contrast, cyclization reactions create rings within molecules by joining adjacent atoms together (Basu, 2013). The rearrangement involves atom shuffling within molecules, leading to structural modifications that can drastically alter their properties and reactivity (Pocha et al., 2023). It often occurs at high temperatures due to increased molecular mobility. Finally, condensation reactions bring about unity by stitching together smaller fragments to form larger molecules. It is through these condensation reactions that valuable products such as biofuels, syngas, and carbonaceous materials are produced (Staš et al., 2020).

2.4 Bio-oil and its Potential as an Alternative Energy Source

Bio-oil has become a viable option to conventional fossil fuels in an era of increasing concern for the environment and the need for sustainable energy sources (Nesterov et al., 2021). It offers a more sustainable solution for meeting global energy needs. Biomass used in the production of bio-oil can be continuously grown through sustainable practices such as

dedicated energy crop cultivation or utilizing agricultural residues more efficiently (Pocha et al., 2023). Bio-oil offers significant potential for reducing greenhouse gas emissions and mitigating climate change effects in a cost-effective manner. Unlike conventional fossil fuels that release large amounts of carbon dioxide when burned, bio-oils are considered carbon-neutral since they only emit the same amount of CO_2 they absorbed during growth (Pierobon et al., 2018). This makes them an attractive option in meeting international climate targets while avoiding costly penalties associated with excessive emissions.

2.4.1 Chemical composition of bio-oil

Bio-oil contains more than 300 distinct compounds, and the precise composition of the final product depends on the feedstock and processing conditions (Bashir et al., 2022; Qu et al., 2021). The most common oxygen containing-molecules presence in bio-oil obtained via fast pyrolysis are water (20-30%), acid (13-15%), phenols (10-18%), ketones (8-10%), aldehydes (8-10%), esters (2-5%), and lignin-based compounds (10-15%) (Oyedun et al., 2020). A general description of bio-oil from various biomass sources is shown in Table 2.2. Water makes about 10–30 weight percent of the product, while other species include hydroxyaldehydes, hydroxyketones, sugars, carboxylic acids, esters, furans, guaiacols, and phenolics, many of which are found as oligomers in the oil. Generally, the amount of carboxylic acid in bio-oil is substantial, giving it a low pH value (2–4) and making it highly unstable (Staš et al., 2020). The acidity in bio-oil increases the rate of condensation reactions, which in turn promotes the ageing of the bio-oil. This results in the deterioration of the properties of the bio-oil and a decrease in its miscibility with Petro-fuels (Gutiérrez-Rubio et al., 2019). Bio-oil's acidity makes it exceedingly corrosive and unstable at high temperatures. Hence, certain strict specifications must be met in the construction of the vessels for the storage of the bio-crude as well as upgrading operations.

Table 2.2: Components of bio-oil according to the biomass sources (Mortensen et al., 2011).

Component	Biomass				
	Hardwood	**Softwood**	**Corn stover**	**Corn Cob**	**Pine**
Water	20-21	29-32	9	25	24
Carbohydrates	3-4	3-7	12	5	34
Aldehydes	0-5	1-17	4	1	7
Ketones	7-8	2-4	7	11	4
Phenolics	2-3	2-3	2	4	15
Acids	5-7	3-10	6	6	4
Alcohols	0-4	0-1	0	0	2
Furans	0-1	0-2	1	2	3
Others	47-58	24-57	57	46	5

It can be derived from its chemical composition that bio-oil is a potential raw material to produce biofuels. However, to work with the current infrastructure, its physicochemical properties need to be improved. As presented in Table 2.3, the conventional fuels (fossil fuels) used in the current infrastructure have very low acidity, water, and oxygen content. While high heating value (HHV) is an indicator of the quality of the fuels (Yang et al., 2019), the following are reported for bio-oil (15–18 MJ kg^{-1}), crude oil (41–45 MJ kg^{-1}), heavy oil (39–41 MJ kg^{-1}), gasoline (46 MJ kg^{-1}), and diesel (40–46 MJ kg^{-1}), respectively (Gea et al., 2023).

As instability in bio-oil is caused by the reactive oxygenates, exposure to high temperatures during storage makes bio-oil undergo thermal cracking and polymerisation reactions (Oyedun

et al., 2020). These reactions break down large molecules into smaller fragments and promote the formation of polymeric compounds with increased molecular weight. As a consequence, the viscosity of bio-oil increases while its energy content decreases, leading to reduced fuel efficiency. Gea et al. (2023) reported that the exposure of bio-oil for seven days at 40 ℃ or 6 h at 80 ℃ caused an increase in the viscosity, which is equivalent to room temperature storage for 3–4 months.

Table 2.3: Physicochemical properties of bio-oil and fossil fuels (Gea et al., 2023).

Fuel property	Bio-oil	Crude oil	Heavy oil	Gasoline	Diesel
C (%)	32–50	84–87	85–86	84–88	85–86
H (%)	8–11	11–14	12.5–14	12–16	13–15
O (%)	45–60	0.08–1.82	1	–	–
N (%)	< 0.4	0.02–1.7	0.2	0.1	0.1
S (%)	< 0.3	0.06–2	> 1	0.08	0.2–0.5
Water (%)	20–30	0.3	0.1	0.025	0.1
Solid (%)	< 1		0.2–2.5		< 0.5
Ash (%)	0.1–0.5	0.02–0.07	> 0.3		< 0.01
Viscosity (cP)	8–72	16–32	16–160	0.48–0.56	1.28–4.64
	(40 ℃)	(40 ℃)	(80 ℃)	(40 ℃)	(40 ℃)
Density (g mL^{-1})	1.2	0.7–1.0	< 0.98	0.7–0.8	0.85
Flash point (℃)	70–100	-10–28	< 130	40–55	-50– -40
HHV (MJ kg^{-1})	15–18	41–45	39–41	46	40–46
pH	2.0–4.0	–	–	–	–
Stability	Unstable	–	Stable	Stable	Stable

Peroxides are formed when bio-oil reacts with oxygen, which subsequently promotes polymerization (Tang et al., 2021). While bio-oil viscosity increases as a result of polymerisation reaction during storage, both acidity and water content also increase (Fan et al., 2020). The increase in acidity is cause by the reaction among ketones, furans, aldehydes, alcohols, levoglucosans, and phenolics. However, an increase in water content is due to the esterification reaction between acids and alcohols. While being stored, bio-oil's viscosity supposed to decrease as the water content rises, however the polymerization and condensation reactions have a significant impact. As a result, the viscosity of bio-oil will continue to rise throughout storage (Gea et al., 2023).

2.4.2 Current developments in bio-oil technology

Bio-oil technology is a growing field, there have been remarkable strides made in recent years, leading to substantial advancements in bio-oil production techniques. These innovations have revolutionized the field and paved the way for a more sustainable and environmentally friendly energy source (Yang et al., 2023). Researchers have introduced catalytic upgrading as an effective method to enhance the quality and properties of bio-oil (Ma et al., 2023). By employing various catalysts such as zeolites or metal oxides, they can optimize the chemical composition of bio-oil and reduce its undesired characteristics like acidity or instability. This advancement not only improves its potential applications but also makes it more compatible with existing infrastructure for energy distribution (Yang et al., 2023).

Another significant development is hydrothermal liquefaction (HTL) shown in Figure 2.2, which utilizes high pressure and temperature conditions to convert wet biomass into a liquid form known as biocrude oil. HTL offers several advantages due to its ability to process a

wider range of feedstocks, including algae or sewage sludge (Elliott et al., 2015). Furthermore, scientists have explored innovative approaches such as microwave-assisted pyrolysis (MAP), Figure 2.3, that utilize electromagnetic radiation for heating biomass rapidly and uniformly (Sridevi et al., 2023). This technique significantly reduces processing time while maintaining product quality by preventing excessive degradation during prolonged exposure to high temperatures (Fan et al., 2022).

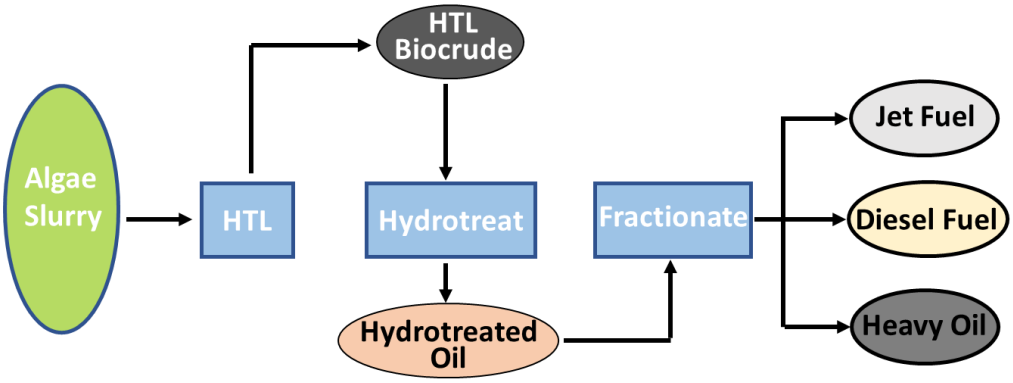

Figure 2.2: *Schematic diagram for hydrothermal liquefaction (Elliott et al., 2015).*

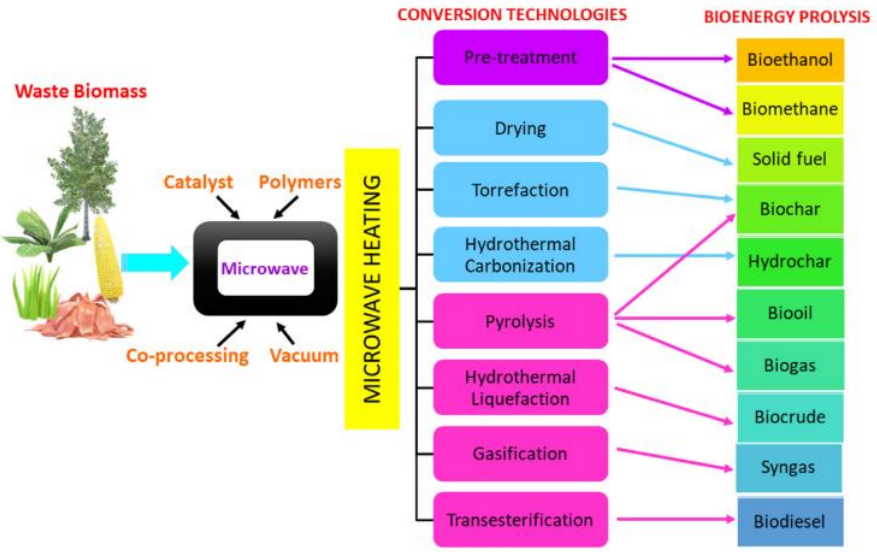

Figure 2.3: *Routes for converting biomass into biofuel using microwave technology (Singh et al., 2022).*

MAP allows for better control over reaction parameters like temperature gradients or residence times, enabling researchers to fine-tune bio-oil production according to specific requirements (Singh et al., 2022). Another development is on plasma hydrodeoxygenation, a ground-breaking technique with a wide range of uses and advantages (Pocha et al., 2023). The application of plasma technology in HDO offers improved reaction rates, higher selectivity towards desired products, and reduced energy consumption (Gea et al., 2023). Furthermore, advancements in catalyst regeneration techniques have addressed one critical issue associated with catalyst deactivation during bio-oil production processes. Researchers have developed novel methods like microwave-assisted regeneration (Mevawala et al., 2023), which effectively restores the catalyst's activity and extends its lifespan. This new development not only improves the economic viability of bio-oil production but also reduces waste generation and enhances overall process sustainability.

2.5 Challenges in Implementing Bio-oil for Energy

Despite its potential benefits, there are challenges and limitations in adopting bio-oil as a mainstream energy source (Sharifzadeh et al., 2019). The production of bio-oil requires vast amounts of land, water, and resources. This poses a significant challenge as it competes with food production and other essential agricultural activities. The cultivation of energy crops for bio-oil extraction often leads to deforestation, which not only contributes to environmental degradation but also disrupts delicate ecosystems. The process of converting biomass into bio-oil involves complex chemical reactions that require specific conditions and catalysts. These conditions may not always be readily available or economically feasible on a large scale, limiting the widespread adoption of this technology (Singhvi and Gokhale, 2019). Additionally, different types of biomass can yield varying qualities and quantities of bio-oil due to factors like soil conditions or climate variations. This inconsistency poses challenges

for industries aiming for standardised production processes and reliable fuel quality control (Tursi and Olivito, 2021).

For the pyrolysis-process and bio-oil specifically, a major drawback of the process is its high energy consumption (Ghashghaee et al., 2019). The process requires a substantial amount of heat to reach the necessary temperatures for decomposition, which increased the overall cost of production. In addition, pyrolysis produces harmful emissions and by-products. The release of toxic gases such as carbon monoxide and nitrogen oxides during the process poses serious health risks to both humans and the environment (Cheah et al., 2023). The ash residue left behind after pyrolysis contains heavy metals and other pollutants that can contaminate soil and water sources. Another disadvantage of pyrolysis is its limited scalability. The process is often slow and inefficient when dealing with large volumes of waste materials. This makes it unsuitable for handling industrial-scale waste management needs (Mortensen et al., 2011). On the other hand, the pyrolysis-oil presents several disadvantages, such as high acidity levels, low energy density and requiring larger quantities for equivalent output when compared to traditional fossil fuels (Ghashghaee et al., 2019). Overcoming the listed challenges will require further research and development to improve production processes, enhance fuel quality control, and address environmental concerns associated with bio-oil production.

2.6 Bio-oil Upgrading

The incompatibility of bio-oil with present industrial facilities and transportation systems remains a major drawback despite the enormous potential it offers (Ruddy et al., 2014). Upgrading processes focus on improving the quality and compatibility of bio-oil to produce market-responsive biofuels and biochemicals (Hansen et al., 2020). The overall aims are to

increase heating value, stability, and miscibility with conventional fuels and decrease viscosity and corrosiveness. This can be accomplished by adding hydrogen to the oil (hydrogenation), deoxygenating the oil, and lowering its water content (Hansen et al., 2020). The improved properties obtained through upgrading make bio-oil suitable for various applications, including transportation fuels, chemical production, and heat generation (Sakka et al., 2023). Upgraded bio-oils can be blended with conventional fuels or used as standalone products, depending on their specific characteristics (Singhvi and Gokhale, 2019).

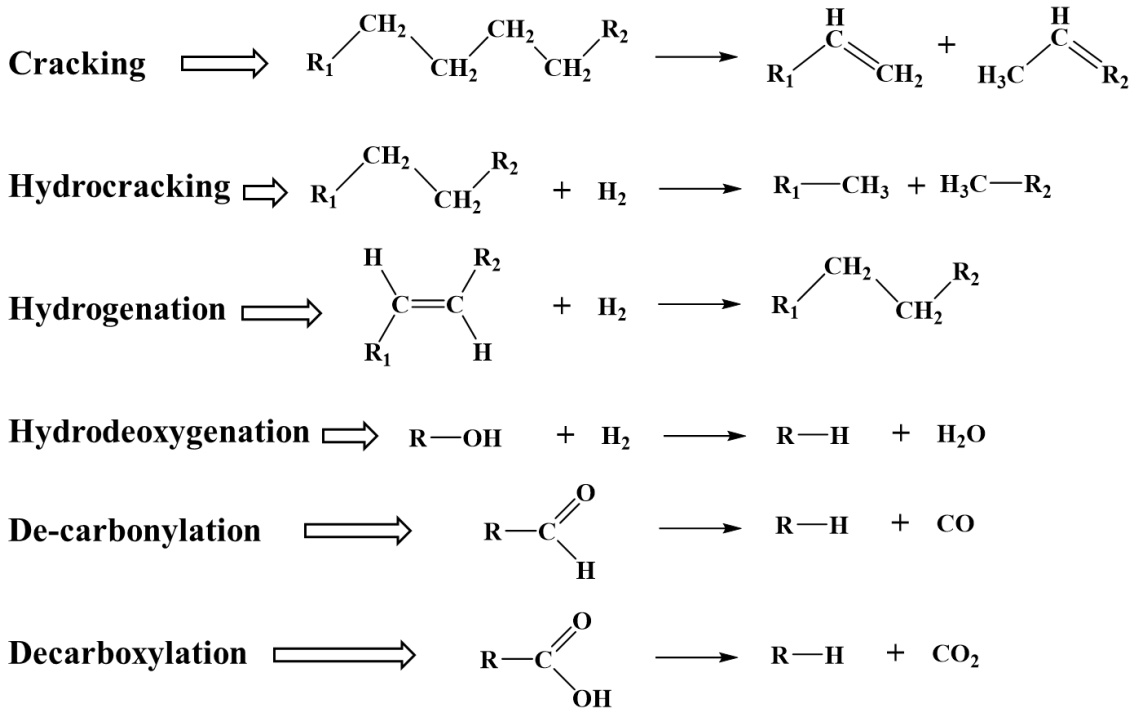

Figure 2.4: *A number of reactions that may be involved during the bio-oil upgrading process (Yang et al., 2023).*

Figure 2.4 shows the various possible reactions that take place during the bio-oil upgrading process. Several techniques that include physical and chemical methods have been used for bio-oil upgrading (Zhao et al., 2023). Some physical techniques reported include vapour filtration, molecular distillation, and emulsification (Pattiya and Suttibak, 2012; Zhang et al., 2013). The chemical methods include steam reforming, hydrogen processing, catalytic

pyrolysis, catalytic cracking, as well as solvent addition (Auersvald et al., 2017; Lee et al., 2016; Xu et al., 2019).

The hydrogen processing method consists of hydrodeoxygenation (HDO), hydrodenitrogenation (HDN), and hydrodesulfurization (HDS) processes where heteroatoms like oxygen, nitrogen, and sulphur are removed from the bio-oil. The HDO of bio-oil has been proven to be the most promising and efficient route of bio-oil upgrading. It allows the removal of oxygen in the form of water, thereby enhancing the properties of pyrolysis bio-oils (Gutiérrez-Rubio et al., 2019; Zhang et al., 2023). The process is normally carried out at a temperature of 300–600 ℃ and a high hydrogen pressure (up to 100 bar) in the presence of a catalyst (Shafaghat et al., 2015; Si et al., 2017).

2.7 Catalytic Hydrodeoxygenation (HDO)

The hydrodeoxygenation (HDO) of bio-oil is an essential process in the upgrading of this renewable energy source. This method involves the removal of oxygen-containing functional groups through catalytic reactions under elevated temperatures and pressures. These are normally achieved via hydrogenolysis of C–O bonds, which subsequently remove oxygen in the form of water (Hansen et al., 2020; Tang et al., 2021). Catalysts are employed to provide the needed activity for the reaction (Luo et al., 2019). Different catalysts have been prepared and used for the HDO reaction (Kim et al., 2022; Niu et al., 2019). Pioneering works on some bio-oil model compounds with traditional hydrodesulphurization/hydrogeneration catalysts showed encouraging results (Oh and Choi 2019). Although, in addition to the requirement to keep the catalyst in sulfated form, quick deactivation due to surface oxide formation in the presence of a large amount of water was observed (Mortensen et al. 2011; Pawelec et al. 2020; Tu et al. 2019). To tackle the shortcomings of sulfide catalysts, new

ones were developed, which include noble and transition metal catalysts (Gutiérrez-Rubio et al., 2019). These catalysts may exhibit superior activity, but are susceptible to coke formation (Keav et al., 2010). In the hydrodeoxygenation of guaiacol using noble metal catalysts, adsorption of large aromatic compounds upon the catalyst surface caused significant coking-related deactivation (Gao et al., 2014). In light of this, large-scale utilisation of these materials was hindered (Niu et al., 2019).

At milder reaction conditions, transition metals have been shown to exhibit excellent hydrogenation activity and by extension, displayed relatively little propensity for water-accelerated deactivation (Pawelec et al., 2020). This is because metal sites mostly promote the hydrogenation function while catalytic HDO of bio-oil progresses through both hydrogenation and deoxygenation. There is a need for a good catalyst support to promote the hydrogenation and deoxygenation reactions. Hence, the focus of recent research works has been to identify better solid-support candidates (Zhang et al. 2020; Zhao et al. 2020).

2.8 Most Widely Used Active Metals for Bio-oil HDO

A variety of metal catalysts, including noble metals such as Pt, Rh, Ru, and Pd, non-noble transition metals like Ni, Fe, Co, and Cu as well as bimetallic or multi-metallic complexes, have been extensively investigated for their application in HDO reactions (Yang et al., 2023). Table 2.4 presents a list the most frequently used active metals. Among these is platinum (Pt) a noble metal known for its exceptional catalytic activity and stability (Guo et al., 2021; Wu et al., 2019). Pt possesses a high resistance to poisoning by sulfur compounds, making it particularly suitable for HDO reactions involving sulfur-containing feedstocks (Shahbeik et al., 2023). Of the four noble metals (Pt, Pd, Rh and Ru) tested in the upgrading of guaiacol, Pt shows the best deoxygenation activity at optimum reaction temperature of 300 ℃ (Gao et

al., 2014). In a related study, a conversion of 99% was recorded during a selective hydrogenation of benzoic acid to cyclohexane-carboxylic acid over a Pt-based catalysts (Guo et al., 2021).

Palladium (Pd) is another commonly used metal, which shares similar catalytic properties with Pt (Gao et al., 2014). Pd-based catalysts are renowned for their high selectivity towards desired HDO products (Tang et al., 2015). Palladium supported catalysts were investigated for the HDO of phenol, o-cresol, m-cresol and guaiacol (Shafaghat et al., 2015). Therein, enhanced catalytic performance was seen following the incorporation of Pd onto the zeolite supports. In addition, it was observed that the selectivity of cresols and guaiacol towards hydrogenation reaction were totally different to that of the phenol molecule. The direct hydrodeoxygenation path was favoured due to the associated methyl group in cresol and the methoxy group in guaiacol. Meanwhile, the selectivity during cresol hydrogenation was affected by the position of the alkyl group. In a similar study, Hunns et al. (2016) reported exceptional catalytic activity and selectivity for methylcyclohexane conferred by the addition of Pd to a mesoporous ZSM-5 that was applied for the HDO of m-cresol. Numerous studies have shown that other noble metals, such as Ru and Rh, have excellent HDO activity for both bio-oil model compounds and real bio-oils (Alhanash et al., 2019; Shinde and Deshpande, 2022; Szczyglewska et al., 2020; Zhao et al., 2020).

Table 2.4: Most frequently used active metals for catalytic hydrodeoxygenation of bio-oil.

Model compound	Reactor type	Catalyst type		Conditions	Solvent	Con. (%)	Products	Ref.
		Metal (Loading)	Support					
Anisole	Batch	Ni (5 wt.%)	MCM-41, Al_2O_3	280 ℃, 48 bar H_2	Hexadecane	97	Cyclohexane, Cyclohexyl methyl ether	(Molina-Conde et al., 2023)
Anisole	Batch	Ni (5 wt.%) Co (5 wt.%)	ZSM-5	220 ℃, 50 bar H_2	Decalin	99	Cyclohexane, methyl-cyclopentane, benzene, phenol, cyclohexene, dimethyl ether	(Sankaranarayanan et al., 2015)
Anisole	Batch	Ni (5 wt.%)	ZSM-5, Hie-ZSM-5, HSZ-b, HSZ-c	200 ℃, 68 bar H_2	n-decane	3, 55, 94, and 98	Methoxy-cyclohexane, cyclohexane	(Li, et al., 2020)
Anisole	Batch	Ru (1 wt.%)	SBA-15 SBA-16 MCM-41	130 ℃, 60 bar H_2		100, 100, and 75	Methoxy-cyclohexane, cyclohexanone, cyclohexanol, cyclohexene toluene, 1,1–dimethoxy cyclohexane, benzene	(Szczyglewska et al., 2020)
Anisole	Fixed-bed	Ni (5 wt.%)	BEA, MOR	500 ℃, 40 bar H_2		-	Toluene, cyclohexane, methylcyclohexane	(Yan et al., 2021)
Anisole	Batch	Ru-MoFeP (wt.%)	Al_2O_3	250 ℃, 50 bar		45–100	Cyclohexane, methyl-cyclohexane, benzene, methyl-benzene	(Ma et al., 2023)

Acetic acid	Fixed-bed	Cu (5 wt.%), Ni (1.5 wt.%)	SiO_2	300 ℃, 36 bar		7	Methane, methanol, ethane, ethyl acetate	(Ezeonu et al., 2023)
Benzoic acid	Batch	RuSn (5, 29 wt.%)	Al_2O_3	240 ℃, 88 bar	Dioxane	40	Benzyl alcohol	(Shinde and Deshpande, 2022)
Benzoic acid	Batch	Pt (5 wt.%)	TiO_2	25–80 ℃, 1–50 bar	Hexane, water, acetic acid	10–99	Cyclohexane carboxylic acid	(Guo et al., 2021)
Benzoic acid	Batch	RuPd (1 wt.% each)	C	85 ℃, 1–10 bar H_2	Water	52–100	Benzyl alcohol, cyclohexane carboxylic acid	(Tang et al., 2015)
Guaiacol	Batch	Co, Ni	C	180 ℃, 20 bar H_2	Isopropanol	95	Cyclohexanol, 2-methylcyclohexanol	(Chen et al., 2023)
Guaiacol	Batch	Co, Ni	SiO_2, ZrO_2	240 ℃, 10 bar H_2	Octane	100	Cyclohexane, cyclohexanol	(Tian et al., 2022)
Vanillin	Fixed bed	Ni, Mo	Al_2O_3	350 ℃, 9 bar H_2S in H_2	Xylene	99.9	Cresol	(Kristensen et al., 2022)
Vanillin	Batch	Ni (15 wt.%)	Biochar	100–150 ℃, 30 –50 bar	2-propanol	97	Vanillin alcohol, p-creosol	(Mudi et al., 2023)
Phenol	Batch	Ni (15 wt.%)	SiO_2 ZrO_2 Al_2O_3	200 ℃, 3.45 bar, H_2	Water	52, 18, 13	Methylcyclopentane, 2-methyl-1-butanol, 2,2-dimetoypropane, cyclohexanol, propioaldehyde	(Lestari et al., 2019)
Phenol	Batch	Pt (3 wt.%) Ir (3 wt.%)	ZSM-5	200 ℃, 30 bar H_2	Tetralin	60	Cyclohexane, methylcyclopentane, benzene, cyclohexanol	(Pawelec et al., 2020)

		Pt-Ir (3wt.%)						
Phenol	Fixed bed	-	ZSM-5	350 – 500 ℃	-		Benzene, toluene, anisole, phenol	(Venkatesan et al., 2021)
m-cresol	Batch	Ni_2P (10 wt.%)	hie-ZSM-5	200 ℃, 25 bar H_2	Dodecane	92	Methylcyclohexane, toluene, methylcyclohexanol	(Berenguer et al., 2018)
m-cresol	Fixed- bed	Pt (1 wt.%)	NaHB	250 ℃, 1 bar		100	Toluene, methylcyclohexanone, methylcyclohexane, ethylcyclopentane, dimethylcyclopentane	(Wu et al., 2019)
Methyl isobutyl ketone (MIBK)	Batch	Rh or Pt or Ru or Ag (2 wt.%)	CsPW	170 ℃, 10 bar H_2	Solvent free	10	2-methylpentane	(Alhanash et al., 2019)
Glucose	Batch	Ni-Fe, Co-Fe (0.5 wt.%,4 wt.%)	SiO_2	350 ℃, 3.1 bar with He/ H_2	1-methyl-naphthalene	82.7	2-methylfuran, 2,5-dimethylfuran, 5-methylfurfural, furfural	(Rogers and Zheng, 2019)
Glucose	Batch	Ni	- Al-alloy	150 ℃	Methanol	100	Fructose, sorbitol, mannitol	(García et al., 2019)
Glucose	Batch	Ru (3.5–5 wt.%)	MCM- 48	190 ℃, 50 bar H_2	n-decane- water mixture	56.6, 29.2	Butane, methylcyclopentane, pentane, hexane, 2,5-dihydroxymethylfuran, Hexanol, cyclopentane, cyclohexane, 2-hexanone, isosorbide, and 1,4-sorbitan	(Romero et al., 2019)
Fructose	Batch	Sn, Zr, or Fe	H-Beta	170 ℃	Valero-	98	Furfural	(Luxin Zhang et al.,

					lactone/water			2017)
Xylose	Batch	Zn-Cr (1 – 1 wt.%)	ZSM-5	400 ℃, 10 bar CH_4	None		Furan and alkyl furan, benzene, toluene, ethylbenzene and xylene, naphthalene, phenolic	(Peng et al., 2019)
Xylose	Batch	Sn- sulfonated	Diatomite	170 ℃	Biphasic	89	Furfural	(Jia et al., 2019)
Guaiacol and propionic acid blend	Batch	Ni (5 wt.%)	ZSM-5, h-ZSM-5, SBA-15, Al-SBA-15	260 ℃, 40 bar H_2	Decalin	>99 guaiacol, 75 propionic acid	Cyclohexane, methyl cyclopentane, dimethyl ether, cyclohexane diol, methane	(Sankaranarayanan et al., 2018)
Eugenol, acetic acid, furfural, and ethylene glycol blend	Batch	Ni (22 wt.%)	Al-SBA-15, ZSM-5	260 ℃, 30 bar H_2	n-docane	-	Methyl-propyl-cyclopentane, cyclopentane, propyl-cyclohexane, propyl-cyclopentane, methyl-cyclohexane, methyl-hexane, others	(Chen et al., 2020)
Bio-oil	Batch	Ni, Mo	Al_2O_3	350–400 ℃, 80 bar H_2	-	-	Aliphatic (24%), aromatics (28%), polyaromatics (11%), N-containing compounds (14), phenols (7%), others (16%)	(Heracleous et al., 2022)
Bio-oil	Batch	Ru	NbOPO4	170 ℃, 50 bar H_2	Hexane	93	Hydrocarbons (88%)	(Zhao et al., 2020)

Beyond noble metals, non-noble transition metals such as nickel (Ni) have also been extensively explored as potential catalysts for HDO processes (Molina-Conde et al., 2023). Nickel-based catalysts offer distinct advantages including low cost and abundance compared to noble metals (Shahbeik et al., 2023). Although they may exhibit lower activities than noble metal counterparts, Ni- or non-noble transition metal-based catalysts can be optimized through various strategies such as alloying with other metals, modifying their surface structures or introducing a good support material to enhance their catalytic performance (Li, et al., 2020). The hydrodeoxygenation of ketone over Cr, Fe, Co, Ni, and Cu based catalysts was conducted by Witsuthammakul and Sooknoi (2015). The outcome demonstrated that Ni and Cu were only active when temperature was above 100 ℃ and that 100% selectivity to alcohol was attained on the two catalysts at optimal ketone conversion. Unlike Cu, the Ni-based catalyst improved both hydrogenation and hydrogenolysis at lower reaction temperature (175 ℃).

Bimetallic and multi-metallic catalyst systems have gained significant attention in recent years due to their synergistic effects on catalytic activity and selectivity (Ma et al., 2023). The combination of different metals within a single catalyst structure allows for enhanced reactivity towards specific reaction pathways, thereby promoting the desired HDO outcomes (Heracleous et al., 2022; Rogers and Zheng, 2019). For instance, a bimetallic catalyst comprising Ru and Pd have been shown to exhibit improved catalytic performance during selective hydrogenation of benzoic acid compared to their monometallic counterparts (Tang et al., 2015). Incorporation of Co as a second metal to the Fe/SiO_2 catalyst stabilized Fe by forming a Co-Fe alloy. This, subsequently, enhanced catalytic activity and stability during the deoxygenation of glucose (Rogers and Zheng, 2019). When a small amount (1.5 wt.%) of nickel metal promoter was applied to the surface of copper on the Cu/SiO_2 catalyst, the rate

of production of ethanol increased by more than an order of magnitude during the HDO of acetic acid (Ezeonu et al., 2023). Ramírez et al. (2019) prepared bimetallic Pd-Ru and Pt-Ru catalysts via incipient wetness impregnation on zeolite Y. When the catalysts were tested for the esterification of 5-hydroxymethylfurfural to 5-acetoxymethylfurfural, pure zeolite showed the highest conversion and selectivity of 87.28% and 71.29%, respectively. However, palladium exhibited better metal-support interaction. In a related study, a reduced rate of hydrogenolysis of alcohol intermediates was seen on Cu-Ni alloy catalysts compared to monometallic Cu and Ni catalysts (Witsuthammakul and Sooknoi, 2015). Similarly, conversion was not recorded during the HDO of guaiacol over Co/SiO_2-ZrO_2 after a 4 h reaction at 240 ℃ (Tian et al., 2022). While the Ni/SiO_2-ZrO_2 catalyst showed 100% guaiacol conversion with a selectivity of 51.9% to cyclohexane, a bimetallic $CoNi/SiO_2$-ZrO_2 catalyst gave 100% conversion and 99.9% selectivity to cyclohexane.

In summary, it is obvious that different metals offer unique advantages in terms of catalytic activity, stability, selectivity, and resistance to deactivation. The choice of metal for catalyst preparation depends on the specific requirements of the HDO process and the nature of the biomass-derived feedstock being treated. However, it should be noted that although noble metals such as Pd, Pt, and Ru produce highly efficient catalysts for bio-oil upgrading, they can also be costly and hydrocarbon-selective (Shafaghat et al., 2015). Meanwhile, catalysts supported by non-noble metals like Ni, Co, Zn, and Mo have the potential to be produced at low-cost, and that they are effective and can be applied at higher temperatures (Shahbeik et al., 2023).

2.9 Catalyst Support Materials

A number of catalyst supports have been investigated in the quest to enhance catalytic performance in bio-oil HDO (Chaihad et al. 2019; Lawal et al. 2019; Liu et al. 2017; Pawelec et al. 2020; Zhao et al., 2020). Activity of a catalyst during HDO reaction is greatly influenced by the acidity and pore structure of a support (Nesterov et al., 2021; Saidi and Safaripour 2022; Szczyglewska et al., 2020). In comparison to metal-microporous support catalysts, metal-mesoporous support catalysts have shown remarkable performances in the HDO of bio-oil. This was attributed to the improved diffusion properties and enhanced metal-support interactions (Li set al. 2020; Niu et al., 2019). For instance, in the HDO of guaiacol using nickel-based bifunctional catalysts, mesoporous Ni/HBeta was more selective to aromatics than microporous Ni/ZSM-5 (Li et al., 2020). Bhoi et al. (2020) reported the HDO of glycerol over Pt and Pd based ZSM-5 and SiO_2 catalysts. Therein, superior catalytic activity was observed on Pd/ZSM-5 as against SiO_2 supported catalyst. The HDO of anisole using natural zeolites (BEA and MOR) supported Ni catalysts revealed that both metal and acid sites are required for the reaction. The transformation of anisole to cyclohexane was made possible by the strong Brønsted acid sites and several small Ni species over 5%Ni/BEA (Yan et al., 2021). Ma et al. (2019) upgraded a mixed bio-oil sample using 5% Ru loaded activated carbon, Al_2O_3, and ZSM-5 in a Parr reactor at 350 ℃ and 38 bar H_2. Selectivity of 8% and 32% for alkenes and benzene were noted on Ru/ZSM-5 catalyst. Niu et al. (2019) synthesized and tested both conventional microporous and mesoporous ZSM-5 supported on platinum for guaiacol upgrading. The outcome of the catalytic test demonstrated enhanced activity and excellent stability of the catalyst from the mesoporous support. Similarly, hydrodeoxygenation of a blend of guaiacol and propionic acid on the mesoporous Ni/ZSM-5 and Ni/Al-SBA-15 was reported. Ni/ZSM-5 showed a conversion of nearly 100% sand produced a high quality bio-oil product (Sankaranarayanan et al., 2018).

2.9.1 Potentials of mesoporous supports

Extensive studies have been carried out on porous materials particularly on the aspect of application in catalysis, adsorption and energy storage. Generally, these materials are classified into three main groups based on their pore size, namely; microporous (< 2 nm), mesoporous (2 – 50 nm) and macroporous (> 50 nm) (Zaarour et al., 2014). The need to design catalysts with controlled pore structure, pore size as well as acidity encourages researchers to focus on the development of new catalysts materials known as hierarchical materials (Lu et al., 2015). In hierarchically structured porous materials, the micropores provide size and shape selectivity for guest molecules, the mesopores increase micropore accessibility, and the macropores provide unimpeded transport paths. The high ranging application of these materials can easily be linked to a high surface area and how easily the materials can be functionalized for catalytic application (Nada et al., 2019). However, mesoporous materials are mostly amorphous solids that possess lower activity compared to zeolite, although the two have similar periodic structure their framework varies greatly (Čejka and Vinu, 2009). Materials such as SBA-15 and MCM-41 exhibited a remarkable mass transfer efficiency. Unfortunately, their poor thermal stability and weak acidity hindered their wide applications in catalysis (Zhu et al., 2013).

Zeolites are microporous aluminosilicate materials that can be modified to form a new version of mesoporous materials. These materials combine the synergetic effect of large pores, large surface area and amorphous wall saturated with hydroxyl groups readily available for the generation of active sites needed for catalytic reaction (Čejka and Vinu, 2009). Mesoporous zeolites have been identified as an important class of materials responsible for improved catalytic performance in a number of reactions compared to their microporous counterparts (Caicedo-Realpe and Pérez-Ramírez, 2010; Hosseinpour et al.,

2020; Xu et al., 2018). Incorporation of secondary pores (mesopores) in the zeolites modifies the acid site distribution and provides room for greater metal-support interaction and dispersion, in addition to improving accessibility and the transfer of species to or from the catalytic active sites (Hosseinpour et al., 2020; Hunns et al., 2016). One key function of acid sites is to activate reactant molecules by protonating or coordinating them. The energy barrier needed for a reaction to occur is lowered by this activation, thereby increasing the reaction rate (Berenguer et al., 2019). Acid sites also act as binding centres for reactant molecules, holding them in close proximity to each other and facilitating their interaction (Zhao et al., 2023). Similarly, metal sites provide active centres for reactant adsorption and subsequent transformation. They normally act as weak acid sites, producing an increase in the polarisation of the reactive bonds of reactants (Albero and García, 2016).

2.9.2 Preparation of mesoporous zeolites

There are several attempts to construct mesopores in convectional zeolites (Berenguer et al., 2018; Dauda et al., 2020; Ivanova et al., 2011; Li et al., 2020; Ni et al., 2011; Sadowska et al., 2013; Xu et al., 2018). This has been achieved by adopting two basic methodologies; either direct synthesis using templating strategies (Che et al., 2019; Zhu et al., 2013) or via post synthesis treatment of a microporous zeolite (Feng et al., 2018). Recently, some researchers have reported a successful synthesis of this material in the absence of a structure-directing agent (template-free synthesis). Presented in Figure 2.5 is a schematic summary of the four main routes through which this special material can be designed. These include hard or soft templating, post-synthesis modification, and assembly (stacking) of zeolite catalyst crystals (Xu et al., 2018).

Mesoporous Zeolites Preparation				
	Hard templating	**Soft templating**	**Post synth. modification**	**Assembly of zeolite crystals**
Route	*-Removable porous or nonporous solid material*	*-Bifunctional surfactants* *-Organosilanes* *-Reverse micelles*	*-Demetalition by acid/base steaming treatment*	*-Dealumination* *-Assembly of aggregation or intergrowth*
Scheme	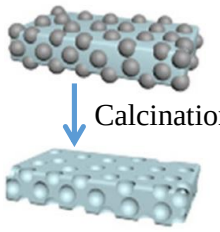	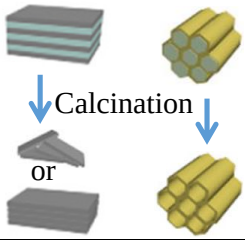	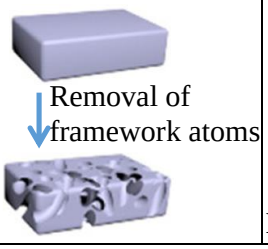	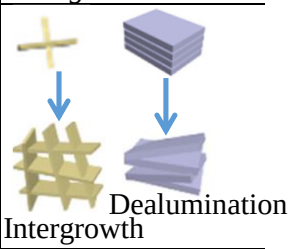

Figure 2.5: *Schematic representation of the different strategies for the construction of mesoporous zeolites (Xu et al., 2018).*

2.9.2.1 Direct synthesis

Synthesis of mesoporous zeolite from primary reagents also known as 'bottom-up' is considered as a non-destructive approach of mesopores construction in zeolites. This can be achieved with or without the addition of a mesoporous surfactant (structure-directing agent) to the synthesis recipe at a gel formation stage (Zhao et al., 2020). Unlike in some post-synthesis modifications, here, the tendency of structural collapse due to the formation of mesopores is completely eliminated and the zeolite skeleton and crystallinity preserved (Che et al., 2019). Several studies describe the preparation of this material using different structure-directing agents (Goodarzi et al., 2020; Petushkov et al., 2011; Zheng et al., 2011). Table 2.5 presents a summary of some of these methods.

Goodarzi et al. (2020) in an attempt to design a catalyst with an improved lifetime synthesized a mesoporous ZSM-5 using carbon black particles (BP-2000) as structure-directing agent. The catalyst was applied in methanol to hydrocarbon conversion on a fixed-bed reactor where enhanced catalytic activity and extended catalyst lifetime were recorded.

Table 2.5: Template-assisted mesoporous zeolite synthesis.

Zeolite type	Template used	Application	Remarks	Ref.
ZSM-5	Carbon black particles (BP-2000)	Methanol to hydrocarbon	Prolong catalyst lifetime and activity recorded	(Goodarzi et al., 2020)
ZSM-5	Sucrose, cellulose and starch (Green templates)	Sawdust pyrolysis	ZSM-5 synthesized using starch as template showed the best mesopore volume of 0.359 cm^3 g^{-1}. hence the highest activity and BTX yield.	(Che et al., 2019)
ZSM-5 β-zeolite	Tetrapropylammonium hydroxide (TPAOH)	Hydrodeoxygenation of phenol	ZSM-5 support shows superior performance attributable to higher metal dispersion and incresed access to active sites.	(Berenguer et al., 2019)
ZSM-5	Tetrapropylammonium hydroxide (TPAOH) + Silanization agent	Hydrodeoxygenation of guaiacol and propionic acid blends	Mesoporous ZSM-5 shows an outstanding HDO activity of about 100% in addition to high estrification efficiency.	(Sankaranarayanan et al., 2018)
ZSM-5	Tetrapropylammonium hydroxide (TPAOH)	Hydrodeoxygenation of m-cresol	Mesoporosity improve metal dispersion and the catalytic activity remarkably	(Berenguer et al., 2018)
ZSM-5	3-glycidoxypropyltrimetho x- ysilane (KH-560)	Methanol to aromatics	The catalyst exhibited high crystallinity, large BET surface and volume, high selectivity to BTX and longer lifetime.	(Jia et al., 2017)
ZSM-5	Cetyltrimethyl ammoniumbromide (CTAB)	Aromatization of Dimethy Ether	In addition to improved stability, mesoporous zeolite has the highiest aromatic selectivity of 85%.	(Lu et al., 2015)
ZSM-5	Tetrapropylammonium hydroxide (TPAOH)	Hydrodeoxygenation of anisole	Hierarchical ZSM-5 outperformed other mesoporous supports and reaveled a promising activity.	(Sankaranarayanan et al., 2015)
ZSM-5	Organosilane (TPOAC)	Selective oxidation of enzene to phenol	Introducing Fe to the mesoporous zeolite incresaes its crystallinity, activity and product turnover.	(Koekkoek et al., 2011)

In a similar study, Petushkov et al. (2011) reported a one-step approach for the synthesis of mesoporous zeolite. Therein, one type of TPA^+ cation was utilized as the template material. The effects of hydrothermal crystallization temperature, synthesis duration and pH of the reacting mixture on the extent of mesoporosity and crystal size were investigated. The results vindicated the aforesaid parameters as the key players in determining the properties of the final material. Highest degree of mesoporosity was exhibited by ZSM-5 sample with an average crystal size of 6.4 nm and 122 $m^2\ g^{-1}$ external surface area.

The quest to minimize the negative environmental impact, cut down cost of production and substitute the hazardous organic templates motivated researchers to look for a green alternative. Che et al. (2019) disclosed a successful synthesis of mesoporous ZSM-5 using starch as a structure-directing agent. The material was applied to improve aromatics production during biomass pyrolysis and the outcome revealed positive correlation between the quantity of BTX produced and the mesoporous volume. Optimal starch loading of 10% gave the best porosity, acidity and catalytic activity. A significant increase in stability which was attributed to the existence of mesopores in Zn/Mo based ZSM-5 during the aromatization of dimethyl ether was reported (Lu et al., 2015). Compared with the traditional ZSM-5, the mesoporous material prepared with cetyltrimethyl ammoniumbromide (CTAB) as an organic template shows aromatic selectivity of 85% against 53% obtained on the microporous zeolite. Koekkoek et al. (2011) employed octadecyl-(3-trimethoxysilylpropyl)-ammonium chloride (TPOAC) to synthesize an MFI (Mobil-type Five) type zeolite with high degree of mesoporosity. It was revealed therein that incorporation of Fe into the zeolite improved the crystallinity. More so, initial catalytic activity and turnover number during selective oxidation of benzene increased with increased crystallization time. However, contrary to the Koekkoek's discovery on the effect of addition of metal on the zeolite crystallinity is the

report of Berenguer et al. (2018). There, hydrogenation of model bio-oil compound was carried out over a mesoporous zeolite catalyst synthesized using tetrapropylammonium hydroxide (TPAOH). Incorporation of metal did not indicate any significant impact on the zeolite crystallinity. Nevertheless, mesoporosity enhances metal dispersion and improved the turnover frequencies of the products. An extension to that is another work in which hierarchical ZSM-5 and zeolite β were synthesized with the aid of TPAOH template and compared in the catalytic HDO of phenol. Superior catalytic activity recorded on ZSM-5 was attributed to the mesopores that provided better metal dispersion and easy access to the active sites (Berenguer et al., 2019).

Jia et al. (2017) prepared a hierarchical ZSM-5 via hydrothermal procedure using 3-glycidoxypropyltrimethoxysilane (KH-560) as the structure-directing agent. The zeolite was characterized using XRD, SEM, TEM, ICP, NH_3-TPD, Py-IR and FTIR techniques. High crystallinity, small crystal size, high BET surface area and volume with more strong acid sites were observed from the results. In addition, the material exhibited high selectivity to aromatics and longer lifetime during methanol conversion. In 2015 Sankaranarayanan and coworker applied mesoporous ZSM-5 prepared using TPAOH in combination with silanization agent for the upgrading of anisole. The catalytic activity of the zeolite was compared with other mesoporous materials; namely, SBA-15 and Al-SBA-15 respectively. Extensive hydrodeoxygenation, isomerization as well as hydrodearomatization occurred over ZSM-5 supported catalyst. Further studies by Sankaranarayanan et al. (2018) examined these mesoporous catalysts for HDO of a blends bio-oil model compound. Among the three, ZSM-5 shows superb HDO activity of about 100% and high level of esterification, hence, a very promising candidate for bio-oil upgrading processes. Recently, Li et al. (2020) reported a template-free synthesis of mesoporous ZSM-5. This was achieved via ‘segmented steam-

assisted crystallization', a process in which the crystallization rate is tuned at a stage of transformation between amorphous to crystalline structures in the material. BET analysis conducted on the synthesized sample confirmed the formation of hysteresis loops that are evidence of mesoporosity. High external surface area (222 m^2 g^{-1}) was recorded, however, low crystallinity was seen on the meso-ZSM-5 compared to micro-ZSM-5 counterparts.

2.9.2.2 Post synthesis modification

There are quite a number of research studies that have been carried out to modify the morphology and structure of existing microporous zeolite such as MFI, BEA (Beta zeolite), and FAU (Faujasite) with the aim of improving their performances in catalytic reactions. This method is also known as 'top-down' procedure for hierarchical materials design which is achieved either by acid treatment (dealumination), alkaline treatment (desilication) or combination of the two. It is desired to obtain well-arranged and ordered mesopores closer to what is achievable from bottom-up approach. This inspired researchers to combine the alkali and/or acid treatment with a structure-directing agent (Wang et al., 2019).

Mesoporous ZSM-5 was prepared by NaOH desilication and applied for methanol to gasoline conversion. The outcome suggested that the mesopores enhances active metal dispersion and improve the coke tolerance capacity of the catalyst (Ni et al., 2011). In a related development, a study conducted by Dauda et al. (2020) was able to demonstrate the optimum NaOH concentration (0.2 M) that provides better silicon-aluminium arrangement, proper mesoporosity and catalytic activity. Nevertheless, Losch et al. (2017) emphasized that, depending on the target application, a particular treatment option has to be selected to optimize catalytic activity and maximize stability. In their work Sadowska et al. (2013) reported a proposed zeolite desilication mechanism and further postulated that during alkaline

treatment Al is extracted from the zeolite framework and eventually reinserted on the zeolite external and/or inner surface. Ideally, the external surface of the zeolite should be enriched with Al after desilication. However, the value of Si/Al ratios for both the surface and bulk of the zeolite treated with 0.1 M and 0.2 M NaOH were practically similar to the parent zeolite. This is contrary to the expectation that the surface will be dense in Al. Hence it can be presumed that the Al debris and some extra framework silica still remain within the created mesopores of a zeolite after desilication.

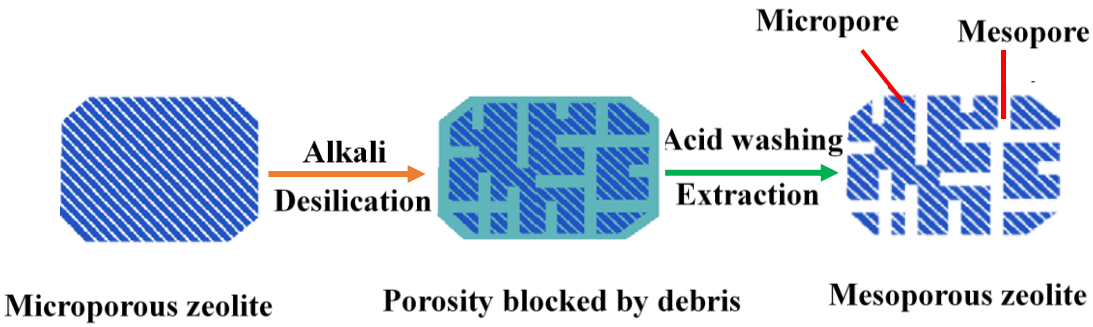

Figure 2.6: *Schematic representation of hierarchical zeolites preparation by two-step route (Sadowska et al., 2013).*

A two-step route, as shown in Figure 2.6, was reported in which microporous zeolite was first treated with alkali followed by acid washing to remove the alumina debris and create secondary mesopores. The results confirmed the generation of 3–4 times surface area in the modified ZSM-5 when compared with the parent zeolite. In addition, the acidity and crystallinity of the material were well-preserved. Unlike the alkali treatment alone, the second step help immensely in regenerating the occupied mesopores (Caicedo-Realpe and Pérez-Ramírez, 2010). In his work Qin et al. (2011) prepared mesoporous zeolite Y by dealumination using ammonium hexa-fluorosilicate (AHFS) and by sequential sodium hydroxide desilication followed by AHFS dealumination. Material with non-uniform

mesopores largely blocked by silicon deposit was obtained from dealumination. The sequential treatment gives a material with better silica-alumina distribution and higher mesoporosity. These facilitate molecular transport and easy access to the active site during catalytic reaction.

Table 2.6: Physio-chemical properties of zeolite treated with different concentration of NaOH and in NaOH/TBAOH (Sadowska et al., 2013).

NaOH conc.	**(Si/Al)*bulk***	**(Si/Al)*suf.***	**S*meso***	**V*meso***	**V*micro***
			($m^2 g^{-1}$)	**($cm^3 g^{-1}$)**	**($cm^3 g^{-1}$)**
0.0 M	31.6	25.0	59	0.068	0.105
0.1 M	24.4	18.2	79	0.147	0.127
0.2 M	18.3	14.2	124	0.225	0.119
0.5 M	4.4	4.4	140	0.271	0.062
0.2 M + TBAOH	22.7	19.6	206	0.275	0.075

In a similar work, mesopores were incorporated into the zeolite via hydrothermal crystallization in aqueous solution of ammonia and by the desilication method (Wang et al., 2019). The catalyst was tested in the aromatization of bio-oil model compound. While cracking dominated on the microporous catalyst, treatment in ammonium environment gives large surface area, small pore volume with narrow channels, hence, lower aromatics yield. Addition of CTAB into the ammonium environment yielded a mesoporous material with relatively small surface area and volume compared to the one obtained from TPAOH assisted desilication. The alkali treated sample produced ordered mesopores that exhibit both large surface area and volume, this was linked to the highest aromatics yield recorded and extended catalyst lifetime seen. It is evident from Table 2.6 that desilicating the zeolite with 0.5 M and

1.0 M NaOH resulted in excessive extraction of intra-crystalline Al, 18% and 63%, causing significant loss of crystallinity. The NaOH treatment gives material with high surface area and pore volume (large diameter). Although, combination of NaOH/TBAOH produced the highest surface area and pore volume, the produced material is dominated by narrower pores.

2.10 HDO of bio-oil Model Compounds

Basically, HDO is classified into two categories: low-temperature HDO and high-temperature HDO (Kadarwati et al., 2017). In the low temperature (175–250 ℃) process, highly unstable oxygenated compounds such as acids are normalised and dissolved water is expelled to enhance energy dispassion. Whereas the high-temperature process (350–400 ℃) involves the total transformation of oxygenated compounds into aromatics and higher carbon-chain alkanes (Bashir et al., 2022). However, due to the complexities of the components in bio-oils, researchers use model compounds instead of real bio-oils to study HDO mechanisms. The study of model compounds is essential because it provides vital information on the reaction pathways and kinetics associated with a particular model compound or functional group.

On the other hand, the study of real bio-oil is also important. It explains a great deal of the additive or inhibitory effects that originate from the complex combinations' interweaving interactions (Kay-Lup et al., 2017; Ruddy et al., 2014). While a small amount of a substrate is needed for the HDO of a model compound, a large quantity is required for the HDO of a real bio-oil. This is to enable adequate evaluation of the fuel's quality (Yu, et al., 2016). It is believed that studying model compounds could serve as a crucial first step in developing more efficient ways to upgrade real bio-oils.

Figure 2.7 gives a summary of the reaction pathways and most likely products during the HDO of the major oxygenate compounds in bio-oil. Phenolics are highly reactive compounds, their presence in pyrolysis bio-oil majorly contribute to the undesirable properties (Shafaghat et al., 2015). Consequently, the HDO of phenolic model compounds has been widely explored. A series of transformations along distinct reaction pathways during the HDO of phenolic compounds have been reported (Zhao et al., 2023). One prevalent pathway is hydrogenation (HYD), wherein hydrogen atoms from co-fed reactants selectively replace oxygen atoms within the phenolic structure (Sirous-Rezaei et al., 2019).

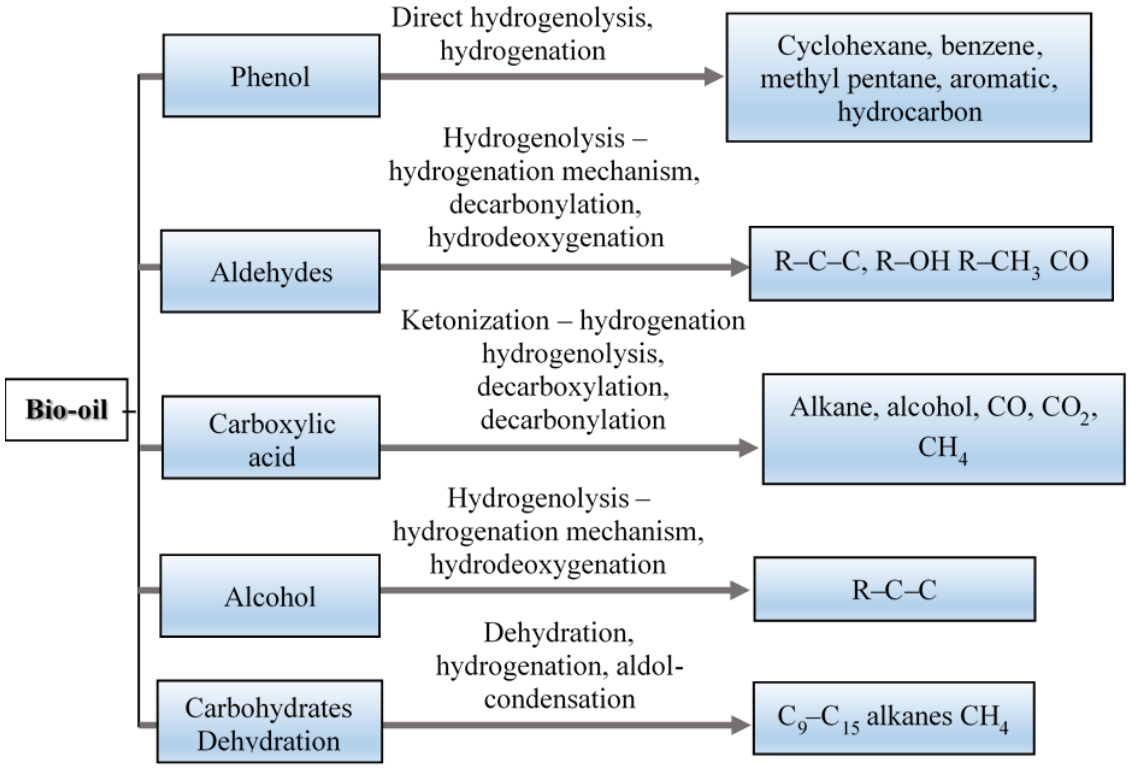

Figure 2.7: *A general summary of the HDO pathways for major oxygenate compounds in bio-oil (Oyedun et al., 2020).*

This process is often facilitated by transition metal-based catalysts possessing high hydrogenation activity. The resulting hydroxylated intermediates are crucial intermediates that further participate in subsequent steps (Sirous-Rezaei et al., 2019). Another

transformation route involves direct C-O bond cleavage via deoxygenation reactions (DDO). This pathway is typically observed when employing catalysts with high metal dispersion and strong metal-support interactions. The C-O bond is selectively broken, resulting in the formation of aromatic hydrocarbons or cyclic alkenes (Berenguer et al., 2018). Additionally, ring-opening reactions catalysed by acid sites present on certain zeolite-based materials or solid acids were reported (Wang et al., 2020; Pawelec et al., 2020). In this pathway, acid sites facilitate protonation of specific carbon atoms within the aromatic ring structure of phenol, followed by the cleavage of carbon-oxygen bonds. This results in the formation of carbonyl compounds or alcohols that can be subsequently subjected to further hydrogenation or dehydration steps (Zhao et al., 2023).

Figure 2.8 presents the various reaction pathways of some phenolic model compounds; guaiaicol (a), phenol (b), o-cresol (c), and m-cresol (d). Li et al. (2020) investigated the HDO of guaiacol over Ni/ZSM-5 catalyst. It was observed that the direct deoxygenation was the most favoured reaction route. Guaiacol HDO mainly follows the guaiacol to anisole with acid sites through dehydration, then cyclohexane formed by hydrogenation. At the initial stage of the reaction only anisole was seen. This implies that the Ni/ZSM-5 catalyst easily removes methoxy group. Hydroxyl group is regarded as the major oxygen group to be eliminated by DDO. However, a trace amount of cyclohexanol was recorded.

As reported by Sirous-Rezaei et al. (2019), the HDO of phenol over $PdReO_X/ZrO_2$ catalyst starts with the formation of keto-tautomer intermediates (cyclohexadieneones). Two possible routes are available to proceed from there; formation of cyclohexadiene via hydrogenation of carbonyl group, which subsequently generates benzene through dehydration (path I). The second route (path II) progresses via sequential hydrogenation of phenolic to cyclohexanone

to cyclohexanol followed by dehydration and further hydrogenation of cyclohexene to produce cyclohexane. In a related study, a methyl-cyclopentane was seen during the HDO of phenol over Pt/ZSM-5 catalyst (Pawelec et al., 2020). Formation of methyl-cyclopentane is an indication of ring-opening reactions catalysed by acid sites present on the Pt/ZSM-5 (Wang et al., 2020). The aromatic ring structure of phenol is made easier to protonate by acidic sites of Pt/ZSM-5, which is followed by the breaking of carbon-oxygen bonds. As a result, carbonyl compounds or alcohols are formed, which can then undergo further hydrogenation or dehydration (Zhao et al., 2023).

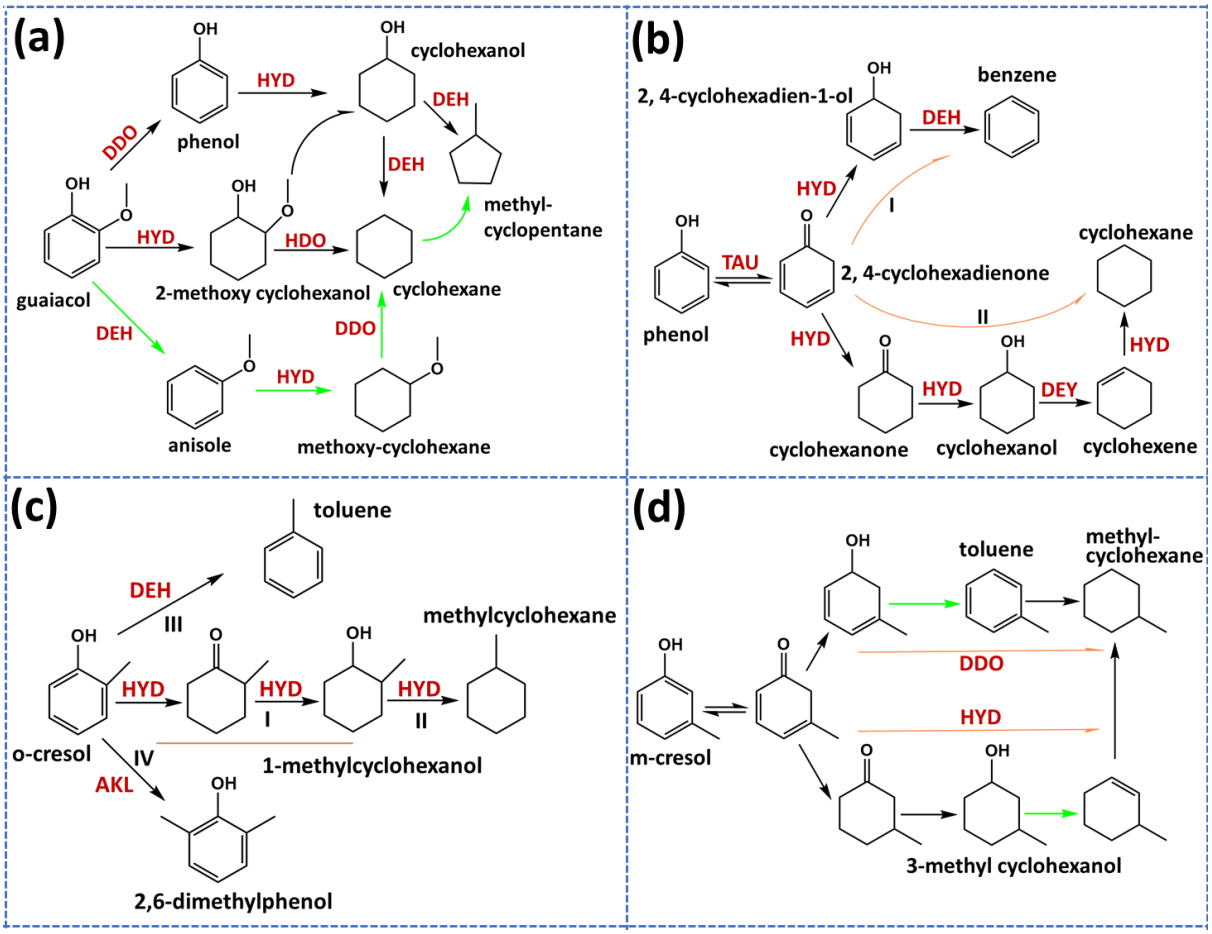

Figure 2.8: *Reaction pathways for the HDO of some phenolic compounds: (a) guaiacol over mesoporous Ni/ZSM-5 catalyst (Li et al., 2020), (b) phenol over $PdReO_X/ZrO_2$ catalyst (Sirous-Rezaei et al., 2019), (c) o-cresol over Pd/C-Zeolite catalyst (Shafaghat et al., 2015), and m-cresol over mesoporous Ni_2P/ZSM-5 catalyst (Berenguer et al., 2018).*

Cresol is another model compound normally employed for bio-oil HDO research (Wu et al., 2019). There are three isomers of cresol: o-cresol, m-cresol, and p-cresol. They are classified based on the position of the methyl group on the phenolic compound. Hydrogenation and dehydration are the two major reactions during cresol HDO, while toluene and methylcyclohexane are the two valuable products normally obtained (Shafaghat-Rezaei, et al., 2015). The reaction pathways for the HDO of o-cresol over Pd/C-Zeolite catalyst are shown in Figure 2.8(c). When Pd/C was used without the zeolite, the HDO reaction only covered route I, which is the hydrogenation of the cresol to form 2-methylcyclohexanone and subsequently 2-methylcyclohexanol. However, adding zeolite to the catalyst formulation enhanced the activity by promoting the dehydration of 2-methylcyclohexanol to generate methyl cyclohexane, route II (Shafaghat-Rezaei et al. 2015). In a related study using a mesoporous Ni_2P/ZSM-5 catalyst, Berenguer et al. (2018) show the hydrogenation (HYD) pathway as the most preferred transformation route since only a trace of toluene was recorded.

Another phenolic compound widely applied for investigating bio-oil HDO is anisole (phenolic ether) (Molina-Conde et al., 2023). Figure 2.9 presents a general reaction network for anisole HDO. The various step include Demethylation-dealkylation, I; direct deoxygenation, II; hydrogenation, III; isomerisation, IV; dehydration, V; alkylation, VI; ring opening reaction, VII (Aqsha et al., 2021; Sankaranarayanan et al., 2015). Tu et al. (2019) proposed that anisole transformation over Ni-Al_2O_3 and Ni/ZSM-5 catalysts proceeds via saturation of aromatic ring, rapid demethylation of methoxy-cyclohexane to cyclohexanone and, subsequently, dehydration of cyclohexanone to cyclohexane. This is referred to as hydrogenation-dehydration route. Anisole HDO on zeolite Y supported Pb, Ni, and Ru catalysts was shown to progress by the same route (Gamliel et al., 2018).

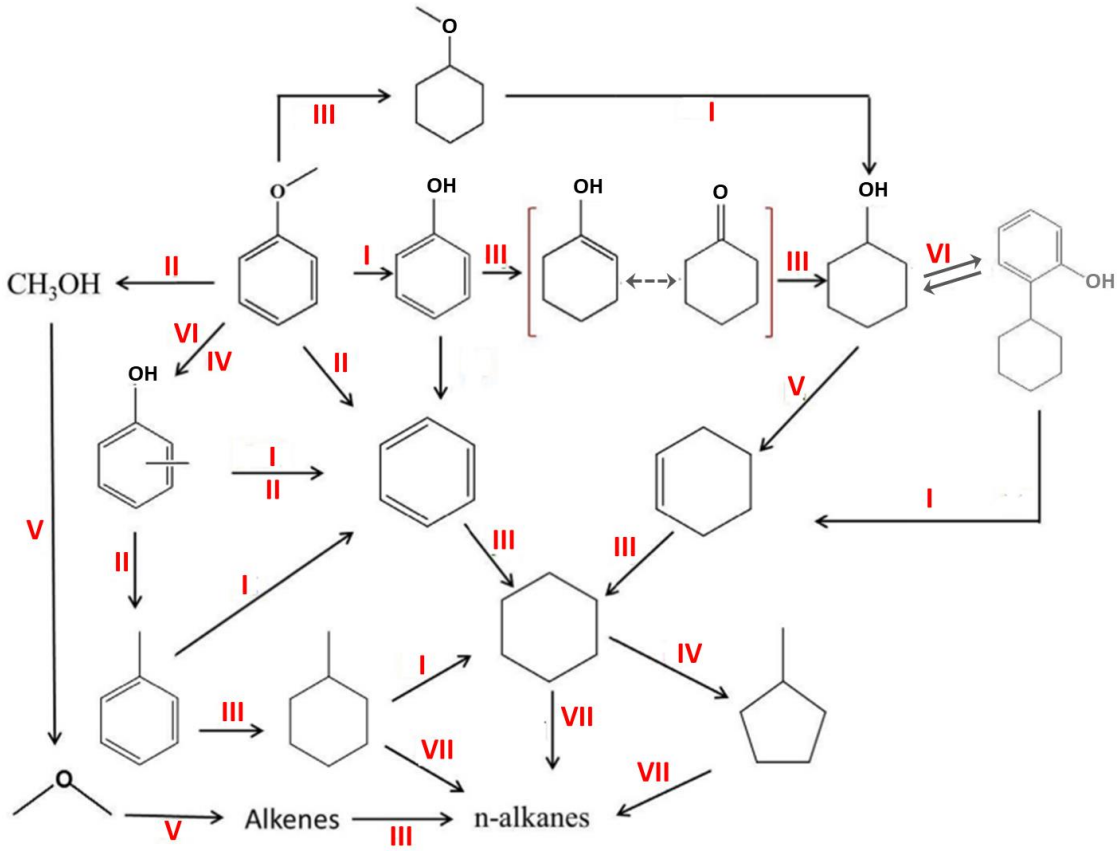

Figure 2.9: *Possible reaction networks for anisole HDO: Demethylation-dealkylation, I; direct deoxygenation, II; hydrogenation, III; isomerisation, IV; dehydration, V; alkylation, VI; ring opening reaction, VII (Sankaranarayanan et al., 2015).*

Another transformation route is direct deoxygenation. (Ghampson et al., 2018; Li, et al., 2020; Sankaranarayanan et al., 2015). Previous works have reported several products from the anisole HDO reaction (Gamliel et al., 2018; Jiang et al., 2020; Sankaranarayanan et al., 2015). Depending on the reaction conditions, such as the type of catalyst, degree of deoxygenation, and extent of hydrogenation, some of the products and intermediates of the reaction are cyclohexane, methylcyclopentane, phenol, benzene, toluene, cyclohexene, cyclohexanone, cyclohexanol, ethers, and transalkylates. In addition, light ends such as methane, ethylene and trace amount of CO may be generated. During the HDO of anisole using Ni-Mo/TiO_2 and Ni-V/TiO_2 catalysts, a total of seven major products were detected. These were toluene, benzene, cyclohexane, phenol, methylcyclohexane, cyclohexanol, and o-, m-, and p-cresols, respectively (Aqsha et al., 2021).

In related research, the impacts of two reaction variables, namely temperature and catalyst support, during anisole HDO were investigated by Szczyglewska et al. (2020). While toluene was the main product of the reaction that Ru/MCM-41 catalysed, where SBA-15 or SBA-16 was used as a support, methoxycyclohexane was the primary product. 100% of anisole conversion was accomplished under the reaction conditions used. Contrary to the Ru-based MCM-41 and SBA, a bimetallic Ni-Cu catalyst produced cyclohexane as the main product of anisole HDO (Nesterov et al., 2021). The HDO of anisole using natural zeolites (BEA and MOR) supported Ni catalysts revealed that both metal and acid sites are required for the reaction. The transformation of anisole to cyclohexane was made possible by the strong Brønsted acid sites and several small Ni species over 5%Ni/BEA (Yan et al., 2021).

On the other hand, organic acids such as carboxylic acid, found in bio-oil are principally responsible for its acidity (Qu et al., 2021; Sulejmanovic et al., 2022). The presence of these molecules in bio-oil poses a serious challenge in the field of renewable energy, leading to the deterioration of structural materials within the processing settings. Among the acidic model compounds studied are the HDO of acetic acid and palmitic acid (Lawal et al., 2019; Liu et al., 2021; Song et al., 2010; Wang et al., 2017). The simple aliphatic hydrocarbon chains of both compounds and the carboxylic acid substitutes are much simpler than their more complex benzene-ring counterparts found in benzoic acid. In bio-oil, oxygenates such as benzoic acid must be converted into aromatic hydrocarbons.

Figure 2.10 presents the reaction networks for the HDO of benzoic acid (a), and that of acetic acid over Ni/SiO_2-Al_2O_3 catalyst (b). For the benzoic acid, the possible reactions are hydrogenation, dehydration, decarboxylation, decarbonylation, demethylation (Shinde and Deshpande, 2017). The production of benzaldehyde from benzoic acid studied over ZnO_2

and ZrO_2 catalysts generated benzyl alcohol, benzophenone, toluene, and benzene as by-products (Guo et al., 2021; Hu et al., 2020; Shinde and Deshpande, 2017).

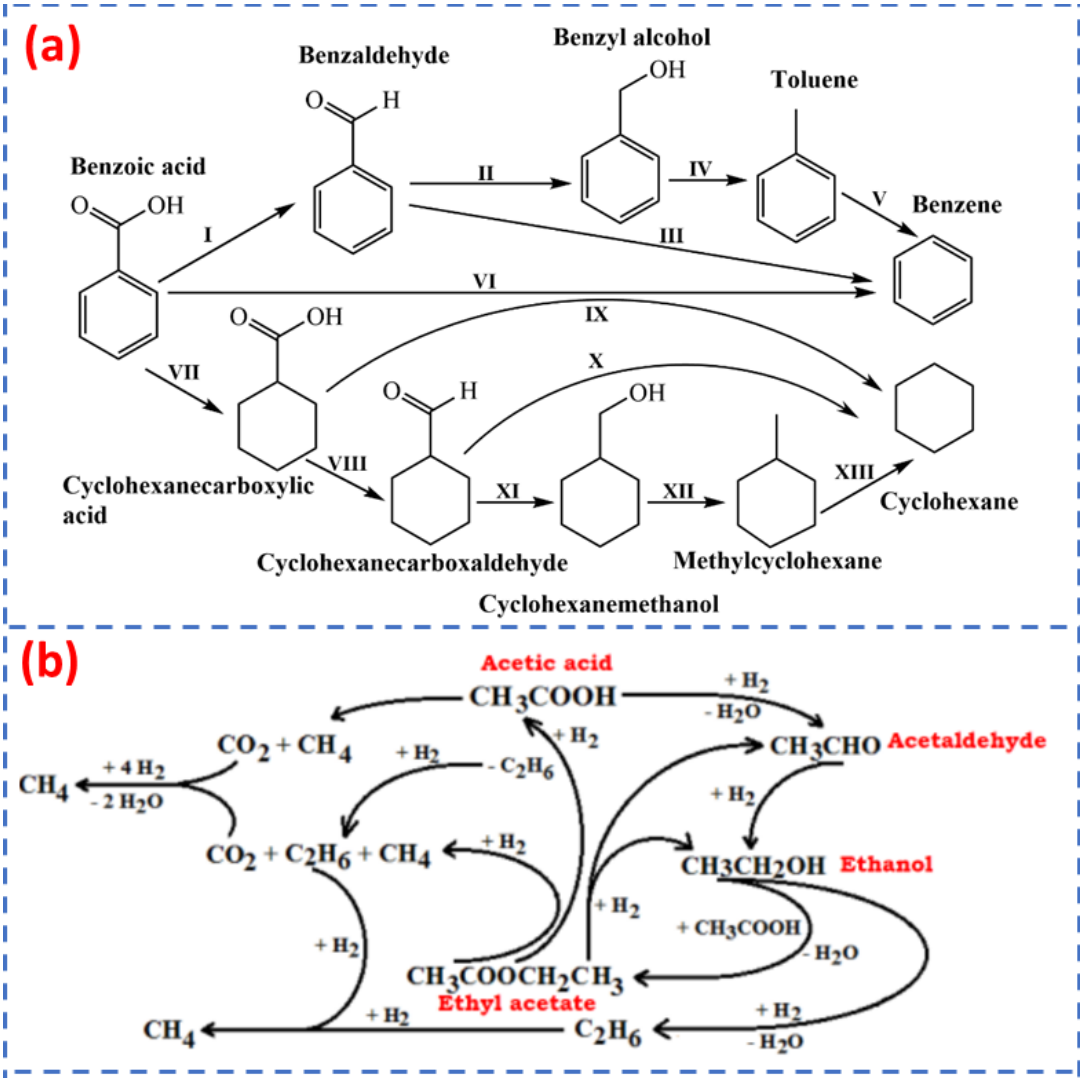

Figure 2.10: *Possible pathways during the HDO reaction of benzoic acid (a) (Chen, 2019). Reaction pathways for acetic acid HDO over Ni/SiO_2-Al_2O_3 catalyst (b) (Jahromi and Agblevor, 2017). Hydrogenation/dehydration; I, IV, VIII, and XII, hydrogenation; II, VII, and XI, decarboxylation; III, VI, IX, and X, hydrogenation/demethylation; V and XIII.*

However, selective hydrogenation over the following catalysts: Pt/C, RuPd-C, Pd-C, Pt/TiO_2 and Ir-based catalyst showed cyclohexane carboxylic acid and benzyl alcohol as the two major products (Guo et al., 2021; Kong et al., 2022). The formation of toluene is due to hydrodeoxygenation and hydrogenation of the carboxylic functional group, while benzene is

the result of the cleavage of the methyl side chain from toluene (Chen, 2019; de Lange et al., 2002).

The possibilities of benzoic acid reacting directly through to toluene or benzene was reported in the literature (Chen, 2019; Tang et al., 2017). Although it is apparent that decarboxylation of benzoic acid is a much slower process than deoxygenation to benzaldehyde or toluene (de Lange et al., 2002). Decarboxylation of methyl-benzoate to benzene proceeds through a radical mechanism reaction, whereby a benzyloxy-radical is formed via a homolytic cleavage of the carboxylic acid (R-COO-Ni). Thereafter, the benzyloxy-radical rapidly decarboxylates to a benzyl radical. Finally, the hydrogen atom reacts with the benzyl radical chain to terminate the reaction (Shinde and Deshpande, 2017). Another possible transformation route is the total hydrogenation of benzoic acid to cyclohexane carboxylic acid, which subsequently undergoes decarboxylation to generate cyclohexane (Chen, 2019; Kong et al., 2022; Xu et al., 2014).

Jahromi and Agblevor (2017) investigated the HDO of acetic acid over Ni/SiO_2-Al_2O_3 at a range of temperatures (150–450 ℃). Depending on the reaction temperature, HDO of acetic acid generated acetaldehyde, ethanol, ethyl acetate, carbon dioxide, methane, and coke in various quantities. Based on the observed end products, reaction routes for acetic acid HDO were suggested. Methane and water were the end products of acetic acid HDO at a reaction temperature of 450 ℃.

2.11 Influence of Process Parameters on Hydrodeoxygenation Efficiency

The efficiency of HDO process is highly dependent on various process parameters, which play a significant role in determining the quality and yield of the final product (Basu, 2013; Xiaohua et al., 2018). Understanding the influence of these parameters is essential for optimizing HDO efficiency and developing sustainable energy solutions (Gea et al., 2023). One key parameter that affects HDO efficiency is temperature (Guo et al., 2021). The temperature at which the HDO reaction takes place significantly influences the reaction rate and product selectivity (Venkatesan et al., 2021). Higher temperatures promote faster reactions but may also lead to undesired side reactions, reducing overall efficiency. Conversely, lower temperatures can result in sluggish reaction rates, prolonging processing times and decreasing productivity. Therefore, finding an optimal temperature range is critical to maximizing HDO efficiency (Bashir et al., 2022). Pressure is another important parameter affecting HDO efficiency (Guo et al., 2021). Higher pressures can enhance mass transfer rates and improve reactant solubility, leading to increased conversion rates. However, excessively high pressures may also cause catalyst deactivation or limit reactor capacity due to safety concerns or equipment limitations (Tang et al., 2015), hence, there is need to balance these factors for efficient HDO processes.

Kristensen et al. (2022) reported a statistically significant linear and quadratic effects of temperature and pressure on the selectivity for cresol during the HDO of vanillin over a sulfided $NiMo/AL_2O_3$ catalyst at 216–350 ℃ and 3–9 bar H_2. Similarly, the effect of hydrogen pressure was clearly demonstrated during anisole HDO over a $Re\text{-}MoOx/TiO_2$ catalyst (Ghampson et al., 2018). An increase in pressure plays a critical role in lowering the C-O reaction barrier, thereby promoting demethoxylation, which generates more benzene. At a higher reaction temperature, a conversion of 100% was seen during the HDO of anisole

over 1 wt.% Ru-based SBA-15 and SBA-16 catalysts with methoxy cyclohexane as the main product (Szczyglewska et al., 2020). Furthermore, the effects of temperature and pressure during vanillin HDO over Ni/Biochar catalysts were reported (Mudi et al., 2023). As the temperature increased from 100 ℃ to 150 ℃, the vanillin conversion increased from 26% to 95%. Likewise, the yield of p-creosol increased from 15% to 90%. Notably, when the same reaction was carried out at a constant temperature of 150 ℃ while changing the hydrogen pressure from 30 to 50 bar, an increase in both the conversion of vanillin and the yield of p-creosol was recorded.

Different catalysts exhibit different activity levels and selectivity towards target products; hence selecting an appropriate catalyst greatly influences overall process performance. Table 2.8 presents the effects of some parameters on the HDO efficiency of bio-oil model compounds. Anisole HDO was studied over 5 wt.% nickel-based Al_2O_3, MCM-41, and Al-MCM-41 catalysts at 280 ℃ and 48 bar H_2. The conversion and selectivity to cyclohexane were determined as 63.4% and 0.7% (Ni/Al_2O_3), 38.6% and 11.8% (Ni/MCM-41), and 96.5% and 97.6% (Ni/Al-MCM-41) respectively. In a similar study, HDO of anisole with 1 wt.% Ru loaded on SBA-15, SBA-16, and MCM-41 supports gave a conversion of 100%, 100%, and 75% respectively. While the main product was methoxy-cyclohexane on SBA support-Ru catalyst, toluene was the major product from the MCM-41-based catalyst (Szczyglewska et al., 2020). A report by Li et al. (2020) revealed that guaiacol conversion over Ni/C-ZSM-5 catalyst was < 1% with cyclohexane selectivity of 61.6%. This low activity was attributed to poor metal dispersion and large metal particle sizes. However, a Ni/H-ZSM-5 catalyst showed a conversion of 87.1%. It was concluded that the catalyst with higher acid sites (Ni/H-ZSM-5) exhibited much higher activity.

Table 2.7: Effluence of some parameters on HDO efficiency.

Reactant	Catalyst	Reaction condition			Solvent	Conversion (%)	Product distribution	Reference
		Temp. (℃)	Pres. H_2 (bar)	Time (h)				
Anisole	5% Ni/Al-MCM-41	280	48	6	Hexadecane	96.5	97.6% cyclohexane	(Molina-Conde et al., 2023)
	5% Ni/Al_2O_3					63.4	0.7% cyclohexane	
	5% Ni/MCM-41					38.6	11.8% cyclohexane	
Benzoic acid	5% Pt/TiO_2	80	50	1	Acetic acid	68	96% cyclohexane-carboxylic acid	(Guo et al., 2021)
					Hexane	> 99	> 99% cyclohexane-carboxylic acid	
					Water	84	99% cyclohexane-carboxylic acid	
Phenol	1% Pt/SBA-Pr	200	30	4	Dichloromethane	63	95.9% cyclohexane	(Gea et al., 2023)
					Dioxane	25	77.6% cyclohexane	
					Ethanol	6.7	52.2% cyclohexane	
					Water	5	74% cyclohexane	
Vanillin	PdRh/Al_2O_3	45	56	0.5	Cyclohexane	90	96% creosol	(Gea et al., 2023)
					Ethyl acetate	99	93% creosol	
					2-propanol	100	100% creosol	
					Toluene	70	3% creosol	
					Water	77	41% creosol	

Furthermore, feedstock composition significantly impacts HDO efficiency (Roy et al., 2023). Different cresol isomers may behave differently during the HDO. According to Shafaghat-Rezaei, et al. (2015), o-cresol had a lower conversion rate than m- and p-cresol, which was likely caused by the steric hindrance to o-cresol's adsorption with methyl groups next to the hydroxyl groups. Meanwhile, the kind of catalyst applied might alter the HDO route. For instance, only hydrogenation to 2-methylcyclohexanone and to 2-methylcyclohexanol was observed during the HDO of m-cresol on Ni_2P/Al_2O_3, but, total deoxygenation was seen over the Ni_2P/ZSM-5 catalyst, producing methylcyclohexane (Berenguer et al., 2018).

Finally, solvent choice and its concentration are critical factors influencing HDO efficiency (Guo et al., 2021). Solvents can enhance mass transfer rates by increasing reactant solubility and improving contact between the reactants and catalyst surfaces (Kim et al., 2022). The selection of an appropriate solvent depends on factors such as solubility of oxygenates, stability under reaction conditions, and economic viability (Ding et al., 2017; Elahi et al., 2019). Three different solvents (acetic acid, hexane, and water) were used in the HDO of benzoic acid over 5% Pt/TiO_2 catalyst (Guo et al., 2021). The degree of conversion and the selectivity to cyclohexane-carboxylic acid achieved were 68% and 96% (acetic acid), > 99% and > 99% (hexane), and 84% and 99% (water) respectively). On the other hand, the HDO of phenol over 1% Pt/SBA-Pr catalyst with dichloromethane, dioxane, ethanol, and water as solvents was investigated Gea et al., 2023). While the phenol conversions were 63%, 25%, 7%, and 5% in the dichloromethane, dioxane, ethanol, and water, the selectivity to cyclohexane were 96%, 78%, 52%, and 74% respectively. When cyclohexane, ethyl acetate, 2-propanol, toluene, and water were compared as solvents in the HDO of vanillin, a complete conversion was recorded in 2-propanol with a 100% selectivity to creosol (Gea et al., 2023). By understanding the influence of these parameters on HDO efficiency, researchers can

develop strategies for improving overall process economics while simultaneously contributing to a more sustainable energy future.

2.12 Catalyst Stability, Poisoning and Deactivation: Key Drivers

A set of Pt/Beta-zeolite catalysts were prepared and tested for the HDO of m-cresol. The effect of varying the ratio of Bronsted site to active metal concentration (BAS/Pt) was investigated at 1 bar and 250 ℃. The result shows a significant increase in the intra-crystallite diffusion limitation with increasing BAS/Pt concentration. This is ascribed to strong chemisorption between the reactant/intermediates and the catalyst surface which limit access to the catalyst active metal sites. Low BAS/Pt ratio has proved beneficial in reducing coke formation, increase stability and lifetime (Wu et al., 2019). In a different study, a combination of NaOH, TEAOH and phosphorus were employed for sequential modification of a high silica microporous to mesoporous ZSM-5. Compared to the parent and the NaOH treated materials, additional treatment with phosphorus gave the zeolite more-stable acid sites, higher catalytic activity and prolonged lifetime (Ding et al., 2015). It is evident that bulky molecules are mostly involved during the HDO of bio-oil, as such, diffusion, adsorption, reaction, and desorption steps were identified as the major points where catalyst deactivation is likely to occur (Luo et al., 2019).

The liquid phase reaction which can cause permanent damage of the catalyst via active metal leaching, sintering, or altering the support nature has been identified as a major catalyst deactivation driver (Logar et al., 2009; Sangnikul et al., 2019). In industry solid catalysts are usually applied in gas-phase reactions, therefore, utilising these catalysts in a reaction that involve the liquid-phase may result in extra-challenges to the catalyst stability (Holm et al., 2011). Furthermore, weak metal-support interaction, poor metal dispersion and increased

metal size are additional potential promoters of deactivation (Cheng et al., 2016). A lower Si/Al ratio is shown to possess high meta-support bond thereby preventing leaching and sintering in Ru/ZSM-5 catalyst (Kumar et al., 2020). The corrosive nature of the biomass-derived oil brings a particular challenge to the stability of a catalyst. The organic acid components of bio-oil can extract part of the framework of the support materials during the HDO reaction thereby deactivating the catalysts. Depending on the bio-oil source, the higher the organic acid concentration the more likely a catalyst is subjected to structural changes via leaching and subsequent deactivation of the catalysts (Qu et al., 2021). Water associated with biomass derived-oil is another major concern on the catalyst stability (Fan et al., 2020). Increase in operating temperature during HDO of bio-oil can leads to an increase in the equilibrium constant of water which in turn produce more hydroxyls and protons, this has significant effect on the catalyst stability (Oyedun et al., 2020). However, the extent of the effect depends largely on the type of support framework. Unlike some topologies that show severe deteriorations, MFI type zeolite supports demonstrate a high degree of stability (Li, et al., 2020; Sankaranarayanan et al., 2018).

2.13 Kinetic Study

Kinetic studies are essentially chemical analysis carried out in order to correlate experimental data with a model of the mechanism that best fits the rate of reaction and describes the chemical process (Taoukis et al., 2014). The study is carried out to evaluate the influence of some reaction variables and determine the magnitude of some important kinetic parameters. These parameters, such as activation energy (E_A), rate constants (k), reaction order (n), enthalpy (ΔH), and entropy (ΔS) changes, can only be estimated accurately if mass transfer limitations are eliminated within the heterogeneous reaction system (Coker, 2001; Falconer, 1998; Liu et al., 2021). It is obvious that reactor configuration and the catalyst's nature can

affect mass transfer during a reaction even at constant temperature and pressure. The elimination of internal and external mass transfer limitations is therefore essential, and a reaction must be controlled kinetically for experimental data to be useful in the development of a kinetic model. To achieve this, perfect mixing is necessary to maintain uniform temperatures and concentrations throughout the reactor (i.e., negligible external transport limitations (Fogler, 2004).

There are two procedures use to analyse kinetic data: the integral, and the differential methods. The integral method provides a mathematical equation of rate expressions and assumes that a plot of a given concentration against reaction time produces a straight line. When the data is plotted and a relatively good straight line is obtained, the kinetic data is considered to accurately fit the rate expression. The integral method is straightforward to apply and is used when evaluating relatively simple rate expressions, or when the data is so dispersed that the derivatives required by the differential method cannot be found reliably. In summary, it is recommended that the integral method be tried first, and if that fails, then the differential method (Fogler, 2004). General expressions for the first-order, second-order, and zero-order are given in equations 2.1–2.3 (integral method) and 2.4–2.6 (differential method);

$$C_i = -kt + C_{i0} \quad (2.1)$$

$$lnC_i = -kt + \ln C_{i0} \quad (2.2)$$

$$\frac{1}{C_i} = kt + \frac{1}{C_{i0}} \quad (2.3)$$

$$r = kC_i \quad (2.4)$$

$$r = kC_i^2 \quad (2.5)$$

$$r = k \quad (2.6)$$

where C_i is the concentration of reactant *i* at time *t*, C_{i0} is the initial concentration of reactant *i*, *t* is the reaction time, *k* is the rate constant, and *r* is the reaction rate.

Kinetic study of a number of bio-oil model compounds have been reported in the literature (Kay Lup et al., 2017). Aqsha et al. (2021) used integral method of analysis to determine kinetic parameters for the HDO of anisole over Ni-Mo/TiO_2 and Ni-V/TiO_2 catalysts. The reaction was carried out in a batch reactor over a wide range of temperatures. Kinetic parameters, such as the reaction order, rate constant, and activation energy were determined. The analysis revealed that the overall reaction order was two (2^{nd} order) on both catalysts. The activation energy values for anisole HDO reactions were 80.9 kJ mol^{-1} (Mo/TiO_2) and 53.9 kJ mol^{-1} (Ni-V/TiO_2) respectively. Similarly, the kinetics of acetic acid HDO over a platinum-supported catalyst have been reported (Lawal et al., 2019). A differential method of analysis was used (method of initial rate), due to the complex nature of the reaction, which involved multiple reaction steps. At different temperatures, a nonlinear reaction rate-dependency on starting concentration was observed, indicating fractional-order-kinetics.

2.13.1 Mass transfer limitation

Mass transfer limitation plays a crucial role in determining the catalytic activity of heterogeneous catalysts. When reactants are present in the gas or liquid phase, they must first diffuse through the bulk fluid to reach the catalyst surface (Falconer, 1998). This diffusion step is often rate-limiting and can significantly impact the overall reaction rate. Therefore, mass transport analysis is a prerequisite when intrinsic kinetics are sought (Wang et al., 2005). It is performed by changing variables such as stirring speed and catalyst particle size while observing their effects on conversion (Perego and Peratello, 1999; Shinde and Deshpande, 2022). The sole aim of this analysis is to remove both internal and external mass

transfer constraints so that reaction rates are determined within a kinetic control regime (Lawal et al., 2019).

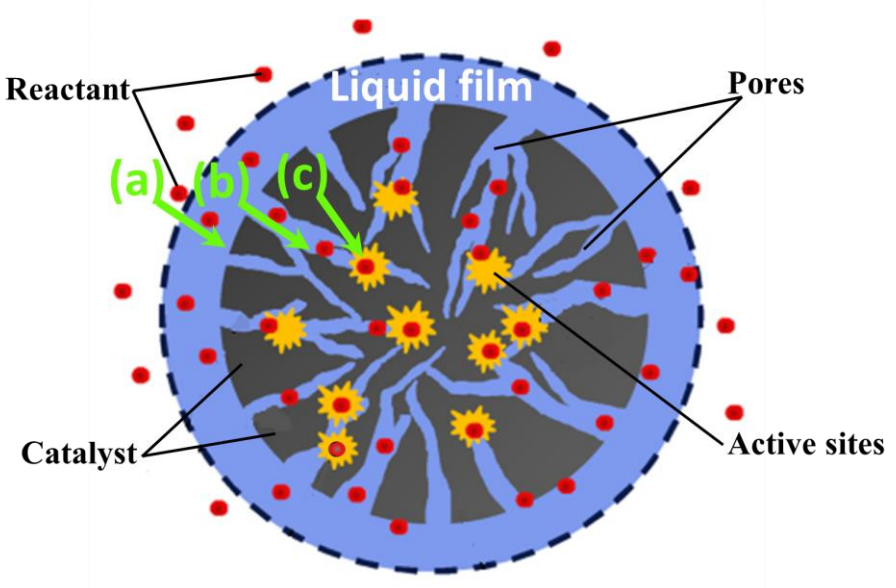

Figure 2.11: *Mass transfer stages in heterogeneous catalysis systems: (a) external mass transfer, (b) internal mass transfer, and (c) adsorption onto the active site (Wang and Guo, 2020).*

Figure 2.11 presents some mass transport stages involved in heterogeneous catalysis systems. The following processes take place in a heterogeneous catalytic reaction involving solid-liquid-gas phases: Mass transfer of reactant from the bulk fluid; Diffusion of reactant through the boundary layer surrounding a catalyst particle; Intraparticle diffusion of reactant into the catalyst pores to the catalyst's active sites; Adsorption of reactant onto the catalyst active sites: Surface reactions to transform the adsorbed reactant into product; Desorption of the product from the catalyst surface; Diffusion of product through pores of the catalyst; And finally, mass transfer of the product to the bulk fluid (Fogler, 2019).

Generally, some criteria are used to evaluate the effect of mass transfer in a heterogeneous reaction system. The Weisz-Prater criterion is one that utilises calculated values of reaction

rates to determine if internal diffusion is limiting a reaction (Aliu et al., 2019; Liu et al., 2021). This correlation provides an estimate of the effectiveness factor (η) based on the Thiele modulus (φ). It is used to evaluate the value of the observable modulus ($\eta\varphi^2$), which is then used to determine whether internal mass transfer limitations exist or not (Ghampson et al., 2018). The effectiveness factor is a measure of how effectively a catalyst utilises its active sites. It is defined as the ratio of the actual rate of reaction to the maximum possible rate if all active sites were available. A value less than 1 indicates that the catalyst is not fully utilized, while a value close to 1 suggests efficient utilization. On the other hand, the Thiele modulus quantifies the diffusion limitations within porous catalyst particles. It considers both external mass transfer limitations and internal diffusion resistance. A high Thiele modulus implies that diffusion limitations are significant, leading to reduced reaction rates (Fogler, 2019). In addition, empirical correlations such as Zwietering are widely used to estimate the minimum impeller speed necessary to maintain catalyst particles in suspension, a critical step taken to eliminate external mass transfer limitations (Armenante et al., 1998; Mak, 1992).

2.13.2 Adsorption kinetics

Adsorption kinetics expressions can be developed from an understanding of potential adsorption mechanisms (Zuliani et al., 2023). This topic deals with the rate of substrate adsorption and the adsorbates' residence time on the solid-liquid boundary (Alghamdi et al., 2021). Adsorption isotherms are important tools for predicting how the adsorbate (reactants) and adsorbent (catalyst) interact as well as the amount of substrate adsorbed at equilibrium at a constant temperature (Abdulhamid and Muhammad, 2022; Amutova et al., 2023). Whilst adsorption thermodynamics provide insight on the feasibility and the spontaneous nature of the adsorption process (Raghav and Kumar, 2018; Wang et al., 2023).

The most commonly used models to describe adsorption kinetics are the pseudo-first-order (PFO) and pseudo-second-order (PSO) models. These models originate from chemical reaction kinetics in homogenous systems and are adaptations for heterogenous systems. They are empirical and called pseudo due to: (i) the assumption that the concentration of the adsorbate in the solution is constant (considering a chemical reaction where one of the reactant species is in excess, with an approximately constant concentration, it has no effect on the observed rate of the reaction); and (ii) the kinetic equation is based on the adsorption capacity of solids instead of the concentration in the liquid phase (adaptation from homogenous systems). The former is, of course, an approximation, as the concentration of the adsorbate species in solution decreases with sorption (Vareda, 2023).

2.13.3 Kinetic models

Generally, the following models are widely used for kinetic analysis: the power-law model, the Eley-Rideal model, and the Langmuir Hinshelwood-Hougen Watson (LHHW) model (Abdulhamid and Muhammad, 2022; April et al., 2016). The power-law model is basically the simplest of these models (Kathiraser et al., 2015). It provides an approximate estimate of the parameters needed. However, it does not accurately portray the reaction's kinetics in a way that is applicable to a variety of catalysts. The ease of application and parameter estimation is the fundamental benefit of the power-law model. This model, however, is unable to adequately explain the multiple mechanistic reactions that occur on the catalyst surface (Kim et al., 2019). On the other hand, most of the reaction mechanisms proposed for the HDO reaction of bio-oil are based on the LHHW model (Aliu et al., 2019; Lawal et al., 2019). The LHHW model assumes the following steps: dissociation and activation of reactants; desorption of elemental and intermediate species onto the catalyst active sites; formation of product species via surface reaction; and desorption of product from the catalyst.

It is generally assumed that one of the listed steps (mostly the reaction step) is slow and rate-determining while the others are in thermodynamic equilibrium (Fogler, 2019; Kathiraser et al., 2015). By identifying rate-determining steps, researchers can focus on optimising these steps to enhance reaction efficiency (Coker, 2001).

The kinetic models of benzofuran HDO were proposed based on the LHHW-model. A first-order model equation was obtained for benzofuran HDO over a sulfided $CoMo/Al_2O_3$ catalyst at 69 bar and below 350 ℃ with the assumption of competitive reactant adsorption, independent H_2 adsorption site and constant H_2 pressure (Kay Lup et al., 2017). Similarly, kinetic data of xylenol and maltol HDO reaction over Ru/C catalyst were collected and modelled using the LHHW kinetics model. The dependency of the initial reaction rates upon H_2 partial pressure was found to be linear in the range of 6.9−20.7 bar. The surface reaction between the chemisorbed reactants, hydrogen and substrate, was considered as rate-determining step (Jain and Vaidya, 2015). Kinetic modelling for the HDO of anisole over a metal-mesoporous zeolite catalyst revealed an increased catalytic activity due to a higher rate of hydrogenation per active metal atom. In addition, the reaction constants for acid-catalysed dehydration were significantly lower for anisole HDO over the mesoporous catalyst compared to the microporous counterpart, probably owing to the limited zeolite acid site (Gamliel et al., 2018). More details on the kinetics are provided in the relevant sections.

2.14 Summary of the Chapter

This chapter provides a comprehensive literature survey in the area of biomass as a sustainable energy source. Various technologies involved in the biomass conversion to biocrude and the subsequent upgrading to biofuels and chemicals are discussed. Recent advancements in the relevant catalysts' development, application, and challenges are

extensively reviewed. The next chapter presents experimentation, covering catalyst preparation, characterization, and activity test.

CHAPTER 3

Materials and Experimental Methods

3.1 Introduction

A complete list of all the materials used in this study is provided in this chapter. Information on the suppliers and the purity of the materials, where applicable, is given. The chapter describes experimental procedures for catalyst preparation and discusses techniques for catalyst characterization. The chapter also provides background information on the working principles of some of the major tools used for the catalyst's characterization. Furthermore, a reactor configuration for catalytic activity tests is described. The design of experiments and the techniques used for product analysis are detailed in this section.

3.2 Materials

For the purpose of this research work, Table 3.1 presents a list of chemical reagents used. The purity of the reagents and the corresponding suppliers are shown. The chemicals were used as supplied.

Table 3.1: List of materials and chemicals.

S/N	Material/Reagents	Formula	Form	Purity	Supplier
1	Anisole	C_7H_8O	Liquid	99%	Sigma-Aldrich
2	Ammonium (II) nitrate	NH_4NO_3	Solid	99%	Sigma-Aldrich
3	Benzene	C_6H_6	Liquid	99.5%	Sigma-Aldrich
4	Cyclohexane	C_6H_{12}	Liquid	99.8%	Sigma-Aldrich
5	Cyclohexanol	$C_6H_{11}OH$	Liquid	99.5%	Sigma-Aldrich
6	Cyclohexanone	$C_6H_{10}O$	Liquid	99%	Sigma-Aldrich

Table 3.1: List of materials and chemicals

S/N	Material/Reagents	Formula	Form	Purity	Supplier
7	Cyclohexene	C_6H_{10}	Liquid	99.5%	Sigma-Aldrich
8	Decahydronaphthalene (cis + trans)	($C_{10}H_{18}$)	Liquid	98%	Alfa Aesar
9	Dimethoxy cyclohexane	$C_8H_{16}O_2$	Liquid	99%	Sigma-Aldrich
10	Formic acid	CH_2O_2	Liquid	96%	Sigma-Aldrich
11	Methyl cyclopentane	$C_5H_9CH_3$	Liquid	99.5%	Sigma-Aldrich
12	n-decane	$C_{10}H_{22}$	Liquid	98%	Sigma-Aldrich
13	Nickel (II) nitrate hexahydrate	$Ni(NO_3)_2 \cdot 6 H_2O$	Solid	99.9%	Sigma-Aldrich
14	Silicon oxide	SiO_2	Solid	90%	Alfa Aesar
15	Sodium hydroxide	NaOH	Solid	98%	Sigma-Aldrich
16	Toluene	$C_6H_5CH_3$	Liquid	99.5%	Sigma-Aldrich
17	ZSM-5 (SiO_2/Al_2O_3 = 30)	SiO_2:Al_2 O_3	Solid	-	Alfa Aesar
18	Hydrogen	H_2	Gas	99.9%	BOC
19	Nitrogen	N_2	Gas	99.9%	BOC
20	5%Hydrogen/Nitrogen	H_2/N_2	Gas	99.9%	BOC
21	Phenol	C_6H_5OH	Liquid	99.5%	Sigma-Aldrich
22	Helium	He	Gas	99.9%	BOC
23	Compressed air	Air	Gas	-	BOC
24	1,2,3,4–tetrahydronaphthalene	$C_{10}H_{12}$	Liquid	98+%	Thermo Scientific
25	Benzoic acid	$C_7H_6O_2$	Solid	99%	Thermo Scientific

Table 3.1: List of materials and chemicals

S/N	Material/Reagents	Formula	Form	Purity	Supplier
26	Benzaldehyde	C_7H_6O	Solid	99+%	Alfa Aesar
27	Benzyl alcohol	$C_6H_5CH_2OH$	Solid	99%	Alfa Aesar
28	Cyclohexane carboxylic acid	$C_7H_{12}O_2$	Solid	98%	Alfa Aesar
29	Sewage sludge oil	-	Liquid	-	University of Birmingham TCR unit

3.3 Catalyst Preparation

Incipient-wetness impregnation is the most commonly used technique for heterogeneous catalyst preparation (Ogunronbi et al., 2015; van Hooff and Roelofsen, 1991; Viswanadham et al., 2004). The technique is appealing due to its inexpensive nature, simple technological requirements, and minimal waste. A support is typically impregnated with a solution that contains a metal precursor. Depending on the requirements, the support can be in powder or pellet form. To ensure even metal dispersion, the support-active metal mixture is adequately stirred; thereafter, the excess solvent is vaporized. The dried product is then subjected to additional activation procedures, which include calcination to convert the precursor into a corresponding metal oxide and reduction to produce an active catalyst. For this research, all the catalysts used are in powdered form. Figure 3.1 presents a summary of the catalyst preparation procedure.

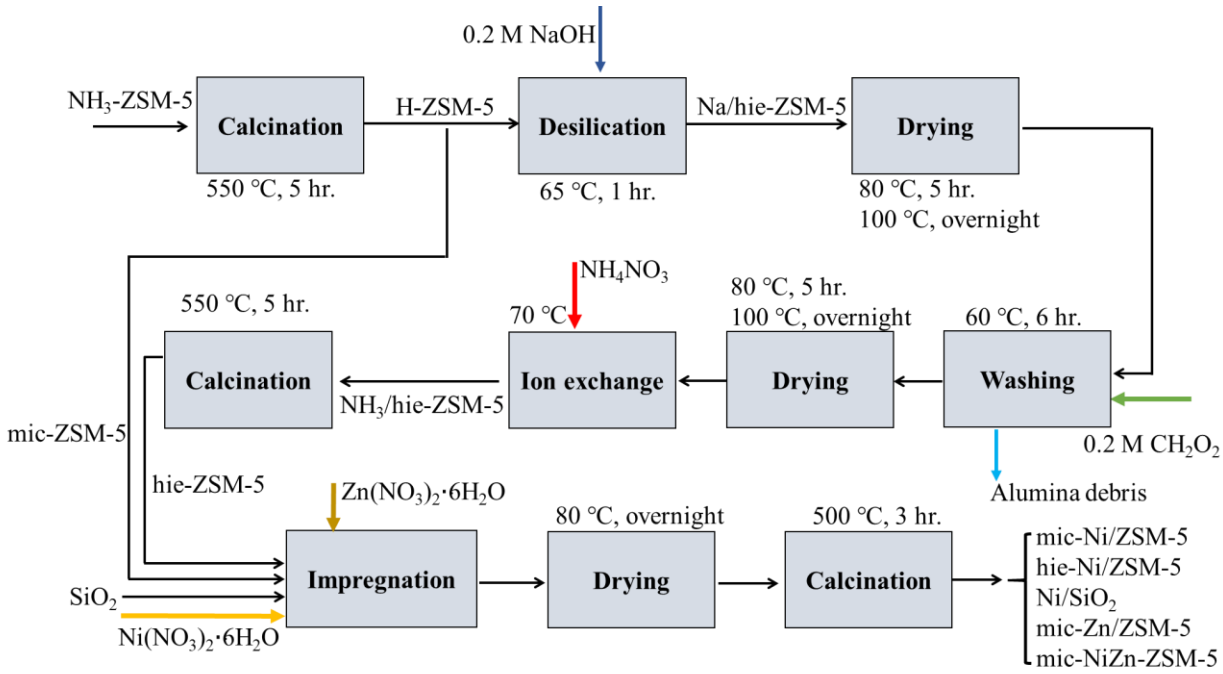

Figure 3.1. *Block diagram for the preparation of 5wt.% mic-Ni/ZSM-5, hie-Ni/ZSM-5 and Ni/SiO_2 catalysts.*

3.3.1 Desilication of microporous ZSM-5 support

Conventional microporous ZSM-5 zeolite with a silica to alumina molar ratio (SiO_2/Al_2O_3) of 30 in ammonium-form was purchased from Alfa Aesar. The zeolite was changed to hydrogen form via calcination in a tubular furnace (Carbolite-Gero 30 – 3000 ℃) under the flow of nitrogen gas, 1 L min^{-1}, for 5 hours at 550 ℃ at a 10 ℃ min^{-1} heating rate. The resulting hydrogen form of the microporous zeolite support, mic-HZSM-5, was transformed into mesoporous support according to the procedure reported in the literature (Dauda et al., 2020; Osatiashtiani et al., 2017; Rac et al., 2013). That is, 5.0 g of the mic-HZSM-5 support was weighed and transferred into a 500 mL glass beaker containing 150 mL of 0.2 M sodium hydroxide solution. The mixture was placed on a magnetic stirrer and maintained at 65 ℃ for 1 hour at a stirring speed of 600 rpm. The mixture was then allowed to cool and filtered. The residue was washed repeatedly with deionized water until a filtrate with a neutral pH was obtained. The recovered sample was first dried at 80 ℃ for 5 hours, then at 100 ℃

overnight. To remove alumina debris, the dried sample was treated with 200 ml of 0.2 M formic acid at 60 ℃ for 6 hours with stirring. Vacuum filtration was used to retrieve the resultant sample, which was then dried. The sample was then converted to ammonium form by ion exchange three times with 500 ml of 0.5 M ammonium nitrate at 60 ℃ for five hours. Finally, the treated ammonium-form ZSM-5 was calcined at 550 ℃ for 5 hours. The retrieved mesoporous support was designated hie-ZSM-5.

3.3.2 Preparation of nickel-based ZSM-5 and SiO_2 catalysts

Nickel was incorporated onto both the mic-HZSM-5, hie-HZSM-5 and the mesoporous silica (SiO_2) support via the incipient wetness impregnation technique. Here, 5 g of support was dispersed in 20 mL deionized water. Thereafter, solutions of nickel (II) nitrate hexahydrate [$Ni(NO_3)_2 \cdot 6\ H_2O$] and zinc nitrate hexahydrate [$Zn(NO_3)_2 \cdot 6\ H_2O$] containing a calculated amount of nickel and/or zinc that is equivalent to 5 wt.% loading was carefully released dropwise into a beaker holding the support slurry. The mixture was maintained at 70 ℃ under magnetic stirring until most of the associated liquid vaporized. Subsequently, the resulting catalyst was dried at 80 ℃ overnight. The dried sample was calcined at 500 ℃ under the flow of nitrogen gas for 3 hours. Finally, these catalysts were obtained; mic-5%Ni/ZSM-5, hie-5%Ni/ZSM-5, 5%Ni/SiO_2, mic-Zn/ZSM-5, and mic-NiZn/ZSM-5. Note, three (3) batches of the catalysts were prepared.

3.4 Catalysts Characterisation

Characterization is critical not only for designing a new catalyst but also for process development and optimization. Heterogeneous catalysts can be quite complex, consisting of metals, oxides, sulfides, supports, and chemical and mechanical promoters. As a result, optimising surface chemistry and structure is critical for achieving desired catalytic

properties, such as the needed activity and selectivity. Characteristics like surface area, particle size, pore size, and pore size distribution are very important parameters used to interpret the diffusion and adsorption properties of a catalyst. As reported below, various techniques were employed to characterise the catalysts used in this research work.

3.4.1 X-ray diffraction

Using an X-ray diffraction (XRD) Bruker D8 Advance machine equipped with Cu-K radiation (1.5406 Å), the crystallographic nature of both the supports and the prepared nickel-based catalysts was determined. Diffraction patterns were recorded for a 2-theta angle range of 5° to 80° with a 0.05 step increase. X-rays are beams of electromagnetic radiation with a smaller wavelength than visible light and a higher level of energy and penetration capacity. It is necessary for a grating's spacing and wavelength to match in order for electromagnetic radiation to be diffracted. As such, X-rays are the appropriate radiation to study crystal structures since the average interatomic separation in crystals is approximately between 2 and 3 Å. This means that the wavelength is similar to the spacing between atoms in a crystalline sample. Hence, XRD techniques are used to retrieve information about solid crystalline materials; metals, oxides, ceramics, minerals, corrosion products, and organic compounds. The technique is a very useful non-destructive characterization method that provides information on the identity and quantity of the crystalline phases in addition to the percentage crystallinity and crystal structure (Gorzin and Yaripour, 2019; Rao and Rao, 2015; Yusuf et al., 2022).

A schematic diagram of X-ray diffraction is shown in Figure 3.2. The analysis is performed by directing an X-ray beam at a sample. The beam interacts with the atomic electrons of the sample, changing the direction of the beam at some different angle θ, from the original beam.

This is the diffraction angle. Some of these diffracted beams cancel each other out, but if the beams have similar wavelengths, then constructive interference occurs. This results in the formation of a higher amplitude, which translates into a greater signal for this specific angle of diffraction.

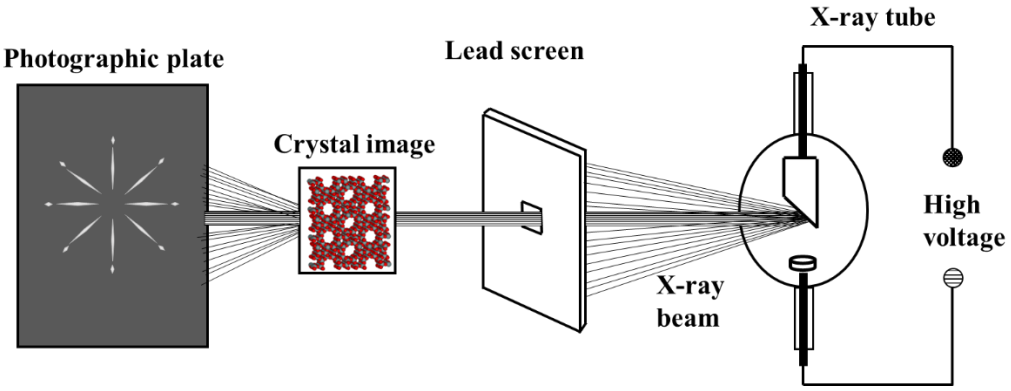

Figure 3.2: *Schematic diagram of X-ray diffraction (Rao and Rao, 2015)*

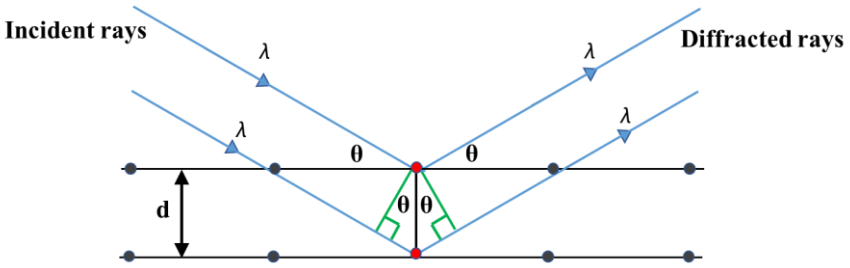

Figure 3.3: *Schematic diagram of Bragg's Law reflection (Suresh and Sundaramoorthy, 2014).*

The angle of diffraction can then be used to determine the difference between atomic planes using Bragg's law, $sin\theta = n\lambda/2d$ (illustrated in Figure 3.3), where λ is the wavelength added, measured in meters (m) or Angstroms (Å), θ is the angle of diffraction in radians (rad), n is the order of diffraction, which is an integer, and d is the distance between atomic planes, also in meters (m) or Angstroms (Å). The distance between atomic plates can then be used to determine composition or crystalline structure (Suresh and Sundaramoorthy, 2014; van Hooff and Roelofsen, 1991).

3.4.2 Brunauer-Emmett-Teller and Barrett-Joyner-Halenda

Evaluating the surface area, pore size distribution, and pore volume of a solid material is vital for many applications, especially surface-sensitive ones like catalysts. The Brunaur-Emmett-Teller (BET) technique is frequently used to determine the specific surface area of solid materials. The BET theory is based on an adsorption isotherm obtained by measuring the amount of nitrogen adsorbed across a wide range of relative pressures at a constant temperature 77K. This is then used to derive a quantitative measurement of the surface area of solid samples based on the coverage of the surface with nitrogen molecules (Kolvenbach et al., 2011; Sing, 2013). To achieve that, the monolayer adsorption gas volume (v_m) needs to be calculated using the BET model equation 3.1;

$$\frac{p}{v_{ads}(p_0-p)} = \frac{1}{v_m C} + \frac{C-1}{v_m C}\frac{p}{p_0} \qquad 3.1$$

where v_{ads} (cm^3) is the volume of the adsorbed gas, v_m (cm^3) is the volume of one monolayer of the adsorbed gas, p_0 (kPa) is the saturation pressure of adsorbate, p (kPa) is the equilibrium pressure of adsorbate, C is a constant (also known as the BET constant), which is related to the adsorption enthalpies.

As shown in Figure 3.4, a plot of equation 3.1 produces a linear graph with a slope of $\frac{C-1}{v_m C}$ and an intercept $\frac{1}{v_m C}$ in the range in which the assumptions of the BET theory are valid. After the v_m is determined, both the total and specific surface areas of a sample can be evaluated as follows;

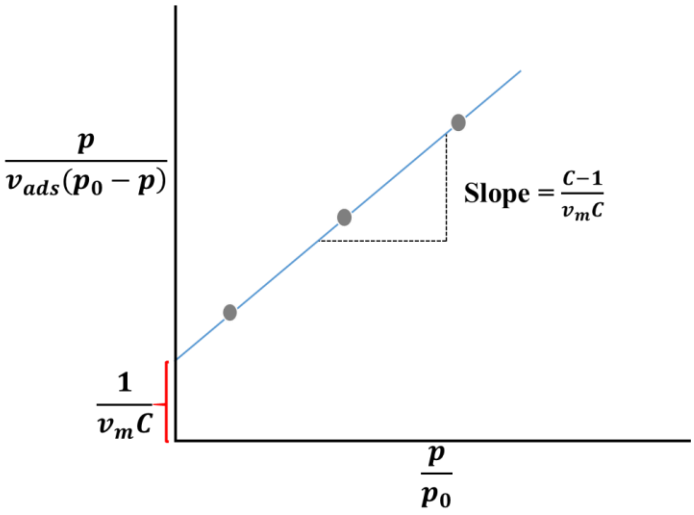

Figure 3. 4: *Schematic diagram of BET equation plot.*

$$S_t = \frac{v_m N s}{V_M} \qquad 3.2$$

$$S_{BET} = \frac{S_t}{m_s} \times 10^{-20} \qquad 3.3$$

where S_t (cm^2) is the total surface area of the sample, N is the Avogadro's number (6.02×10^{23} molecules mol^{-1}), s (cm^2 molecules^{-1}) is cross-sectional area of adsorbed gas molecule, V_M (cm^3 mol^{-1}) is the molar volume of adsorbed gas, S_{BET} (m^2 g^{-1}) is specific surface area and m_s (g) is mass of the sample. In practice, many probe gases that do not chemically react with the material surfaces are used as adsorbates. However, nitrogen is the most commonly used gas in BET analysis due to its high purity, low cost, inertness, and well-known molecular size (Llewellyn et al., 2013; Sing, 2013).

In this research work, nitrogen adsorption-desorption analyses were performed on a Micromeritics 3-Flex analytical instrument at 77 K. Initially, about 100 mg of a sample was degassed to ensure that any undesirable gases and vapours were removed. This was achieved by heating a sample gradually from the ambient temperature to 500 ℃ in 6 hours. The

temperature was maintained for additional 6 hours. The degassed sample cell was then moved to the analysis port, where a dewar of liquid N_2 was used to cool it and keep it at 77 K. A low temperature was maintained for a proper and strong interaction between the gas molecules and the sample surface, resulting in a measurable amount of adsorption. The catalyst surface area was calculated based on the BET equation. Pore size distribution was determined by t-plot and BJH methods. According to the BJH model, the pore size distribution and pore volume are estimated using the principle of capillary condensation of nitrogen gas. The model also classified particles as either microporous, mesoporous, or macroporous (Sing, 2013).

3.4.3 Scanning electron microscope-energy-dispersive X-ray

Morphologies and chemical compositions of the catalysts were analysed using a Hitachi TM3030 SEM-EDX machine. While a scanning electron microscope (SEM) produces high-resolution images of a sample by scanning its surface, the energy dispersive X-ray (EDX) technique uses the X-ray spectrum emitted by a solid sample bombarded with a focused beam of electrons to obtain a localised chemical analysis. Thus, the SEM-EDX system is a robust complementary characterization method that provides vital information on the morphology, size, and chemical composition of a sample.

The general operating principle, shown in Figure 3.5, is that an electron beam hits a sample and transfers energy to the atoms of the sample. As the electron of the atom gains energy, it either jumps to a shell with a higher energy level (the outer shell) or is knocked off from the atom. When this energy transition occurs, a positively charged hole is created. The hole will then attract a negatively charged electron from a higher-energy shell to fill the vacancy. When an electron moves from the outer to the inner shell of the atom, there will be energy

emitted as an X-ray. The energy of the X-ray is indicative of the energy difference between these two shells. It depends on the atomic number, a property unique to each element. As a result, the types of elements contained in a sample can be determined. Backscattered electrons are used to generate a high-resolution image of the sample (Garzon-Roman et al., 2020; Pachauri et al., 2013; Rades et al., 2014; Srivastava et al., 2009).

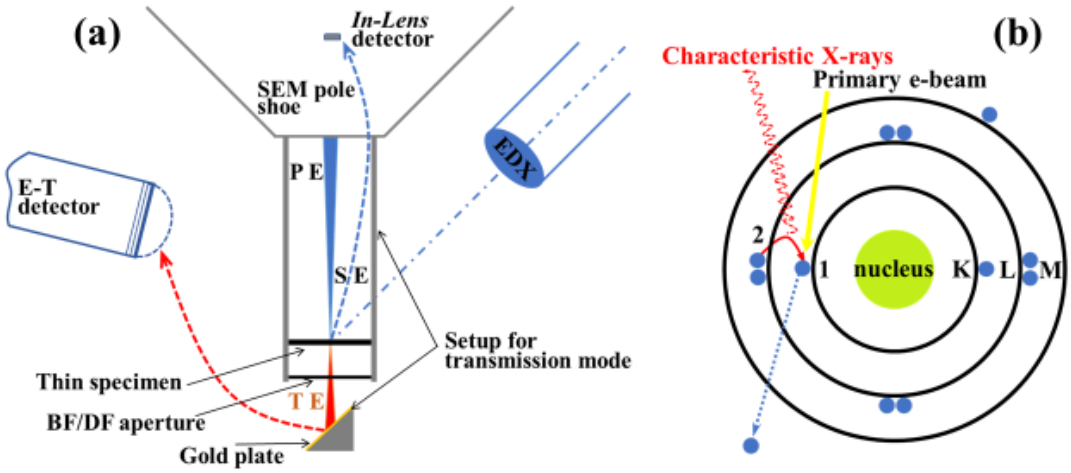

Figure 3.5: *Schematic diagram of a SEM-EDX system in a transition mode (a), and X-ray generation process (b)(Rades et al., 2014) (PE: primary electrons; SE: secondary electrons; TE: transmitted electrons; BF: bright field; DF: dark field; E–T: Everhart–Thornley detector).*

3.4.4 Transmission electron microscopy

Transmission electron microscopy (TEM) images were recorded using the Jeol 1400 instrument. The machine has a magnification of 10 – 1,200,000×, a resolution of 0.38 nm, and an accelerating voltage of 40 – 120 kV. Prior to the analysis, a sample was prepared by dissolving about 1 mg of a powdered catalyst in a vial containing 1 ml of high-purity ethanol. The mixture was sonicated for a few minutes, after which some solution was pipetted up and a drop was placed on a carbon film TEM grid. The carbon grid was air-dried. Thereafter, the grid was baked on a hot plate for a few seconds before it was imaged.

Figure 3.6 shows a schematic diagram of a TEM machine. Unlike in light microscopes, where photons are used to create images of specimens, in the transmission electron microscope, a beam of electrons is passed through a very thin specimen, interacting with the specimen as it passes while forming a magnified image. Typically, a gun at the top of the TEM machine is used to generate the beam of electrons. These electrons are transmitted down the TEM machine's long column.

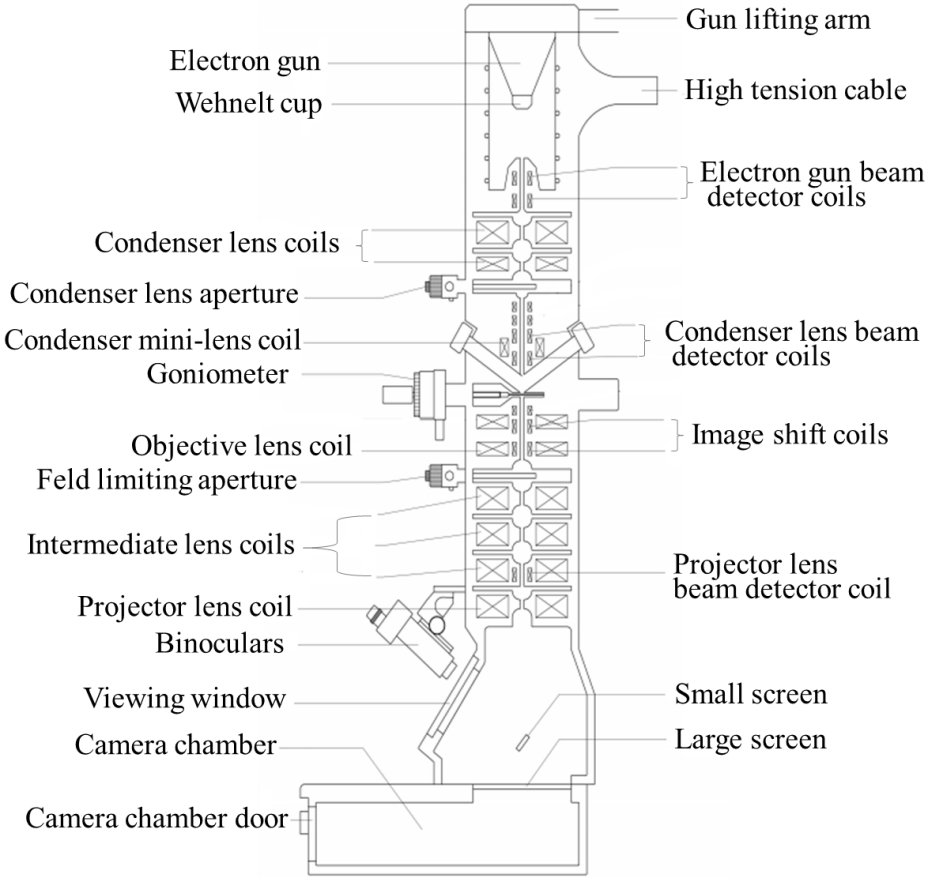

Figure 3.6: *Schematic diagram of a Transmission Electron Microscopy (TEM) machine (Hummelgård, 2009).*

Various types of electromagnetic lenses placed along the column are used to focus and project the beam onto an electron-sensitive fluorescent screen. Once a sample is placed in the beam direction at an appropriate position, a magnified image of the sample will be visible on the screen. The TEM analysis is performed in a high vacuum environment. The vacuum is

created by evacuating the air within the system to a pressure of 10 – 50 Pa. This is very important for the analysis as, without the vacuum, the electrons being aimed at the sample will be deflected when they collide with the air particles (Baruwati, 2007; van Hooff and Roelofsen, 1991).

3.4.5 Ammonia temperature programmed desorption

Temperature-programmed desorption (TPD) is extensively used to evaluate the type, amount, and strength of active sites present on the surface of a catalyst. This is achieved by measuring the quantity of desorbed gas at various temperatures. Two types of probe molecules usually used are NH_3 to estimate acid sites and CO_2 to determine basic sites. Depending on what is required, the sample is pre-treated before a gas stream containing the probe molecule is flowed through a bed holding the sample. The probe gas will then react with the active sites accessible within the sample. Thereafter, a programmed desorption begins by raising the temperature linearly with time while a steady stream of inert carrier gas flows through the sample. At a particular point, the thermal energy becomes greater than the activation energy; hence, the bond between the probe molecule and active metal breaks. The desorbed molecules are then released from the catalyst surface. A carrier gas flushes away the released molecules. If a variety of active metal species are present on the surface of the catalyst, there is a likelihood that the bond strength between the active metal and the adsorbed molecules will differ. Therefore, the thermal energy required to break the bond between these different active metal species and the absorbed molecules will be different. Thus, a plot of temperature versus the TCD output signal will produce distinct peaks (Benaliouche et al., 2008; Gorzin and Yaripour, 2019; McClure et al., 2009).

The acidity of the materials (catalysts and supports used in this work) was determined by ammonia temperature-programmed desorption (NH_3-TPD) on a ChemBET machine, shown in Figure 3.7, equipped with a thermal conductivity detector. The analysis was performed at the UK Catalysis Hub laboratory, Research Complex at Harwell. Approximately 100 mg of the sample was pre-treated at 300 ℃ under flowing helium (30 ml min^{-1}) for 1 hour. It was then cooled to 50℃ and adsorbed to saturation by NH_3 for 30 minutes. Physically adsorbed NH_3 on the catalyst was removed by flushing the sample with helium (30 ml min^{-1}) for 1 hour at the adsorption temperature. Subsequently, thermal desorption signals were recorded in the temperature range of 50 –1000 ℃ at 10 ℃ min^{-1} ramp rate.

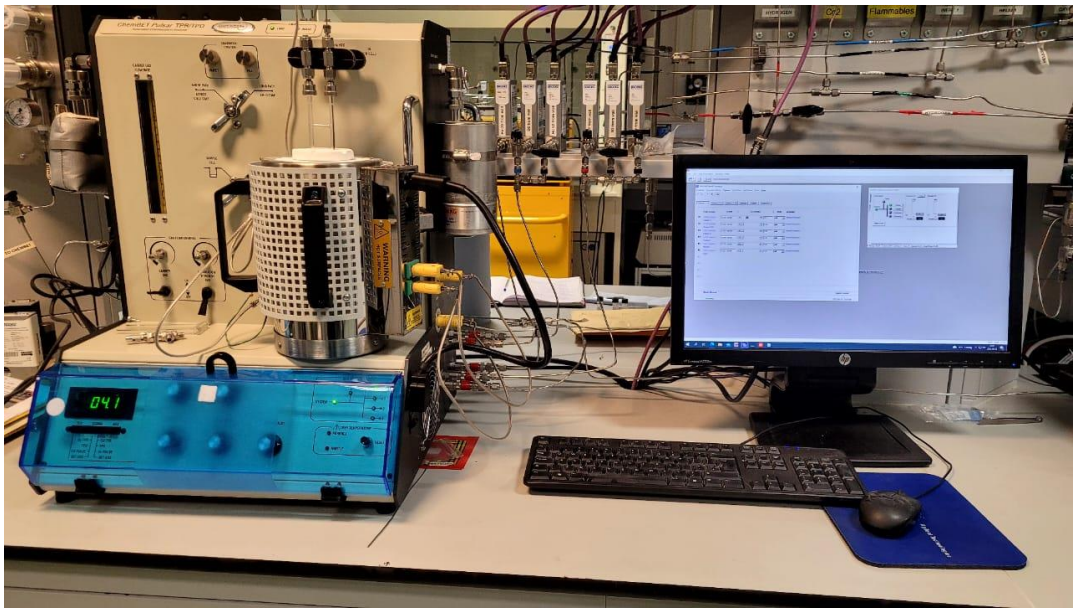

Figure: 3.7: *ChemBET machine (Source: Research Complex at Harwell).*

3.4.6 Hydrogen temperature programmed reduction

The Hydrogen Temperature Programmed Reduction (H_2-TPR) technique is a popular method for characterising solid catalysts containing reducible materials. The analysis provides information on the reduction temperature, which gives an idea about the nature of interaction between different components of a catalyst. Low temperatures imply ease of reduction and

weak interaction between the various species present in the catalyst sample. High reduction temperatures imply difficulty in reduction, which is further linked to a strong metal-support interaction. For a typical H_2-TPR plot, a single reduction peak is recorded when the active metal on the support is uniform. However, when the active metal exists in different forms, there will be multiple peaks, indicating variations in the degree of interaction between the reducible metal species and support (Gamliel et al., 2018).

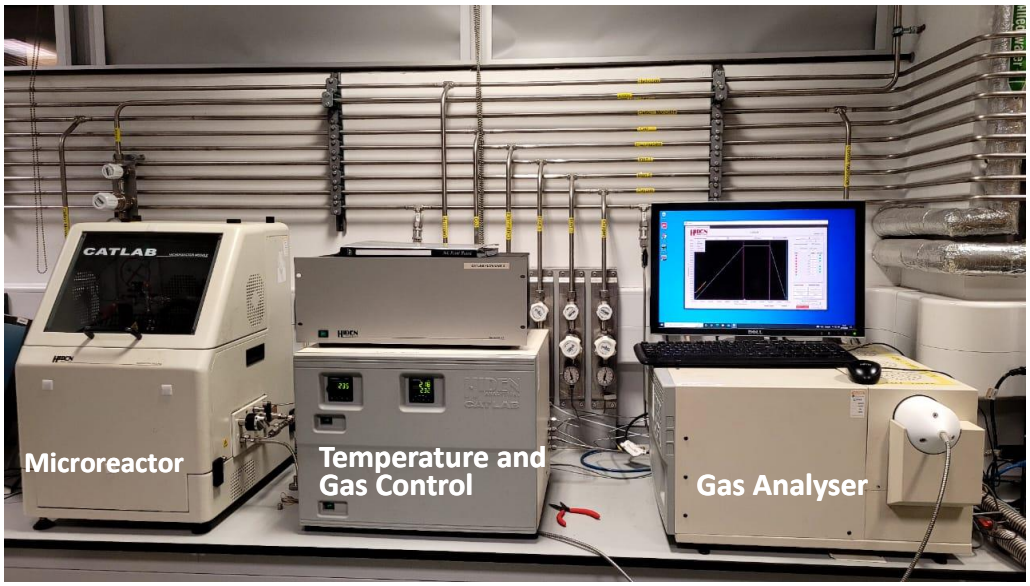

Figure 3.8: *Hiden Analytical CatLab Instrument (Source: Research Complex at Harwell).*

In this research work, chemisorption data was collected on a Hiden Analytical CatLab instrument, shown in Figure 3.8. The system consists of a microreactor, a QGA gas analyser, and a temperature and gas control unit. The instrument has a maximum operating temperature and pressure of 1000 ℃ and 1 bar respectively. Firstly, 100 mg of the catalyst sample was weighed and pre-treated in 20% O_2/Ar at 600 ℃ for 30 min. The sample was cooled to 50 ℃ after which the H_2-TPR was recorded in 10% H_2/Ar with a heating rate of 10 ℃ min^{-1} and a final temperature of 800 ℃.

3.4.7 Thermogravimetric analysis

Thermogravimetric analysis (TGA) is a technique that measures the mass of a material as a function of temperature and/or time. The material is exposed to a controlled temperature program in a controlled environment. A TGA machine has a very high-precision balance attached to a sample pan and is housed inside a furnace. During the analysis, the mass of a sample is monitored as a stream of gas (sample purge gas) is flowed through the system to control the furnace environment. This gas, which passes over the sample and leaves via an exhaust, may be inert (such as N_2, He, or Ar) or reactive (such as air, O_2, or CO_2). The sample is heated at a controlled rate while the change in weight as a function of temperature at different time intervals is recorded for a known initial mass of the sample. Subsequently, a plot of weight loss against temperature is generated. In general, the TGA analysis provides information on the thermal stability of a material within a desired temperature range. A thermally stable material will show an insignificant change in mass, corresponding to little or no slope in the temperature versus weight plot. The TGA also specifies the maximum use temperature of a material. Above this temperature, the material starts to deteriorate (McClure et al., 2009; Wang et al., 2017; Yang et al., 2019).

Herein, the thermogravimetric analysis was performed on a PerkinElmer TGA 8000 machine. The instrument has a hanging pan type of balance, a furnace (temperature range, sub-ambient to 1200 °C), and a maximum balance capacity of 1300 mg with a precision of 0.001%. Nitrogen was used as the sample purge gas. The furnace temperature was increased to 900 °C at a heating rate of 20 °C min^{-1}.

3.5 Process Variables Optimization

Various Design of Experiment (DOE) approaches have been reported to provide predictive knowledge of complex and multivariable processes with fewer numbers of experimental runs (Lawal et al., 2019; Lee and Yoo, 2018; Moersidik et al., 2020). Here, Multilevel Factorial Design using Minitab software was employed to analyse the contributions of temperature and pressure towards conversion and yield of products during the HDO reaction over the mic-Ni/ZSM-5 catalyst. Temperatures of 150 ℃, 200 ℃, 250 ℃ were tested, as well as pressures of 20 bar, 40 bar, 60 bar. A preliminary run guided the choice of minimum temperature used. At 120 ℃, virtually no reaction was seen at all pressures, whereas about 30% conversion of anisole was recorded at 150 ℃. Table 3.2 presents the factors examined in DOE studies and their levels.

Table 3.2: Reaction factors and their levels.

	Factor Level								
Temperature (℃)	150	150	150	200	200	200	250	250	250
Pressure (bar)	20	40	60	20	40	60	20	40	60

3.6 Catalytic Activity Test

All hydrodeoxygenation reactions were carried out in a 1×10^{-4} m^3 high pressure batch reactor, model 9045 supplied by the Parr Instrument Company, US. Figure 3.9 presents a schematic diagram of the reactor set-up. The reactor has a maximum operating temperature and pressure of 350 ℃ and 200 bar. It was equipped with a vessel of 3.3×10^{-2} m internal diameter, 2.0×10^{-2} m impeller diameter, and 5.8×10^{-2} m depth. Additionally, it has a heating system, a mechanical stirrer, a thermowell, and a pressure gauge. Also, there is a gas

inlet/sample collection valve, a gas vent valve, and a rapture disc. The sampling line is well-inserted into the reactor to ensure easy liquid sample collection. The thermowell is well-immersed for accurate measurement of the reactor content's temperature. Both the stirring speed and the reactor temperature were controlled via a Parr reactor controller model 4848.

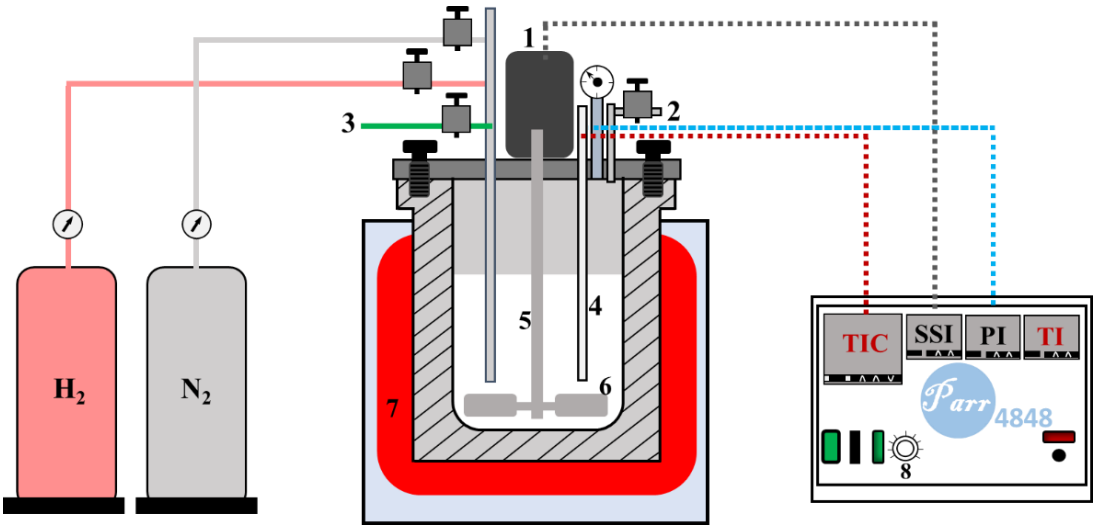

Figure 3.9: *Schematic diagram of the reactor set up 1: stirrer; 2: gas vent; 3: sampling point; 4: thermocouple; 5: stirrer shaft; 6: impeller; 7: heater; 8: stirrer controller; TIC: temperature indicator and control; SSI: stirrer speed indicator; PI: pressure indicator; TI: temperature indicator.*

The catalytic upgrading reaction was carried out with anisole, benzoic acid, a mixture of anisole-benzoic acid as the bio-oil model compounds, and the real bio-oil from sewage sludge. Prior to the hydrodeoxygenation reaction, the catalyst was reduced *ex-situ* in a furnace at 500 °C for 3 hours under a continuous flow of hydrogen (5% H_2/N_2) at a heating rate of 5 °C min^{-1}. Decalin (decahydronaphthalene), tetralin (1,2,3,4–tetrahydronaphthalene), and n-decane were used as the solvents. In a typical run, a 50 mL mixture containing 1–9 wt.% of the reactant(s) and 50–150 mg of the catalyst was charged into the reactor. The reactor was flushed three times with nitrogen, then pressurised to 20 bar and heated to the desired reaction temperature (120–340 °C). Stirring speed was maintained at 100 rpm during

the heating-up period. Following that, the nitrogen was replaced with 20 to 60 bar hydrogen. Subsequently, the reactor was mixed for 1–5 hours at a stirring rate of 800 rpm. Heating-up and cooling-down periods were not considered as part of the reaction time. The liquid product was recovered from the solid catalyst by filtration.

3.7 Product Analysis

Liquid products from the HDO reaction were analysed using an Agilent GC (model 6890N) equipped with a flame ionisation detector (FID) and a Zebron ZB-Wax capillary column (30 m × 0.25 mm × 0.25 μm). Injector and detector temperatures were set at 250 ℃ and 270 ℃ respectively. While the carrier gas was helium, liquid injection volume was 1 μm and a split ratio of 280:1 was used. The oven was programmed as follows; initial temperature of 35 ℃ was held for 2 min, increasing to 200 ℃ at a ramp rate of 20 ℃ min^{-1}, then to 220 ℃ at a ramp rate of 35 ℃ min^{-1} and held for 2.5 min. Before sample analysis, the GC was calibrated with the chemical standard of the expected products. These include methyl-cyclohexane, cyclohexane, cyclohexene, cyclohexanol, cyclohexanone, anisole, methoxycyclohexane, benzene, toluene, dimethoxy cyclohexane, methyl cyclopentane, phenol, benzaldehyde, benzyl alcohol, and cyclohexane carboxylic acid for identification and quantification.

In addition, GC-MS analysis was carried out at the Birmingham Energy Innovation centre, Tyseley, UK. Prior to the analysis, about 10 μL of the sample was dissolved in 900 μL dichloro-methane. The mixture was vigorously shaken. It was then filtered using a syringe filter, making it ready for the analysis. An Agilent 8890 equipped with a Q-TOF MS and a 7693A automatic liquid sampler was used to analyse the sample. The GC-MS machine has a DB-5 MS column with dimension 30 m, 250 μm, 0.25 μm. The following settings were used for the analysis: a scan range of 50 to 600 m/z, a He gas flow rate of 1 ml min^{-1}, and oven

temperature of 50 ℃, which was hold for 1 min and rose to 300 ℃ at 5 ℃ min^{-1} ramp rate. The NIST library was used to identified the chemical compounds in the analysed sample. The observed peak area was used to evaluate the mass spectra. To evaluate the extent of conversion, yield, and selectivity of products, degree of hydrodeoxygenation (selectivity to products with no oxygen), degree of hydrodearomatization (selectivity to products with no aromatics), and carbon balance, the following expressions were used;

$$X_i\ (\%) = \frac{n_{iR}}{n_{iF}} \times 100 \qquad 3.4$$

$$Y_j\ (\%) = \frac{n_{jP}}{n_{iF}} \times 100 \qquad 3.5$$

$$S_j\ (\%) = \frac{n_{jP}}{n_{iR}} \times 100 \qquad 3.6$$

$$X_{HDO}\ (\%) = \left(1 - \frac{\Sigma\left(n_{jP} \times NOA_j\right)}{n_{iF} \times X_i}\right) \times 100 \qquad 3.7$$

$$X_{HDA}\ (\%) = \left(1 - \frac{\Sigma\left(n_{jP} \times NAR_j\right)}{n_{iF} \times X_i}\right) \times 100 \qquad 3.8$$

$$C_{mb}\ (\%) = \frac{TMC_{DP}}{TMC_{FS}} \times 100 \qquad 3.9$$

where X_i is the conversion of reactant i, Y_j is the yield of product j, S_j is the selectivity of product j, X_{HDO} is the degree of hydrodeoxygenation, X_{HDA} is the degree of hydrodearomatisation, C_{mb} is the carbon mass balance, n_{iR} is the number of moles of i reacted, n_{iF} is the number of moles of i in the feed, n_{jP} is the number of moles of j in the products, NOA_j is the number of oxygen atoms in j, NAR_j is the number of aromatic rings in j, TMC_{DP} is the total mass of carbon atoms of detectable products in the reaction solution, and TMC_{FC} is the total mass of carbon atoms of i in the feed solution. Subscript i represents any of the reactants, while j represents any of the products, respectively.

A kinetic study was performed to evaluate the influence of some reaction variables. Important parameters such as activation energy, reaction order, reaction rates, and rate constants were estimated. To achieve this, it is a prerequisite to ensure the effect of mass transfer limitation is eliminated during the HDO reaction over the prepared catalysts and that reaction is kinetically controlled. Hence, a study was carried out on the effect of stirring rate and catalyst particle size on the initial rate of reaction. At constant pressure and temperature, the stirring speed was varied from 300 to 1200 rpm. The minimum stirring speed required to keep the catalyst particles suspended and eliminate external mass transfer limitations during the reaction was determined. For the internal mass transfer and intraparticle diffusion, the influence of the catalyst particle size was investigated. The catalyst was sieved into different sizes ranging from <75, 75–90, 90–120, and >120 µm, respectively. These various sizes of the catalyst were employed for the HDO reaction under the same temperature and pressure. Subsequently, the combined effects of the stirring speed and the catalyst particle size were used to establish the kinetically controlled region and were used for the remaining kinetic studies.

To estimate the kinetic parameters, some proposed correlations were adopted. Fogg and Gerrard correlations were employed to determine the value of hydrogen concentration in mg L^{-1} (Pintar et al., 1998; Srivastava, 2018; Wilke and Chang, 1955);

$$C_{H_2} = y_{H_2} \times \frac{P_{total}}{P_{total=1bar}} \times \frac{x_{H_2}}{1-x_{H_2}} \times \rho_s \frac{M_{H_2}}{M_s} \times 1000 \qquad 3.10$$

$$x_{H_2} = \exp\left(-125.939 + \frac{5528.45}{T} + 16.8893 \times ln(T)\right) \qquad 3.11$$

where C_{H_2} is the concentration of hydrogen, y_{H_2} is the mole fraction of hydrogen in gas phase, x_{H_2} is the mole fraction of hydrogen in liquid phase, ρ_s is the density of solvent in g L^{-}

[1], M_{H_2} is the molar mass of hydrogen in g mol^{-1}, M_s is the molar mass of solvent in g mol^{-1}, and T is the reaction temperature in Kelvin.

The measure of the ability of reactants and the solvent to diffuse through one another, also known as diffusivity or diffusion coefficient, was calculated using Díaz correlations (Díaz et al., 1987; Siddiquee et al., 2016). For accuracy, this correlation considered diffusivity at both 25 °C and the actual reaction temperature;

$$(D_{ei})_T = 4.996 \times 10^3 \times [(D_{ei})_{T=25}] \times e^{-2539/T} \qquad 3.12$$

but

$$(D_{ei})_{T=25\,^{\circ}\mathrm{C}} = 6.02 \times 10^{-5} \frac{V_A^{0.36}}{\mu_A^{0.61} V_i^{0.64}} \qquad 3.13$$

where $(D_{ei})_T$ is the diffusion coefficient of reactant i in solvent A at a given temperature T in cm^2 s^{-1}, $(D_{ei})_{T=25\,^{\circ}C}$ is the diffusion coefficient at 25 °C in cm^2 s^{-1}, T is absolute temperature in Kelvin, μ_A is the viscosity of tetralin in cP, V_i is the molar volume of reactant at the normal boiling point temperature in cm^3 gmol^{-1}, and V_A is the molar volume of solvent at normal boiling temperature in cm^3 gmol^{-1}.

To further confirm the absence of intraparticle diffusion, a criterion suggested by Weisz and Prater (1954) was deployed. This states that if the value of the observable modulus $(n\varphi^2)$, a dimensionless quantity, is less than 0.3 for a reaction order of less than or equal to 2, effect of internal diffusion is eliminated. Then the experimental observations are appropriate for kinetic study;

$$\eta\varphi^2 = \frac{r_0 \omega L^2}{C_i D_{iA}} \qquad 3.14$$

where η is the effectiveness factor, φ is the Thiele modulus, r_0 is the initial rate of reaction, ω is the catalyst loading, L is the length of a spherical catalyst particle, and C_i is the concentration of reactant i, respectively.

Reaction rate constant (k) was obtained at different reaction temperatures. A plot of ln$k$ against the inverse of temperature T was generated according to the Arrhenius equation and the activation energy was determined. In addition, the thermodynamic parameters for the adsorption of the reactant i were evaluated using the Van't Hoff equation (Fogler, 2019; Srivastava, 2018);

$$\ln k = \frac{-Ea}{R}\frac{1}{T} + \ln A \qquad 3.15$$

$$lnk_{ads} = \left(\frac{-\Delta H_{ads}}{RT}\right) + \left(\frac{\Delta S}{R}\right) \qquad 3.16$$

where; E_a is the activation energy (J mol^{-1}), R is the gas constant (8.3145 J K^{-1} mol^{-1}) A is the Arrhenius constant known as frequency factor (s^{-1}), $-\Delta H_{ads}$ represents the enthalpy of adsorption, ΔS represent the entropy, and k_{ads} is the adsorption equilibrium constant, respectively.

3.8 Summary of the Chapter

This chapter provides a list of materials and chemicals used in this research work. Procedures for catalyst preparation have been discussed. The basic principles for some major catalyst characterisation techniques have been reviewed. Procedures for various techniques used to characterise materials prepared in this research work have been discussed. In addition, the chapter presents procedures for the activity test (catalytic upgrading of bio-oil

on a high-pressure batch reactor) and product analyses. The next chapter (Chapter 4) presents the catalyst characterisation results.

CHAPTER 4

Catalyst Characterisation Results

4.1 Introduction

This chapter presents the result of the prepared catalyst's characterisation. Catalyst characterisation is very important because it allows linkage between the catalyst properties and its activity during a reaction. The primary objective of characterisation is to evaluate the physical, chemical, and surface properties of a catalyst and relate these properties to the catalytic activity. Characterisation is also used for the purposes of optimisation and control, as it applies to examining the catalyst's properties during preparation, at the activation stage, and during and after the reaction. In this work, the following characterisation techniques were employed: X-Ray Diffraction (XRD) was used for the determination of the crystallographic nature of both the SiO_2, mic-ZSM-5, and hie-ZSM-5 supports and the prepared nickel-based catalysts. Brunaur-Emmett-Teller and Barrett-Joyner-Halenda (BET-BJH) methods were used to evaluate both the total and specific surface areas in addition to the pore size distribution and pore volume of the catalysts. A Scanning Electron Microscope with Energy-Dispersive X-ray (SEM-EDX) was used to determine information on the morphology, size, and chemical composition of the catalysts. Transmission Electron Microscopy (TEM) was also used for the catalyst's texture and micro-structure examination. Ammonia Temperature Programmed Desorption (NH_3-TPD) was used to evaluate the type, amount, and strength of active sites present on the surface of the catalyst. Hydrogen Temperature Programmed Reduction (H_2-TPR) was employed to check the presence of reducible species on the catalyst and the nature of the interaction between the catalyst's surface and the reducible component. Thermogravimetric Analysis (TGA) was used to measure the catalyst's thermal stability and weight loss, if any, as a function of temperature.

4.2 X-ray Diffraction (XRD)

The XRD patterns of the parent zeolite (mic-ZSM-5), NaOH treated zeolite (hie-ZSM-5), their Ni-based catalysts, SiO_2 and Ni/SiO_2 are presented in Figure 4.1.

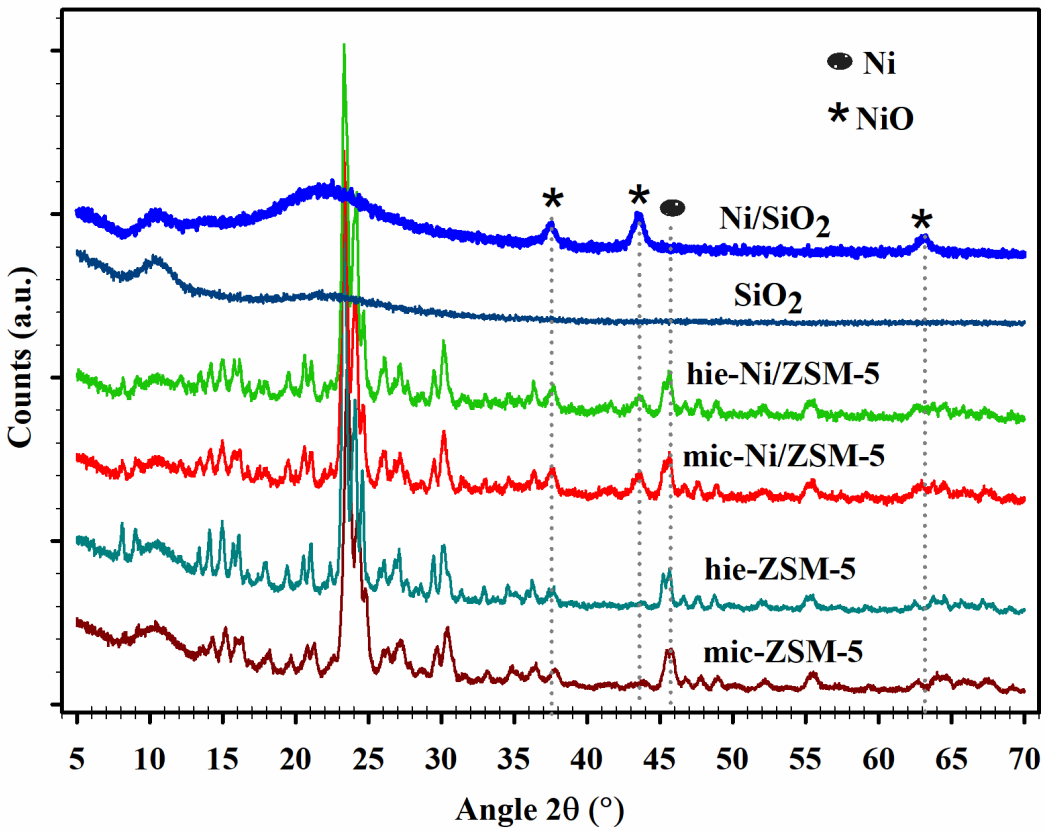

Figure 4.1: *XRD patterns of ZMS-5 and SiO_2 supports and their 5 wt.% Ni-based catalysts.*

No noticeable destruction of the zeolite framework was observed due to the NaOH treatment, hie-ZSM-5 retained all the characteristic diffraction peaks observed in the parent material. A peak at 2θ value of 21.6° confirmed that the zeolite support was intact after the treatment (Sarkar et al., 2012). However, a reduction in the peaks' intensity in the treated material compared to the parent zeolite was noticed. Possible factors that can cause decreases in peak intensity in crystallite materials are decreases in crystallite size, lattice strain (the measure of the distribution of the lattice constant due to crystal disorder), or the emergence of amorphous materials (Freitas et al., 2018; Gorzin and Yaripour, 2019). Extraction of framework silicon

due to NaOH treatment could possibly result in lattice dislocation (Dauda et al., 2020). Hence, a decrease in crystallinity from 100% in the mic-ZSM-5 support to 89.9% in the hie-ZSM-5 was noted, as shown in Table 4.1.

Following nickel impregnation, new diffraction peaks at 2θ = 37.6°, 43.7°, and 46.7° were observed for both mic-Ni/ZSM-5 and hie-Ni/ZSM-5 catalysts, which were ascribed respectively to NiO (111), NiO (200), and Ni (111) planes (Li et al., 2020; Tu et al., 2019). The peak at 43.7° was the typical diffraction peak of NiO crystals (G. Chen et al., 2020). It could also be seen from Figure 4.1 and Table 4.1 that, following the addition of metal to the supports, a further decrease in crystallinity was recorded. The crystallinity of the mic-ZSM-5 changed from 100% to 87.6%, while that of the hie-ZSM-5 decreased to 84.4% from 90.1%. Similarly, successful deposition of nickel on the SiO_2 support could be confirmed from the XRD spectra with the identification of peaks at 2θ = 37.5°, 43.7°, and 63.2°, corresponding respectively to NiO planes (111), (200), and (220) (Lestari et al., 2019; Lovell et al., 2015). A broad peak was observed between 2θ = 20° and 30°, which indicates the amorphous nature of the silica support.

Table 4.1 presents the results of the average crystallite sizes of the materials estimated from the XRD data using a line broadening technique (Scherrer equation). The Anderson (1975) equation was used to evaluate the degree of metal dispersion, on the catalysts. It can be seen that both the mic-ZSM-5 and hie-ZSM-5 have average crystallite sizes of 27.1 ± 0.2 nm and 26.8 ± 0.4 nm, respectively. These crystallite sizes increased to 30.7 ± 0.7 nm and 29.1 ± 0.5 nm after nickel was impregnated onto the respective supports. Crystallite sizes of NiO were determined to be 12.6 ± 0.9 nm, 11.9 ± 0.8 nm, and 14.8 ± 0.2 nm for mic-Ni/ZSM-5, hie-Ni/ZSM-5, and Ni/SiO_2 catalysts, respectively.

Table 4.1: Percentage crystallinity, crystallites sizes, and percentage metallic dispersion estimated from the XRD data.

Sample ID	Crystallinity[a] (%)	Average Crystallite size (nm)[b]		Dispersion[c] (%)
		Support	Metal (NiO)	
mic-ZSM-5	100 ± 0.0	27.1 ± 0.2	-	-
hie-ZSM-5	90.1 ± 0.2	26.8 ± 0.4	-	-
mic-Ni/ZSM-5	87.6 ± 0.2	30.7 ± 0.7	12.6 ± 0.9	8.0 ± 0.5
hie-Ni/ZSM-5	84.4 ± 0.9	29.1 ± 0.4	11.9 ± 0.8	8.5 ± 0.6
Ni/SiO_2	-	-	14.8 ± 0.2	6.8 ± 0.1

[a] Peak to noise ratio
[b] Scherrer equation
[c] Anderson equation

Similarly, the degree of metal dispersion was respectively 8.0 ± 0.5 %, 8.5 ± 0.6 %, and 6.8 ± 0.1 % for mic-Ni/ZSM-5, hie-Ni/ZSM-5, and Ni/SiO_2 catalysts. According to Anderson (1975), the degree of metal dispersion on a support is strongly correlated with its particle size. The effect of particle size on catalytic activity has been reported in the literature (Silva et al., 2014; Wang, et al., 2020). Fu et al. (2018) noticed the effect of smaller crystallite size during the hydrogenation of glucose over a nickel-supported carbon catalyst. A particle size of 17 nm exhibited superior catalytic activity, with higher glucose conversion and product yield compared to catalysts with a 22 nm nickel particle size. Similarly, during the methanation of CO_2, the highest catalytic activity and CH_4 selectivity were recorded on a Ni-supported catalyst with a particle size of 19 nm, compared with 32 nm and 46 nm (Kesavan et al., 2018). These effects could be attributed to the improved metal accessibility and dispersion that occurs for smaller particles.

4.3 Brunaur-Emmett-Teller (BET) and Barrett-Joyner-Halenda (BJH) Analysis

Figure 4.2 presents the nitrogen adsorption-desorption isotherms of both the supports and their corresponding nickel catalysts. The BJH method was used for the determination of pore size distribution. The BET surface area and total pore volume calculated from the measurements are summarised in Table 4.2.

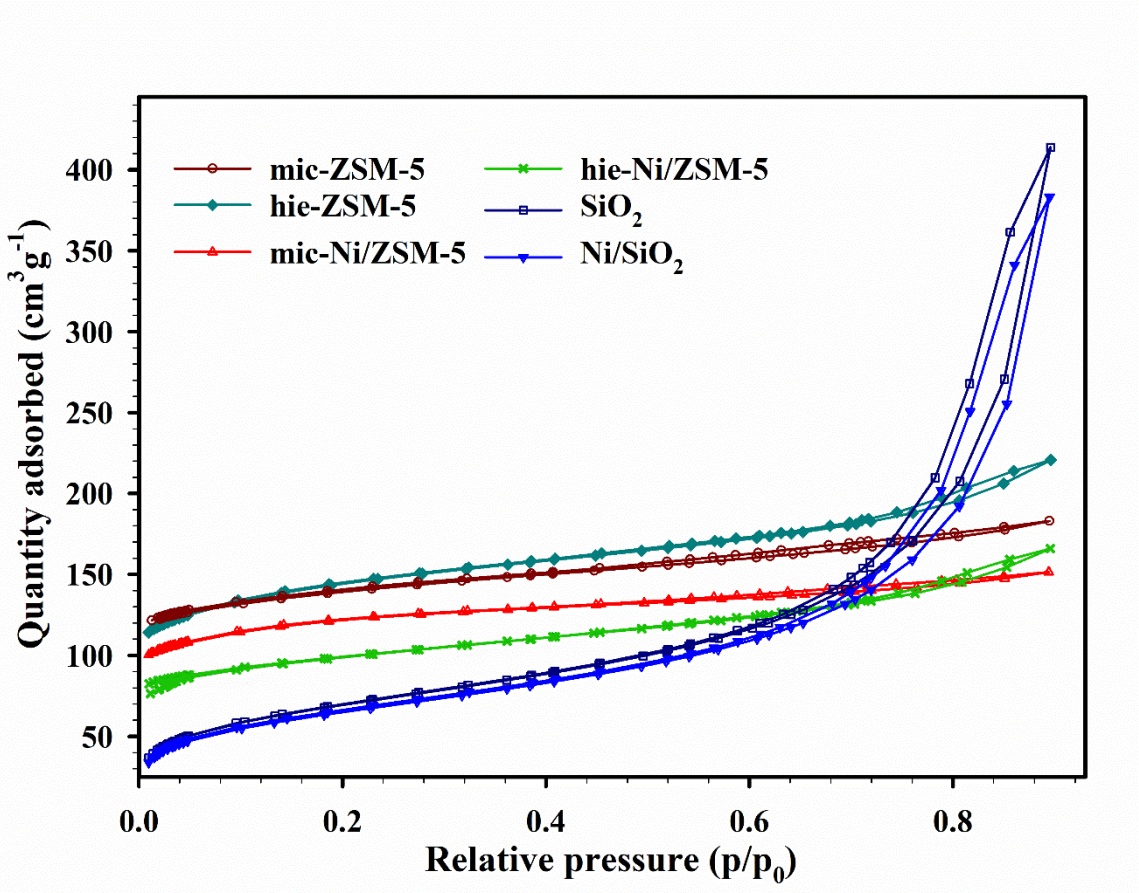

Figure 4.2. *Nitrogen adsorption-desorption isotherms of ZSM-5 and silica supports and their 5 wt.% Ni-based catalysts at 77K.*

An increase in N_2 adsorption between p/p_0 = 0.4 and 0.8 on the mic-ZSM-5 support indicates the presence of some mesopores in the material. In addition, the isotherm is more like a Type I isotherm, which is characterised by high fractions of fine micropores and low fractions of mesopores, based on IUPAC classification (Dauda et al., 2020; Haul et al., 1982). There was a noticeable increase in the quantity of adsorbed N_2 and a shift from Type I to Type II

isotherms after the mic-ZSM-5 was treated with 0.2 M NaOH to produce the hi-ZSM-5 support. The hie-ZSM-5 shows a hysteresis loop (Type H4) at higher relative pressures, indicating the presence of mesopores (Li et al., 2020). The SiO_2 and Ni/SiO_2 exhibit marked uptake of Type IV isotherm with H2 type hysteresis loop at $p/p_0 > 0.75$, showing mesoporous characteristics due to a capillary condensation process (Al Soubaihi et al., 2020).

Table 4.2: Textural properties of ZSM-5 and SiO_2 supports and the prepared Ni catalysts.

Sample	S_{BET} $(m^2\,g^{-1})^a$	S_{micro} $(m^2\,g^{-1})^b$	$S_{ext.}$ $(m^2\,g^{-1})^c$	V_{total} $(m^3\,g^{-1})^d$	V_{micro} $(m^3\,g^{-1})^e$	V_{meso} $(m^3\,g^{-1})^f$
mic-ZSM-5	434	276	158	0.284	0.147	0.137
hie-ZSM-5	459	238	221	0.342	0.126	0.216
hie-Ni/ZSM-5	316	166	150	0.257	0.088	0.169
mic-Ni/ZSM-5	378	236	142	0.235	0.126	0.109
SiO_2	248	10	237	0.642	0.004	0.638
Ni/SiO_2	232	9	222	0.594	0.003	0.591

[a] From N_2 adsorption measurement.
[b] From N_2 adsorption measurement (t-plot).
[c] From N_2 adsorption measurement (t-plot).
[d] From N_2 adsorption measurement at $P/P_0 = 0.8942$.
[e] From N_2 adsorption measurement (t-plot).
[f] Difference between c and d ($V_{total} - V_{micro}$).

Following the NaOH treatment, the surface area of the mic-ZSM-5 support increased in addition to the formation of more mesopores. The BET surface area increased from 434 to 459 $m^2\,g^{-1}$. There was a reduction in the micropore surface area to 238 $m^2\,g^{-1}$ from 276 $m^2\,g^{-1}$ corresponding to a 12 % increase in the mesopore surface area. The total pore volume of the supports increased to 0.342 $m^3\,g^{-1}$ in hie-ZSM-5 from 0.284 $m^3\,g^{-1}$ in the mic-ZSM-5, with mesopore volumes of 0.137 $m^3\,g^{-1}$ and 0.216 $m^3\,g^{-1}$ for the mic-ZSM-5 and hie-ZSM-5

respectively. Compared to the conventional microporous ZSM-5, a hierarchical ZSM-5 is characterised by enhanced surface area (Rac et al., 2013; Sadowska et al., 2013; Sankaranarayanan et al., 2015; Serrano et al., 2011). Loading of the nickel caused an evident decrease in the surface area and total pore volume for all the supports, suggesting that nickel has been effectively deposited (Sankaranarayanan et al., 2015). The BET surface area decreased from 434 $m^2 g^{-1}$ to 378 $m^2 g^{-1}$ for the mic-ZSM-5, from 459 to 316 $m^2 g^{-1}$ for the hie-ZSM-5, and from 248 to 232 $m^2 g^{-1}$ for the SiO_2.

Similarly, a decrease in the total pore volume was noticed. The 0.284, 0.342, and 0.642 $m^3 g^{-1}$ recorded for mic-ZSM-5, hie-ZMS-5, and SiO_2 supports decreased to 0.235, 0.257, and 0.594 $m^3 g^{-1}$ on the mic-Ni/ZSM-5, hie-Ni/ZSM-5, and Ni/SiO_2 catalysts, respectively. The observed decrease in pore volumes and surface area after nickel incorporation is attributed to partial blockage of pores due to the metal loading (Ghampson et al., 2016). As established from Table 4.2, there was a decrease of 0.049 $m^3 g^{-1}$, 0.085 $m^3 g^{-1}$, and 0.048 $m^3 g^{-1}$, respectively, in the total pore volume after 5 wt.% nickel impregnations on the mic-ZSM-5, hie-ZSM-5, and the SiO_2 supports. For all the supports, metal loading caused a greater decrease in mesopore volumes than micropore volumes. The decrease was 57.1%, 55.3%, and 97.9% for mic-ZSM-5, hie-ZSM-5, and SiO_2, respectively.

4.4 Scanning Electron Microscope-Energy-Dispersive X-ray

The morphologies of the mic-ZSM-5, hie-ZSM-5, and SiO_2 supports and the corresponding Ni-based catalysts were investigated using SEM (shown in Figure 4.3). All samples show agglomerates of fine particles having approximate sizes ranging between 30 and 180 nm for the mic-ZSM-5 and hie-ZSM-5, and 60 and 170 nm for SiO_2. However, the ZSM-5 supports exhibited less agglomeration with more defined crystal shapes compared to the SiO_2 support.

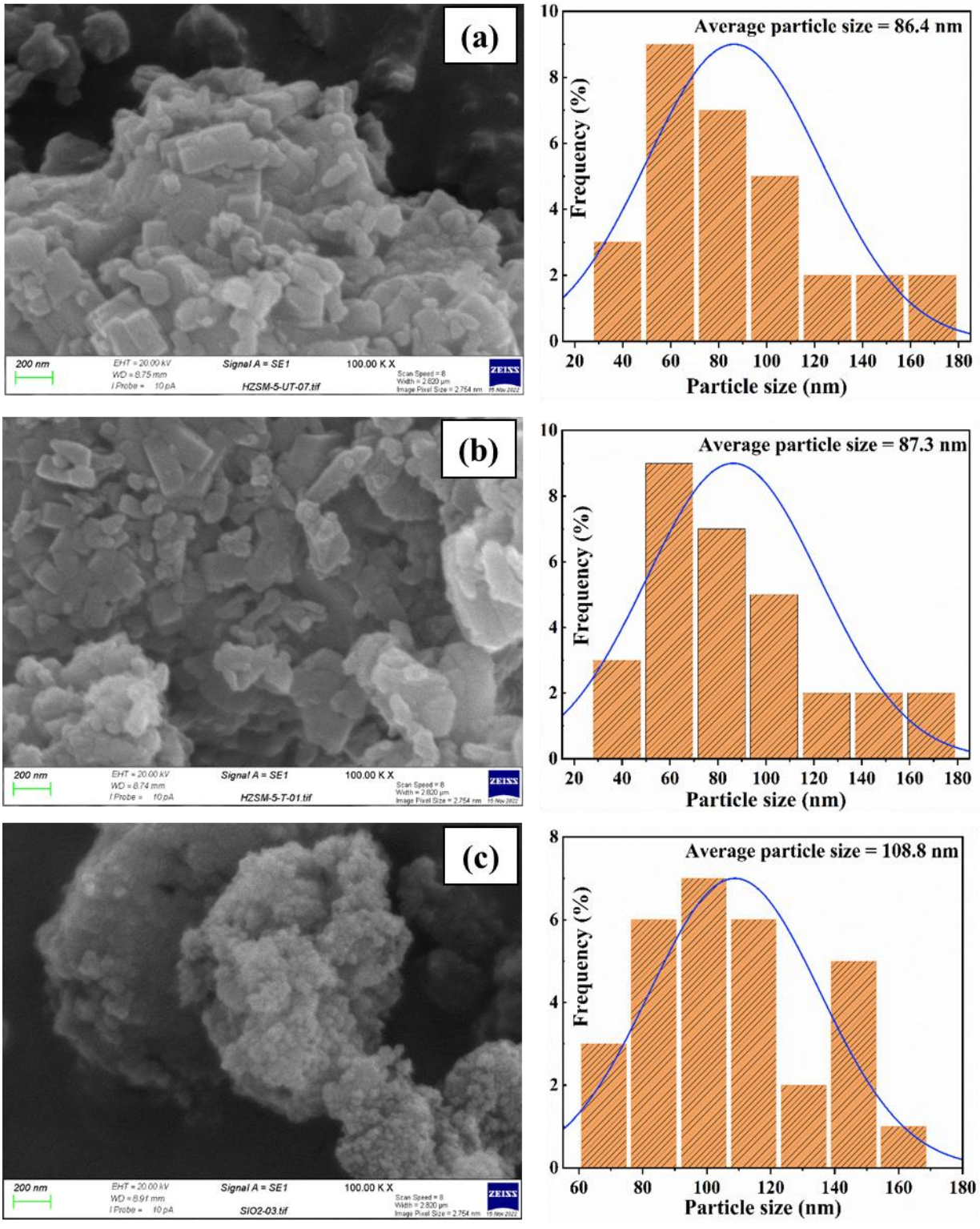

Figure 4.3: *SEM images of the catalyst supports, (a) mic-ZSM-5, (b) hie-ZSM-5, and (c) SiO_2.*

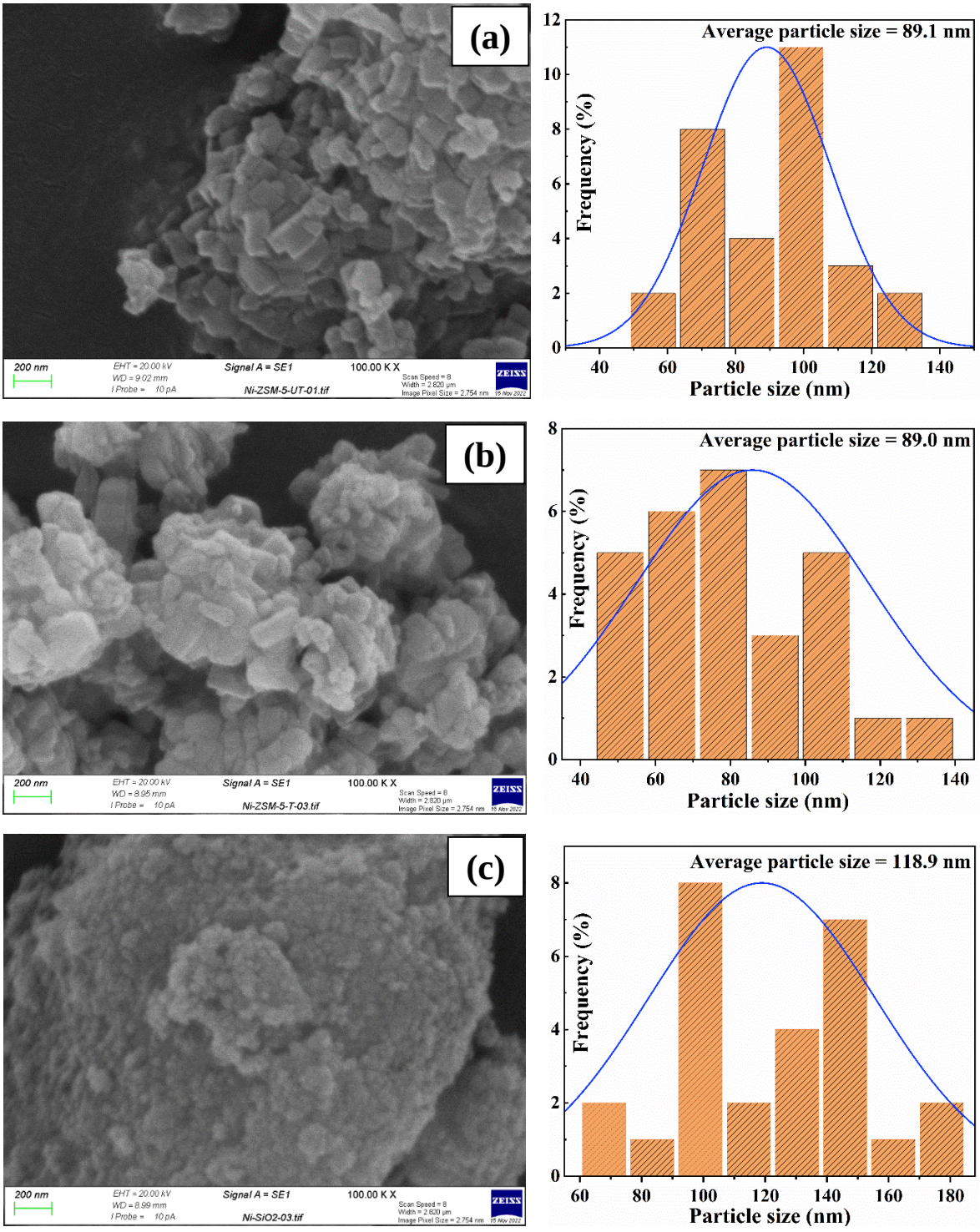

Figure 4.4: *SEM images of the prepared catalysts, (a) mic-Ni/ZSM-5, (b) hie-Ni/ZSM-5, and (c) Ni/SiO_2.*

Similar findings were reported by Sompech et al. (2016) when an amorphous silica obtained from a rice husk and bagasse were analysed. Oertel et al. (2014) highlighted a similar trend

for fume silica and pyrogenic silica. Vennestrøm et al. (2011) demonstrated a sponge-like and aggregated morphology as a typical characteristic shown by a mesoporous material. Analysis of the particle size further using ImageJ software revealed that 50 to 70 nm particles are the most dominant in the ZSM-5 supports. The average particle size was 86.4 nm for mic-ZSM-5 and 87.3 nm for the hie-ZSM-5. But larger particles of around 90 to 110 nm with a mean size of 108.8 nm have the highest frequency in the SiO_2 support. Noteworthy is the similarity of the particles in both the mic-ZM-5 and hie-ZSM-5 supports, suggesting that the NaOH treatment did not significantly affect the morphology of the support. The SEM result is in full agreement with the XRD data.

After the incorporation of 5 wt.% nickel on the different catalyst supports, as shown in Figure 4.4, increases in the particle size in the range of 90 to 110 nm and 70 to 90 nm were observed in the mic-Ni/ZSM-5 and hie-Ni/ZSM-5 catalysts. The range of particle sizes remains nearly the same, 90 to 110 nm, for SiO_2 and its Ni-based catalyst. However, there was an increase in the mean particle size of all the catalysts compared to their corresponding supports. The calculated values were 86.4 to 89.1 nm, 87.3 to 89.0 nm, and 108.8 to 118.9 nm for mic-ZSM-5, hie-ZSM-5, and SiO_2 respectively. The SEM images revealed somehow more compact structures.

EDX elemental mapping was used to visualise and quantify the distribution of elements on the catalysts. Table 4.3 presents the percentage compositions of Si, Al, O, C, and Ni in the samples. The ZSM-5 zeolite, which is an aluminosilicate material, has silica and alumina as its major constituents. An increase in the amount of carbon content from 7.35% in the mic-ZSM-5 to 9.68% in the hie-ZSM-5 supports was observed. This probably arose as the mic-ZSM-5 passed through a series of preparation steps to generate the hie-ZSM-5 support.

Some trace amount of nitrogen, 1.21 %, was detected in the parent zeolite support. As expected, there was no evidence of nickel in either the mic-ZSM-5 or hie-ZSM-5 supports.

Table 4.3: EDX elemental mapping result of ZSM-5 supports and the Ni-based catalysts.

Element (%)	**mic-ZSM-5**	**hie-ZSM-5**	**mic-Ni/ZSM-5**	**hie-Ni/ZSM-5**	**Ni/SiO_2**
O	53.77	52.29	50.52	50.43	50.24
Si	35.46	35.70	28.68	28.27	35.23
Al	2.21	2.39	1.81	1.75	0.00
Ni	0.00	0.00	4.26	4.60	5.44
C	7.35	9.68	14.73	13.70	9.09
N	1.21	-	-	1.25	-
Total (%)	**100**	**100**	**100**	**100**	**100**
Si/Al	16	15	15	16	-

Following Ni impregnation, there was a noticeable decrease in the amount of oxygen, silicon, and aluminum content in all the samples. However, carbon content increased to 14.73 % in the mic-ZSM-5 and 13.70 % in the hie-ZSM-5, respectively. The targeted metal loading of 5 wt.% was approximately achieved (± 0.51 mean deviation). A spectrum of the EDX elemental mapping is shown in Figure 4.5 which demonstrates the uniform distribution of Ni and, by extension, confirms the successful deposition of Ni on the supports. The EDX results are consistent with the XRD data presented in Figure 4.1. There, new diffraction peaks ascribed to the nickel metal appeared after Ni impregnation on the supports.

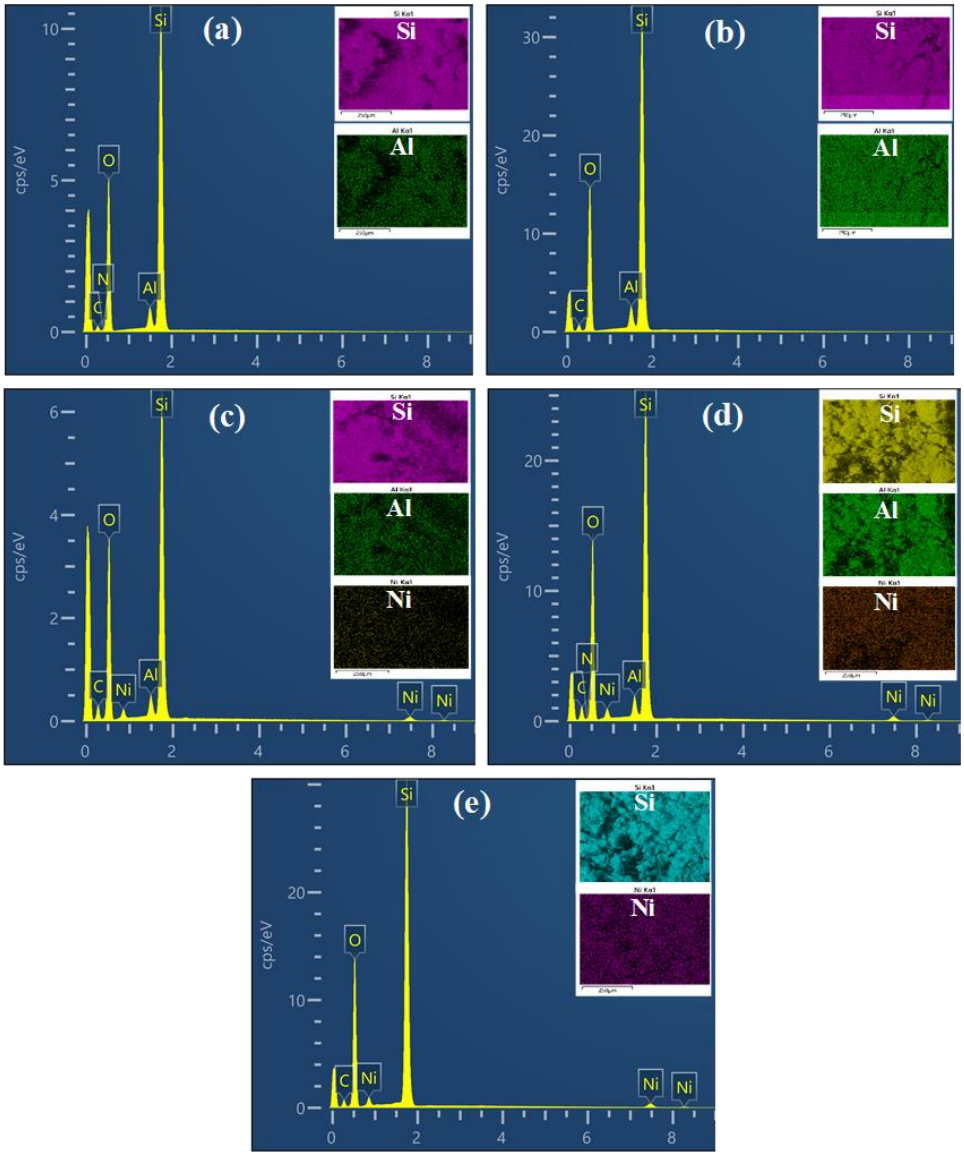

Figure 4.5: *Spectra of the EDX elemental mapping of the ZSM-5 supports and the Ni-based catalysts; (a) mic-ZSM-5, (b) hie-ZSM-5, (c) mic-Ni/ZSM-5, (d) hie-Ni/ZSM-5, and (e) Ni/SiO_2.*

A slight decrease in the Si/Al ratio from 16 to 15, which is shown in Table 4.3 above, is caused by the extraction of framework silica due to the NaOH treatment. There were reports of a decrease in Si/Al ratio when microporous ZSM-5 was treated with 0.1 M, 0.2 M, 0.3 M and 0.4 M of NaOH (Dauda et al., 2020; You and Park, 2014). However, a pioneering study by Rac et al. (2013) reported improved mesoporous properties and demonstrated nearly full preservation of both the Si/Al ratio and the acid site strength when ZSM-5 (SiO_3/Al_2O_3 = 50) was treated with 0.2 M NaOH.

4.5 Transmission Electron Microscopy

TEM images were captured to display finer detail and shown in Figure 4.6.

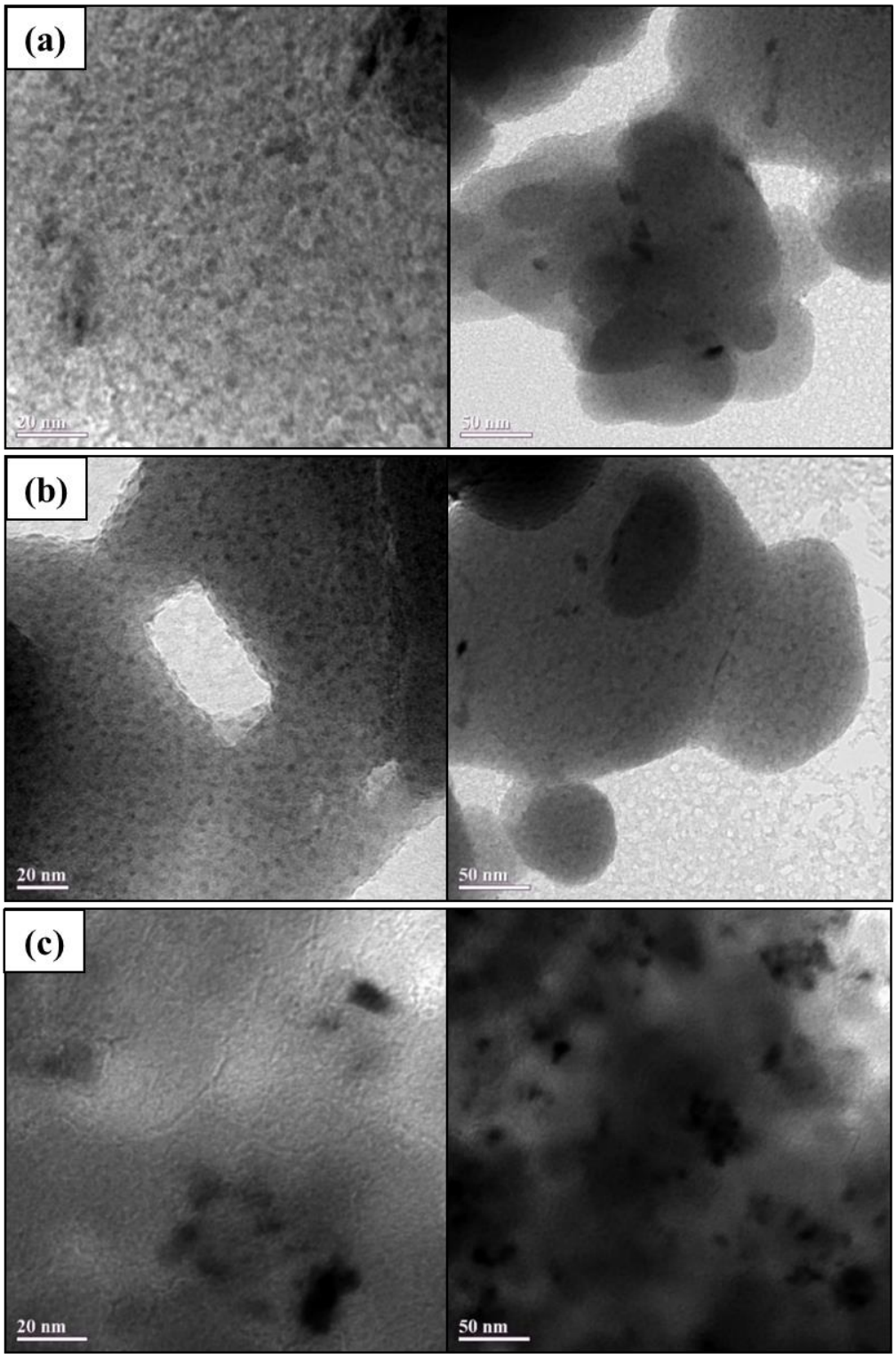

Figure 4.6. *TEM image of mic-Ni/ZSM-5 (a), hie-Ni/ZSM-5 (b) and Ni/SiO_2 (c) catalysts.*

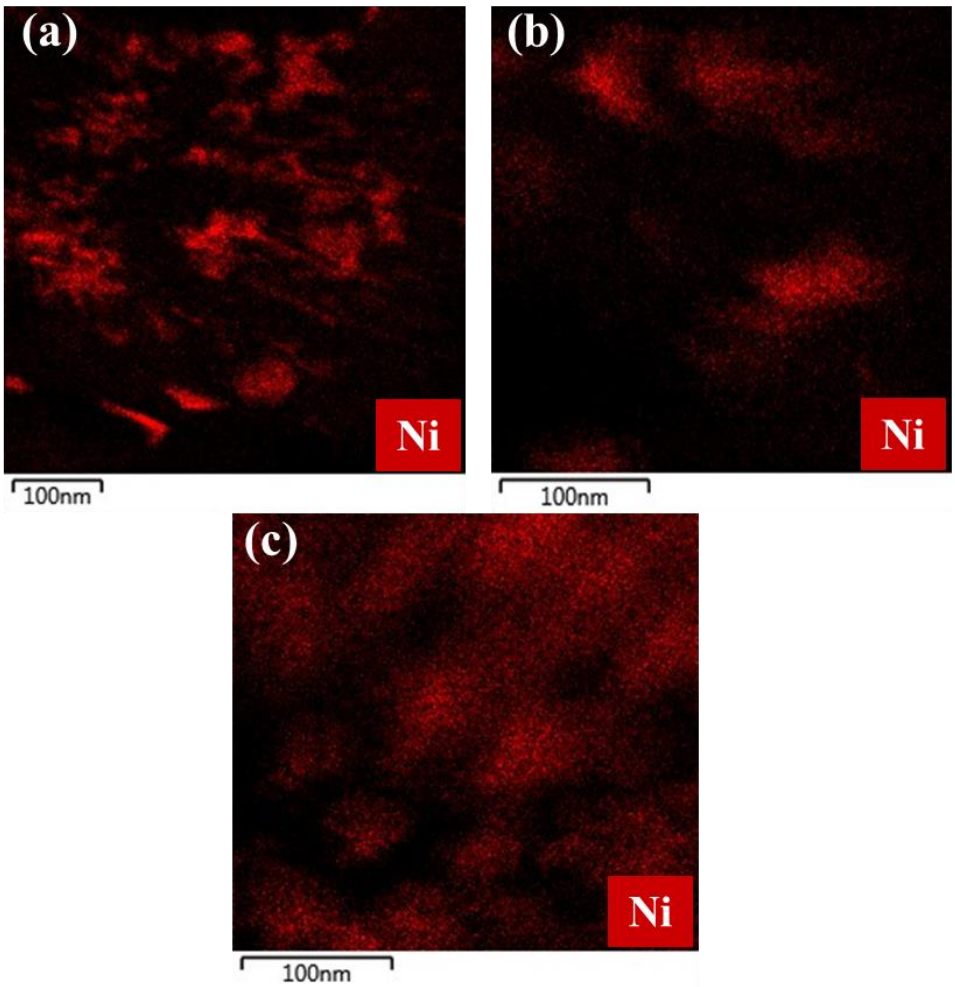

***Figure 4.7**: Elemental mapping by dark-field scanning transmission electron microscopy; mic-Ni/ZSM-5 (a), hie-Ni/ZSM-5 (b) and Ni/SiO_2 (c) catalysts.*

It is clear from Figure 4.6 that there is a high degree of metal dispersion, particularly in mic-Ni/ZSM-5 and hie-Ni/ZSM-5. The nickel particles there are smaller than those on Ni/SiO_2 catalysts. The particle sizes range from 2 to 8 nm, 2 to 7 nm, and 5 to 16 nm respectively, with an average size of 5, 3.5, and 9.5 nm for mic-Ni/ZSM-5, hie-Ni/ZSM-5, and Ni/SiO_2 catalysts. The degree of metal dispersion on the respective catalysts was evaluated using Anderson (1975) equation as 20% for mic-Ni/ZSM-5, 29% for hie-Ni/ZSM-5, and 11% for Ni/SiO_2. When these results were compared with the ones obtained from the XRD data, the trend was consistent. However, smaller nickel particle sizes were observed from the TEM results as compared to the XRD data, hence a higher degree of metal dispersion was

recorded. To further investigate the likely positions of the metal particles on the catalysts, an elemental mapping by dark-field Scanning Transmission Electron Microscope was performed. It is obvious from Figure 4.7 that Ni is more visible on the mic-Ni/ZSM-5 and Ni/SiO_2 catalysts than on the hie-Ni/ZSM-5 catalyst, suggesting high dispersion of nickel within the mesopores of the treated support, hie-ZSM-5.

4.6 Ammonia Temperature Programmed Desorption

Figure 4.8 presents the measure of acidity of the catalysts performed by temperature programmed desorption (TPD) using ammonia as a probe molecule.

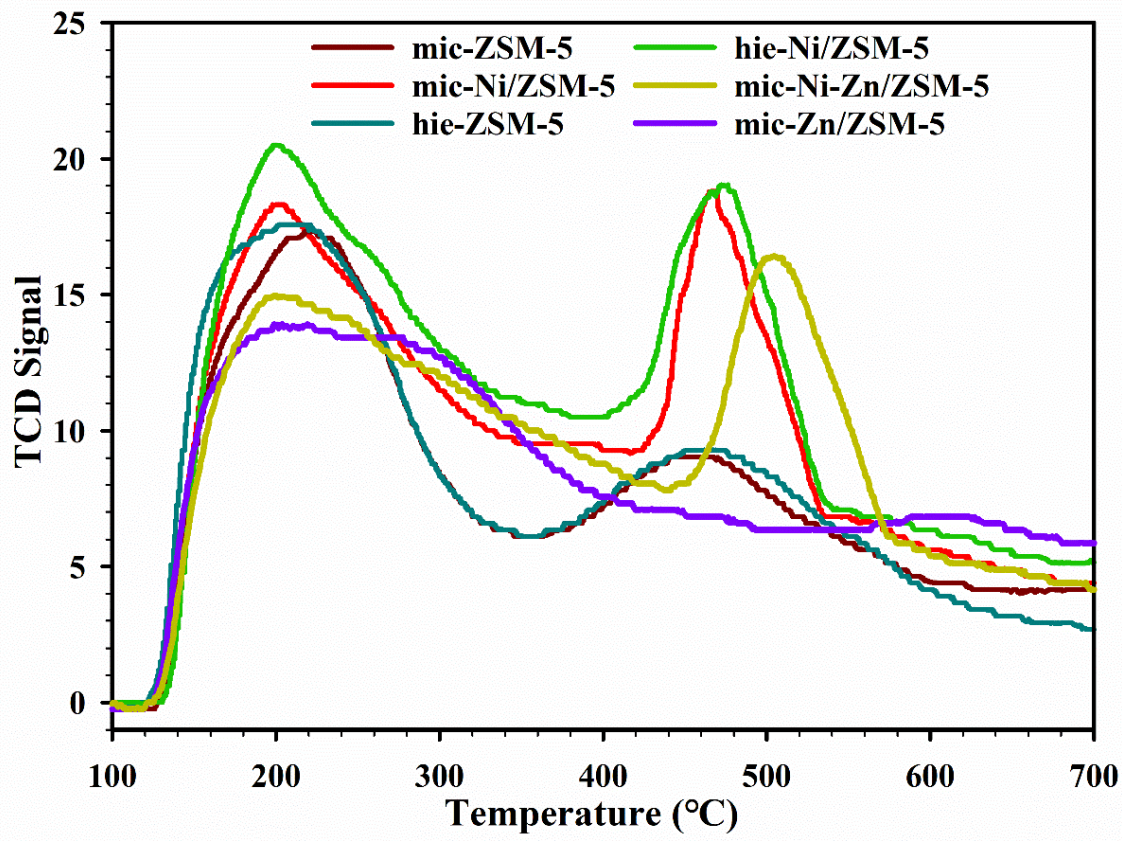

Figure 4.8: *The NH_3-TPD profile of the mic-ZSM-5 and hie-ZSM-5 supports; 5 wt.% nickel-based mic-Ni/ZSM-5 and hie-*Ni/ZSM-5 catalysts; 5 wt.% zinc-based mic-Zn/ZSM-5 and 3 wt.% zinc–2 wt.% nickel mic-Ni-Zi/ZSM-5 catalysts.

The zeolite sample exhibited dual desorption peaks between 130 ℃ to 350 ℃ and 350 ℃ to 580 ℃ which agrees with the acidity data for MFI materials reported in the literature (Gorzin and Yaripour, 2019). The high-temperature and low-temperature peaks were respectively attributed to the NH_3-desorption from the strong and weak acid sites. Peak temperature and area are linked to acid strength and acid site concentration. High desorption temperatures indicate high acid strength, while the area of the desorption peak is proportional to the acid site concentration (Feng et al., 2020; Tu et al., 2019; Yang et al., 2019). It could be seen from the Figure 4.8 that both the mic-ZSM-5 and the hie-ZSM-5 supports showed low-temperature peaks centred at 204 ℃, and a high-temperature desorption peak centred at 460 ℃. The peak intensity of the hie-ZSM-5 support is higher than that of mic-ZSM-5. It is also obvious that peaks intensities increased when nickel was added, especially those centred at around 460 ℃. Notably, introducing 2 wt.% zinc into a 3 wt.% nickel-containing mic-Ni/ZSM-5 reduced the intensities of the two major peaks in addition to shifting the centre of the high-temperature desorption peak from around 470 ℃ to 505 ℃. However, complete substitution of the active metal with 5 wt.% zinc reduced further both the high and low-temperature desorption peaks. The peak centre at 505 ℃ almost totally flattens whereas the peak initially centred at 205 ℃ broaden to a wide range of temperature, 195 – 270 ℃.

Figure 4.9 presents the NH_3 desorption profile of the silica support and its catalyst. The SiO_2-based sample displayed a broad range of peaks between 300 ℃ to 800 ℃. There was a small increase in the desorption peak intensity following nickel impregnation, in addition to generating a new desorption peak centred at 640 ℃. Formation of new peaks was reported when transition metals such as nickel were introduced onto a catalyst support (Tu et al., 2019).

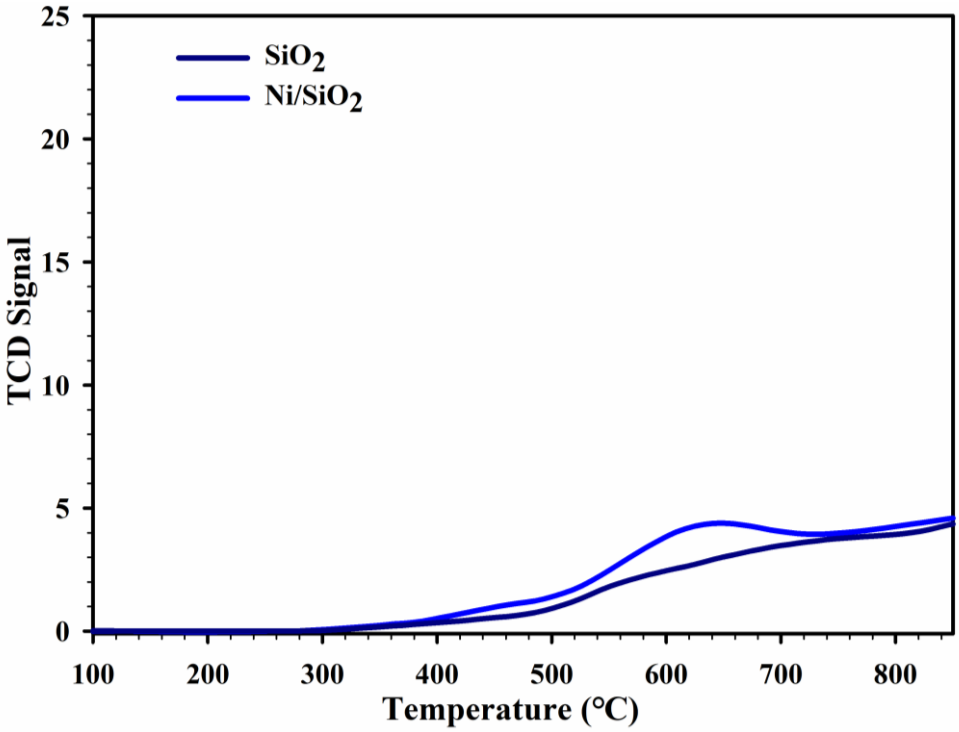

Figure 4.9: *The NH_3-TPD* profile of the silica support, SiO_2, and the 5 wt.% nickel-based, Ni/SiO_2, catalyst.

For a quantitative evaluation of the acid sites, the NH_3-TPD profiles were deconvoluted into three distinct peaks corresponding to weak, medium, and strong acid sites using the Gaussian fitting method, shown in Figures 4.10 and 4.11 as reported elsewhere (Loricera et al., 2011; Sangnikul et al., 2019). A summary of the acid site concentration and distribution from the deconvoluted NH_3-TPD curves is shown in Table 4.4. There was an increase in the total peak area from 4018 to 4465 (a.u) owing to the treatment of the mic-ZSM-5 with 0.2 M NaOH to produce the hie-ZSM-5 support. This implies an increase in the acid site concentration in the hie-ZSM-5 compared to the mic-ZSM-5. The distribution of acid sites in both supports was nearly identical, with strong acid sites having higher proportions of 48.8% and 47.6 % in the mic-ZSM-5 and hie-ZSM-5 supports, respectively. With a low degree of crystallinity and more mesopores, as quantified accordingly from the XRD and BET data, hie-ZSM-5 is expected to possess less coordinating aluminium in the framework, leading to a lower strong acid site concentration. Although the margin in the strong acid site concentration between

the two zeolite supports is not wide, this finding is still in agreement with the previous report that microporous zeolites usually have higher strong acid site concentrations than their mesoporous counterparts (Tu et al., 2019).

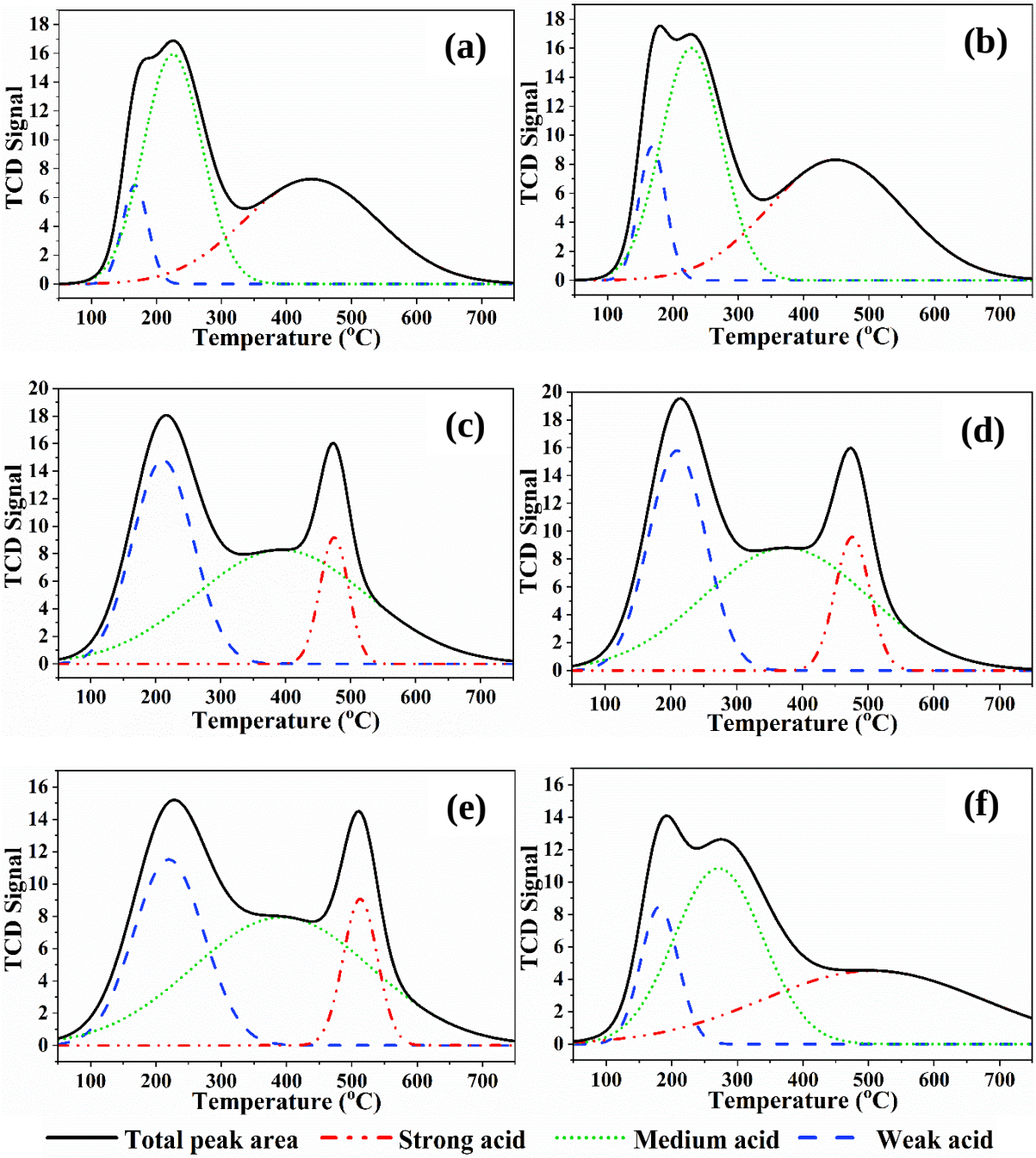

Figure 4.10: *Deconvolution profile of the NH_3-TPD results for the support; (a) mic-ZSM-5, and (b) hie-ZSM-5; 5 wt.% nickel catalyst, (c) mic-Ni/ZSM-5, and (d) hie-Ni/ZSM-5; 3 wt.% nickel-2wt.% zinc catalyst, (e) mic-NiZn/ZSM-5, and 5 wt.% zinc catalyst, (f) mic-Zn/ZSM-5.*

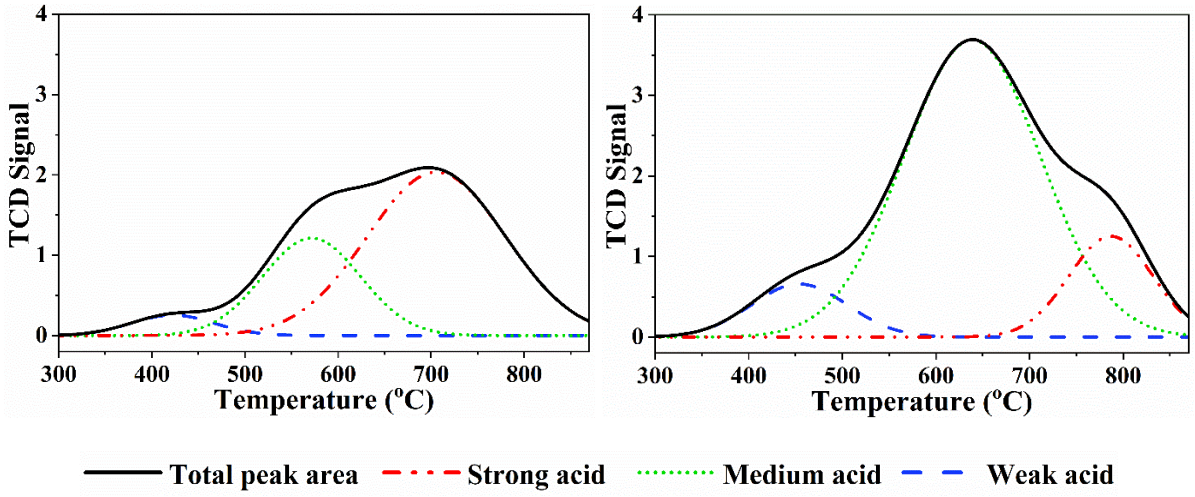

Figure 4.11: *Deconvolution profile of the NH_3-TPD results for the silica support, (a) SiO_2 and the 5 wt% nickel-silica catalyst, (b) Ni/SiO_2.*

Table 4.4: Acidic property of the supports and the corresponding 5 wt.% nickel, 5 wt.% zinc, and 3–2 wt.% Ni/Zn-based catalysts.

		Acid site concentration (%)			Peak temperature (°C)		
Sample	**Total peak area (a.u)**	**Weak**	**Medium**	**Strong**	**T_{pw}**	**T_{pm}**	**T_{ps}**
mic-ZSM-5	4018	8.4	42.8	48.8	167	225	438
hie-ZSM-5	4465	11.7	41.7	47.6	168	228	449
mic-Ni/ZSM-5	4967	35.0	54.8	10.2	210	393	475
hie-Ni/ZSM-5	5289	33.2	55.2	11.6	209	380	475
mic-Ni-Zn/ZSM-5	4844	31.9	55.8	12.3	219	392	512
mic-Zn/ZSM-5	4325	14.1	42.4	43.5	181	271	506
SiO_2	562	5.1	28.4	66.5	422	572	705
Ni/SiO_2	898	9.4	75.3	15.3	454	638	787

T_{pw}, T_{pm}, T_{ps} = Peak temperature for weak, medium and strong acid sites

Impregnating the parent and the treated ZSM-5 with nickel increased, significantly, the acid sites concentration as the total peak area charged from 4018 to 4967 (a.u) for mic-ZSM-5 and from 4465 to 5289 (a.u) for hie-ZSM-5. There was a significant change in the distribution of acid sites. The concentration of weak sites remarkably increased from 11.7% in the hie/ZSM-5 to 33.2% in the hie-Ni/ZSM-5, and from 8.4% in the mic-ZSM-5 to 35.0% in the hie-Ni/ZSM-5. While there was an increase in the medium acid sites' concentration from 42.8 to 54.8%, and from 41.7 to 55.2%, a decreasing trend was observed for the strong acid sites' concentration from 48.8 to 10.2%, and from 47.6 to 11.6% for mic-ZSM-5 and hie-ZSM-5, respectively. It should be noted that medium acid sites possess a higher acidity compared to weak acid sites, but are still less acidic than strong acid sites (Loricera et al., 2011). These sites can donate protons more readily and are usually associated with strong (Brønsted) acids (Sangnikul et al., 2019).

As mentioned earlier, some major effects of metal impregnation on a support are the generation of new acid sites in addition to altering the acid sites distribution (Gorzin and Yaripour, 2019). Metals such as platinum, palladium, and nickel can interact with the acidic sites on the zeolite surface, leading to a change in their electronic properties (Ezeonu et al., 2023; Gamliel et al., 2018; Shafaghat et al., 2015). This interaction can either enhance or weaken the acid-site concentrations, depending on the nature of the metal and its coordination with the zeolite framework. A decrease in weak acid sites concentration was reported when Ni and Fe were added to a HBeta zeolite (Shafaghat et al., 2016). Similarly, in addition to the decrease in the concentration of strong acid sites, the incorporation of Ga onto ZSM-5 generates additional sites with relatively lower acid strength (Ausavasukhi et al., 2009). A significant decrease in the total acid sites concentration attributed to the passivation effects of SiF_6^{2-} was seen when HZSM-5 was modified with $ZnSiF_6 \cdot 6\ H_2O$ (Jia et al., 2017).

Moreover, the introduction of Zn caused an increase in the concentration of weak acid site, whereas that of strong acid site clearly decreased. According to Tu et al. (2019), nickel-based catalysts normally show improved weak acid site concentration. A similar trend was reported by a number of researchers (Berenguer et al., 2018; Feng et al., 2018; Sankaranarayanan et al., 2015).

Notably, there was a shift in the peak centres following nickel impregnation, indicating an increase in the desorption temperature and stronger interaction at acid sites. In the mic-ZSM-5 and hie-ZSM-5, the desorption peak centres shifted to 210 from 167 ℃, and to 209 from 168 ℃ for weak acid sites; to 393 from 225 ℃, and 380 from 228 ℃ for medium acid sites; and to 475 from 438 ℃, and 475 from 449 ℃ respectively, for strong acid sites. A 2 wt.% zinc and 3 wt.% nickel bimetallic mic-Ni-Zn/ZSM-5 catalyst exhibited reduced acid site concentration with a total peak area of 4844 (a.u) compared to the 4967 (a.u) recorded in the 5 wt.% nickel mic-Ni/ZSM-5 catalyst. The presence of Zn also caused a reduction in the amount of weak acid site concentration from 35% to 31.9%, whereas the strong acid site concentration increased to 12.3% from the 10.2% seen in the mic-Ni/ZSM-5. Further decrease in the acidity is obvious on complete substitution of the active metal in the catalyst with zinc; a monometallic 5 wt.% zinc-based catalyst, mic-Zn/ZSM-5, yielded a total peak area of 4325 (a.u). The mic-Zn/ZSM-5 has shown the lowest proportion of weak acid sites, 14.1%, compared to that of the mic-Ni/ZSM-5, 35.0%, and the mic-Ni-Zn/ZSM-5, 31.9%. In contrast, it possessed the highest amount of the strong acid site concentration, 43.5%.

The SiO_2 catalysts showed trends in desorption patterns that were comparable to those shown for the zeolite-based catalysts. There was an increase in the weak acid sites concentration after the impregnation of nickel as well as a reduction in the strong acid sites' concentration.

Desorption temperatures for the weak, medium, and strong acid sites were higher than the ones recorded on the zeolite-based catalysts. The total acidity of the Ni/ZSM-5 catalyst is about five times greater than the total acidity of the Ni/SiO_2 catalyst. The deconvoluted profile of Ni/SiO_2 shows a peak centred at 454 °C, which might be linked to weak acid sites, owing to the presence of unreduced nickel species in the form of Ni-Si (Li et al., 2018; Li et al., 2011).

4.7 Hydrogen Temperature Programmed Reduction

Using H_2-TPR analysis, it was possible to further analyse the existence of Ni species on the catalysts. H_2-TPR provides information on the metal reduction temperature, the strength of the metal-support interaction, and the reducibility of the metal within a support (Gamliel et al., 2018). Figure 4.12 presents the H_2-TPR profile of the prepared 5 wt% nickel-based catalysts. Two reduction peaks at 418 ℃ and 575 ℃ were found for the Ni/SiO_2 catalyst, indicating the presence of two different types of NiO species (Li et al., 2020). While three reduction peaks centred around 345 ℃, 430 ℃ and 575 ℃ were recorded for mic-Ni/ZSM-5 catalyst, only two peaks were observed for hie-Ni/ZSM-5 catalyst. However, a shift in the position of peaks from 430 ℃ and 575 ℃ on mic-Ni/ZSM-5 to 461 ℃ and 613 ℃ on hie-Ni/ZSM-5 was noticed. Comparing the hydrogen consumption of the three catalysts, the hie-Ni/ZSM-5 shows the highest intensity, followed by mic-Ni/ZSM-5, and Ni/SiO_2. The intensity of the H_2-TPR profile provides valuable information about the active sites of catalysts. A high-intensity peak indicates a strong interaction between hydrogen and the catalyst surface, suggesting a high concentration of active sites. On the other hand, a low-intensity peak suggests weak interaction and fewer active sites (Gamliel et al., 2018). Furthermore, lower temperature peaks were attributed to a weak interaction between nickel oxide and the surface of the supports. A reduction temperature below 400 ℃ shows the

presence of very little ion exchange and that NiO is on the exterior surface of the support. A peak at a higher temperature implies strong metal-support interaction. Similarly, high temperature is required for the reduction of a nickel-based catalyst when the NiO species are beside the support surface or the NiO crystallites are larger (He et al., 2020; Sankaranarayanan et al., 2015; Tu et al., 2019).

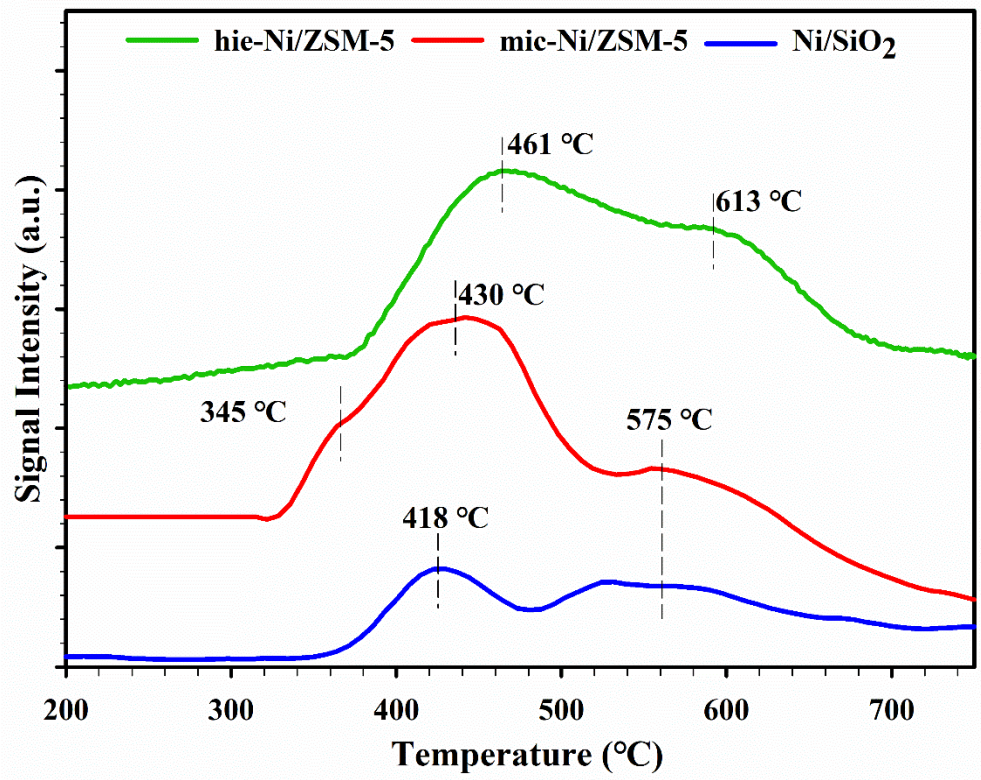

Figure 4.12: *H_2-TPR profile of the prepared 5 wt% nickel-based catalysts*

It is significant to note that mic-Ni/ZSM-5 shows a minor peak at 345 °C indicating some NiO particles are likely dispersed on the external surface of the support. This agrees with the observation from the dark-field Scanning Transmission Electron Microscopy elemental mapping results presented in Figure 4.7, where a pronounced image of the nickel metal was observed on the mic-Ni/ZSM-5 catalyst. Compared with hie-Ni/ZSM-5 and Ni/SiO_2 catalysts, the hydrogen consumption peaks for temperatures beyond 400 °C were 430 and 575

℃ for mic-Ni/ZSM-5, 461 and 613 ℃ for hie-Ni/ZSM-5, and 418 and 575 ℃ for the Ni/SiO_2 catalysts, respectively. The high reduction temperatures are a sign of good dispersion of NiO within the pores of the supports and/or larger NiO particles on the exterior surface of the supports. However, it was already established from the XRD and TEM results that nickel particles are relatively larger in the Ni/SiO_2 catalyst than in the ZSM-5-based catalysts. Hence, this might be one of the reasons for the high reduction temperature in the Ni/SiO_2 catalyst. On the other hand, with the decrease in total pore volume observed after the nickel impregnation, based on the BET results, it could be concluded that a reasonable amount of nickel was properly dispersed within the pores of hie-ZSM-5. The decrease in total pore volumes after the nickel impregnation on the supports, as was determined from Table 4.2, were 0.085 $m^3\ g^{-1}$, 0.049 $m^3\ g^{-1}$ and 0.048 $m^3\ g^{-1}$ for hie-ZSM5, mic-ZSM-5, and SiO_2, respectively.

It is obvious from Figure 4.12 that the hie-ZSM-5 has a higher metal-support interaction compared to the other catalysts. This can be attributed to the combine effects of acidity and mesoporosity of the support, as seen from the NH_3-TPD and BET results. Acidic supports can provide a favourable environment for active metal species by stabilizing them through coordination interactions (Ezeonu et al., 2023). The presence of acid sites on the support-surface allows for strong bonding between metal ions or complexes and the support material. This stabilization enhances dispersion and prevents leaching of metal species during catalytic reaction, ensuring their long-term stability and activity (Kumar et al., 2019). Therefore, the strength of metal-support interaction for the three catalysts decreases in the following order: hie-Ni/ZSM-5 > mic-Ni/ZSM-5 > Ni/SiO_2.

4.8 Thermogravimetric Analysis

The TGA analysis was carried out on the fresh mic-Ni/ZSM-5, hie-Ni/ZSM-5, and Ni/SiO_2 catalysts. This was done to provide information on the thermal stability of these materials within the intended reaction temperature range. A substance that is thermally stable will experience a negligible change in mass, which corresponds to little or no slope on a temperature versus weight plot. The TGA also specifies the maximum use temperature of a material. Above this temperature, the material starts to deteriorate or decompose (McClure et al., 2009; Wang et al., 2017; Yang et al., 2019). Figure 4.13 presents plots of weight loss and the derivative thermogravimetry (DTG) against temperature for the fresh catalysts. This was recorded between 100 ℃ and 900 ℃ at a heating rate of 10 ℃ min^{-1}.

Below 300 ℃, weight loss was ascribed to desorption of water and volatile components in the catalysts (Shafaghat et al., 2015), and above 300 ℃ loss was associated to the deposited coke or organic residue on the catalyst surface, generated either during the catalyst preparation process or when it is employed for a reaction. The fresh catalysts displayed weight losses of 5.4% (mic-Ni/ZSM-5, Figure 4.13a), 4.2% (hie-Ni/ZSM-5, Figure 4.13b), and 0.8% (Ni/SiO_2, Figure 4.13c) below 300 ℃, respectively, on account of the desorption of adsorbed water. Above 300 ℃, further losses of 2.2% (mic-Ni/ZSM-5), 1.5% (hie-Ni/ZSM-5), and 1.4% (Ni/SiO_2), were recorded. This weight loss could be linked to the presence of some organic residue in the catalysts. Something interesting to note here is that the TGA result is consistent with the EDX analysis data, which is shown in Table 4.3. It could be seen from the EDX results that the biggest weight loss was demonstrated by the catalyst with the highest carbon concentration. This is in the order mic-Ni/ZSM-5 (14.7% Carbon) > hie-Ni/ZSM-5 (13.7 % Carbon) > Ni/SiO_2 (9.1 % Carbon).

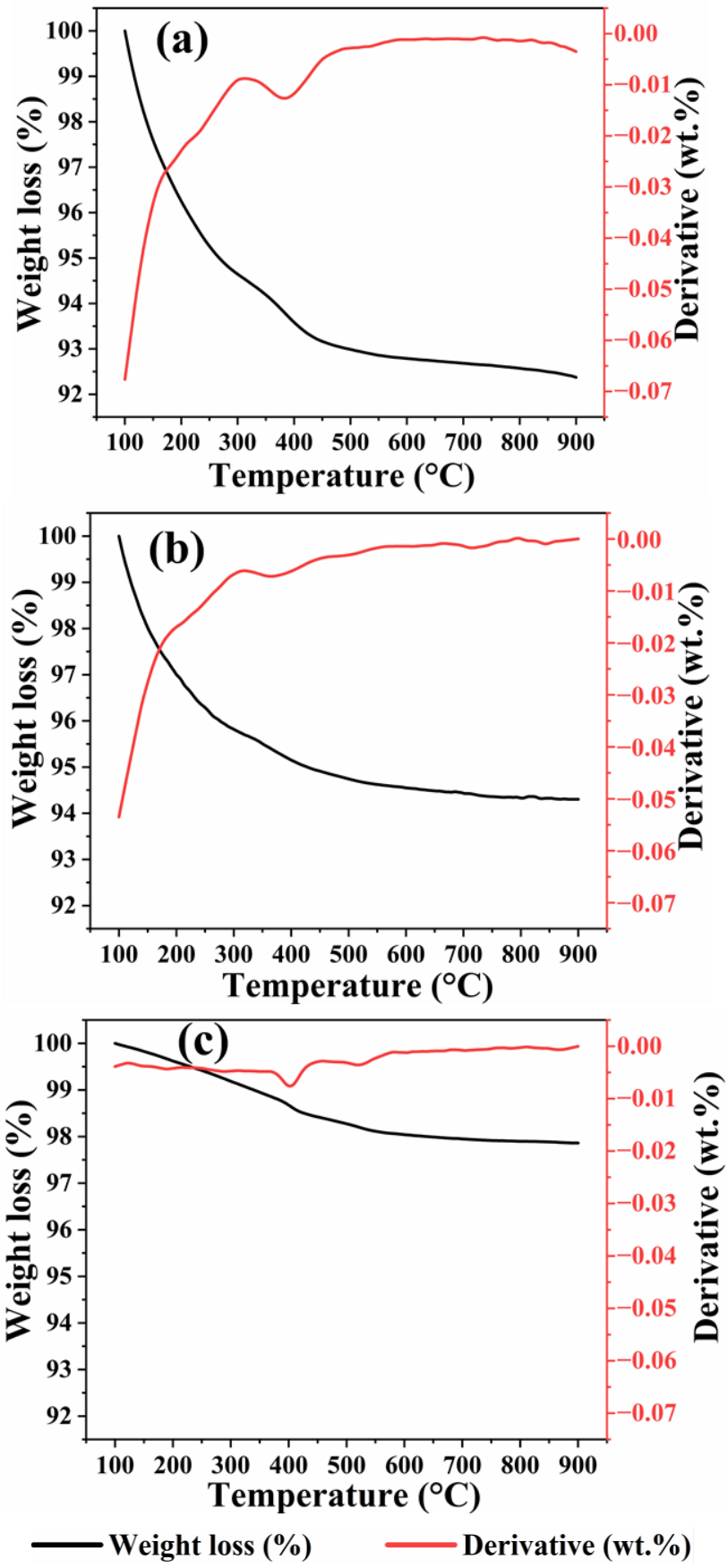

Figure 4.13: *TGA-DTG profile of the fresh catalysts; (a) mic-Ni/ZSM-5, (b) hie-Ni/ZSM-5, and (c) Ni/SiO_2.*

4.9 Summary of the Chapter

The prepared catalysts, mic-Ni/ZSM-5, hie-Ni/ZSM-5, mic-NiZn/ZSM-5, and Ni/SiO_2 have been characterised using a number of techniques, including XRD, BET, SEM-EDX, TEM, H_2-TPR, NH_3-TPD, and TGA. The characterisation results have been presented and discussed in this chapter. The next chapter (Chapter 5) presents the results of the activity test of these catalysts in the HDO of anisole as a bio-oil model compound.

CHAPTER 5

Anisole Hydrodeoxygenation Over Ni, Zn, and bimetallic NiZn-based Catalysts: Influences of Solvent and Support Properties

5.1 Introduction

In this chapter the effect of support properties and solvent during the HDO reaction of anisole have been investigated. Anisole has been selected as the model compound for the catalytic test because it has a methoxy-phenyl group which is typical of lignin depolymerization fractions present in pyrolysis bio-oils derived from lignocellulosic biomass. To explore further the relationship between the reacting molecule size, acidity and pore size of a support, as well as diffusion properties in the pores several supports have been selected for testing; a microporous nickel-based HZSM-5 catalyst (mic-Ni/ZSM-5, Si/Al = 16), a hierarchical nickel-based ZSM-5 catalyst (hie-Ni/ZSM-5, Si/Al = 15), a nickel-supported mesoporous silica catalyst (Ni/SiO_2), a zinc-based microporous ZSM-5 catalyst (mic-Zn/ZSM-5), and a bimetallic mic-NiZn/ZSM-5 catalyst. Since solvent compositions could have significant effect on the degree of hydrodeoxygenation and product distribution, an aromatic compound, decahydronaphthalene (decalin), and an aliphatic hydrocarbon, n-decane, were tested as solvents in this study. Finally, a kinetic study of anisole HDO over the hie-Ni/ZSM-5 catalyst was carried out.

5.2 Process Variables Optimization

Various Design of Experiment (DOE) approaches have been reported to provide predictive knowledge of complex and multivariable processes with fewer numbers of experimental runs (Lawal et al., 2019; Lee and Yoo, 2018; Moersidik et al., 2020). Here, Multilevel Factorial Design (Minitab software version 20.4.0.0) was employed to analyse the contributions of

temperature and pressure towards conversion and yield of products during the HDO of anisole over the mic-Ni/ZSM-5 catalyst. Temperatures of 150 ℃, 200 ℃, 250 ℃ and pressures of 20 bar, 40 bar, 60 bar were tested. Optimum catalyst loading and anisole concentration reported elsewhere were adopted (Gamliel et al., 2018; Ghampson et al., 2018; Szczyglewska et al., 2020). A preliminary run guided the choice of minimum and maximum temperatures used. Virtually no reaction was seen at 120 ℃ at all pressures, whereas about 30% conversion was recorded at 150 ℃. Conversion reached 100% at 250 ℃ and 280 ℃, however, lower cyclohexane yield was generated at the higher temperature. To ensure the effect of mass transfer was eliminated during the HDO reaction of anisole over the prepared catalysts and that reaction is kinetically controlled, another preliminary study was carried out on the effect of stirring rate on anisole conversion. Increase in the stirring speed from 800 rpm to 1000 rpm and subsequently to 1200 rpm did not show any significant improvement in the conversion. Therefore, since the conversion plateaued at 800 rpm, it was selected for subsequent experimental runs. Table 5.1 presents both the factors and levels examined and the responses recorded.

Response in terms of anisole conversion and cyclohexane yield were recorded at 140 minutes reaction period. Conversion increased to 29.5% from 21.3% while cyclohexane yield increased to 27.2% from 19.5% as the pressure changed from 20 bar to 60 bar, respectively. This clearly shows how pressure influences the formation of cyclohexane in a similar manner as it affects anisole conversion. However, at constant pressure of 20 bar hydrogen, increase in temperature from 150 ℃ to 200 ℃ changed anisole conversion and cyclohexane yield to 54.4% and 46.5 % from 21.3% and 19.5%. Similarly, conversion reached 91.8% and 100% at 60 bar hydrogen pressure with a higher cyclohexane yield of 82.5% and a lower yield of 81.0% at 200 ℃ and 250 ℃ respectively. Thereafter, the data in Table 5.1 were processed

using a factorial design analyser (stepwise method, $\alpha = 0.1$) and the results is presented in Table 5.2.

Table 5.1: Reaction factors, levels, and responses during the HDO of anisole over mic-Ni/ZSM-5: 50 mL mixture of 3.0 wt.% anisole; solvent, decalin; catalyst loading, 100 mg.

Factor	**Level**								
Temp. (℃)	150	150	150	200	200	200	250	250	250
Pressure (bar)	20	40	60	20	40	60	20	40	60
Conversion (%)	21.3	25.4	29.5	54.4	70.4	92.1	61.1	93.6	100.0
Cyclohexane yield (%)	19.5	23.2	27.2	46.5	61.0	82.5	50.7	77.0	81.0

Table 5.2: Analysis of Variance for anisole conversion and cyclohexane yield.

	Anisole conversion			**Cyclohexane yield**		
Source	**DF**	**F-Value**	**P-Value**	**DF**	**F-Value**	**P-Value**
Model	4	18.48	0.008	4	14.20	0.012
Linear	4	18.48	0.008	4	14.20	0.012
Temperature (℃)	2	30.68	0.004	2	22.56	0.007
Pressure (bar)	2	6.28	0.058	2	5.84	0.065
Model summary	R-square = 0.949			R-square = 0.934		

It can be seen from Table 5.2 that the P-values for temperature with respect to both conversion and yield were 0.004 and 0.007. For the pressure, the P-values recorded were

0.058 and 0.065 respectively for anisole conversion and cyclohexane yield. The P-value is a proof for or against a null hypothesis. Reasons to reject a null hypothesis get stronger as the P-value get smaller. Though the P-values for the two factors investigated are small, temperature, with smaller P-value has more effect on anisole conversion and cyclohexane yield. This is further shown in Figure 5.1 below.

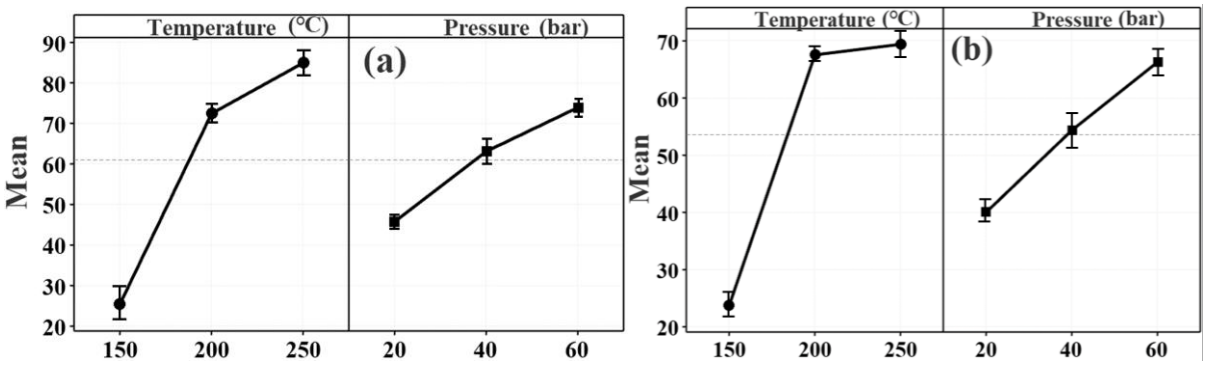

Figure 5.1: *Main effects plot for anisole conversion (a) and cyclohexane yield (b) at different temperature and pressure.*

As seen in the plot of anisole conversion (Figure 5.1a) and cyclohexane yield (Figure 5.1b), these parameters exhibited a linear relation within the range of pressure considered in this study. As a function of temperature conversion and yield showed rapid increase between 150 °C and 200 °C followed by a slow increment between 200 °C and 250 °C. It is clear that the analysed experimental observations (especially for temperature) produced P-values that are far less than the specified significance level, 0.05 (Verykouki and Nakas, 2023), as such it can be confidently deduced that there is significant difference in the data generated, rejecting the null hypothesis.

5.3 Effect of Catalyst Support on Conversion and Product Distribution During the HDO of Anisole over Ni-based Catalysts

Hydrodeoxygenation of anisole involves a number of parallel/series transformation steps. Previous works have reported several reaction sequences (Gamliel et al., 2018; Ghampson et al., 2018; Jiang, et al., 2020; Sankaranarayanan et al., 2015). Depending on the type of catalyst, degree of deoxygenation and extent of hydrogenation, some of the possible products and intermediates of the reaction are; cyclohexane, methylcyclopentane, phenol, benzene, toluene, cyclohexene, cyclohexanone, cyclohexanol, ethers and transalkylates. In addition, light ends such as methane, ethylene and trace amount of CO may be generated. Figure 5.2 presents time-dependent conversion, yield and selectivity profile of products during the HDO of anisole. Prior to the reaction, the catalysts were reduced *ex-situ* in a furnace at 500 ℃ for 3 hours at a heating rate of 5 ℃ min^{-1} under a continuous flow of 5% H_2/N_2. Conversions were 100%, 82.6%, and 48.9% respectively over hie-Ni/ZSM-5, mic-NiZSM-5 and Ni/SiO_2 catalysts within 2 hours. The highest conversion on NaOH desilicated catalyst (hie-NiZSM-5) was attributed to the enhanced catalytic activity, as the reactant has access to more active sites based on the catalyst characterisation results presented in Chapter 4. In a related work, higher conversion and yield of product were recorded after mesopores were introduced to a conventional HZSM-5 via desilication (Wang, et al., 2020). The aforementioned results are in agreement with the XRD, BET, and NH_3-TPD results (Sections 4.2, 4.3, and 4.6 of Chapter 4) which revealed good preservation of ZSM-5 structure after the NaOH treatment, high surface area and pore volume for metal dispersion, and relatively high acid site concentration. Lowest conversion was recorded on the Ni/SiO_2 catalyst, suggesting low catalytic activity. This can be related to the nature of the SiO_2 support which is a function of the type and concentration of acid sites available for the reaction.

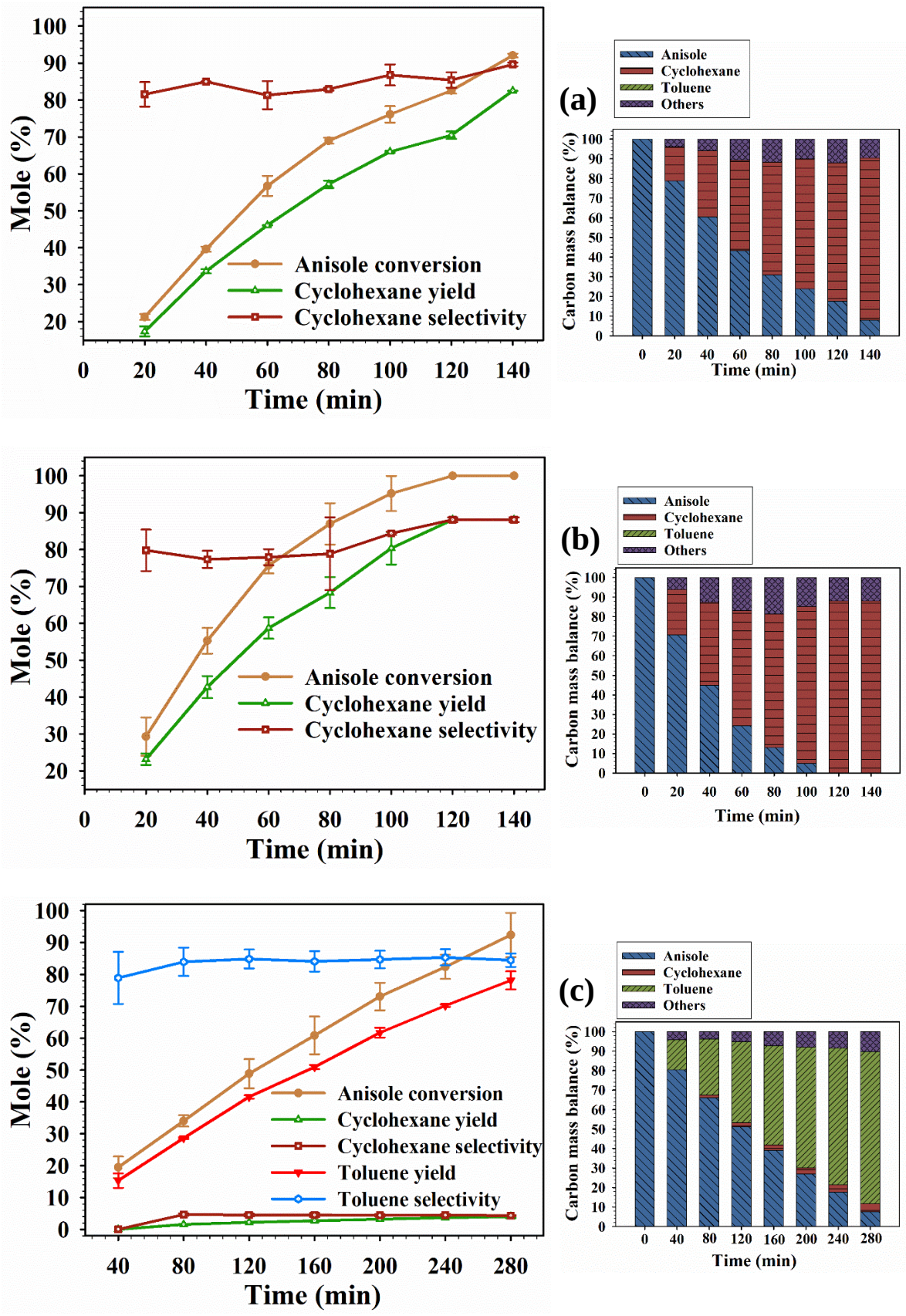

Figure 5.2: *Time-dependent anisole conversion, yield and selectivity of liquid products and carbon mass balance at 200 °C, 60 bar H_2, 48.65 mL decalin, 1.35 mL anisole, 100 mg catalyst; (a) mic-Ni/ZSM-5, (b) hie-Ni/ZSM-5, and (c) Ni/SiO_2.*

However, conversion eventually reached 92.4% over the Ni/SiO_2 catalyst when the reaction was allowed to proceed for 280 minutes. The liquid products obtained during the reaction were majorly toluene and a trace of cyclohexane. An elemental carbon balance, shown in Figure 5.2, was carried out to determine the material balance within the reactor and quantify the carbon lost.

The total lost, referred to as "others", is the amount of carbon in the unquantified gaseous products and possibly in liquid products below the detection limit of the GC instrument. Sankaranarayanan et al. (2015) observed the formation of methane, and a trace quantity of CO, ethylene, and some isomers of propyl and butyl during the HDO of anisole over supported Ni and Co catalysts. In this work, the three catalysts, mic-Ni/ZSM-5, hie-Ni/ZSM-5 and Ni/SiO_2 achieved cyclohexane yields of 70.5%, 88.1% and 2.2% while the yield of other products was 12.0%, 11.9% and 5.1% respectively in 2 hours at 200 °C. Notably, toluene was not seen from the ZSM-5-based catalysts, in contrast to the Ni/SiO_2 catalysts with 41.6% yield of toluene. It could also be noticed that the amount of cyclohexane generated on hie-Ni/ZSM-5 catalyst differed markedly compared with the amount of cyclohexane obtained from the mic-Ni/ZSM-5 and Ni/SiO_2 catalysts. This might be explained by the improved properties of the hie-ZSM-5 support in term of acidity, and pore structure. While acidity of a catalyst support provides more active sites that might participate in the HDO reaction, mesoporosity allowed reactant more access to the active sites and products to desorb easily from the catalyst surface after formation. Acid sites on a support are shown to promote demethylation, demethoxylation, and ring-opening reactions during the HDO of bio-oil model compounds (Pawelec et al., 2020; Wang et al., 2020). Noteworthy, despite high concentration of acid sites on mic-ZSM-5 support, a preliminary experiment showed anisole conversion of only 2% without any yield of liquid product. A similar trend

was reported by Tu et al. (2019). Interestingly, in this work, after nickel impregnation on SiO_2 support, which is almost neutral compared to the mic-ZSM-5 support, a reasonable conversion as well as a yield of liquid products were obtained. This clearly demonstrated a synergy between the acid sites of the support and active metal sites. Ni/SiO_2 catalyst, which has larger pores, and few acid sites mostly from the active metal, was more selective to toluene than cyclohexane. This clearly suggests a promotion of demethylation, demethoxylation, and ring-opening reactions of anisole by the acid sites of the ZSM-5.

Several reaction pathways during anisole HDO were reported in literature. Tu et al. (2019) proposed that anisole transformation over $Ni\text{-}Al_2O_3$ and Ni/ZSM-5 catalysts proceed via saturation of aromatic ring, rapid demethylation of methoxy-cyclohexane to cyclohexanone and, subsequently, dehydration of cyclohexanone to cyclohexane. This is referred to as hydrogenation-dehydration route. Anisole HDO on zeolite Y supported Pb, Ni and Ru catalysts was shown to progress by the same route (Gamliel et al., 2018).

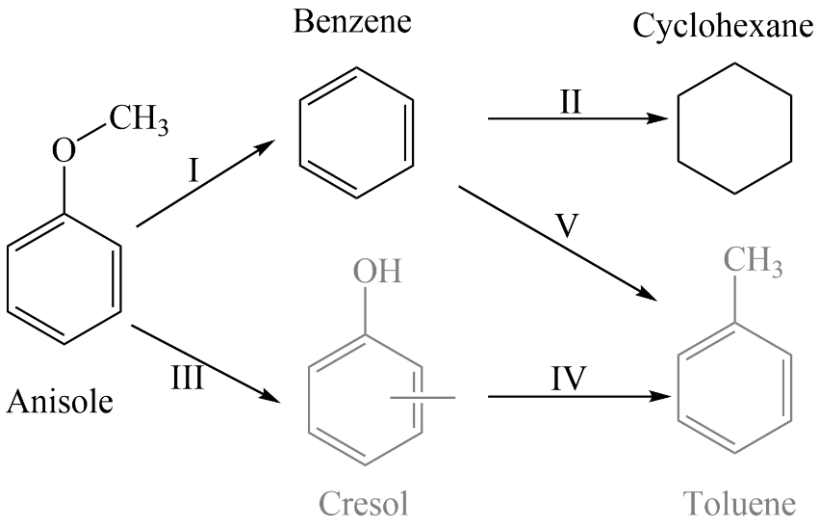

Figure 5.3: *Proposed reaction scheme in anisole transformation over 5 wt.% Ni/ZSM-5 and 5 wt.% Ni/SiO_2 catalysts: (I) demethoxylation, (II) hydrogenation, (III) isomerisation, (IV) direct deoxygenation (V) alkylation.*

Another transformation route is direct deoxygenation (Ghampson et al., 2018; Li, et al., 2020; Sankaranarayanan et al., 2015). An example of the latter is HDO anisole reaction over Co/SBA-15 catalyst which was achieved by breaking down the methoxy-phenyl bond to form benzene. Thereafter, the benzene is hydrogenated to cyclohexane. Based on the product distribution observed from the mic-Ni/ZSM-5, hie-Ni/ZSM-5 and Ni/SiO_2 catalysts, a simple reaction scheme was proposed and presented in Figure 5.3. Selectivity to cyclohexane was 88.1% and 89.6% on hie-Ni/ZSM-5 and mic-Ni/ZSM-5, respectively, at the end of the reaction. Of particular interest is that no intermediate product was seen, as samples were withdrawn from the reactor and analysed at regular intervals of 20 minutes. It is hypothesised that the cleavage of methoxy group and hydrogenation of benzene to cyclohexane occurs very fast via direct deoxygenation-hydrogenation pathway. On the other hand, high selectivity towards toluene on the Ni/SiO_2 catalyst could be interpreted as follows; anisole adsorbs onto the acidic sites of the catalyst which prompt a nucleophilic attack between R–O bond forming a carbenium ion (Mortensen et al., 2011). The cleaved methyl carbenium ion is then transferred onto the aromatic ring to form cresol. Afterwards, the cresol undergoes direct deoxygenation to produce toluene (Ghampson et al., 2018).

5.4 Effects of Temperature on Anisole Conversion and Product Distribution over mic-Ni/ZSM-5, hie-Ni/ZSM-5, and Ni/SiO_2 Catalysts

The effects of temperature on anisole conversion and product distribution were investigated. Figure 5.4 presents results for the HDO reaction over the temperature range between 150 ℃ and 250 ℃. Anisole conversion increases with temperature, from 29.5% to 92.1% and 100% at 150 ℃, 200 ℃ and 250 ℃ respectively over mic-Ni/ZSM-5. In addition to the large increase in conversion when the reaction temperature increased from 150 ℃ to 200 ℃, an increase in cyclohexane yield was also seen, going from 27.2% to 82.5% with selectivity of

92.5% at 150 ℃ and 89.6% at 200 ℃. However, yield of other products increased from 2.2% at 150 ℃ to 9.6% and 15.0% at 200 ℃ and 250 ℃. This implies an increase of side reactions and generation of more light ends, as the reaction temperature increases.

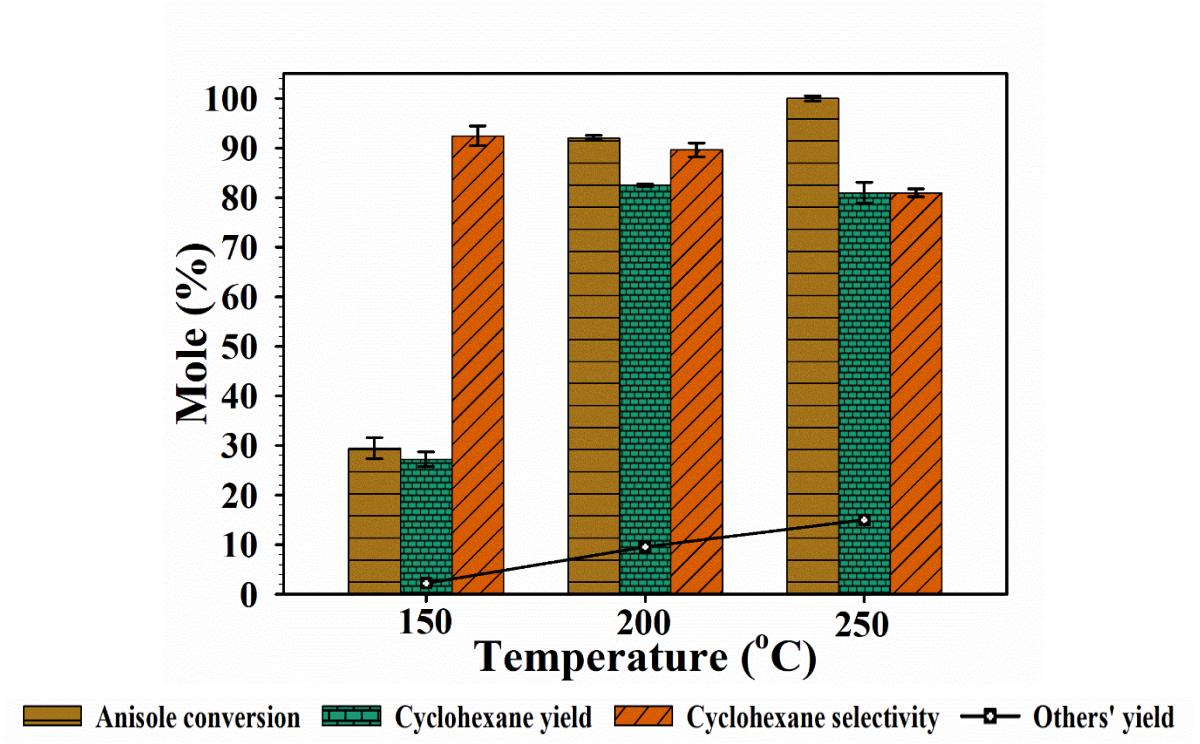

Figure 5.4: *Temperature dependency of anisole conversion and product distribution over mic-Ni/ZSM-5: 50 mL mixture of 3.0 wt.% anisole, 100 mg catalyst, 60 bar H_2, 140 min.*

Contrary to this, Tu et al. (2019) reported variations in selectivity during the HDO of anisole using hierarchical Ni-zeolite catalyst. Therein, as the reaction temperature increased from 100 ℃ to 200 ℃, conversion increased from 4.6% to 100%. The selectivity at the lower temperature was 86.5% to methoxy-cyclohexane, and 97.0% to cyclohexane at 200 ℃. The most notable points in this work are that there was total deoxygenation of the reactant and 89.6% selectivity to cyclohexane over the mic-Ni/ZSM-5 catalyst. Since cyclohexane was the only liquid product detected, further purification of the product might not be required after separating from the solid catalyst.

For comparative analysis of the temperature effects, further experiments were carried out at 180, 200, 220, and 240 ℃ over the mic-Ni/ZSM-5, hie-Ni/ZSM-5 and the SiO_2, respectively. Table 5.3 presents the results.

Table 5.3: Influence of temperature on product distribution during the HDO of anisole (60 bar H_2, 48.65 mL decalin, 1.35 mL anisole, 100 mg catalyst).

Sample	**Temperature**	**Conversion**	**Selectivity (mole %)**		
	(℃)	**(mole %)**	**Cyclohexane**	**Toluene**	**Others**
mic-Ni/ZSM-5	180	71.3	93.8	0.0	6.2
	200	92.1	89.6	0.0	10.4
	220	100	82.6	0.0	17.4
	240	100	79.3	0.0	20.7
hie-Ni/ZSM-5	180	73.6	95.6	0.0	4.4
	200	100	88.1	0.0	11.9
	220	100	87.2	0.0	12.8
	240	100	82.2	0.0	17.8
Ni/SiO_2	180	32.7	4.5	92.6	2.9
	200	92.4	4.3	84.6	11.1
	220	100	7.3	75.8	16.9
	240	100	13.0	72.4	14.6

It can be seen that an increase in temperature from 180 ℃ to 240 ℃ improved the overall catalytic activity by changing the conversion from 71.3% to 100% and from 73.6% to 100% on mic-Ni/ZSM-5 and hie-Ni/ZSM-5 respectively. It is evident that cyclohexane selectivity decreased from 95.6% to 82.2% on hie-Ni/ZSM-5 and from 93.8% to 79.3% over the mic-

Ni/ZSM-5 catalysts as the temperature increased from 180 ℃ to 240 ℃. However, selectivity to other products increased with increasing reaction temperature in both cases. On the other hand, anisole conversion increased from 32.7% at 180 ℃ to 100% at 240 ℃ over Ni/SiO_2 catalyst. Unlike the mic-Ni/ZSM-5 and hie-Ni/ZSM-5 catalysts, the Ni/SiO_2 catalyst was 92.6% selective to toluene at 180 ℃. However, increasing the reaction temperature to 240 ℃ reduced the selectivity to 72.4%. In addition, there was an increase in cyclohexane selectivity from 4.5% at 180 ℃ to 13.0% at 240 ℃. It is obvious that when temperature is raised, the average kinetic energy of molecules rises, resulting in a greater number of collisions between reactant particles. This explains why an increase in anisole conversion was recorded, as the HDO temperature increases. However, this also means that there is an increased probability for reactants to collide in unfavourable orientations or with excessive force, leading to side reactions. This phenomenon justified the decreasing trend in the yield of cyclohexane and the increase in other-products recorded herein. Similar observation was reported by Lestari et al. (2019) and Szczyglewska et al. (2020).

In general, the Ni/SiO_2 catalyst was kinetically very slow compared with the mic-Ni/ZSM-5 and hie-Ni/ZSM-5 catalysts. In addition, toluene was the major product from Ni/SiO_2 while cyclohexane was the only liquid product from the zeolite-based catalysts. The difference in the catalytic activity is linked to the nature of the supports, which in turn, affect the overall activity of the catalysts. Acidic support such as ZSM-5 allows for strong bonding between metal ions and the support material. This enhance metal dispersion and ensure long-term stability and activity (Kumar et al., 2019). Acid and metal sites were shown to promote the following reactions during the HDO of phenol; formation of cyclohexanol by the metal sites; dehydration to cyclohexene by the acid site; hydrogenation to cyclohexane by the metal sites; and isomerisation to methylcyclopentane by the acid sites (Berenguer et al., 2019).

5.5 Effects of Temperature on Anisole Conversion and Product Distribution over mic-Zn/ZSM-5, mic-Ni-Zn/ZSM-5 Catalysts

The effect of reaction temperature on anisole conversion and product distribution over 5 wt.% zinc mic-Zn/ZSM-5 catalyst is presented in Figure 5.6. Anisole conversion increases with an increase in reaction temperature from 200 ℃ to 260 ℃. The lowest conversion of 13.0% was recorded at 200 ℃ while the highest of 28.2% was at 260 in 140 minutes. Selectivity for cyclohexane was 14.0%, observed only at 240 ℃ while toluene was recorded at all the studied temperatures. Other products (light ends) have the highest selectivity from the anisole HDO with Zn-based catalyst, which increased with the increases in temperature from 76.3% (200 ℃) to 76.5% (240 ℃), and 80.71% (260 ℃.), respectively.

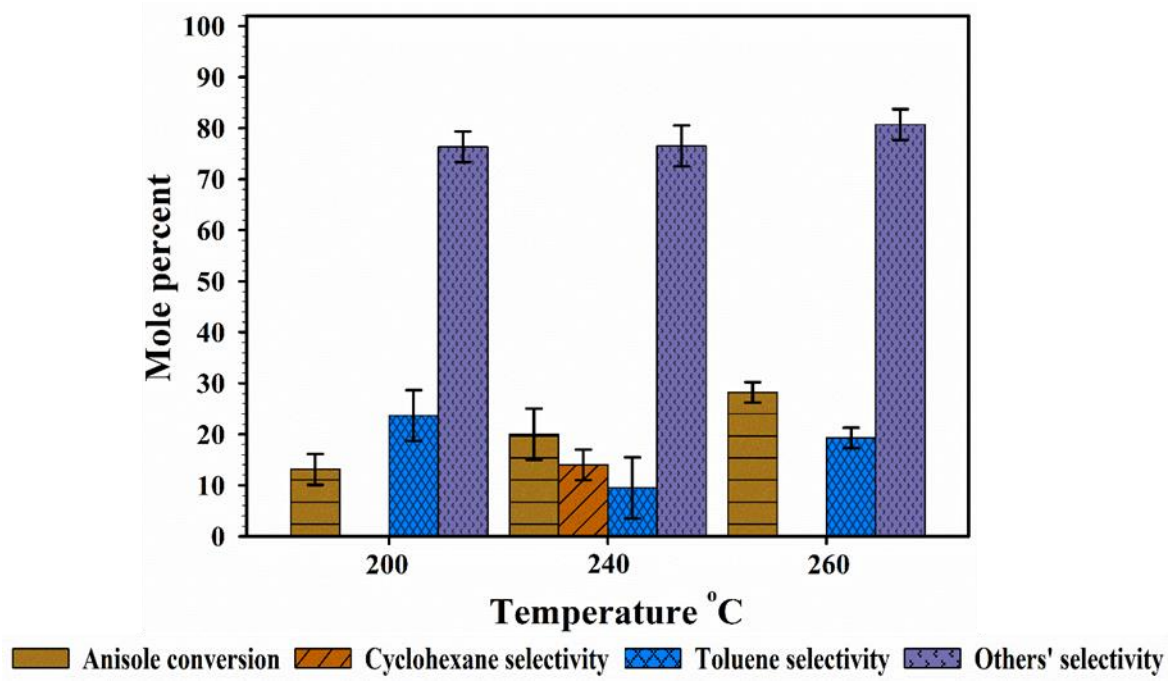

Figure 5.5: *Effect of temperature on anisole conversion and product distribution over 5 wt.% zinc mic-Zn/ZSM-5: 50 mL mixture of 3.0 wt.% anisole, 100 mg catalyst, 200 ℃, 60 bar H_2, 140 min.*

Compared with the mic-Ni/ZSM-5 catalyst, which shows anisole conversion of 92.1%, cyclohexane selectivity of 89.6%, and 10.4% selectivity to others in 140 minutes (Figure

5.2c), there was a noticeable decrease in catalytic activity when nickel was replaced with zinc in the microporous zeolite support. This decrease in activity may be due to the reduction in the total active sites on the mic-Zn/ZSM-5 catalyst, as shown by the NH_3-TPD result (In Chapter 4, Table 4.4). In other words, the species of zinc present on the mic-Zn/ZSM-5 catalyst might not be the desired active ones. During a study on the dehydroaromatisation of methane over a Zn-based ZSM-5 catalyst, Abdelsayed et al. (2015) revealed poor performance on a catalyst with more inactive zinc species (ZnO) compared with a catalyst having reactive species $[Zn(OH)]^+$ acting as a strong Lewis acid.

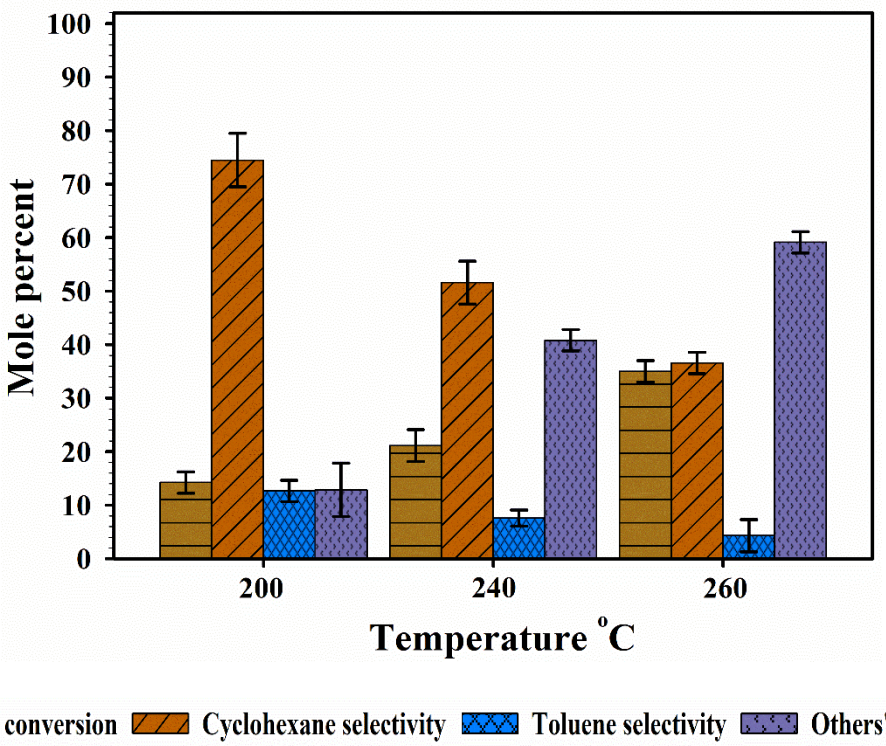

Figure 5.6: *Effect of temperature on anisole conversion and product distribution over 3 wt.% nickel, 2 wt.% zinc mic-Ni-Zn/ZSM-5: 50 mL mixture of 3.0 wt.% anisole, 100 mg catalyst, 200 ℃, 60 bar H_2, 140 min.*

In a similar study with a bimetallic nickel-zinc (3 wt.%–2 wt.%) catalyst, the effect of temperature on anisole conversion and product distribution was investigated. It could be seen from Figure 5.7 that 14.2%, 21.1%, and 35.0% conversion of anisole were obtained at 200

℃, 240 ℃, and 260 ℃ respectively. Although there was an increase in the catalytic activity compared to the pure zinc-based ZSM-5 catalyst, the overall activity is still far less than what was seen from the monometallic Ni-based ZSM-5. However, a consistent trend of decreasing selectivity of the liquid products and increasing selectivity of the other products was observed as the reaction temperature increased. Selectivity to cyclohexane and toluene was 74.5% and 12.7% (200 ℃), 51.6% and 76.0% (240 ℃), and 36.6% and 4.3% (260 ℃), respectively. In summary, despite the high acidity of the ZSM-5 support, the mic-Zn/ZSM-5 catalyst shows very poor activity and liquid product selectivity during the HDO of anisole. This clearly shows how crucial metal-sites are for the HDO.

5.6 Effect of Hydrogen Pressure on Anisole Conversion and Product Distribution over mic-Ni/ZSM-5 Catalyst

Figure 5.7 shows the effect of hydrogen pressure on anisole conversion and product distribution.

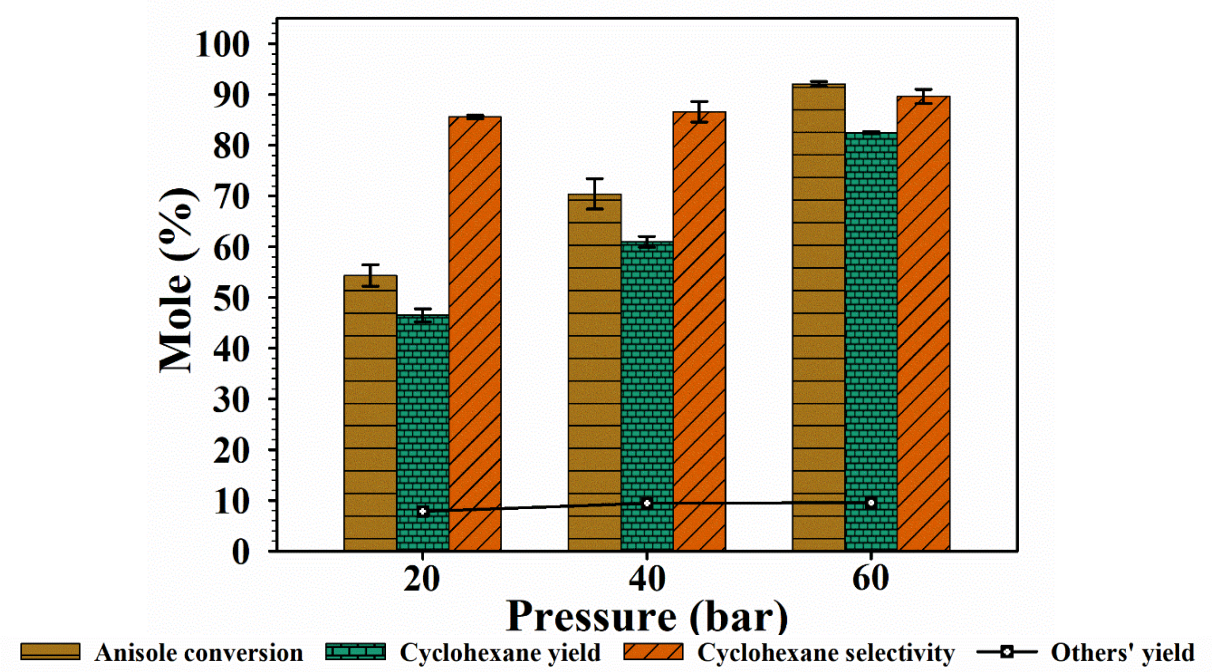

Figure 5.7: *Effects of hydrogen pressure on anisole conversion and product distribution over mic-Ni/ZSM-5: 50 mL mixture of 3.0 wt.% anisole, 100 mg catalyst, 200 ℃, 140 min.*

This was investigated at a fixed temperature of 200 ℃ and pressures of 20 bar, 40 bar and 60 bar. A strong influence of hydrogen pressure could be clearly seen in the conversion of anisole and yield of products. A proportional relationship was evident between the pressure, anisole conversion and product yield. As the pressure increased from 20 bar to 40 bar and 60 bar, the conversion increased from 54.4%, 70.4% to 92.1% while the cyclohexane yield increased from 46.5%, 61.0% to 82.5% respectively. Although, at high pressure, it is widely known that aromatic ring hydrogenation is favoured over direct deoxygenation (Yan et al., 2022). Herein, no liquid product containing an oxygen atom was detected at any point during the reaction within the range of pressure investigated. A significant dependency of anisole conversion on hydrogen pressure was also reported by Ghampson et al. (2018), who demonstrates that demethoxylation (direct deoxygenation) pathway is most significantly influenced by changing hydrogen pressure. This may also support the anisole transformation route over mic-Ni/ZSM-5 proposed in this work.

5.7 Effect Solvent Composition on the Performance of the mic-Ni/ZSM-5 Catalyst

The effect of solvent composition on the overall catalytic performance of mic-Ni/ZSM-5 was further evaluated. The reaction was performed at a temperature of 200 ℃, 60 bar hydrogen for 140 minutes, the results are shown in Figure 5.8. Anisole conversion and cyclohexane selectivity were 92.1% and 89.6% respectively in decalin while 94.1% conversion and 86.7% selectivity were seen in the n-decane environment. Although the two solvents used are different in that, decalin is a bicyclic hydrocarbon consisting of two fused cyclohexane rings, whereas, n-decane is a straight chain hydrocarbon (alkane hydrocarbon) the overall catalytic activity was virtually the same. In addition, there was complete hydrodearomatization of the products in both solvents.

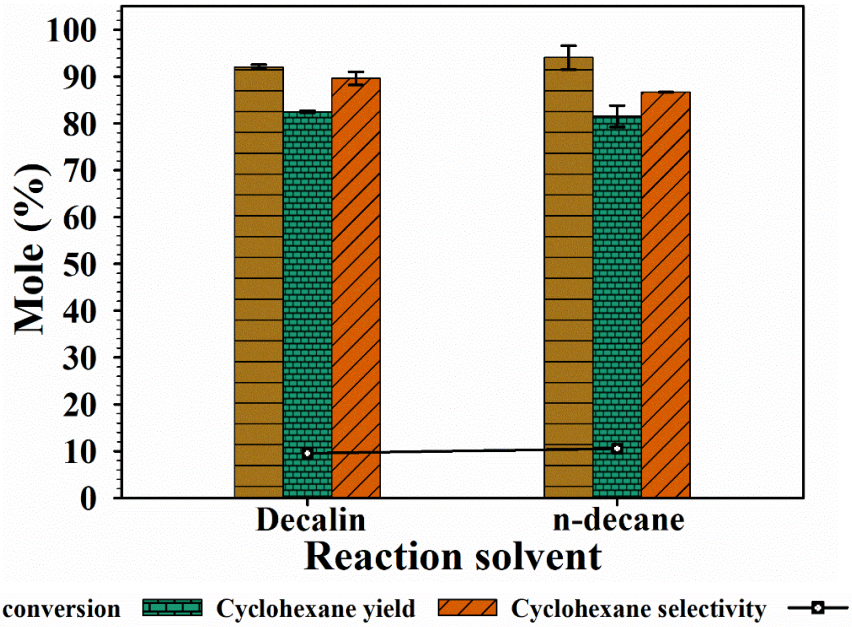

Figure 5.8: *Effect solvent compositions on anisole conversion and product distribution over mic-Ni/ZSM-5: 50 mL mixture of 3.0 wt.% anisole, 100 mg catalyst, 200 ℃, 60 bar H_2, 140 min.*

In contrast to what is reported here, changes in conversion and product yield during the hydrodeoxygenation of guaiacol in water, octane and decalin over Ni/TiO_2–ZrO_2 catalyst at 300 ℃ and 40 bar hydrogen pressure, were reported in the literature. Conversion and cyclohexane selectivity were 35% and 20% in water, 60% and 30% in octane and, 100% and 89% in decalin respectively (Zhang et al., 2014).

5.8 Degree of Hydrodeoxygenation (X_{HDO}) and Hydrodearomatisation (X_{HDA}) over mic-Ni/ZSM-5, hie-Ni/ZSM-5, and the Ni/SiO_2 Catalysts

The degree of hydrodeoxygenation ***(X_{HDO})*** and hydrodearomatisation (***X_{HDA})*** were calculated based on equations 3.7 and 3.8. Figure 5.9 presents the results. Since no products containing oxygen atom or aromatic ring were visible over the hie-Ni/ZSM-5 and mic-Ni/ZSM-5 catalysts, it could be concluded there was complete hydrodeoxygenation and hydrodearomatisation of the transformed reactant. However, Ni/SiO_2 catalyst showed very low hydrodearomatisation capacity of 15.4%, as 84.6% of the products contained an aromatic

ring, confirming the need for appropriate combination of active metal and support for effective bio-oil upgrading.

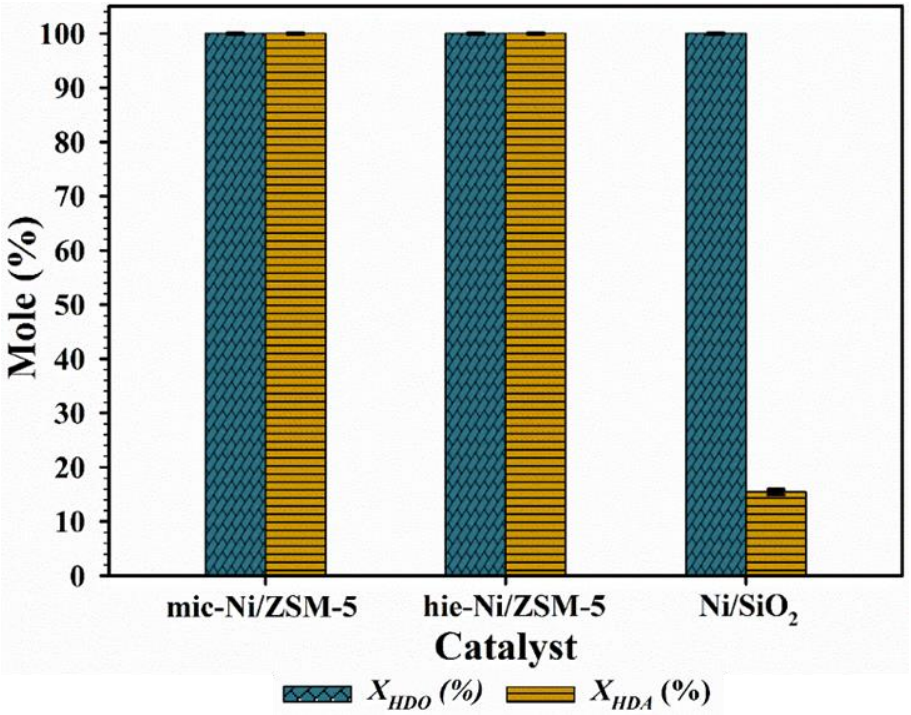

Figure 5.9: *Degree of hydrodeoxygenation X_{HDO} (%) and hydrodearomatisation X_{HAD} (%) over mic-Ni/ZSM-5, hie-Ni/ZSM-5, and Ni/SiO_2 catalysts: 50 mL mixture of 3.0 wt.% anisole, 100 mg catalyst, 200 ℃, 60 bar H_2.*

5.9 Catalysts Reusability Test

A catalyst reusability study was carried out on the mic-Ni/ZSM-5, hie-Ni/ZSM-5 and the Ni/SiO_2 catalysts for three reaction cycles and the results are shown in Figure 5.10. As reported in the literature, coke formation and catalyst deactivation during bio-oil hydrodeoxygenation are thought to be primarily caused by the presence of phenolic compounds (Gao et al., 2014; Si et al., 2017). The oxygen functionalities in the phenolic compounds have the tendency to bond on the catalyst surface thereby accelerating the rate of deactivation (Tu et al., 2019).

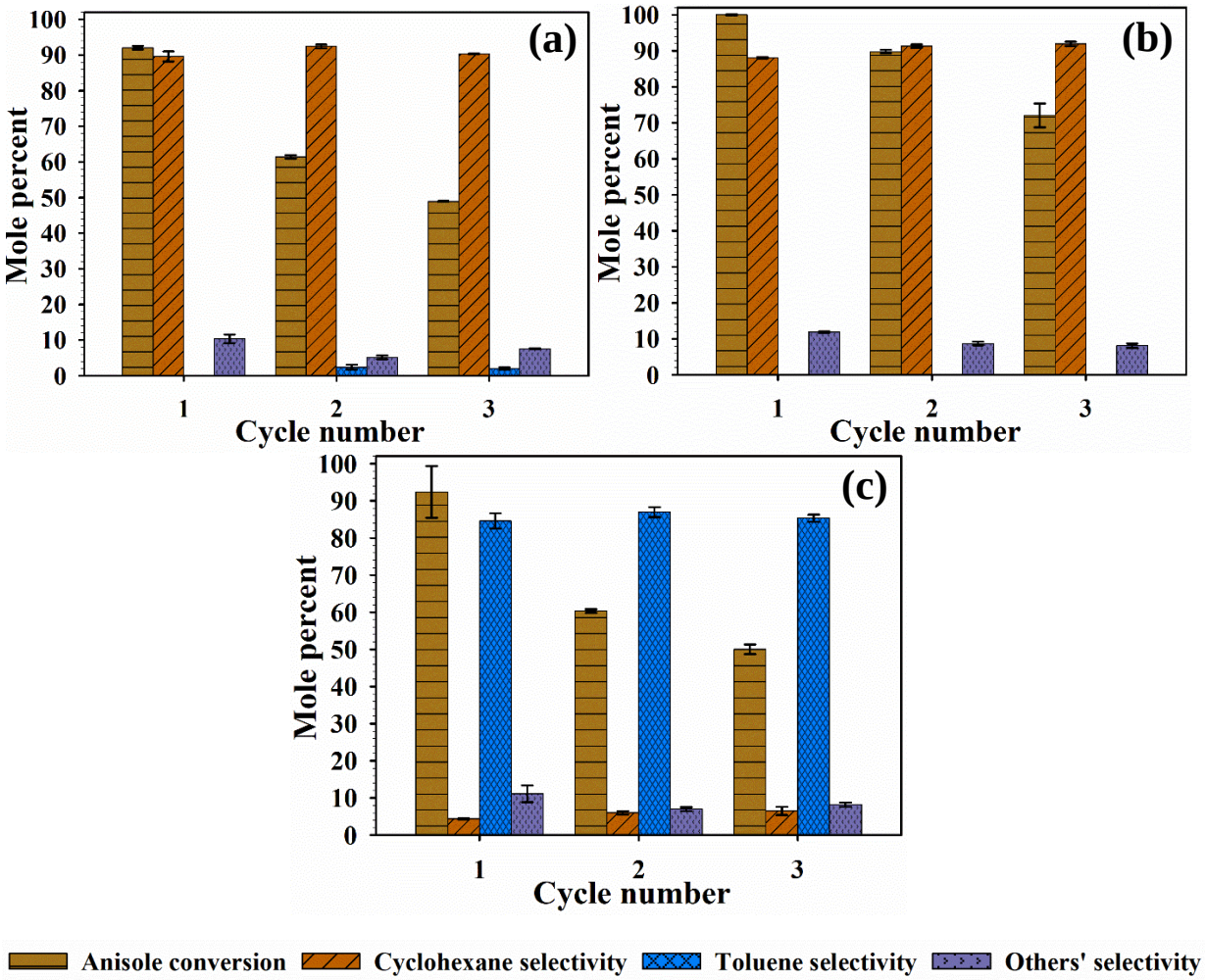

Figure 5.10: *Catalysts reusability test via conversion and selectivity after each of three cycles at 200 ℃, 60 bar H_2, 48.65 mL decalin, 1.35 mL anisole, 0.1 mg catalyst; (a) mic-Ni/ZSM-5 (b) hie-Ni/ZSM-5 (c) Ni/SiO_2.*

From the results presented here, catalyst deactivation was evident, as the anisole conversion decreased with increasing number of reaction cycles, suggesting coke deposition or metal particle aggregation on the catalyst surface. Conversion dropped to 49.0% on the mic-Ni/ZSM-5 catalyst, from 92.1% recorded on the fresh catalyst. For hie-Ni/ZSM-5 and Ni/SiO_2 catalysts, conversion decreased from 100% and 92.4 to 72.0% and 50.0%, respectively. Compared to the mic-Ni/ZSM-5 and Ni/SiO_2 catalysts, the hie-Ni/ZSM-5 catalyst shows the best stability in terms of liquid products selectivity. Cyclohexane selectivity only changed from 88.1% to 91.9% with no other liquid product detected

throughout the three reaction cycles. However, a small amount of toluene emerged in the product from the second and third hydrodeoxygenation reaction cycle over mic-Ni/ZSM-5 catalyst. This implies a decrease in the demethoxylation ability of the catalyst owing to the low acidity, which made part of the reactant transform via isomerisation-direct deoxygenation pathway.

The reusability test suggested improved metal dispersion on the hie-Ni/ZSM-5 as explained in the previous section. Metal particles on the external surface of a catalyst are less stable than those within the zeolite pores, as such, the tendency of metal sintering and aggregation is high on the catalyst surface (Kumar et al., 2019; Tu et al., 2019). Recently, Pt/HZSM-5 was employed in the hydrodeoxygenation of levulinic acid at 200 ℃ and 10 bar hydrogen pressure. It was found that an increase in the number of Pt particles on the external surface of the ZSM-5 negatively affects the turn over frequency of the pentanoic acid product due to the agglomeration of Pt during the reaction (Luo et al., 2019). In addition to coke deposition and metal sintering, another major catalyst deactivation driver during hydrodeoxygenation reaction is the solvent (Ding et al., 2020; Gorzin and Yaripour, 2019; Tu et al., 2019). The extent of metal washing or leaching from a support depends on the type of solvent, conditions of the reaction as well as the nature of metal-support interaction, potentially a weak interaction leads to high metal loss. In this work, metal leaching from the three catalysts was insignificant as revealed by the EDX elemental mapping result, shown in Table A1 (Appendix A), hence coke might be one of the major causes of the decreased in catalytic activity noticed. Therefore, thermogravimetric analysis (TGA) was performed on both the used and the fresh catalysts. Figure 5.11 presents the TGA-DTG profile of the used mic-Ni/ZSM-5 (a), hie-Ni/ZSM-5 (b), and Ni/SiO_2 (c) catalysts.

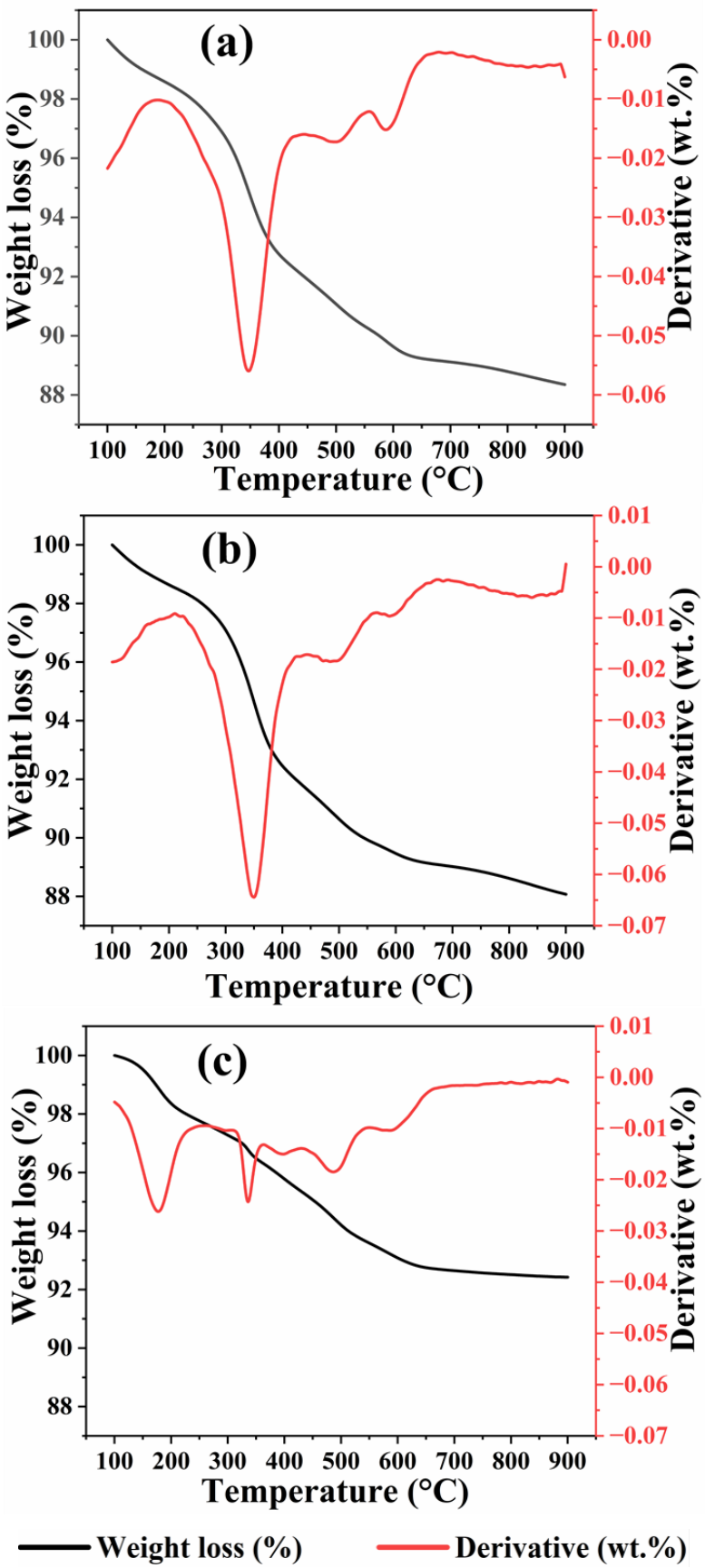

Figure 5.11: *TGA-DTG profile of the used catalysts; (a) mic-Ni/ZSM-5, (b) hie-Ni/ZSM-5, and (c) Ni/SiO₂.*

The TGA data was recorded between 100 ℃ and 900 ℃ at a heating rate of 10 ℃ min^{-1}. Below 300 ℃, weight loss was ascribed to water content and other volatile matter in the catalysts and above 300 ℃ loss was associated with the deposited coke on the catalyst surface during the hydrodeoxygenation reaction. The used catalysts displayed weight losses of 2.7% (Ni/SiO_2), 3.3% (mic-Ni/ZSM-5), and 2.8% (hie-Ni/ZSM-5) below 300 ℃, respectively. Between 300 ℃ and 900 ℃, further losses of 4.8% (Ni/SiO_2), 8.4% (mic-Ni/ZSM-5), and 7.8% (hie-Ni/ZSM-5) were recorded. This weight loss could be linked to the presence of some organic residue in the catalysts, due to coke formation during the HDO reaction (Nie et al., 2021). Thus confirming the accumulation of organic compounds on the surface of the catalysts. Noticeably, Ni/SiO_2 catalyst with the least density of acid sites and shortest life span has the lowest coke content. Although the hie-Ni/ZSM-5 showed higher amount of coke deposit compared to the Ni/SiO_2, it demonstrated the highest activity and product selectivity in the catalyst reusability test. The bifunctional property (acid sites of the support plus the metal sites) of hie-Ni/ZSM-5 might be the reason for the high catalytic activity. This result is in agreement with the observation of Ni et al. (2011) who reported superior catalytic activity over Zn-Al/ZSM-5-T catalyst with the highest quantity of coke deposit compared with Zn-Al/ZSM-5 catalyst during aromatization of methanol.

5.10 Kinetics of Anisole Hydrodeoxygenation over hie-Ni/ZMS-5 Catalyst

This section presents the kinetics of anisole hydrodeoxygenation over the hie-Ni/ZSM-5 catalyst. Among the catalysts prepared and tested for the HDO of anisole herein, the hie-Ni/ZSM-5 shows the best activity and is therefore selected for the kinetic study. The study was carried out to determine some important kinetic parameters. These parameters, such as activation energy (E_A), rate constants (k), reaction order (n), enthalpy (ΔH), and entropy (ΔS) changes, can only be estimated accurately if mass transfer limitations are eliminated within

the heterogeneous reaction system (Coker, 2001; Falconer, 1998; Liu et al., 2021). Mass transport analysis is a prerequisite when intrinsic kinetics are sought (Wang et al., 2005). It is performed by changing variables such as stirring speed and catalyst particle size while observing their effects on conversion (Perego and Peratello, 1999; Shinde and Deshpande, 2022). The sole aim of this analysis is to remove both internal and external mass transfer constraints so that reaction rates are determined within a kinetic control regime (Lawal et al., 2019).

5.10.1 Eliminating external mass transfer limitation

The catalytic HDO of anisole occurs in three phases. The gas phase is hydrogen, the liquid phase is anisole dissolved in decalin, and the solid phase is the hie-Ni/ZSM-5 catalyst. Stirring speeds between 300 rpm and 1200 rpm were investigated experimentally to examine how changing the speed affects anisole conversion. Figure 5.12 presents the results.

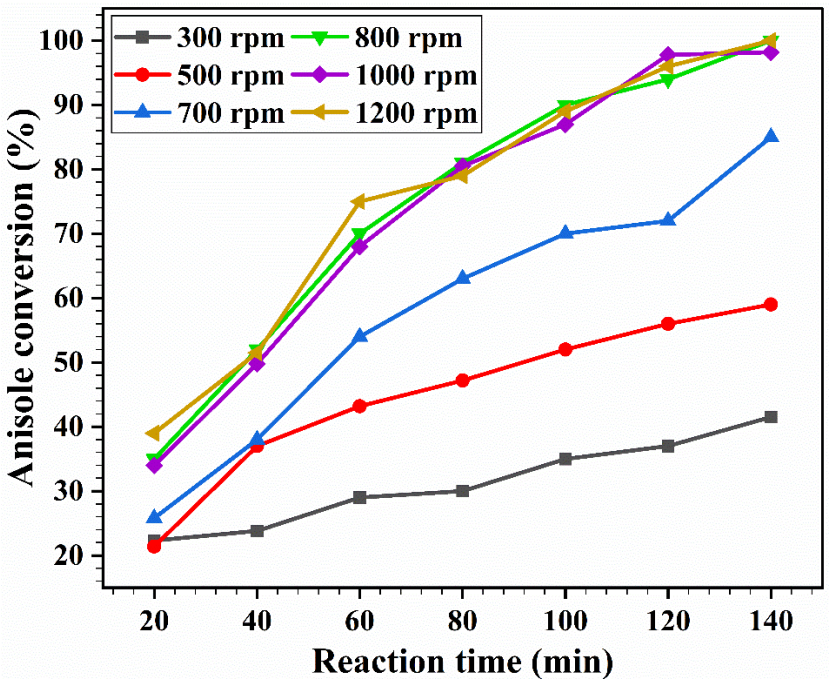

Figure 5.12: *Effect of stirring rate on the conversion of anisole: 50 mL mixture of 48.65 mL decalin and 1.35 mL anisole (3.0 wt.% anisole), 100 mg catalyst, 200 ℃ reaction temperature, 60 bar H_2, and 140 min reaction time.*

It is obvious that anisole conversion increased as the impeller stirring rate increased from 300 rpm to 1200 rpm. Conversion was 41.5%, 59.1%, 85.2%, 100%, 98.9%, and 100% at 300 rpm, 500 rpm, 700 rpm, 800 rpm, 1000 rpm, and 1200 rpm, respectively, in 140 min. Notably, the conversion was unaffected by a further increase in impeller speed from 800 rpm to 1200 rpm. This implies that the reaction rate at these points doesn't increase any more with an increase in the impeller stirring speed. As a result, impeller speeds of 800 rpm (giving a Reynolds number of 1.1×10^6) and above seem to eliminate external transport limitations during HDO of anisole. A similar reactor configuration (Parr series 4590) was used in the HDO of anisole over Re-MoO_x/TiO_2 catalyst with dodecane as a solvent. In that study, 700 rpm, corresponding to a Reynolds number of 1.3×10^6, was used as the optimum impeller stirring speed (Ghampson et al., 2018). In a related study, Tu et al. (2019) used a stirring speed of 1000 rpm during the HDO of anisole over Ni/IM-5-h catalyst. A conversion of 98.7% was recorded in 140 minutes. Accordingly, the subsequent results reported in this chapter are based on experiments performed at an impeller speed of 800 rpm.

5.10.2 Eliminating internal mass transfer limitation

One of the key elements determining the extent of a reactant's transformation in a catalytic reaction process is its ability to reach the available active sites. Among the problems caused by internal transport limitations is pore diffusion, which can severely slow down the reaction rate (Fogler, 2006; Hill, 2014). The rate at which hydrogen and anisole diffuse through the porous network of a 5% hie-Ni/ZSM-5 catalyst considerably influences the reaction rate in this case (Yang et al., 2019). Thus, it is critical to eliminate intraparticle diffusion resistance in order to ensure that anisole HDO is taking place in a kinetically controlled regime. Hence, the effect of catalyst particle size on the rate of anisole disappearance was examined. It is believed that as the particle size decreases, the diffuse path length to the active sites within

the catalyst decreases, thereby reducing intraparticle diffusion. Figure 5.13 presents the effect of catalyst particle size on anisole conversion during the HDO at 200 ℃ and 60 bar hydrogen. The catalyst powder was sieved into the following particle size distributions: 75 µm < d_p < 90 µm, 90 < d_p < 120 µm, and 120 µm < d_p < 140 µm.

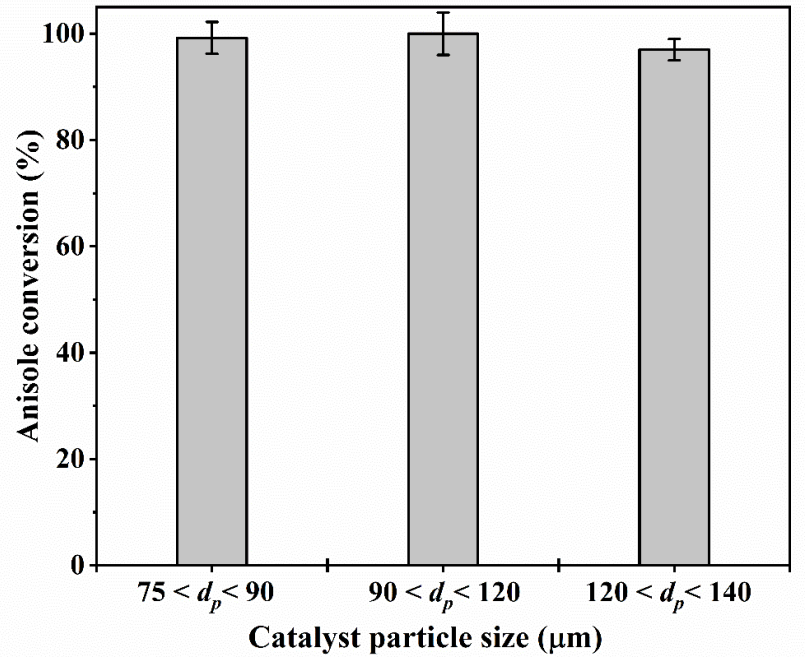

Figure 5.13: *Effect of catalyst particle size on anisole conversion. Reaction temperature, 200 ℃; pressure, 60 bar H_2; solvent, 48.65 mL decalin; anisole, 1.35 mL (3.0 wt.%); catalyst loading, 100 mg; reaction time, 140 min.*

It is clear from the result (Figure 5.13) that complete anisole conversion was achieved over 5% hie-Ni/ZSM-5 catalyst particle size 75 µm < d_p < 90 µm and 90 < d_p < 120 µm. A slight decrease in conversion (97.4%) for particle size 120 µm < d_p < 140 µm was noticed. While particle size may influence the initial reaction rate and conversion, it appears to be less sensitive to the changes from 75 to 90 µm and 90 to 120 µm. This result shows that catalyst particles with a diameter of less than or equal to 120 µm eliminate intraparticle diffusion limitations or internal mass transport restrictions.

5.10.3 Effect of catalyst loading on initial rate of anisole disappearance

Catalyst loading is an important factor that can strongly influence the rate of chemical reactions (Xekoukoulotakis et al., 2010). Therefore, the effect of hie-NiZSM-5 catalyst loading on the initial rate of anisole disappearance was investigated. Catalyst loadings of 50 mg, 100 mg, and 150 mg were considered.

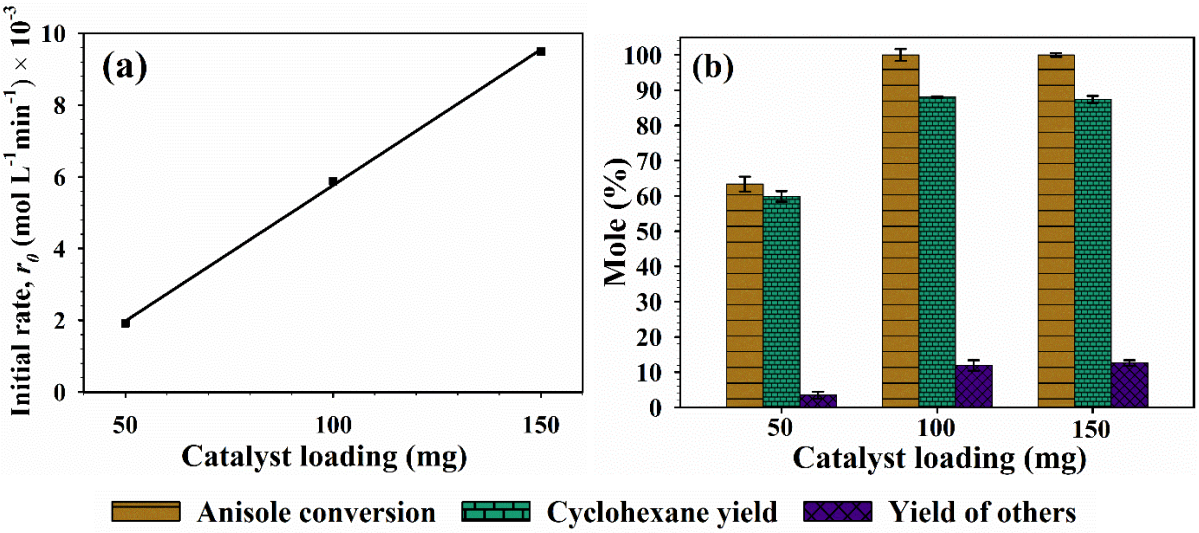

Figure 5.14: *Effect of catalyst loading on initial rate of anisole disappearance (a) and product distribution (b). Reaction temperature, 200 °C; pressure, 60 bar H_2; solvent, 48.65 mL decalin; anisole, 1.35 mL (3.0 wt.%); catalyst loading, 50 mg, 100 mg, and 150 mg; reaction time, 140 min.*

It is obvious from the result shown in Figure 5.14 that changing the catalyst loading affected the initial rate of anisole HDO. The rate increased linearly as the catalyst loading increased, from 1.92 × 10^{-3} mol L^{-1} min^{-1} (50 mg) to 5.88 × 10^{-3} mol L^{-1} min^{-1} (100 mg) and 9.49 × 10^{-3} mol L^{-1} min^{-1} (150 mg), respectively. This is expected as increased catalyst loading provides more active sites for the HDO reaction. Total conversion of anisole was recorded over 100 mg and 150 mg, while 63.4% was seen for 50 mg. The yield of cyclohexane was 59.9% (50 mg), 88.1% (100 mg), and 87.4% (150 mg), respectively. The yield of other products, mostly light ends and possibly undetected liquid products, was 3.5%, 11.9%, and 12.6%, respectively.

5.10.4 Determination of reaction order, rate constants, and activation energy for anisole HDO

The integral method of kinetic data analysis was used for the determination of reaction order and rate constants. The method provides a mathematical equation of rate expressions and assumes that a plot of a given concentration against reaction time produces a straight line. When the data is plotted and a relatively good straight line is obtained, the kinetic data is considered to accurately fit the rate expression. The integral method is straightforward to apply and is used when evaluating relatively simple rate expressions, or when the data is so dispersed that the derivatives required by the differential method cannot be found reliably. In summary, it is recommended that the integral method be tried first, and if that fails, then the differential method (Fogler, 2004).

Anisole HDO over hie-Ni/ZSM-5 catalyst generated cyclohexane as the only liquid product (as seen in Sections 5.3 and 5.8). In addition, the carbon balance (Figure 5.2 and Table 5.3) accounted for about 85–95% of the total carbon in the liquid product, implying most of the anisole was converted to cyclohexane. This suggests a simple chemical equation (like equation 5.1) leading to a simple rate expression. Hence, zero-order, first-order, and second-order integral form of rate expressions (equations 5.2, 5.3, and 5.4) were used for the kinetic analysis.

$$C_7H_8O \xrightarrow[-H_2O]{+3H_2} C_6H_8 + CH_4 \qquad 5.1$$

$$C_A = -kt + C_{A0} \qquad 5.2$$

$$lnC_A = -kt + \ln C_{A0} \qquad 5.3$$

$$\frac{1}{C_A} = kt + \frac{1}{C_{A0}} \qquad 5.4$$

where C_A is the concentration of anisole (mol L^{-1}) at time *t*, C_{A0} is the initial concentration of anisole (mol L^{-1}), *t* is the reaction time (sec), and *k* is the rate constant (units of rate constants for the zero order, first order, and second order are mol L^{-1} s^{-1}, s^{-1}, and L mol^{-1} s^{-1}).

At temperatures between 160 and 240 °C, a pressure of 60 bar H_2, decalin as the solvent, and a catalyst loading of 100 mg, the change in anisole concentration was recorded at an interval of 20 minutes. From the set of concentration-time data obtained, plots for the zero-order (a), first-order (b), and second-order (c) were generated and shown in Figure 5.15. A plot that shows the best linear fit is thought to reveal the reaction order in relation to anisole conversion. It is apparent from the result that at all of the temperatures tested, the first-order plot (Figure 5.15b) exhibits the best fit. The coefficients of determination for the first-order plot were 0.9972 (160 ℃), 0.9950 (180 ℃), 0.9963 (200 ℃), 0.9889 (220 ℃), and 0.9991 (240 ℃) respectively. Hence, the HDO reaction over the 5 wt.% nicked-based catalyst is believed to be first-order with respect to anisole.

Values of the rate constants *k* at different reaction temperatures were calculated from the slope of the first-order plot and presented in Table 5.4. The values increased with an increase in the reaction temperature implying an increasing in the reaction rate. These were used to determine the activation energy and the frequency factor during anisole HDO over the hie-Ni/ZSM-5 according to the Arrhenius equation (5.6).

$$\ln k = \frac{E_A}{R}\frac{1}{T} + \ln A \qquad 5.6$$

where *k* is the rate constant (s^{-1}), E_A is the activation energy (kJ mol^{-1}), *T* is the temperature (*K*), *A* is the frequency factor (s^{-1}), and *R* is the molar gas constant (8.314 J mol^{-1} $\cdot K^{-1}$).

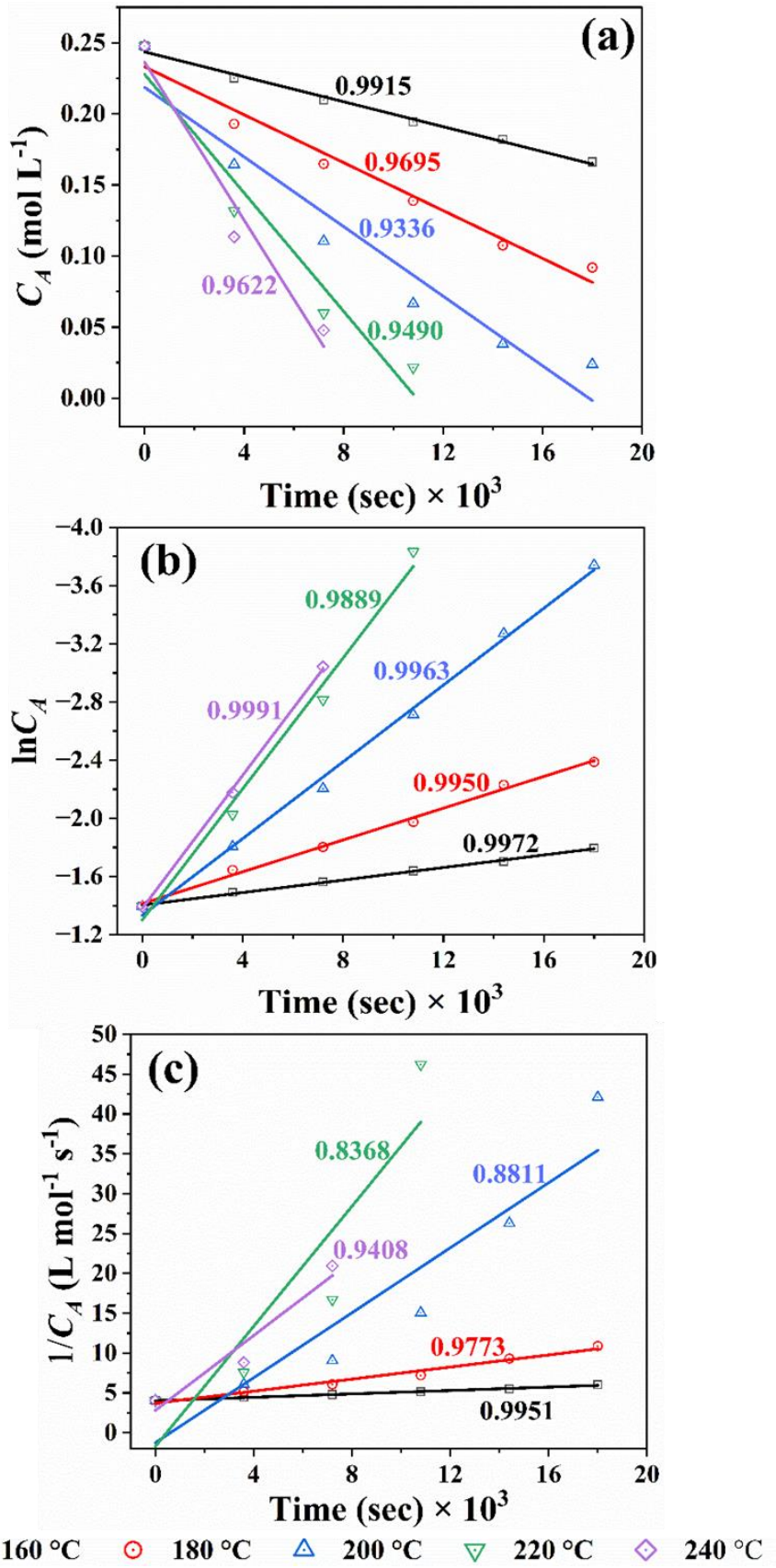

Figure 5.15: *Plots of rate laws for the HDO of anisole over hie-Ni/ZSM-5 catalyst: Zero-order (a), first-order (b), and second-order (c). Reaction temperature, 160-240 ℃; pressure, 60 bar H_2; solvent, 48.65 mL decalin; anisole, 1.35 mL (3.0 wt.%); catalyst loading, 100 mg.*

Table 5.4: Values of rate constant (*k*) at different HDO temperatures, activation energy (*Ea*), and frequency factor (*A*) from the Arrhenius plot.

Temperature (°C)	***k* ×10^{-5} (s^{-1})**	***Ea*** **(kJ mol^{-1})**	***A*** **(s^{-1})**
160	7.5		
180	16.1		
200	35.5	53.3	227.5
220	58.5		
240	68.6		

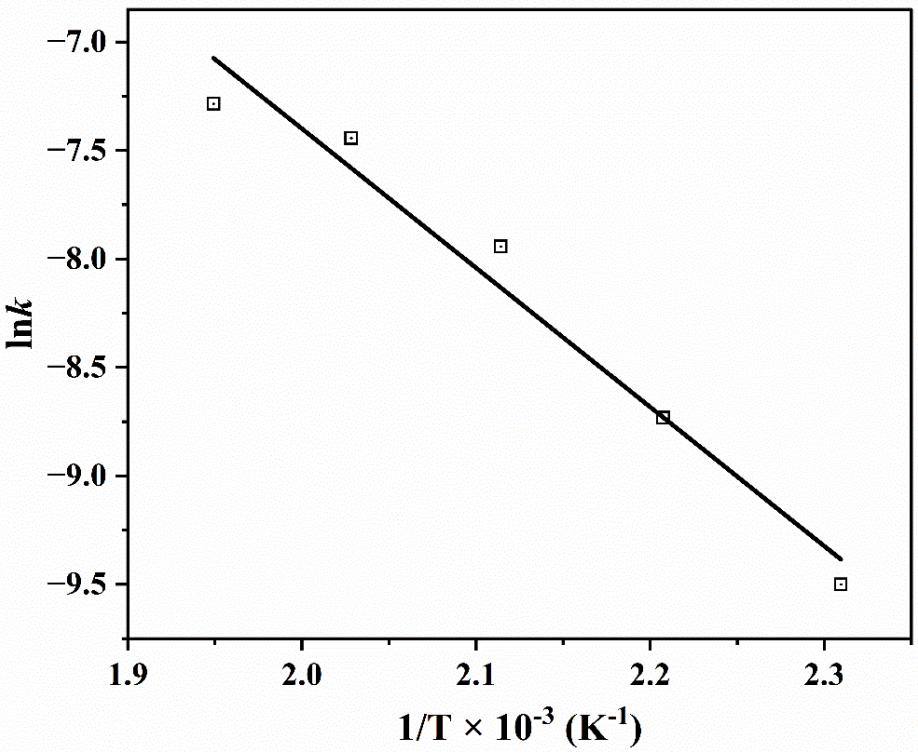

Figure 5.16: *Arrhenius plot for anisole HDO over hie-Ni/ZSM-5 catalyst. Reaction temperature, 160-240 °C; pressure, 60 bar H_2; solvent, 48.65 mL decalin; anisole, 1.35 mL (3.0 wt.%); catalyst loading, 100 mg.*

Figure 5.16 presents the Arrhenius plot from which the activation energy and frequency factor were evaluated (shown in Table 5.4). The calculated activation energy for anisole HDO over hie-Ni/ZSM-5 catalyst is 53.3 kJ mol^{-1}. Interestingly, a comparable value of 53.9 kJ mol^{-1} was reported by Aqsha et al. (2021) for the HDO of anisole over a Ni-V/TiO_2 catalyst. In a related study, 56.0 kJ mol^{-1} was obtained during the HDO of anisole to cyclohexane over a Re-MoO_x/TiO_2 catalyst (Ghampson et al., 2018).

5.10.5 Anisole adsorption kinetics, isotherm, and thermodynamics

Adsorption kinetic studies can provide useful details on potential adsorption mechanisms (Zuliani et al., 2023). They deal with the rate of substrate adsorption and the adsorbates' residence time at the solid-liquid boundary (Alghamdi et al., 2021). Adsorption isotherms predict how the adsorbate (in this case, anisole) and adsorbent (hie-Ni/ZSM-5) interact as well as the amount of substrate adsorbed at equilibrium at a constant temperature (Abdulhamid and Muhammad, 2022; Amutova et al., 2023). The adsorption thermodynamics provide insight on the feasibility and the spontaneous nature of the adsorption process (Raghav and Kumar, 2018; Wang et al., 2023).

Herein, the kinetics study was carried out at three different temperatures: 180 ℃, 200 ℃, and 220 ℃ respectively. Prior to the adsorption, 100 mg of the adsorbent (hie-Ni/ZSM-5) was reduced at 500 ℃ for 3 hours under 5 % H_2/N_2. The total volume of the solution (a mixture of anisole and decalin) is 50 mL, containing 3 wt.% anisole. The two most widely used adsorption kinetic models, pseudo-first-order and pseudo-second-order models (Souza et al., 2020; Vareda, 2023; Wang and Guo, 2020), were employed for the analysis. Equations 5.5 and 5.6 present the linear form of these models.

$$log\,(q_e - q_t) = log\,(q_e) - \frac{k_1 t}{2.303} \quad 5.5$$

$$\frac{t}{q_t} = \frac{1}{k_2 q_e^2} + \frac{t}{q_e} \quad 5.6$$

where q_t is the adsorption capacity at time t (mg g^{-1}), q_e is the equilibrium adsorption capacity (mg g^{-1}), k_1 is the rate constant for the pseudo-first-order (min^{-1}), and k_2 is the rate constant for the pseudo-second order (g mg^{-1} min^{-1}). However, q_e can be recalculated at each point in time for an experiment in which equilibrium was not reached, yielding an out-of-equilibrium value of q_e that falls over the course of the experiment as the adsorption process advances (Bullen et al., 2020). Thus, the q_e was evaluated from the expression in equation 5.7.

$$q_e = \frac{(C_0 - C_e)V}{m} \quad 5.7$$

where C_o is the initial anisole concertation (mg L^{-1}), C_e is the anisole concentration after adsorption (mg L^{-1}), V is the volume solution (L), and m is the mass of the dry adsorbent (g).

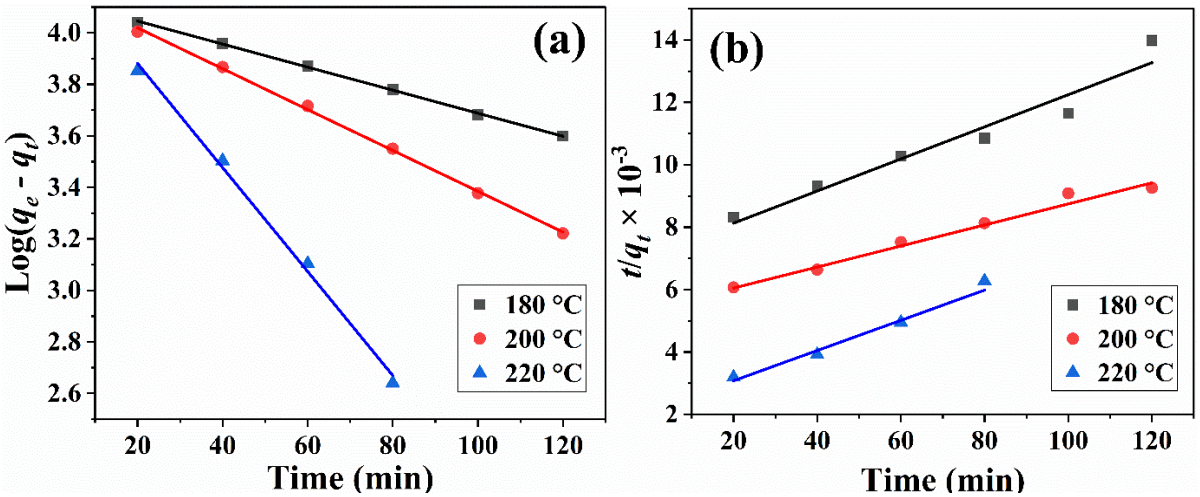

Figure 5.17: *Pseudo-first-order (a) and pseudo-second-order (b) kinetic plots for anisole adsorption onto the hie-Ni/ZSM-5 catalyst: temperature, 180-220 ℃; pressure, 60 bar H_2; volume of solution, 50 mL containing 1.35 mL adsorbate; stirring rate, 800 rpm.*

Figure 5.17 presents (a) the pseudo-first-order and (b) pseudo-second-order plots of the experimental data. Table 5.5 lists the kinetic parameters and the correlation coefficients determined from the plots. It is clear from the result that as the adsorption temperature increased from 180 to 220 ℃ there was an increase in the rate constant in the pseudo-first-order model. However, a reversed trend was noticed for the pseudo-second-order model, where the values of the adsorption rate constant decreased as the reaction temperature increased. Noteworthy, the pseudo-first-order model showed a higher coefficient of determination ($R^2 \geq 0.9967$) compared to the pseudo-second-order model ($R^2 \leq 0.9825$). In addition, values of the q_e calculated (or modeled) at 180 ℃, 200 ℃, and 220 ℃ were 13,652 mg g^{-1}, 14,931 mg g^{-1}, and 13,948 mg g^{-1} for the pseudo-first-order and 21,880 mg g^{-1}, 26,609 mg g^{-1}, and 20,048 mg g^{-1} for the pseudo-second-order, respectively.

Table 5.5: Kinetic parameters for the adsorption of anisole onto the hie-Ni/ZSM-5 catalyst.

		Pseudo-first-order			**Pseudo-second-order**		
Temp. (℃)	q_e ***expt.*** **(mg g^{-1})**	q_e ***cal.*** **(mg g^{-1})**	k_1 **min^{-1}**	R^2	q_e ***cal.*** **(mg g^{1})**	k_2 **g mg^{-1} min^{-1}**	R^2
180	12,952	13,652	10.4×10^{-3}	0.9993	21,880	2.8×0^{-7}	0.9798
200	13,392	14,931	18.0×10^{-3}	0.9999	26,609	2.7×0^{-7}	0.9819
220	13,392	13,948	46.5×10^{-3}	0.9967	20,048	1.2×0^{-6}	0.9825
Constant (mg L^{-1})	$C_0 = 26{,}784$						

In practice, the following three requirements must be met for a kinetic model to be suitable for the obtained experimental data: the graph line must pass through all of the points; the calculated value of the q_e should be close to the experimental q_e; and the coefficient of

determination (R^2) should be close to unity (Alghamdi et al., 2021; Vareda, 2023). Having satisfied all these requirements, pseudo-first-order is considered the best model that describes the kinetics of anisole adsorption onto the hie-Ni/ZSM-5.

The adsorption isotherm was modeled with the Freundlich and Langmuir adsorption isotherm models. The linear forms of these models are given by equations 5.8 and 5.9.

$$ln\, q_e = ln\, K_F + \frac{1}{n} ln\, c_e \quad 5.8$$

$$\frac{1}{q_e} = \frac{1}{c_e} \frac{1}{q_m K_L} + \frac{1}{q_m} \quad 5.9$$

where K_F (mg g^1)(L mg^{-1})$^{1/n}$ and n are the Freundlich constants associated to the adsorption capacity and intensity, K_L (L mg^{-1}) is the Langmuir isotherm constant, and q_m (mg g^{-1}) is maximum monolayer adsorption capacity (theoretical).

Figure 5.18 shows the isotherm plot for anisole adsorption at 180 ℃ and 200 ℃ and 60 bar H_2. It can be seen that a better linear fit was obtained from the Langmuir isotherm plot compared to the Freundlich. The coefficient of determination, shown in Table 5.6, are 0.9875 (180 ℃, 0.9904 (200 ℃), and 0.9803 (220 ℃) for Freundlich and 0.9936 (180 ℃), 0.9993 (200 ℃), and 0.9967 (220 ℃) for Langmuir, respectively. In addition, the adsorption isotherm parameters are also presented in Table 5.6. For the Langmuir model, the maximum theoretical monolayer adsorption capacity, q_m, increased from 5.20×10^3 mg g^{-1} (180 ℃) to 7.73×10^3 mg g^{-1} (200 ℃), and 14.10×10^3 mg g^{-1} (220 ℃), respectively. Furthermore, the Freundlich constant, 1/n, which is linked to the adsorption intensity of the hie-Ni/ZSM-5, increased from 0.69 (180 ℃), to 0.72 (200 ℃), and 0.75 (220 ℃). These imply ideal

adsorption conditions with increasing heterogeneity of the adsorbent's sites as the value of 1/n becomes closer to zero (Alghamdi et al., 2021; Yao et al., 2020).

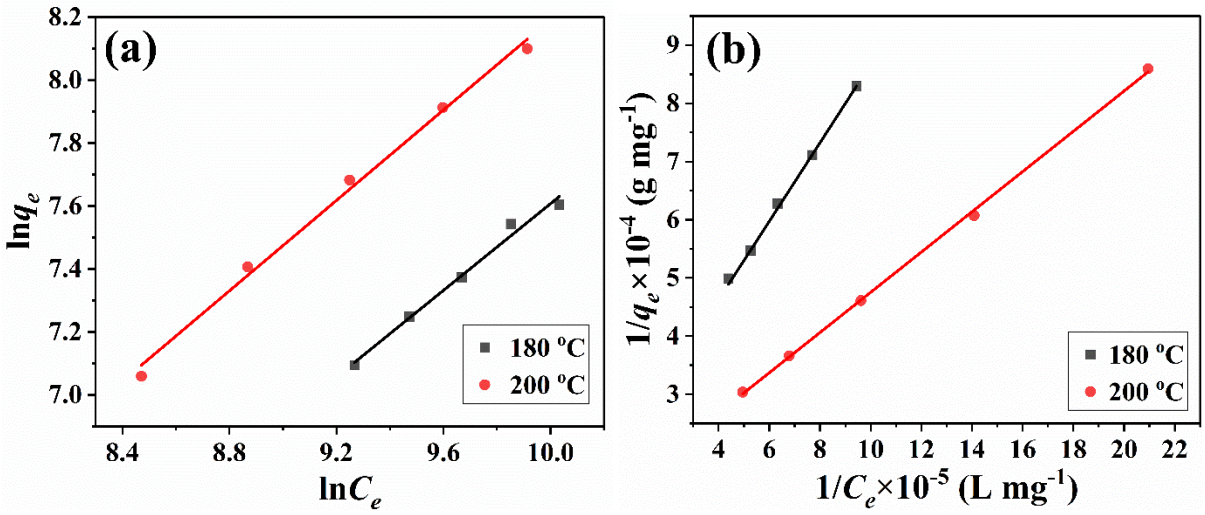

Figure 5.18: *Freundlich 'a' and Langmuir 'b' isotherm plots. for anisole adsorption onto the hie-Ni/ZSM-5 catalyst: temperature, 180 and 200 ℃; pressure, 60 bar H_2; volume of solution, 50 mL containing 1.35 mL adsorbate; stirring rate, 800 rpm.*

Table 5.6: Freundlich and Langmuir isotherm parameters for the adsorption of anisole onto the hie-Ni/ZSM-5 catalyst.

Temp.	**Freundlich**			**Langmuir**		
(℃)	K_F **(mg g^1) (L mg^{-1})$^{1/n}$**	***1/n***	R^2	q_m **(mg g^{-1})**	K_L **(L m g^{-1})**	R^2
180	2.07	0.69	0.9875	5.20×10^3	2.85×10^{-5}	0.9936
200	2.76	0.72	0.9904	7.73×10^3	3.74×10^{-5}	0.9993
220	5.40	0.75	0.9803	14.10×10^3	6.59×10^{-5}	0.9967

The effect of heat on the anisole adsorption over the hie-Ni/ZSM-5 was evaluated. This was carried out over a rage of temperature (160 – 220 ℃) at 60 bar. The volume of the solution

was maintained at 50 mL at a stirring rate of 800 rpm. The thermodynamic parameters were calculated using equations 5.10 (Van't Hoff equation) and 5.11.

$$lnK_{ac} = \left(\frac{-\Delta H}{RT}\right) + \left(\frac{\Delta S}{R}\right) = \left(\frac{-\Delta G}{RT}\right) \qquad 5.10$$

but $$K_{ac} = \frac{q_e}{C_e} \qquad 5.11$$

where ΔH is the enthalpy change in kJ mol^{-1}, ΔS is the entropy change in J mol^{-1}K^{-1}, ΔG is the Gibbs free energy change in kJ mol^{-1}, R is the universal gas constant in J mol^{-1}K^{-1}, T is temperature in Kelvin, and K_{ac} is the apparent equilibrium constant in L g^{-1}.

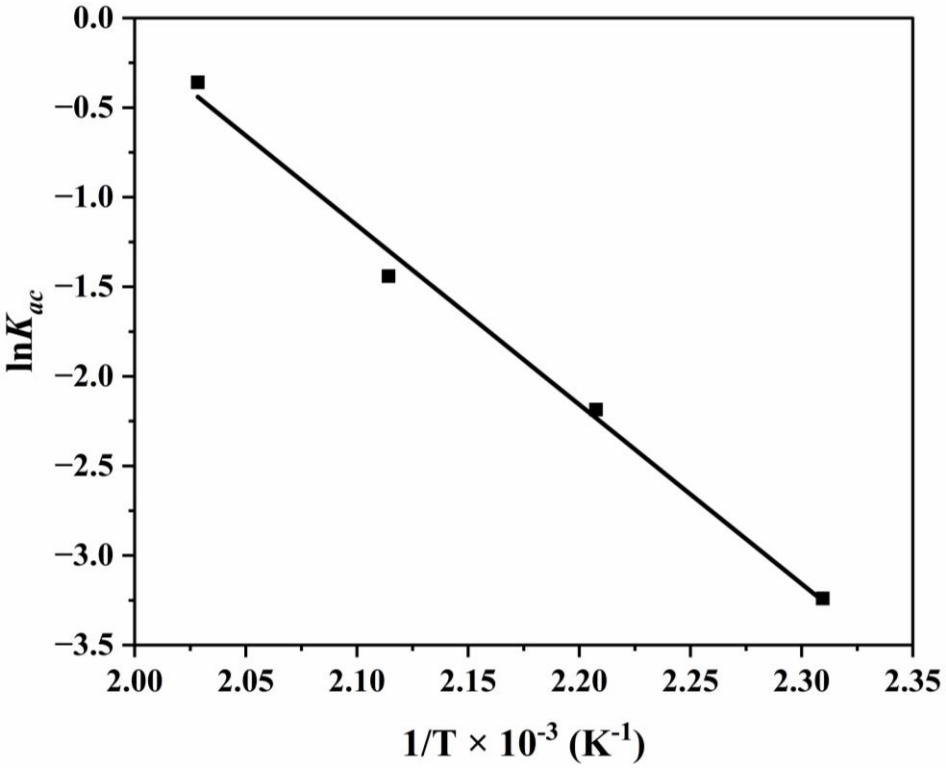

Figure 5.19: *Van't Hoff's plot for anisole adsorption onto hie-Ni/ZSM-5. Adsorption temperature, 160-220 ℃; pressure, 60 bar H_2; volume of the solution, 50 mL; mass of adsorbent, 100 mg*

.

Figure 5.19 (Van't Hoff's plot) presents the graph of lnK_{ac} versus 1/T generated using equation 5.10. The data used for the plot and the thermodynamic parameters obtained from the slope and intercept of the graph are shown in Table 5.7. The positive values of ΔG, 11.7 kJ mol^{-1} (160), 8.2 kJ mol^{-1} (180), 5.7 kJ mol^{-1} (200), and 1.5 kJ mol^{-1} (220), indicate the non-spontaneous nature of the anisole adsorption. However, it is evident that an increase in temperature favours the adsorption of anisole, as the value of ΔG decreases with an increase in adsorption temperature, implying an increase in spontaneity (Alghamdi et al., 2021; Wang et al., 2023).

Table 5.7: Observed thermodynamic parameters of anisole adsorption onto hie-Ni/ZSM-5.

Temp. (°C)	K_{ac} **(L g^{-1})**	**lnK_{ac}**	**ΔG (kJ mol^{-1})**	**ΔH (kJ mol^{-1})**	**ΔS (J mol^{-1} K^{-1})**
160	3.9×10^{-2}	-3.2	11.7		
180	11.2×10^{-2}	-2.2	8.2	83.2	165.1
200	23.7×10^{-2}	-1.4	5.7		
220	69.9×10^{-2}	-0.4	1.5		

The adsorption enthalpy (ΔH) and entropy (ΔS) were 83.2 kJ mol^{-1} and 0.17 kJ mol^{-1} K^{-1} respectively. These parameters are key indicators of the nature of the bond between the adsorbate and adsorbent and the randomness of the adsorption process (Raghav and Kumar, 2018). The positive values of ΔH and ΔS recorded suggest the type of adsorption between anisole and hie-Ni/ZSM-5 is chemisorption and that it is endothermic in nature.

5.11 Summary of the Chapter

This chapter presents the results of the catalytic HDO of anisole as a bio-oil model compound. Using a high-pressure batch reactor, reactions were carried out over nickel-based

ZSM-5, zinc-based ZSM-5, nickel-zinc bimetallic ZSM-5, and nickel-SiO_2 catalysts. The effects of catalyst support, active metal, temperature, pressure, and solvent on anisole conversion and product distribution have been demonstrated. In addition, a kinetic study for anisole HDO over the hie-Ni/ZSM-5 catalyst has been performed. In the next chapter (Chapter 6), the HDO of benzoic acid as a typical bio-oil model compound is presented.

CHAPTER 6

Benzoic Acid as a Typical Bio-oil Model Compound: Hydrodeoxygenation Reaction and Kinetics

6.1 Introduction

Hundreds to thousands of oxygenates (such as phenol, ketones, aldehydes, furans, sugars, and carboxylic acids) are present in bio-oil. These compounds confer on bio-oil high viscosity, low heating value, thermal instability, and acidity, which limit its use as a direct substitute for petroleum-based fuels and chemical feedstocks (Dahman et al., 2019; Lawan Muhammad, 2018). Organic acids such as carboxylic acid, acetic acid, and formic acid found in bio-oil are principally responsible for its acidity (Qu et al., 2021; Sulejmanovic et al., 2022). The presence of these molecules in bio-oil poses a serious challenge in the field of renewable energy, leading to the deterioration of structural materials within the processing settings. This could further result in a total failure of the equipment or a high maintenance cost (Oasmaa et al., 2010). Several solutions have been proposed to tackle this issue, including using catalysts to reduce the formation of acids during the biomass pyrolysis process (Chen et al., 2017; Sharifzadeh et al., 2019). Kumar et al. (2019) investigated the catalytic pyrolysis of pine wood biomass over Cu and Ni-based zeolite catalysts via *in-situ* and a combination of *in-situ* and *ex-situ* catalytic pyrolysis. While the former promoted acid formation in the product, the latter has two reaction stages, each requiring a substantial amount of heat and catalyst, making it capital-intensive. As a result, researchers are currently exploring hydrogenation and hydrodeoxygenation (HDO) as efficient methods for removing acidic functionalities from bio-oils. Many researchers studied catalytic hydrogenation and HDO mechanisms using model compounds rather than bio-oils because of the complexity of bio-oil components. Among the acidic model compounds studied are the HDO of acetic acid and

palmitic acid (Lawal et al., 2019; Liu et al., 2021; Song et al., 2010; Wang et al., 2017). The simple aliphatic hydrocarbon chains of both compounds and the carboxylic acid substitutes are much simpler than their more complex benzene-ring counterparts found in benzoic acid. In bio-oil, oxygenates such as benzoic acid must be converted into aromatic hydrocarbons. In this chapter, the results of an investigation of benzoic acid, which is an organic acid compound containing benzene as the ring core and carrying a carboxylic acid substituent, are presented. Considering the complexity of bio-oil, the aim here is to study typical model compounds like benzoic acids in order to gain insight into the kinetics and development of a bio-oil catalyst that will be effective and robust. In addition to contributing to a greater understanding of how catalytic upgrading of bio-oil works, the study of model compounds could be an important step towards further developing effective methods to produce and upgrade it.

To make high-quality oil and valuable products, it is important to minimise the oxygenate content of bio-oil by converting it into its respective aromatic and aliphatic hydrocarbons via HDO. This chapter reports the reaction mechanism and kinetics of HDO of benzoic acid, as a model compound, over 5 wt.% Ni-based catalysts. The effect of reaction temperature and hydrogen pressure on benzoic acid conversion is presented and discussed in Section 6.2 using mic-Ni/ZSM-5, hie-Ni/ZSM-5, and Ni/SiO_2 catalysts at 100 mg loading. In addition, the effect of both process factors on product distribution is also analysed, presented, and discussed. In Section 6.4, a study of the effects of changing the initial concentration of benzoic acid on the conversion and distribution of products is reported. These studies are essential to understanding the HDO of benzoic acid. The results of the kinetic modeling study are reported in Section 6.6 over hie-Ni/ZSM-5 catalyst. An analysis of concentration-time reaction data was conducted so that kinetic parameters, such as order of reaction, rate

constants, and activation energies, could be estimated. As a result of the complex reactions occurring during HDO of benzoic acid, the method of initial rate was used to model the kinetic data. Also, a Langmuir-Hinshelwood type of kinetic model was used to fit the experimental data.

6.2 Effect of Temperature and Pressure on Benzoic acid Conversion

Increases in both temperature and hydrogen pressure have been shown to affect the rate of anisole HDO in Chapter 5. Similar results have been reported for HDO of bio-oil model compounds such as vanillin, phenol, acetic acid, and guaiacol (Gea et al., 2023; Lawal et al., 2019; Tian et al., 2022). Hence the effects of change in reaction temperature and hydrogen pressure on conversion during the HDO of benzoic acid have been investigated. Preliminary experiments were carried out at temperatures of 200, 250, and 300 ℃ and pressures of 20, 40, and 60 bar, respectively. However, only at 300 ℃ and 60 bar a noticeable conversion of benzoic acid was seen (about 10% in 6 hours). Since the maximum operating temperature for the 0.1 L batch reactor (Parr reactor 9045) is 350 ℃, a temperature range of 310 ℃ to 340 ℃ with a step increase of 10 ℃ was chosen. Prior to the reaction, the 5 wt.% nickel-based catalyst was activated in a tubular furnace at 500 ℃ (5 ℃ min^{-1} ramp rate) for 3 h under a 5% H_2/N_2 mixture flowing at 1 L min^{-1}. The activated catalyst is then transferred to the reactor containing 50 mL mixture of benzoic acid and tetralin solvent (3 wt.% benzoic acid). Nitrogen was used to flush the reactor three times before heating to the reaction temperature. At that point the nitrogen gas is released and a desired pressure of hydrogen is introduced into the reactor. The plots presented in Figure 6.1 show the time-dependent conversion of benzoic acid as a function of reaction temperature and the effect of reaction pressure on conversion using 100 mg loading of mic-Ni/ZSM-5, hie-Ni/ZSM-5, or Ni/SiO_2 catalysts.

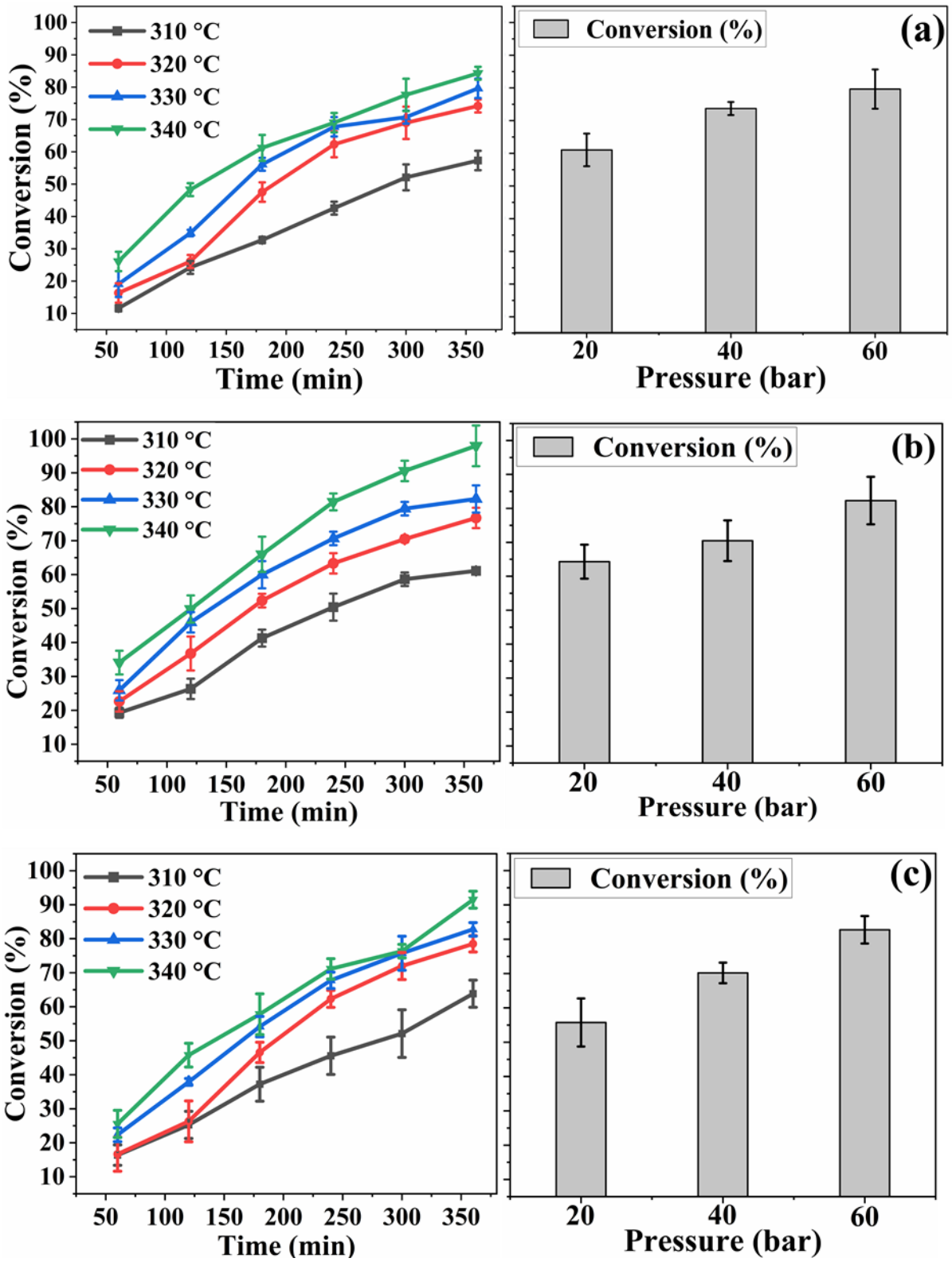

Figure 6.1: *Effect of temperature (at 60 bar H_2 pressure) and pressure (at 330 °C) on benzoic acid conversion over mic-Ni/ZSM-5 (a), hie-Ni/ZSM-5 (b), and Ni/SiO_2 (c). Catalyst loading; 100 mg, solvent; tetralin, benzoic acid initial concentration; 0.24 M, reaction time; 6 hours.*

While the conversion of benzoic acid increases with time-on-stream at any given temperature studied, the conversion also increases as the reaction temperature increases from 310 °C to 340 °C for each catalyst. This suggests that the rate of HDO reaction increases as temperature increases. Likewise, benzoic acid conversion increases as the hydrogen pressure increases, signifying an increase in the availability of hydrogen at the surface of the catalyst following an increase in hydrogen pressure in the reactor. Nonetheless, after 6 h of reaction, the following conversions were achieved: 57.3% (310 °C), 74.2% (320 °C), 79.6% (330 °C), and 84.3% (340 °C) over the mic-Ni/ZSM-5. However, when the HDO reaction was carried over the hie-Ni/ZSM-5 catalyst, higher conversions of 61.1%, 76.7%, 82.3%, and 97.9% were obtained at the corresponding temperatures.

These results imply that hie-Ni/ZSM-5 demonstrated superior catalytic performance compared to mic-Ni/ZSM-5. In addition to the higher acid sites concertation of the hie-Ni/ZSM-5 as can be seen from the NH_3-TPD analysis result in Table 4.4, the superior activity can be attributed to the differences in the porous structure of the catalysts. It's evident from the BET result in Section 4.3 that the hie-Ni/ZSM-5 has higher mesopore volume of 0.169 m^3 g^{-1} compared to the 0.109 m^3 g^{-1} seen in the mic-Ni/ZSM-5. In addition, the TEM results (section 4.5) revealed better nickel dispersion of 29% on hie-Ni/ZSM-5 against 20% recorded over the mic-Ni/ZSM-5. Hence, the mic-Ni/ZSM-5 is more likely to be mass transport limited than the hie-Ni/ZSM-5 catalyst. Also, a relatively higher activity than what was observed on the mic-Ni/ZSM-5 at all the examined temperatures was achieved over the mesoporous Ni/SiO_2 catalyst. HDO reaction over the mesoporous Ni/SiO_2 catalyst for the respective temperatures studied achieved benzoic acid conversions of 63.8% (310 °C), 78.5% (320 °C), 82.7% (330 °C), and 91.5% (340 °C).

As previously noted, the NH_3-TPD analysis result in Section 4.6 shows the Ni/SiO_2 catalyst has a lower concentration of acid sites (area of the NH_3 desorption peak is 898 a.u) compared to the mic-Ni/ZSM-5 catalyst (area of the NH_3 desorption peak is 4967 a.u). So, it is expected that the Ni/SiO_2 catalyst will show low activity compared to the mic-Ni/ZSM-5 catalyst. However, the former outperformed the latter at all temperatures studied. This might be linked to the mesoporous nature of the SiO_2 support, which will possibly allow the bulk aromatic carboxylic acid group to diffuse and access most of the available active site presence on the catalyst. In other words, the HDO reaction is more sensitive to the active metal dispersed on the carrier than the acidity of the catalyst support. This was noticed during the catalytic HDO of anisole over the mic-ZSM-5 and hie-ZSM-5 supports (without Ni nanoparticles dispersed) presented in Chapter 5. At 200 °C, 50 bar H_2, 100 mg of catalyst loading, and decalin as a solvent, an anisole conversion of around 2 to 4% was recorded in 140 minutes. However, there was no selectivity for liquid products (Appendix B). Similar result was obtained by Kim et al. (2022) when HDO of vanillin was carried out over HZSM-5 (Si/Al = 23) at the same pressure, temperature, and catalyst loading as that of anisole, with a mixture of water/n-octane as reaction solvent.

At a constant temperature of 330 ℃ (shown in Figure 6.1), there were changes in benzoic acid conversion as the hydrogen partial pressure increased during the HDO reaction. Conversion reached 79.7% (60 bar) from 61.0% (20 bar) over mic-Ni/ZSM-5 catalyst, 82.3% (60 bar) from 64.3% (20 bar) when hie-Ni/ZSM-5 catalyst was used, and 82.7% (60 bar) from 55.7% (20 bar) over Ni/SiO_2 catalyst, respectively. This increase could be related to an increase in the number of moles of hydrogen present in the reaction medium as hydrogen pressure increases (Appendix C), thus making it more readily available for reaction at the

catalyst surface. This is due to an increase in the solubility of hydrogen in tetralin (which is the solvent for the reaction) as the partial pressure of hydrogen in the reactor increased.

6.3 Effect of Temperature and Pressure on Product Distribution

It is obvious from Section 6.2 that reaction temperature and hydrogen pressure play a critical role in the conversion of benzoic acid via HDO. These variables are also expected to influence the distribution of products from the reaction. As a result, different products have been reported in the literature during selective deoxygenation and hydrogenation of benzoic acid (Chen, 2019; Hu et al., 2020; de Lange et al., 2002; Tang et al., 2017). Table 6.1 shows product distribution as a function of catalyst support and reaction temperature during the HDO reaction. It is clear from Table 6.1 that benzene and toluene were the two major products from the nickel-based ZSM-5 catalysts during the reaction. The formation of toluene is due to hydrodeoxygenation of the carboxylic functional group and hydrogenation, while benzene is the result of the cleavage of the methyl side chain from toluene (Chen, 2019; de Lange et al., 2002). As the selectivity of benzene kept increasing with an increase in the reaction temperature, a decreasing trend was noticed for toluene. This suggests that the increasing temperature favours the C-C bond cleavage, leading from toluene to benzene. For instance, when mic-Ni/ZSM-5 catalyst was used, the selectivity towards benzene increased from 18.7% at 310 ℃ to 24.3% at 320 °C, 29.3% at 330 °C, and 36.1% at 340 °C, respectively. On the other hand, the selectivity for toluene was 56.6%, which is the highest at 310 ℃ but decreases as the temperature increases to 47.6% (320 °C), 40.7% (330 °C), and 36.0% (340 °C), respectively.

A similar pattern was observed on the catalyst made of hie-Ni/ZSM-5 (Table 6.1). However, the selectivity towards benzene was 18.4% at 310 ℃, and increased to 42.1% at 340 ℃.

Table 6.1: Product distribution as a function of catalyst support and temperature during the HDO of benzoic acid over 5 wt.% nickel-based ZSM-5 and SiO_2 catalysts.

mic-Ni/ZSM-5	**Selectivity (%)**				**Total yield**
Temp. (°C)	**Benzaldehyde**	**Benzylalcohol**	**Toluene**	**Benzene**	**(%)**
310	16.2 ± 3.5	8.5 ± 4.0	56.6 ± 2.5	18.7 ± 5.0	54.0 ± 2.1
320	19.0 ± 2.4	9.1 ± 2.6	47.6 ± 2.1	24.3 ± 6.2	72.9 ± 3.5
330	21.9 ± 4.2	8.1 ± 3.5	40.7 ± 1.6	29.3 ± 2.1	78.6 ± 2.9
340	16.3 ± 6.2	11.6 ± 5.2	36.0 ± 3.4	36.1 ± 2.6	83.7 ± 5.8
hie-Ni/ZSM-5	**Selectivity (%)**				**Total yield**
Temp. (°C)	**Benzaldehyde**	**Benzylalcohol**	**Toluene**	**Benzene**	**(%)**
310	8.5 ± 3.4	23.6 ± 5.6	49.5 ± 3.8	18.4 ± 4.3	59.7 ± 5.6
320	13.6 ± 6.1	17.3 ± 7.2	42.6 ± 2.6	26.6 ± 1.7	73.9 ± 4.2
330	13.9 ± 3.7	16.1 ± 3.5	37.4 ± 3.4	32.6 ± 5.6	81.3 ± 2.3
340	12.8 ± 5.6	20.1 ± 4.8	25.0 ± 5.7	42.1 ± 3.8	94.7 ± 6.2
Ni/SiO_2	**Selectivity (%)**				**Total yield**
Temp. (°C)	**Benzaldehyde**	**Benzylalcohol**	**Toluene**	**Benzene**	**(%)**
310	15.7 ± 6.2	2.3 ± 6.4	82.1 ± 3.5	0.0 ± 0.0	63.5 ± 3.5
320	14.5 ± 5.4	7.6 ± 4.2	77.9 ± 2.6	0.0 ± 0.0	78.3 ± 4.1
330	20.3 ± 3.8	9.3 ± 3.5	70.4 ± 2.4	0.0 ± 0.0	82.5 ± 5.2
340	23.0 ± 5.8	11.0 ± 4.5	66.0 ± 1.7	0.0 ± 0.0	89.3 ± 1.3

Whereas, at 310 °C, a selectivity of 49.5% to toluene was obtained, which decreased to 25% when the reaction temperature was increased to 340 °C. Another key product of the HDO of benzoic acid identified is the benzaldehyde formed from deoxygenation of the functional group -COOH to -COH. The effect of catalyst porous structure on the selectivity towards benzaldehyde was evaluated by comparing the results obtained when mic-Ni/ZSM-5 and hie-

Ni/ZSM-5 catalysts were used. For the hie-Ni/ZSM-5 catalyst, the selectivity towards benzaldehyde at the respective temperatures was as follows: 8.5% (310 °C), 13.6% (320 °C), 13.9% (330 °C), and 12.8% (340 °C), and for the mic-Ni/ZSM-5 catalyst, 16.2% (310 °C), 19.0% (320 °C), 21.9% (330 °C), and 16.3% (340 °C), respectively. At all temperatures investigated, the selectivity towards benzaldehyde is higher with mic-Ni/ZSM-5 catalyst than hie-Ni/ZSM-5. Since higher benzoic acid conversion was recorded over hie-Ni/ZSM-5 compared to mic-Ni/ZSM-5, it can be concluded that there is a high rate of transformation to benzyl alcohol from benzaldehyde on hie-Ni/ZSM-5. This can be attributed to the strength of catalytic active sites (NH_3-TPD result in Table 4.4), extent of metal dispassion (TEM result in Section 4.5), and pore size distribution (the BET result in Table 4.2), indicating that microporous ZSM-5 favours benzaldehyde. In the literature, the production of benzaldehyde from benzoic acid studied over ZnO_2 and ZrO_2 catalysts generated benzyl alcohol, benzophenone, toluene, and benzene as by-products (Guo et al., 2021; Hu et al., 2020; Shinde and Deshpande, 2017). However, selective hydrogenation over the following catalysts: Pt/C, RuPd-C, Pd-C, Pt/TiO_2 and Ir-based catalyst showed cyclohexane carboxylic acid and benzyl alcohol as the two major products (Guo et al., 2021; Kong et al., 2022). Herein, both benzaldehyde, benzyl alcohol, toluene, benzene, and cyclohexane were observed during the HDO of benzoic acid over mic-Ni/ZSM-5, hie-Ni/ZSM-5, and Ni/SiO_2 catalysts at different reaction temperatures and pressures. But since the main objective of HDO is to maximise the removal of oxygenates, toluene, benzene, and cyclohexane are considered the most desired products.

Notably, over the course of the experiment, the total yield of liquid product steadily increased with increasing reaction temperatures. The yield was 54.0%, 72.9%, 78.6%, and 83.7% over the mic-Ni/zsm-5 catalyst, and 59.7%, 73.9%, 81.3%, and 94.7% over the hie-Ni/ZSM-5

catalyst, respectively, at 310 °C, 320 °C, 330 °C, and 340 °C. The proportionality relation observed between the reaction temperature and selectivity to benzene could be explained based on de Lange et al. (2002) that when there is high adsorption of benzoic acid onto the catalyst active surface, it decomposes at high temperature to produce benzene or benzophenone. Unlike the mic-Ni/ZSM-5 and hie-Ni/ZSM-5 catalysts, the Ni/SiO_2 catalyst shows zero selectivity towards benzene at all the reaction temperatures studied under 60 bar hydrogen partial pressure. The reason for this is that unlike ZSM-5 support, which has higher acid sites, SiO_2 support is nearly neutral based on the NH_3-TPD analysis result presented in Section 4.6 (Chapter 4). This explains why C-C bond cleavage (methyl group side chain cleavage) during the process of conversion of toluene to benzene could not take place with a Ni/SiO_2 catalyst. This also agrees with the observation reported in Chapter 5 during the HDO of anisole over the same catalysts. However, a high selectivity of 82.1% for toluene was recorded at 310 °C, which decreased to 66.0% at 340 °C. This can be ascribed to the HDO and hydrogenation of the -COOH functional groups that are induced by the Ni nanoparticles impregnated on the SiO_2 support. However, the first-degree HDO of benzoic acid over a Ni/SiO_2 catalyst yielded intermediate benzaldehyde, resulting in benzyl alcohol upon further hydrogenation. The selectivity towards the intermediates benzaldehyde and benzyl alcohol products increased from 15.7 and 2.3% to 23.0 and 11.0%, respectively, as the reaction temperature changed from 310 to 340 °C. Though the intermediates conversion to the desired product decreased as the selectivity to toluene (the only desired product on Ni/SiO_2 catalyst) decresed from 82.2% (310 °C), to 77.9% (320 °C), to 70.4% (330 °C), and to 66.0% (340 °C). Likewise, the total yield of liquid product increased from 63.5% at 310 °C to 78.3% at 320 °C, 82.5% at 330 °C, and 89.3% at 340 °C. Based on the products identified from the HDO of benzoic acid over mic-Ni/ZSM-5, hie-Ni/ZSM-5, and Ni/SiO_2 catalysts, the reaction pathways can be summarised using the scheme presented in Figure 6.2.

In brief, the reaction scheme can be explained as follows: at a high reaction temperature and hydrogen partial pressure, there will be a high concentration of oxygen vacancies, making a favourable condition for surface reaction. At this point, benzoic acid is deoxygenated to benzaldehyde and subsequently to benzyl alcohol via hydrogenation. The benzyl alcohol is further deoxygenated into toluene. The formation of benzene requires that the toluene produced from the benzyl alcohol undergo demethylation. This was only recorded over the highly acidic Ni/ZSM-5 catalyst, herein.

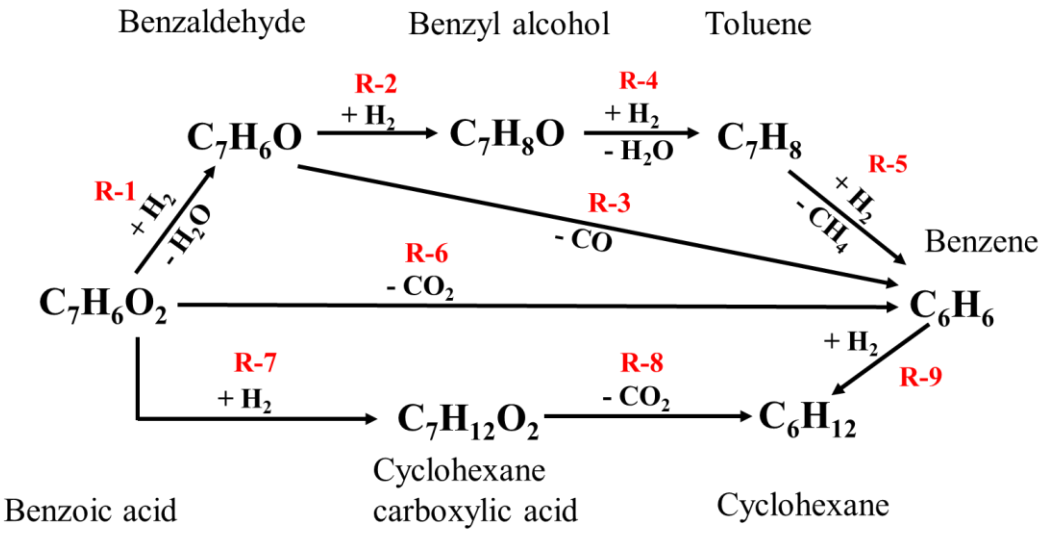

Figure 6.2: *Simplified reaction pathway for the benzoic acid transformation over mic-Ni/ZSM-5, hie-Ni/ZSM-5, and Ni/SiO_2 catalysts. (R-1; Deoxygenation, R-2; hydrogenation, R-3; decarboxylation, R-4; deoxygenation, R-5; demethylation, R-6; decarboxylation, R-7; hydrogenation, R-8; decarboxylation, R-9; hydrogenation).*

The possibilities of benzoic acid reacting directly through to toluene or benzene was reported in the literature (Chen, 2019; Tang et al., 2017). Although it is apparent that decarboxylation of benzoic acid is a much slower process than deoxygenation to benzaldehyde or toluene (de Lange et al., 2002). Decarboxylation of methyl-benzoate to benzene proceeds through a radical mechanism reaction, whereby a benzyloxy-radical is formed via a homolytic cleavage of the carboxylic acid (R-COO-Ni). Thereafter, the benzyloxy-radical rapidly decarboxylates

to a benzyl radical. Finally, the hydrogen atom reacts with the benzyl radical chain to terminate the reaction (Shinde and Deshpande, 2017). Another possible transformation route is the total hydrogenation of benzoic acid to cyclohexane carboxylic acid, which subsequently undergoes decarboxylation to generate cyclohexane (Chen, 2019; Kong et al., 2022; Xu et al., 2014).

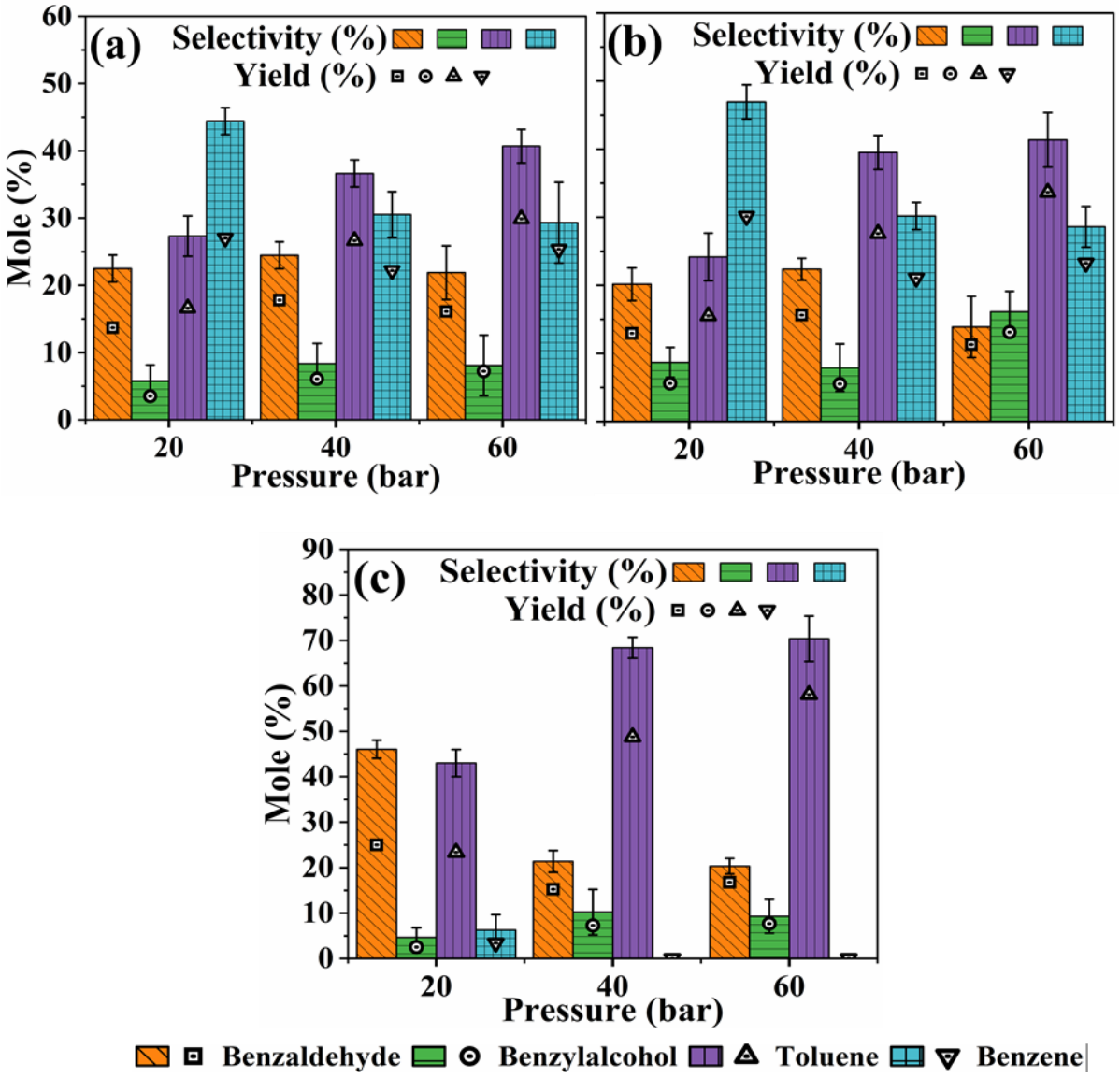

Figure 6.3: *Influence of H_2 pressure on product distribution during the HDO of benzoic acid over mic-Ni/ZSM-5 (a), hie-Ni/ZSM-5 (b), and Ni/SiO_2 (c). Catalyst loading; 100 mg, reaction temperature; 330 ℃, solvent; tetralin, benzoic acid initial concentration; 0.24 M, reaction time; 6 hours.*

Figure 6.3 shows the results of the impact of H_2 pressure on product distribution during the HDO of benzoic acid over mic-Ni/ZSM-5, hie-Ni/ZSM-5, and Ni/SiO_2 catalysts. With an increase in hydrogen pressure, both mic-Ni/ZSM-5 and hie-Ni/ZSM-5 catalysts show increased selectivity towards toluene but decreased selectivity towards benzene. The selectivity to toluene was 27.3% and 24.2% (20 bar), 36.6% and 39.5% (40 bar), and 40.7% and 41.4% (60 bar) over the m-Ni/ZSM-5 and hie-Ni/ZSM-5, respectively. More so, selectivity to benzene over these catalysts was 44.4% and 46.9% (20 bar), 30.5% and 30.2% (40 bar), and 29.3% and 28.6% (60 bar) respectively. Thus, HDO and hydrogenation reactions increase as more hydrogen molecules become available, leading to more toluene being produced as hydrogen pressure increases from 20 bar to 60 bar. Low hydrogen partial pressure was shown to favour benzene selectivity during the catalytic hydrogenation of benzoic acid to benzaldehyde (Shinde and Deshpande, 2017). Similarly, toluene selectivity increased from 43.0% to 68.4% to 70.4% over Ni/SiO_2 as hydrogen pressure increased from 20 to 40 to 60 bar. Except at a lower hydrogen pressure of 20 bar, where the liquid product was 6.3% selective to benzene, there is no benzene observed with the Ni/SiO_2 catalyst at 40 and 60 bar hydrogen partial pressure. This may be linked to the low acidity of the SiO_2 support, leading to a lack of C-C bond cleavage functionality at the acid sites. This observation implies that, as the hydrogen partial pressure increased, the concentration of oxygen vacancies also increased. This means that with more neighbouring oxygen vacancies available, benzaldehyde can be re-adsorbed on the catalyst's active sites for further transformation, leading to the generation of more toluene (Shinde and Deshpande, 2017). Hence, the selectivity of benzaldehyde decreased with an increase in hydrogen pressure, while that of benzyl alcohol increased (Figure 6.3c). However, the selectivity of both benzaldehyde and benzyl alcohol followed a similar trend for both mic-Ni/ZSM-5 and hie-Ni/ZSM-5 catalysts, except at the hydrogen pressure of 60 bar (Figure 6.3a, b). As recorded

with temperature, there was an increase in the yield of liquid products as the reaction pressure increased for all the catalysts studied.

6.4 Effect of Changing the Initial Benzoic Acid Concentration on Conversion and Product Distribution

A study was also conducted to examine how varying the initial concentration of benzoic acid affects the conversion and distribution of the product. The results of the study for the three catalysts prepared are presented in Figure 6.4.

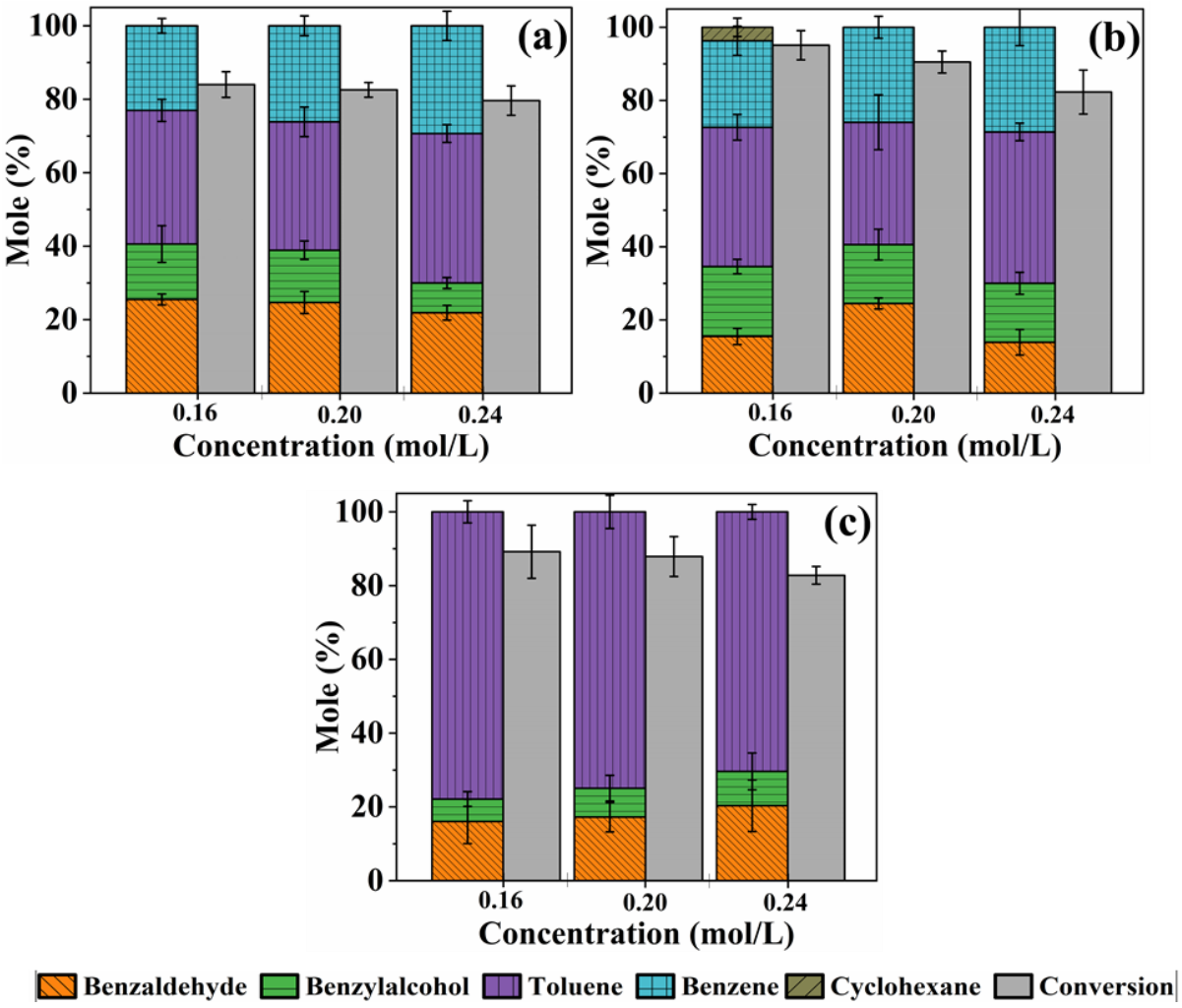

Figure 6.4: *Conversion and product distribution as a function of initial concentration during the HDO reaction of benzoic acid over mic-Ni/ZSM-5 (a), hie-Ni/ZSM-5 (b), and Ni/SiO_2 (c). Catalyst loading; 100 mg, reaction temperature; 330 ℃, solvent; tetralin, benzoic acid initial concentration; 0.16 – 0.24 M, reaction time; 6 hours.*

It can be observed that in all the three catalysts, the benzoic acid conversion decreases as its initial concentration increases from 0.16 M to 0.24 M. This observed trend could be explained by increasing competition between the reactants to occupy a limited number of active sites on the catalyst as initial concentrations rise (Aliu et al., 2019). As the ratio of the concentration of the catalyst active sites to benzoic acid in the reaction mixture decreases, conversion also decreases. Hence, a decrease in benzoic acid conversion from 84.0 to 82.6 to 79.6% on mic-Ni/ZSM-5, 95.0, 90.5 to 82.3% on hie-Ni/ZSM-5, and 89.2, 87.9, to 82.8% over Ni/SiO_2 was observed as the initial concentration increased from 0.16 to 0.20 to 0.24 M, respectively.

The amount of benzene produced from the HDO of benzoic acid increased slightly, from 23.0% (0.16 M), 26.2% (0.20 M), to 29.3% (0.24 M) for mic-Ni/ZSM-5 and from 23.7% (0.16 M), 26.0% (0.20 M), to 28.6% (0.24 M) for hie-Ni/ZSM-5 catalysts. In contrast, for both mic-Ni/ZSM-5 and hie-Ni/ZSM-5 catalysts, toluene selectivity decreased slightly at 0.2 M (34.9 and 33.4%) compared to 0.16 M (36.4 and 38.1%) and increased at 0.24M (40.7 and 41.3%) initial concentrations of benzoic acid. When the Ni/SiO_2 catalyst was used, the amount of toluene produced decreased as the initial concentration of benzoic acid increased, while both benzaldehyde and benzyl alcohol increased slightly (Figure 6.4c). Notably, about 3.7% cyclohexane was formed when the hie-Ni/ZSM-5 catalyst was used on a 0.16 M benzoic acid initial concentration (Figure 6.4b). For the same concentration (0.16 M), cyclohexane was seen at reaction temperatures of 320, 330, and 340 ℃ respectively, over the hie-Ni/ZSM-5 catalyst (Appendix D). The formation of cyclohexane was possible via hydrogenation of benzoic acid to cyclohexane carboxylic acid, which decarboxylates to cyclohexane (Chen, 2019; Shinde and Deshpande, 2017). However, as the cyclohexane carboxylic acid was not detected at any point during the reaction while the samples were

being withdrawn from the reactor for analysis, and that decarboxylation is a much slower process than deoxygenation (de Lange et al., 2002), cyclohexane may possibly emerge from the hydrogenation of benzene.

6.5 Degree of Hydrodeoxygenation (X_{HDO}) and Hydrodearomatisation (X_{HDA}) of Benzoic Acid During the Reaction

In bio-oil upgrading, minimising the amount of oxygenate is one of the primary objectives. The overall aim is to increase heating value, stability, and miscibility with conventional fuels and decrease viscosity and corrosiveness. This is achieved through deoxygenation and hydrogenation reactions (Gutiérrez-Rubio et al., 2019; Hansen et al., 2020). Therefore, the degree of benzoic acid hydrodeoxygenation and hydrodearomatization over the mic-Ni/ZSM-5, hie-Ni/ZSM-5 and Ni/SiO_2 catalysts was studied. Figure 6.5 presents the results.

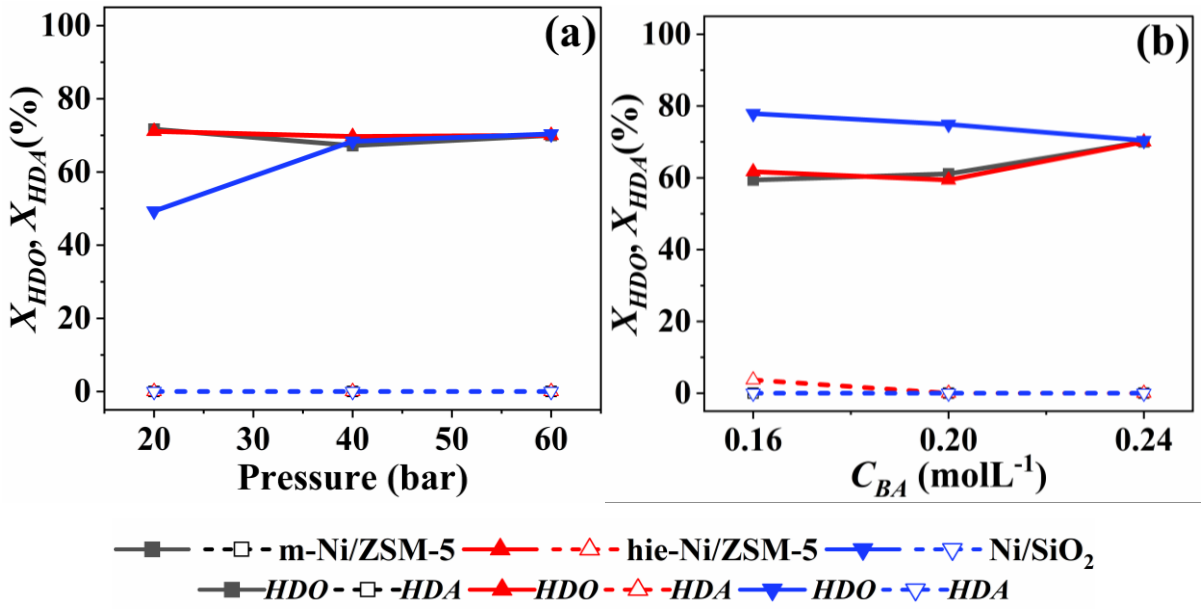

Figure 6.5: *Degree of hydrodeoxygenation (X_{HDO}) and hydrodearomatisation (X_{HDA}) of the benzoic acid over mic-Ni/ZSM-5, hie-Ni/ZSM-5, and SiO_2; (a) at 330 ℃, 0.24 M benzoic acid, and H_2 pressure of 20 – 60 bar (b) at 330 ℃, H_2 pressure of 60 bar, 0.16 – 0.24 M benzoic acid. Reaction time; 6 hours.*

The degree of hydrodeoxygenation (X_{HDO}), which is the selectivity for products with no oxygen, achieved on all the catalysts was about 70%. X_{HDO} did not change significantly as the hydrogen partial pressure increased for both mic-Ni/ZSM-5 and hie-Ni/ZSM-5 (Figure 6.5a). However, with an increase in hydrogen pressure, the degree of hydrodeoxygenation (X_{HDO}) over the Ni/SiO_2 catalyst increased from 49.3% to 68.4% and 70.4%, respectively. Figure 6.5b shows the effect of changing the benzoic acid concentration on the degree of hydrodeoxygenation and hydrodearomatisation. There was an increase from 59.5% to 61.1% and to 70.0% on the mic-Ni/ZSM-5 as the initial benzoic acid concentration increased. However, the X_{HDO} decreased from 61.7% (0.16 M) to 59.4% (0.20 M) and thereafter increased to 70.0% (0.24 M) over the hie-Ni/ZMS-5. Notably, a 3.7% X_{HDA} was recorded from the hie-Ni/ZSM-5 catalyst at a 0.16 M benzoic acid initial concentration. In contrast, the Ni/SiO_2 catalyst revealed a decreasing trend of X_{HDO} with increasing benzoic acid concentration. However, the highest value of X_{HDO} (77.9%) was seen from Ni/SiO_2.

6.6 Kinetic Study

This section reports the kinetics of benzoic acid hydrodeoxygenation over hie-Ni/ZSM-5 catalyst. The study was performed to evaluate the influence of some reaction variables and estimate some vital kinetic parameters such as activation energy, rate constants, reaction order, enthalpy, heat of adsorption, and entropy. These parameters can only be calculated accurately if mass transport limitations are removed. It is obvious that reactor configuration and the catalyst's nature can affect mass transfer during a reaction even at constant temperature and pressure. The elimination of internal and external mass transfer limitations is therefore essential, and a reaction must be controlled kinetically in order for experimental data to be useful in the development of a kinetic model. To achieve this, perfect mixing is

necessary to maintain uniform temperatures and concentrations throughout the reactor (i.e., negligible external transport limitations) (Fogler, 2004).

6.7 Determination of the Kinetic Control Regime

6.7.1 External mass transfer

In heterogeneous catalysis involving solid-liquid-gas phases present, it is imperative to maintain the solid catalyst in suspension for effective contact and subsequent reactions. This is achieved in agitated reactors by rotating impellers. Thus, a critical impeller speed, *Njs*, at which no particles are stationary at the bottom of the vessel for more than a second or two, as defined by Zwietering (1958), was determined using equation (6.1). According to the Zwietering empirical correlation, herein, only 19, 20, or 21 rpm are needed to retain the hie-Ni/ZSM-5 catalyst with particle sizes of 75 – 90 µm, 90 – 120 µm, or 120 – 140 µm in suspension during the benzoic acid HDO experiments. The minimum stirring speed observed in this work is far lower than what was reported by Lawal et al. (2019), for the hydrogenation of acetic acid over a 4% Pt/TiO_2 catalyst. The lower values of *Njs* obtained in this study may be associated with the nature of the 5% hie-Ni/ZSM-5 catalyst and the properties of solvent (e.g., density and viscosity) used as the reaction medium. Although this is true, it does not completely eliminate the possibility that external mass transfer limitations may exist within the reaction mixture. Arora et al. (2019) highlighted a limited transfer of hydrogen across the gas–liquid boundary and perhaps to the catalyst surface during the HDO of stearic acid at a lower stirring speed of 500 rpm. This stirring speed was higher than the minimum stirring speed needed for the system. Additionally, the product yield was comparable to that observed at low hydrogen pressure, suggesting a restricted supply of hydrogen at the catalyst surface and a low rate of product turnover. Therefore, the impact of various stirring speeds on reaction rates was examined;

$$N_{js} = S_Z \left(\frac{g(\rho_{cat}-\rho_s)}{\rho_s}\right)^{0.45} \frac{X_w{}^{0.13} d_p^{0.2} v^{0.1}}{D_{imp}{}^{0.85}} \qquad 6.1$$

where N_{js} is the just suspended speed (rpm), S_Z represents the Zwietering correlation parameter, v is the kinematic viscosity of the solvent ($m^2\ s^{-1}$), d_p represents the particle size (m), g is the gravitational constant (9.81 m s^{-2}), ρ_{cat} and ρ_s is the densities of the catalyst and the solvent, respectively (kg m^{-3}), X_w is the weight percent of the solid (solid loading, g g^{-1} ×100), and D_{imp} is the impeller diameter (m).

The Zwietering correlation parameter S_Z, which is a function of reactor geometry, was estimated using a relationship for a straight blade impeller reported by Devarajulu and Loganathan, (2016);

$$S_Z = 13.98 \left(\frac{C_c}{Td}\right)^{0.639} \left(\frac{H}{Td}\right)^{-0.055} \qquad 6.2$$

where C_c is the impeller clearance, Td is the reactor diameter, and H is the liquid level in the reactor.

The catalytic HDO of benzoic acid occurs in three phases. The gas phase is hydrogen, the liquid phase is benzoic acid dissolved in tetralin solvent, and the solid phase is the catalyst. A range of stirring speeds from 400 rpm to 1000 rpm was investigated experimentally to examine how stirring speed affects benzoic acid conversion and initial rate during the HDO reaction. By fitting a polynomial to the concentration-time data, the initial reaction rate was determined using the differentiation method described in the literature (Fogler, 2019; Lawal et al., 2019). The experimental results are presented in Figure 6.6. Both the initial rate of

reaction and benzoic acid conversion increase as the impeller stirring rate increases from 400 rpm to 800 rpm. Conversion was 54.3%, 77.1% 96.4% and 95.2% at 400, 600, 800, and 1000 rpm respectively. Similarly, the initial rate of benzoic acid HDO reaction plateaued at 800 rpm (1.44×10^{-3} mol L^{-1} min^{-1}).

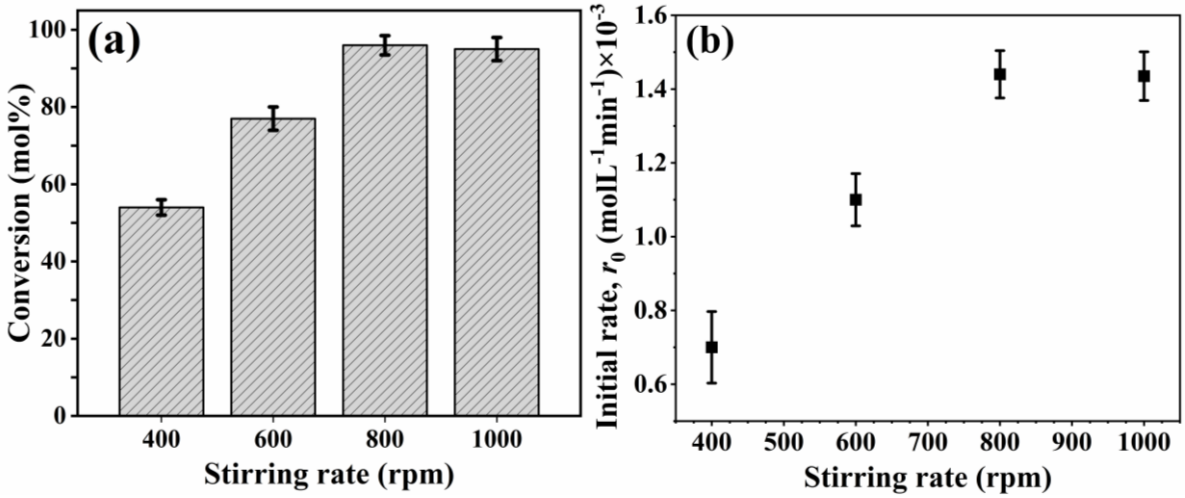

Figure 6.6: *Effect of varying stirring rate on conversion 'a', and initial rate of benzoic acid disappearance 'b': Reaction temperature; 340 °C, pressure; 60 bar H_2, benzoic acid initial concentration; 0.24 M, catalyst loading; 100 mg, reaction time 6 hours.*

Notably, the initial reaction rate and conversion were unaffected by the further increase in impeller speed from 800 rpm to 1200 rpm. As a result, impeller speeds of 800 rpm and above seem to eliminate external transport limitations during HDO of benzoic acid, which is a three-phase reaction of gas-liquid-solid phases. Accordingly, the subsequent results reported in this chapter are based on experiments performed at an impeller speed of 800 rpm.

6.7.2 Internal mass transfer

In a catalytic reaction process, one of the major factors that determines the extent of the transformation a reactant undergoes is its ability to reach the catalytically active sites. Among the problems caused by internal transport limitations is pore diffusion, which can

severely slow down the reaction rate (Fogler, 2006; Hill, 2014). Herein, the reaction rate is greatly influenced by the pace at which hydrogen and benzoic acid diffuse through the porous network of a 5% hie-Ni/ZSM-5 catalyst. Thus, it is critical to eliminate intraparticle diffusion resistance in order to ensure the HDO of benzoic acid is happening in a kinetically controlled regime. Hence, the effect of catalyst particle size on the rate of benzoic acid disappearance was examined. It is believed that as the particle size decreases, the diffuse path length to the active sites within the catalyst decreases, thereby reducing intraparticle diffusion.

To eliminate internal mass transport limitations, the catalyst powder was sieved into the following particle size distributions: 75 µm < d_p < 90 µm, 90 < d_p < 120 µm, and 120 µm < d_p < 140 µm, respectively. The results of the effect of particle size distribution on benzoic acid conversion and initial reaction rates are shown in Figure 6.7.

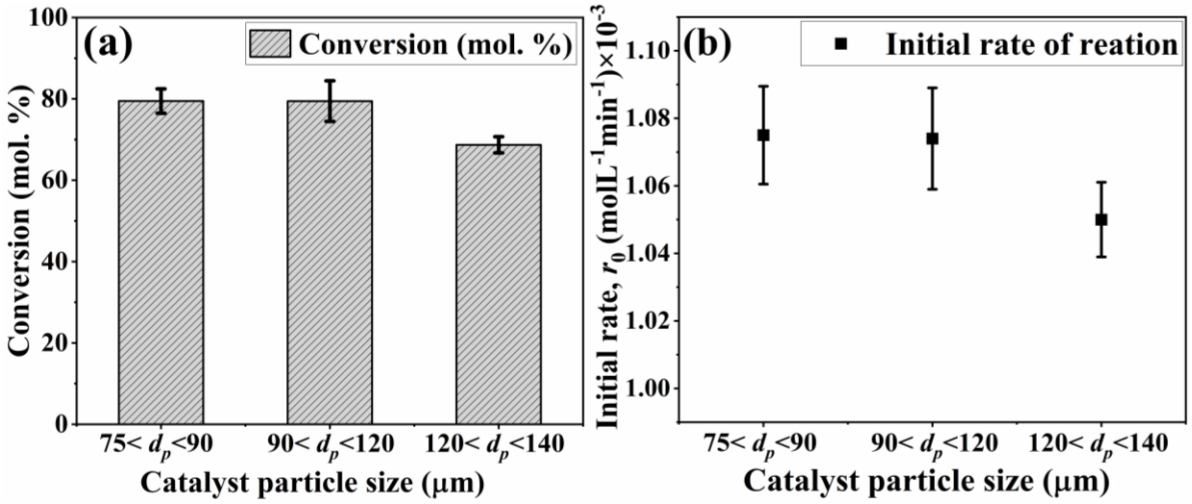

Figure 6.7: *Determination of intraparticle diffusion resistance based on the catalyst particle size. Reaction temperature, 330 ℃; pressure, 60 bar H_2; initial benzoic acid concentration, 0.24 M; stirring rate, 800 rpm; catalyst loading, 100 mg; reaction time, 6 hours.*

Benzoic acid conversion was 79.5%, 79.4% and 68.7% while the initial reaction rate was 1.075 × 10^{-3}, 1.074 × 10^{-3}, and 1.051 × 10^{-3} molL^{-1}min^{-1} respectively, for 75 µm < d_p < 90

μm, 90 < d_p < 120 μm, and 120 μm < d_p < 140 μm particle sizes. It is obvious that both the conversion and initial reaction rate are similar for 5% hie-Ni/ZSM-5 catalyst particle size 75 μm < d_p < 90 μm and 90 < d_p < 120 μm but slightly decreased for particle size 120 μm < d_p < 140 μm. While particle size may influence the initial reaction rate and conversion, it appears to be less sensitive to the changes from 75 to 90 μm and 90 to 120 μm. This result shows that catalyst particles with a diameter of less than or equal to 120 μm eliminate intraparticle diffusion limitations or internal mass transport restrictions.

To further confirm the absence of intraparticle diffusion, a criterion suggested by Weisz and Prater (1954) was deployed. This states that if the value of the observable modulus ($\eta\varphi^2$), as shown in equation (6.3), a dimensionless quantity, is less than 0.3 for a reaction order of less than or equal to 2, the effect of internal diffusion is eliminated. Then the experimental data are appropriate for kinetic model development;

$$\eta\varphi^2 = \frac{r_0 \omega L^2}{C_i D_{ei}} \qquad 6.3$$

where i represent H_2 or benzoic acid (BA), D_e is the effective diffusivity, η is the effectiveness factor, φ is the Thiele modulus, r_0 is the initial rate of reaction, ω is the catalyst loading, L is a characteristic length of a catalyst particle, and C_i is the concentration of reactant i. The characteristic length was determined from the relationship presented in equation (6.4), where D_{cat} is the catalyst particle diameter;

$$L = \frac{D_{cat}}{6} \qquad 6.4$$

Fogg and Gerrard correlations shown in equations (6.5) and (6.6) were employed to determine the value of hydrogen concentration in mg L^{-1} (Pintar et al., 1998; Srivastava, 2018; Wilke and Chang, 1955);

$$C_{H_2} = y_{H_2} \times \frac{P_{total}}{P_{total=1bar}} \times \frac{x_{H_2}}{1-x_{H_2}} \times \rho_s \frac{M_{H_2}}{M_s} \times 1000 \qquad 6.5$$

$$x_{H_2} = \exp\left(-125.939 + \frac{5528.45}{T} + 16.8893 \times ln(T)\right) \qquad 6.6$$

where C_{H2} is the concentration of hydrogen, y_{H_2} is the mole fraction of hydrogen in the gas phase, x_{H_2} is the mole fraction of hydrogen in the liquid phase, ρ_s is the density of solvent in g L^{-1}, M_{H_2} is the molar mass of hydrogen in g mol^{-1}, M_s is the molar mass of solvent in g mol^{-1}, and T is the reaction temperature in Kelvin.

Table 6.2: List of parameters used to confirm the absence of intraparticle diffusion.

Temperature (°C)	**310**	**320**	**330**	**340**
C_{H_2} (mM)	49	54	60	66
$r_0 \times 10^{-6}$ (kmol kg^{-1}_{cat} s^{-1})	5.77	7.03	8.92	12.00
$D_{e\,H_2} \times 10^{-7}$ (m^2 s^{-1})	1.72	1.85	1.98	2.12
$D_{e\,BA} \times 10^{-8}$ (m^2 s^{-1})	8.13	8.75	9.39	10.06
$\eta\varphi^2{}_{H_2} \times 10^{-7}$	3.60	3.71	3.98	4.54
$\eta\varphi^2{}_{BA} \times 10^{-7}$	1.56	1.77	2.09	2.63
Constants	ω = 2 (kg m^{-3}), $C_{BA} = 240$ mM, L = 1.625×10^{-5} m			

The mole fraction of hydrogen in the liquid phase was obtained from solubility data for the tetralin-hydrogen system available in solubility data series volume 5/6 (International Union of Pure and Applied Chemistry). Table 6.2 displays the Weisz-Prater values for both hydrogen and benzoic acid reactants at the different reaction temperatures investigated. The results show that the value of Weisz-Prater is significantly lower than 0.3, which agrees with the results presented in Figure 6.6, implying that at 800 rpm and catalyst particles with a diameter of less than or equal to 120 µm both external and internal mass transport limitations are eliminated.

6.8 Concentration-Time Plots

Figure 6.8 shows concentration-time plots for different initial concentration of benzoic acid.

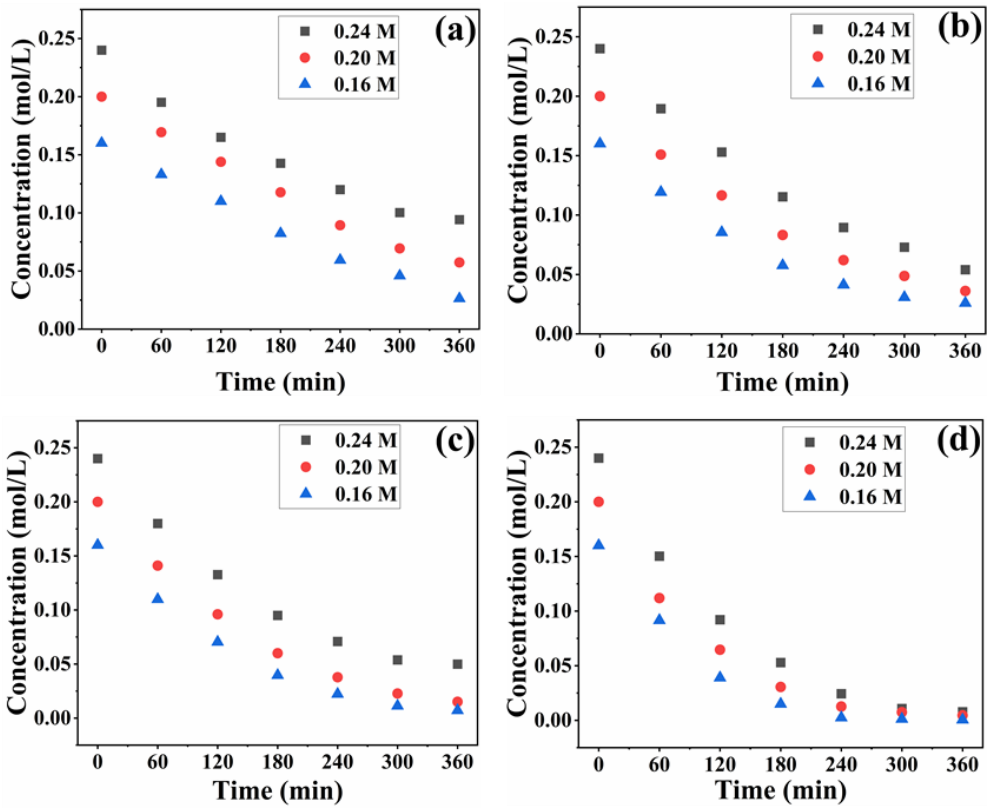

Figure 6.8: *Concentration versus time profile for the benzoic acid hydrodeoxygenation, initial concentration of benzoic acid, 0.16 – 0.24 M; catalyst loading, 100 mg hie-Ni/ZSM-5; stirring rate, 800 rpm; reaction pressure, 60 bar H_2; solvent, tetralin; reaction temperature, (a) 310 ℃, (b) 320 ℃, (c) 330 ℃, and (d) 340 ℃.*

The experiment was carried out with 0.16 M, 0.20 M, and 0.24 M benzoic acid at temperatures in the range of 310 ℃ to 340 ℃ using 100 mg of 5 wt.% nickel-based hie-Ni/ZSM-5 catalyst (particle size ≤ 120 μm) and an impeller speed of 800 rpm. For each experimental data set, the concentration-time data was fitted with second-order polynomial equations, which were further differentiated to obtain the initial reaction rate (r_0). The obtained initial reaction rates (r_0) were used in the development of reaction rate, order of reaction, and activation energy. Additionally, kinetic models based on the Langmuir-Hinshelwood expressions were devised and fitted the experimental data in order to allow a more precise and thorough assessment of the kinetic parameters.

6.9 The Effect of Initial Concentration and Hydrogen Pressure on Initial Reaction Rate (r_0)

It has been shown previously in Sections 6.3 and 6.4 that temperature, pressure, and the initial concentration of benzoic acid influence conversion and product distribution. Changes in these process parameters can, therefore, have a considerable impact on the initial rate of reaction. Figure 6.9 shows the effect of changes in initial benzoic acid concentration and hydrogen pressure on the initial reaction rate (r_0).

The initial reaction rate increased at both 320 °C and 330 °C with increasing initial benzoic acid concentrations (Figure 6.8a). At 320 ℃ the rates were 7.51×10^{-3} (0.16 M), 8.27×10^{-3} (0.20 M), and 8.93×10^{-3} mol L^{-1} min^{-1} (0.24 M). While 8.97×10^{-3} (0.16 M), 1.06×10^{-3} (0.20 M), and 1.07×10^{-3} mol L^{-1} min^{-1} (0.24 M) were recorded, respectively, at 330 ℃. It can be seen from these results that, at a fixed initial concentration, the initial reaction rate increased with increasing reaction temperature. In a nutshell, the rate of the benzoic acid HDO reaction increased as the temperature and concentration increase.

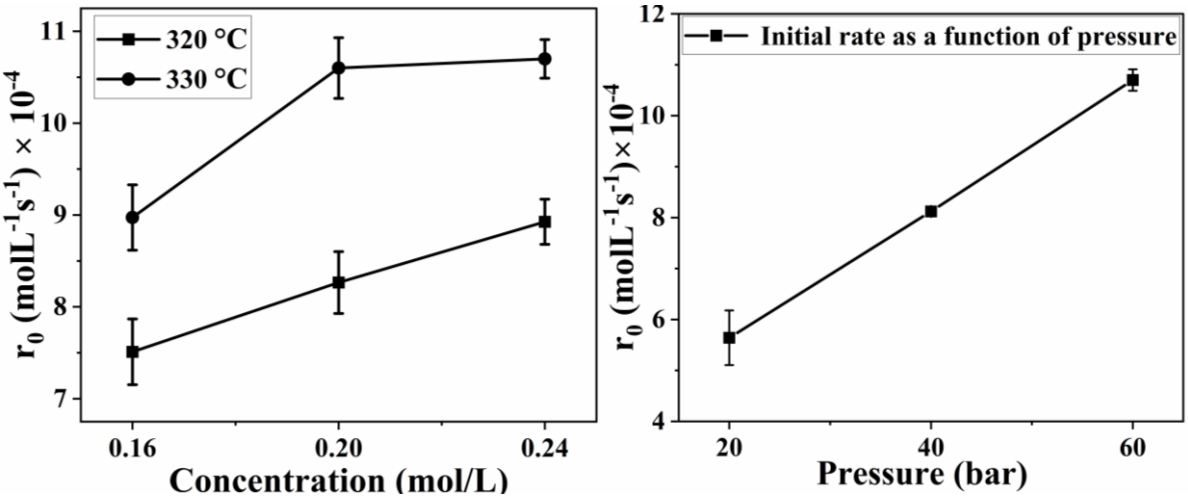

Figure 6.9: *Effect of changing benzoic acid initial concertation at 60 bar H_2 (a) and changing the hydrogen pressure at 330 ℃ (b) on the initial rate of benzoic acid disappearance. Catalyst loading, 100 mg hie-Ni/ZSM-5; stirring rate, 800 rpm; solvent, tetralin.*

Consequently, the initial reaction rate (r_0) at 330 °C increased with increasing hydrogen pressure from 5.64 × 10^{-4} mol L^{-1} min^{-1} (20 bar), 8.12 × 10^{-4} mol L^{-1} min^{-1} (40 bar), and 1.07 × 10^{-3} mol L^{-1} min^{-1} (60 bar), as shown in Figure 6.8b. As hydrogen pressure increases, hydrogen dissolves more readily in the tetralin solvent used, increasing the amount of hydrogen available for HDO of benzoic acid. Thus, the initial reaction rate (r_0) increases as more hydrogen reactant becomes available.

6.10 Power Law Rate Equation

Benzoic acid HDO is a three-phase reaction that involves hydrogen (gas), benzoic acid dissolved in tetralin (liquid), and a heterogeneous catalyst, 5% hie-Ni/ZSM-5 (solid). It is necessary for hydrogen to diffuse from the gas phase into the bulk liquid phase via the gas-liquid boundary layer and then to the surface of the catalyst in order for a chemical reaction to occur. Benzoic acid must also be transferred from the liquid phase to the catalyst surface before the HDO reaction can take place. These mass transport limitations have been

eliminated at an impeller speed of 800 rpm and a catalyst particle size less than or equal to 120 µm used for all the experiments. The general power law rate equation is given by equation 6.7. The rate of disappearance of benzoic acid can be described by a linear expression of the power law shown in equation 6.8. The order of reaction (n) and rate constant (k) values are determined from a log-log plot of the initial reaction rate (r_0) against the corresponding initial benzoic acid concentration based on equation 6.8.

$$r = kC_{BA}^{n} \qquad 6.7$$

$$\ln r_0 = \ln k + n \ln C_{BA} \qquad 6.8$$

The *ln – ln* plot of r_0 versus initial benzoic acid concentration at the different investigated reaction temperatures are shown in Figure 6.10. Values for ln(k) at the reaction temperatures of 310, 320, 330, and 340 ℃ were recorded from the intercepts of this plot as -11.08, -10.76, -10.34, and -9.85, respectively. In addition, from the slopes of the plot, the reaction order was found to be 0.21 at 310 ℃, 0.29 at 320 ℃, 0.42 at 330 ℃, and 0.55 at 340 ℃. The order of reaction is less than 1, and it changes significantly as the reaction temperature increases.

As part of the study to mathematically describe the reaction rate constant's dependence on temperature, activation energy was estimated from data obtained at temperatures between 310 °C and 340 °C at 0.24 M of benzoic acid. The Arrhenius equation (equation 6.9) connects reaction rate constants and temperature. Based on experimental data, the Arrhenius plot developed for rate constants estimated at different temperatures from Figure 6.10 is presented in Figure 6.11.

$$ln\, k = \frac{-E_A}{R}\left(\frac{1}{T}\right) + \ln A \qquad 6.9$$

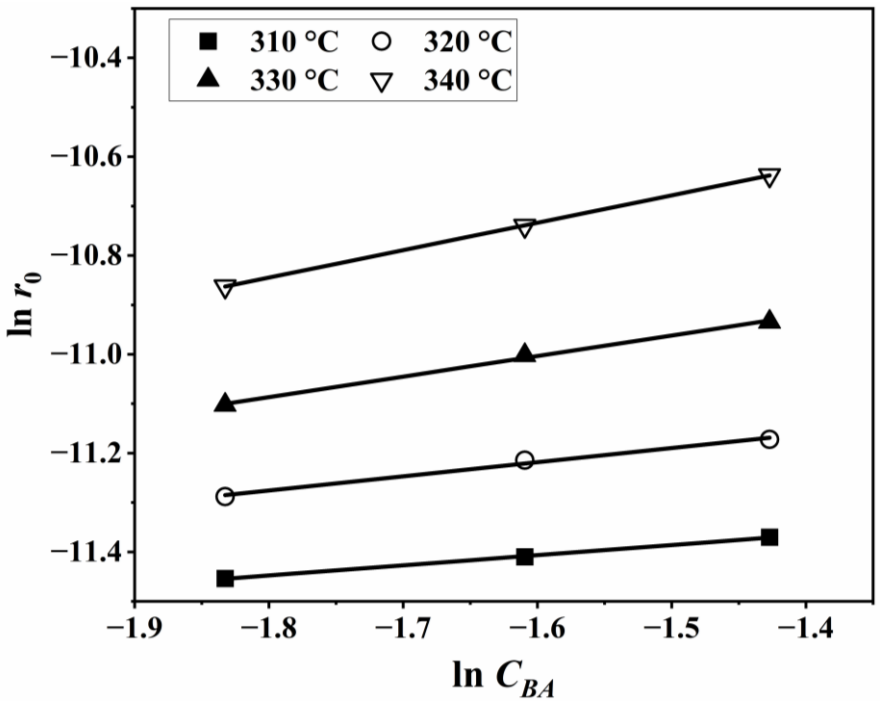

Figure 6.10: *Plot of natural-log of initial rate (ln r_0) against the natural-log of initial concentration (ln C_{BA}), temperature; 310 ℃, 320 ℃, 330 ℃, and 340 ℃, pressure; 60 bar H_2, catalyst loading; 100 mg hie-Ni/ZSM-5, stirring rate; 800 rpm, solvent; tetralin.*

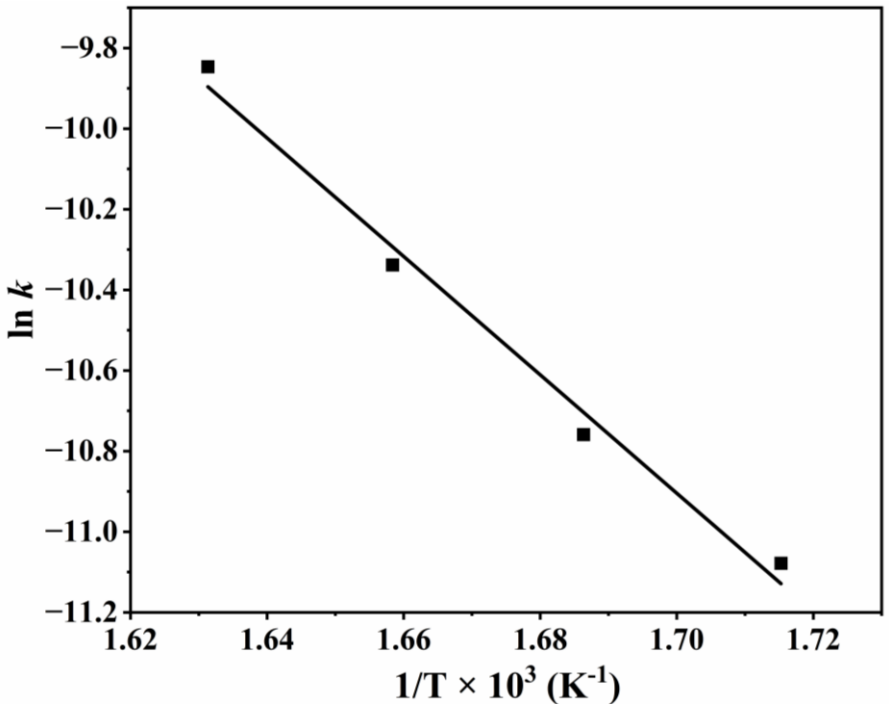

Figure 6.11: *Arrhenius plot for the estimation of the activation energy of benzoic acid hydrodeoxygenation over the hie-Ni/ZSM-5 catalyst (Catalyst loading, 100 mg; hydrogen pressure, 60 bar; solvent, tetralin; temperature, 310 – 340 ℃; benzoic acid concentration, 0.16–0.24 M).*

From the Arrhenius plot, the calculated activation energy is 122.1 kJ mol^{-1} and a frequency factor of 1.3×10^6 s^{-1} was obtained. Shinde and Deshpande (2022) reported an activation energy of 81.6 kJ mol^{-1} for the chemoselective hydrogenation of benzoic acid to benzyl alcohol over a bimetallic Ru-Sn/Al_2O_3 catalyst. Though the value recorded herein is higher, perhaps the different nature of the catalysts and the additional reaction steps (decarboxylation and demethylation) may account for the increase in the activation energy observed.

6.11 Langmuir–Hinshelwood Type Kinetic Model

This study evaluated Langmuir–Hinshelwood–Hougen–Watson (LHHW) kinetic type models to determine their suitability for describing the reaction of benzoic acid over the hie-Ni/ZSM-5 catalyst. It is generally believed that hydrogen is adsorbed either dissociatively or non-dissociatively onto the catalyst surface in three-phase gas-liquid-solid catalytic reaction modeling via the LHHW method. Specifically, mechanistic steps were used to develop the kinetic models using the initial rates of benzoic acid HDO, involving the various elementary steps for the chemisorption of benzoic acid and hydrogen reactants. Four different model expressions with different assumptions were derived to determine the best fit for the experimental data, as follows:

Single site adsorption of dissociatively chemisorbed H_2;

$$BA + S \underset{k_{-1}}{\overset{k_1}{\rightleftharpoons}} BA{\cdot}S \qquad 6.10$$

$$H_2 + S \underset{k_{-2}}{\overset{k_2}{\rightleftharpoons}} 2H{\cdot}S \qquad 6.11$$

$$BA{\cdot}S + 2H{\cdot}S \xrightarrow{k_s} \text{Products} \qquad 6.12$$

Dual site adsorption of dissociatively chemisorbed H_2;

$$BA + S_1 \underset{k_{-1}}{\overset{k_1}{\rightleftharpoons}} BA{\cdot}S_1 \qquad 6.13$$

$$H_2 + S_2 \underset{k_{-2}}{\overset{k_2}{\rightleftharpoons}} 2H{\cdot}S_2 \qquad 6.14$$

$$BA{\cdot}S_1 + 2H{\cdot}S_2 \xrightarrow{k_s} \text{Products} \qquad 6.15$$

Single site adsorption of non-dissociatively chemisorbed H_2;

$$BA + S \underset{k_{-1}}{\overset{k_1}{\rightleftharpoons}} BA{\cdot}S \qquad 6.10$$

$$H_2 + S \underset{k_{-2}}{\overset{k_2}{\rightleftharpoons}} H_2{\cdot}S \qquad 6.16$$

$$BA{\cdot}S + H_2{\cdot}S \xrightarrow{k_s} \text{Products} \qquad 6.17$$

Dual site adsorption of non-dissociatively chemisorbed H_2;

$$BA + S_1 \underset{k_{-1}}{\overset{k_1}{\rightleftharpoons}} BA{\cdot}S_1 \qquad 6.13$$

$$H_2 + S_2 \underset{k_{-2}}{\overset{k_2}{\rightleftharpoons}} H_2{\cdot}S_2 \qquad 6.18$$

$$BA{\cdot}S_1 + H_2{\cdot}S_2 \xrightarrow{k_s} \text{Products} \qquad 6.19$$

For all the proposed models, the surface reaction step (equations 6.12, 6.15, 6.17, and 6.19) was assumed to be the rate-limiting step. This is because more than 75% of all heterogeneous reactions that are not diffusion-limited are surface reaction-limited (Fogler, 2006). The HDO of acetic acid over a supported platinum catalyst was modeled based on the LHHW kinetics (Lawal et al., 2019). A model assuming dual-site adsorption of dissociative H_2 and acetic acid, with surface reaction step as the rate-determining, fitted the experimental data. Similarly, the LHHW kinetic model was successfully employed to investigate the HDO of m-cresol over Pt/SiO_2 catalyst. Surface reaction was assumed the rate-determining step

(Nie and Resasco, 2014). In addition, the deoxygenation step has been identified as the rate-determining step in the HDO of oxygen-containing components such as phenolics (Yu et al., 2021).

Table 6.3 shows the different LHHW-type kinetic models developed to describe the overall rate expression of benzoic acid consumption during the reaction and the corresponding mechanism involved. To identify the best LHHW kinetic model that describes the HDO of benzoic acid, the different developed models were linearised (equations 6.20 to 6.23). Models I to VI were fitted to experimental data using the linearised format of rate equations in Table 6.3. A linearised method is used to check if a model, accurately, predicts the behaviour of the experimental data (Fogler, 2006). When the coefficient of determination (R^2) is greater than or equal to 0.99, the experimental data is well fitted by the kinetic model.

Table 6.3: Proposed kinetic models for benzoic acid hydrodeoxygenation over 5% nickel hie-Ni/ZSM-5 catalyst.

Model	Mechanism	Rate expression
I	Single site adsorption of dissociatively adsorbed H_2	$r = \frac{k_s K_{BA} C_{BA} K_{H_2} C_{H_2}}{(1 + K_{BA} C_{BA} + \sqrt{K_{H_2} C_{H_2}})^3}$
II	Dual sites adsorption of dissociatively adsorbed H_2	$r = \frac{k_s K_{BA} C_{BA} K_{H_2} C_{H_2}}{(1 + \sqrt{K_{H_2} C_{H_2}})^2 (1 + K_{BA} C_{BA})}$
III	Single site adsorption of non-dissociatively adsorbed H_2	$r = \frac{k_s K_{BA} C_{BA} K_{H_2} C_{H_2}}{(1 + K_{BA} C_{BA} + K_{H_2} C_{H_2})^2}$
IV	Dual sites adsorption of non-dissociatively adsorbed H_2	$r = \frac{k_s K_{BA} C_{BA} K_{H_2} C_{H_2}}{(1 + K_{BA} C_{BA})(1 + K_{H_2} C_{H_2})}$

$$\left(\frac{C_{BA}}{r}\right)^{\frac{1}{3}} = m_I C_{BA} + b_I \qquad 6.20$$

$$\frac{C_{BA}}{r} = m_{II} C_{BA} + b_{II} \qquad 6.21$$

$$\left(\frac{C_{BA}}{r}\right)^{\frac{1}{2}} = m_{III} C_{BA} + b_{III} \qquad 6.22$$

$$\frac{C_{BA}}{r} = m_{IV} C_{BA} + b_{IV} \qquad 6.23$$

where

$$m_I = \frac{K_{BA}}{(k_s K_{H2} K_{BA} C_{H2})^{1/3}} \qquad b_I = \frac{1+(K_{H2} C_{H2})^{1/2}}{(k_s K_{BA} K_{H2} C_{H2})^{1/3}}$$

$$m_{II} = \frac{(1+\sqrt{K_{H2} C_{H2}})^2}{k_s K_{H2} C_{H2}} \qquad b_{II} = \frac{(1+\sqrt{K_{H2} C_{H2}})^2}{k_s K_{BA} K_{H2} C_{H2}}$$

$$m_{III} = \frac{K_{BA}}{(k_s K_{H2} K_{BA} C_{H2})^{1/2}} \qquad b_{III} = \frac{1+K_{H2} C_{H2}}{(k_s K_{BA} K_{H2} C_{H2})^{1/2}}$$

$$m_{IV} = \frac{1+K_{H2} C_{H2}}{k_s K_{H2} C_{H2}} \qquad b_{IV} = \frac{1+K_{H2} C_{H2}}{k_s K_{BA} K_{H2} C_{H2}}$$

Figure 6.12 shows the linearised model fit to the experimental data at the different temperatures investigated. Although all the models show very good fit, models II (Figure 6.12b) and IV (Figure 6.12d) with R^2 values greater than 0.99 at all temperatures are considered to have the best fit. This leads to the decision to discard other models in favour of models II and IV. Furthermore, it implies that the experimental data is in accordance with a LHHW dual-site adsorption isotherm. To determine which of the two best fitted models (II or IV) is more appropriate to use in evaluating the kinetics parameters, the kinetic data was further analysed with Excel's solver optimizer. Equation 6.24 defines the objective function to be minimised to solve the model and determine its parameters;

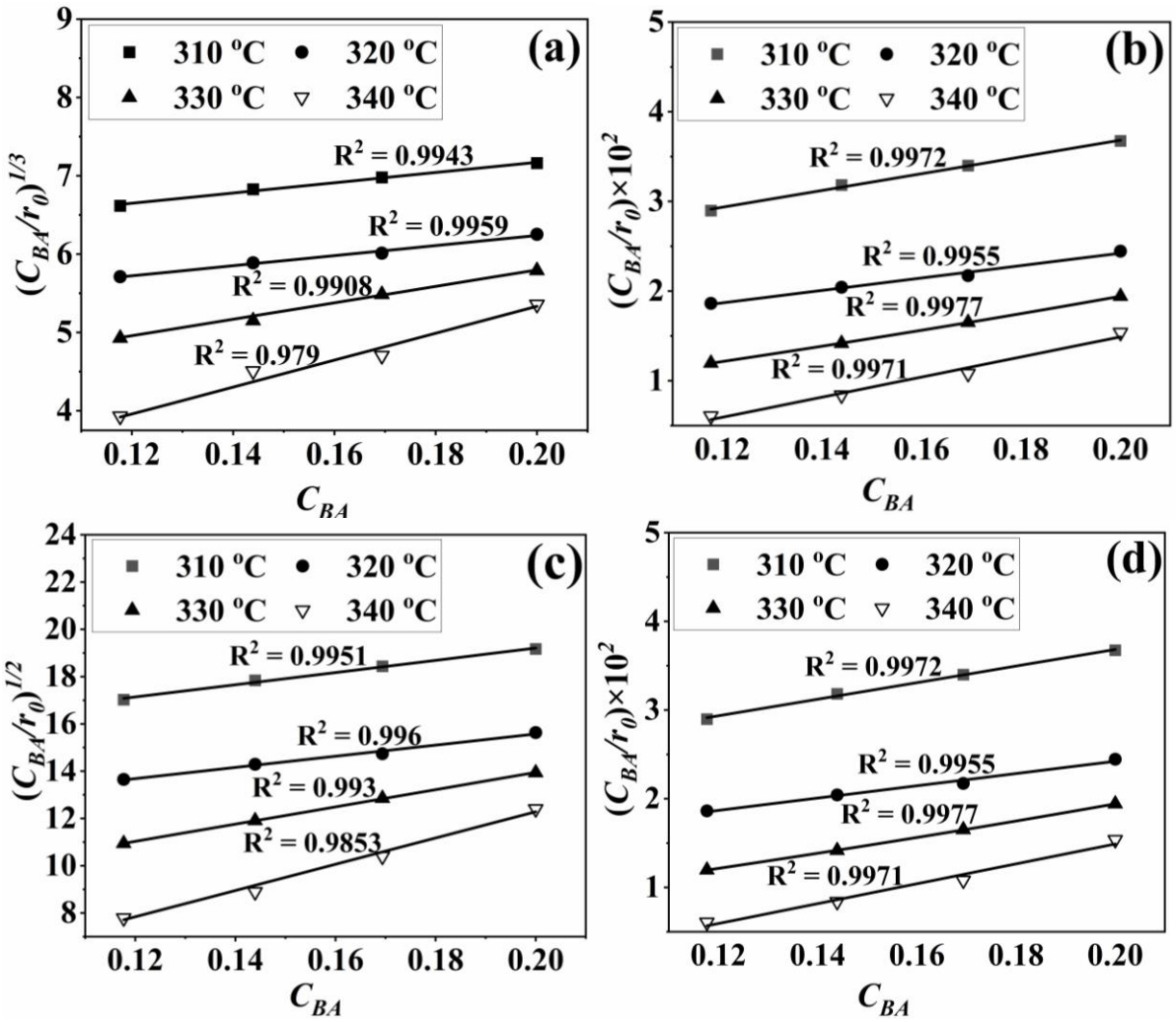

Figure 6.12: *Plots of the linearised form of the proposed kinetic models; (a) Single site adsorption of dissociatively adsorbed H_2; (b) Dual sites adsorption of dissociatively adsorbed H_2; (c) single site adsorption of non-dissociatively adsorbed H_2.*

$$RSS = \sum_n (r_{Exp} - r_{Mod})^2 \qquad 6.24$$

$$R^2 = 1 - \frac{RSS}{\sum (r_{Exp} - r_{Mean})^2} \qquad 6.25$$

where *RSS* is the residual sum of squares, r_{Exp} is the experimental reaction rate, r_{Mod} is the modeled reaction rate, and r_{Mean} is the average of the experimental reaction rates. The values of the residual sum of squares (*RSS*) as defined by equation 6.24 were minimised. Simultaneously, values for the coefficient of determination, R^2 (equation 6.25) were maximised.

Table 6.4: Observed values of the kinetic parameters from the best fitted model (Model II).

Kinetic parameters	310 ℃	320 ℃	330 ℃	340 ℃
k_s $(kmol \cdot kgcat^{-1} \cdot mim^{-1})$	0.145 ± 0.001	0.249 ± 0.001	0.378 ± 0.001	0.587 ± 0.016
K_{BA} $(m^3 \cdot kmol^{-1})$	3.090 ± 0.007	2.455 ± 0.013	1.850 ± 0.005	1.637 ± 0.016
K_{H2} $(m^3 \cdot kmol^{-1})$	0.225 ± 0.001	0.204 ± 0.004	0.184 ± 0.001	0.175 ± 0.006
RSS	6.131×10^{-10}	1.129×10^{-8}	2.289×10^{-8}	2.584×10^{-8}
Variance	1.004×10^{-8}	4.485×10^{-8}	1.153×10^{-7}	2.071×10^{-7}
$R^2_{model-II}$	0.991	0.968	0.974	0.978
$R^2_{model-IV}$	0.969	0.942	0.930	0.950

The significance of the R^2 value determines how applicable a model is. Model IV with low values of R^2 compared to the model II (Table 6.4) was regarded as not adequately describing the experimental data and therefore rejected. Based on model II (dual-sites adsorption of dissociatively adsorbed H_2), kinetic parameters such as the surface reaction rate constant (*ks*), hydrogen equilibrium constant (K_{H2}), and benzoic acid equilibrium constant (K_{BA}) were estimated using a non-linear solver in Microsoft Excel. The results are displayed in Table 6.4.

The reaction activation energy was estimated using the Arrhenius expression presented in equation 6.9, and the enthalpy of adsorption was estimated using the Van't Hoff isochore as shown in equation 6.26. Table 6.5 shows the activation energy, frequency factor, the enthalpy of adsorption for both hydrogen and benzoic acid, and their entropies.

$$ln\, K_{ads} = \left(\frac{-\Delta H_{ads}}{RT}\right) + \left(\frac{\Delta S}{R}\right) \qquad 6.26$$

Table 6.5: Observed activation energy, heats of adsorption, and expressions for rate constant dependency on temperature.

Parameter	Value	Rate constant dependency on temperature
E_A *(kJ mol^{-1})*	137.23	$k_s = 2.93 \times 10^{11} \exp\left(\frac{-16505}{T}\right)$
A (kmol kgcat^{-1} mim^{-1})	2.93×10^{11}	
ΔH_{BA} *(kJ mol^{-1})*	- 65.14	$k_{BA} = 4.46 \times 10^{-6} \exp\left(\frac{7834}{T}\right)$
ΔS_{BA} *(kJ mol^{-1} K^{-1})*	- 0.102	
A_{BA} *(m^3 kmol^{-1})*	4.46×10^{-6}	
ΔH_{H2} (kJ mol^{-1})	- 25.61	$k_{H_2} = 1.14 \times 10^{-3} \exp\left(\frac{3080}{T}\right)$
ΔS_{H2} *(kJ mol^{-1} K^{-1})*	- 0.056	
A_{H2} *(m^3 kmol^{-1})*	1.14×10^{-3}	

The estimated activation energy is 137.2 kJ mol^{-1}, while 2.9×10^{11} kmol kgcat^{-1} min^{-1} is the frequency factor. The observed activation energy from the developed LHHW kinetic model is higher than the value observed using the power law, 122.1 kJ mol^{-1} (±10.7 kJ mol^{-1} deviation). These values are higher than the 81.6 kJ mol^{-1} reported for the hydrogenation of benzoic acid to benzyl alcohol over a bimetallic Ru-Sn/Al_2O_3 catalyst (Shinde and Deshpande, 2022). Similarly, an activation energy of 96.6 kJ mol^{-1} was reported for the hydrogenation of benzoic acid over Pt-Sn/Al_2O_3 catalyst (Chen, 2019).

With an R^2 value greater than 99%, Figure 6.13 shows the parity plot for model II and the experimental data, which supports the claim that experimental and predicted reaction rates are highly correlated. Therefore, model II can also predict the benzoic acid concentration at various reaction temperatures, which agrees with experimental results. Consequently, it can be concluded that model II, which includes a dual-site adsorption and hydrogen is

dissociatively adsorbed, is accurately representative of the kinetics of the three-phase benzoic acid HDO reaction conducted in a batch reactor with 5% hie-Ni/ZSM-5 catalyst.

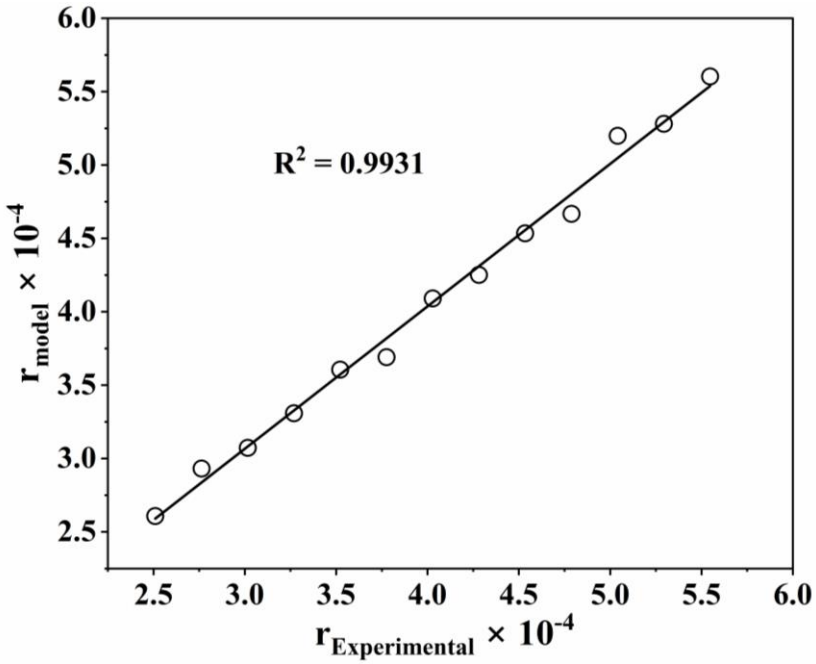

Figure 6.13: *Parity plot for the best fitted kinetic model (dual sites adsorption of dissociatively adsorbed H_2).*

6.12 Summary of the Chapter

The hydrodeoxygenation of benzoic acid as a typical bio-oil model compound has been reported. The effects of reaction temperature, pressure, and initial concentration of benzoic acid on conversion and product distribution were investigated over mic-Ni/ZSM-5, hie-Ni/ZSM-5 and Ni/SiO_2 catalysts. Furthermore, a kinetic model was developed using the LHHW approach. A mechanism assuming dual-site adsorption of dissociatively adsorbed hydrogen was shown to be the most accurate representation of the three-phase benzoic acid HDO performed over the 5 wt.% hie-Ni/ZSM-5 catalyst. The next chapter (Chapter 7) presents the HDO of a binary mixture of bio-oil model compounds (anisole and benzoic acid). In addition, the HDO of a real bio-oil obtained from thermo-catalytic reforming (TCR) of sewage sludge.

CHAPTER 7

Hydrodeoxygenation of Binary Mixture of Oxygenate Compounds Benzoic acid and Anisole found in Bio-oil and Real Bio-oil obtained from Thermo-Catalytic Reforming (TCR) of a Sewage Sludge

7.1 Introduction

Typically, bio-oil contains phenolics, carboxylic acids, and other oxygenates that must be deoxygenated in order to transform it into liquid hydrocarbon fuels (Cheah et al., 2023). The mixture of oxygenated compounds varies widely based on biomass and process variables used in the synthesis (Sharifzadeh et al., 2019). The complexity of bio-oil makes it challenging to explore its HDO and catalytic hydrogenation mechanisms (Kristensen et al., 2022; Yin et al., 2017). Model compounds are frequently used to acquire a better understanding of the reaction pathway and the parameters that affect it (Chang et al., 2013; Zhang et al., 2023). In addition to advancing knowledge of the mechanisms underlying the catalytic upgrading of bio-oil, studying model compounds could be a significant step in the development of more efficient and robust catalysts. In the previous chapters, HDO of anisole (Chapter 5) and HDO of benzoic acid (Chapter 6) were presented. Therein, the optimum reaction temperatures, hydrogen partial pressures, the best catalysts, reaction solvents, and the reaction mechanisms for the individual model compounds were reported. Depending on the nature of the catalyst, different model compounds have different adsorption coefficients and reactivity (Guvenc et al., 2023; Kristensen et al., 2022). However, information is limited in the literature on how catalytic activity is affected by the competitive adsorption of a blend of model compounds onto the catalyst's available active sites during the HDO process (Chen et al., 2020; Sankaranarayanan et al., 2018).

A wide variety of oxygenate compounds mimicking the complexities of the bio-oil itself are needed to gain insight into compound-compound interactions, compound-catalyst interactions, and product-compound interactions. Therefore, to understand the impact of cross-reactivity between the diverse chemical components of bio-oil and learn more about the network of chemical reaction taking place during the HDO process, a binary mixture of model compounds (benzoic acid and anisole) is studied and presented in this Chapter. This is aimed at elucidating the complex interactions between oxygenate compounds, catalyst, and products during the HDO and hydrogenation. In this context, the HDO and interaction of an ether (anisole) and a carboxylic acid (benzoic) with the developed catalysts is studied and reported. Sections 7.2 and 7.3 present and discuss the conversion profile and product distribution of the binary mixture of oxygenates (i.e., benzoic acid and anisole) as a function of HDO reaction temperature. In addition, the chapter also presents the HDO of a real bio-oil (derived from the TCR of sewage sludge) over a commercial HDO catalyst (TK-341), hie-Ni/ZSM-5, and the Ni/SiO_2 catalysts. The overall aim of the study is to evaluate catalytic activity under different reaction conditions and the catalysts' suitability for bio-oil stabilisation, which is a prerequisite to the generation of green fuels from biomass.

7.2 Effect of Reaction Temperature on Mixed Bio-oil Conversion

With the hie-Ni/ZSM-5 catalyst, 60 bar hydrogen pressure, reaction time of 6 h, and temperature range 300 to 340 °C, the effect of temperature on the HDO of binary mixtures of oxygenate compounds (benzoic acid and anisole) found in bio-oil was investigated. Prior to the reaction, the hie-Ni/ZSM-5 catalyst was activated *ex-situ* in a tubular furnace at 500 °C for 3 hours under a flow of 5% H_2/N_2 mixture. Figure 7.1 displays a time-dependent conversion of the mixed oxygenates at different reaction temperature of 300 °C, 320 °C and 340 °C, respectively.

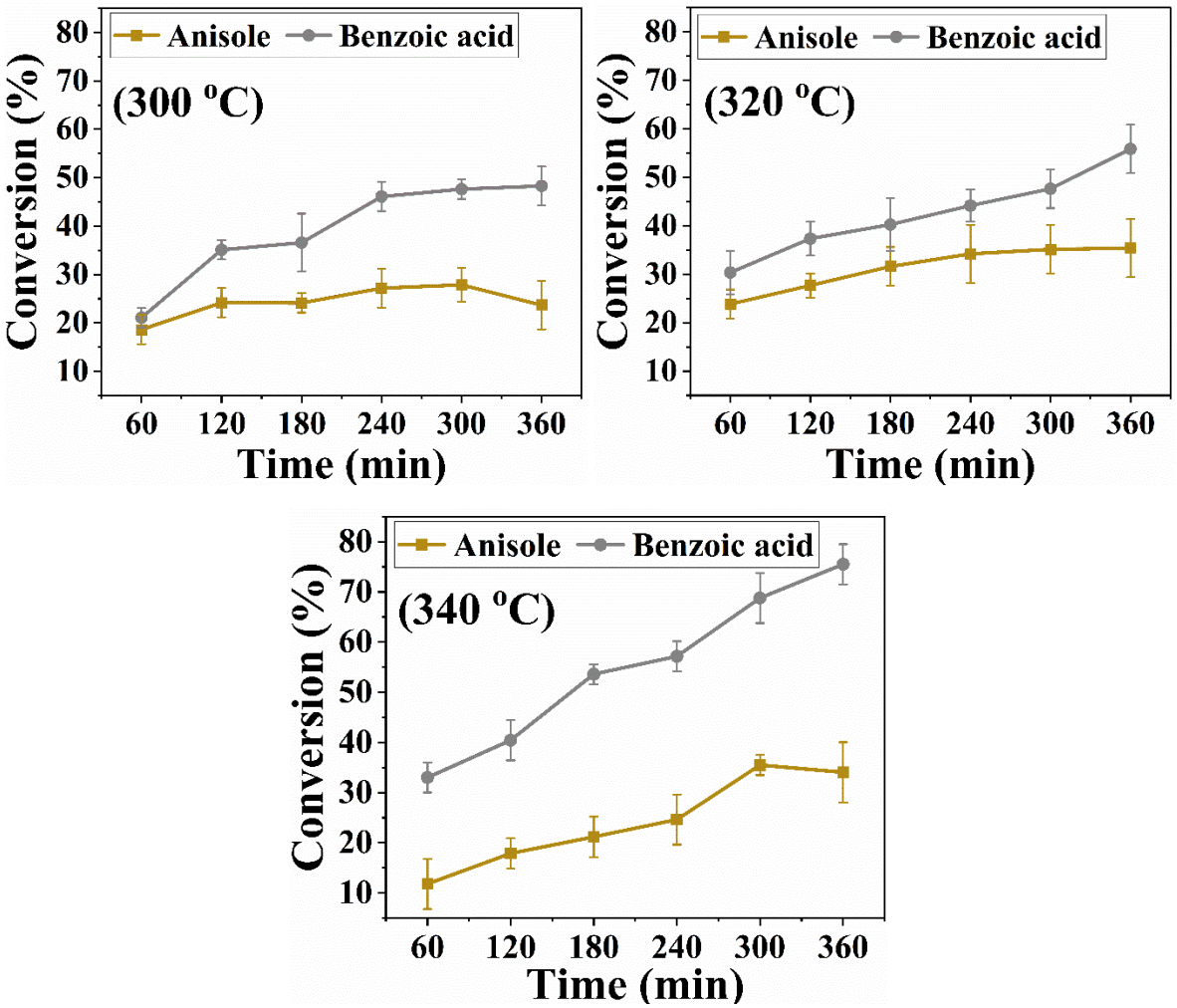

Figure 7.1: *Effect of temperature on mixed bio-oil (benzoic acid and anisole) conversion over hie-Ni/ZSM-5. Pressure; 60 bar H_2, catalyst loading; 100 mg, solvent; tetralin, reaction time; 6 hours.*

The effect of temperature on the conversion during the HDO of the mixed bio-oil oxygenate model compounds (0.1 M benzoic acid and 0.12 M anisole) was studied over 100 mg of hie-Ni/ZSM-5 catalyst in tetralin as solvent. Generally, the conversion of both the benzoic acid and anisole increases as a function of time. An interesting finding is that the fraction of benzoic acid converted is significantly higher than anisole at the same reaction temperatures. It appears that benzoic acid should have exhibited superior interactions with hie-Ni/ZSM-5 catalysts than anisole. Additionally, previous chapters have reported on their respective

conversion rates when each oxygenate was studied individually. The higher conversion observed from the reported data for each oxygenate reinforced this notion. It is likely that the competition for the catalyst active sites is responsible for the drop-in conversion in the binary-system (23.1% for anisole and 48.3% for benzoic acid at 300 ℃) compared to the mono-system (100% for anisole at 200 ℃, Section 5.4, and 63.8 % for benzoic acid at 310 ℃, Section 6.2).

The adsorption of reactants onto a solid catalyst occurs due to various intermolecular forces such as van der Waals force, hydrogen bonding, and electrostatic attractions (Llewellyn, 2013). The strength and specificity of these forces determine which reactant species will preferentially occupy the active sites on the catalyst surface. For instance, if two reactants are competing for adsorption onto a catalyst surface, their relative affinities towards the active sites will dictate their respective concentrations at any given time (Rouquerol et al., 2014). In addition, the presence of multiple reactants can lead to changes in the activation energy and reaction pathway, thereby affecting the overall rate of reaction (Bykova et al., 2013). When binary mixtures were studied, furfuryl alcohol was found to significantly inhibit the hydrogenation of the other model compounds (guaiacol and methyl isobutyl ketone) owing to their very strong adsorption (Shumeiko et al., 2019). Co-feeding guaiacol with catechol significantly decreased guaiacol conversion (Chang et al., 2013). Similarly, acetic acid conversion was supressed during the HDO of a mixed bio-oil system (acetic acid and *p*-cresol) over Ru/C catalyst (Si et al., 2017). This was attributed to the competitive adsorption on the catalyst active surface.

It can be seen from Figure 7.1 that at 300 ℃, a conversion of 18.6% in 1 hour was recorded for anisole. This increased to 23.1% as the reaction was allowed to proceed for 6 hours.

However, a higher conversion of 23.6% in 1 hour, which increased to 48.3% in 6 hours, was recorded for benzoic acid. As the reaction temperature increased to 320 ℃, anisole and benzoic acid conversion increased to 23.8% and 30.3% in 1 hour and 35.4% and 55.8% in 6 hours, respectively. A further increase in the reaction temperature to 340 ℃ gave a higher benzoic acid conversion of 33.0% and 75.5%, respectively. However, a lower anisole conversion of 11.8% and 34.1% compared to that recorded at 320 ℃ was observed. The kinetic energy of reactants increases with increasing temperature. As a result, more collisions occur between the reacting species, resulting in higher reaction rates and conversions.

The effect of temperature on anisole conversion was reported in Section 5.3 over the same catalyst used herein for the mixed bio-oil model compound (hie-Ni/ZSM-5). At 200 ℃, anisole conversion of 100% was seen in 2 hours (Chapter 5). Similarly, when the effect of catalyst support was investigated, conversion of 48.9% and 82.6% were recorded from 5 wt.% nickel-based SiO_2 and mic-ZSM-5 catalysts in 2 hours. In addition, conversion of 91.1% and 94.1% were reported in section 5.6 for the HDO of anisole over mic-Ni/ZSM-5 catalyst with decalin and n-decane as solvents. In agreement with this, high conversion of anisole has been reported in the literature at a moderate reaction temperature (180 – 250 ℃) over different catalysts and solvents (Aqsha et al., 2021; Wang, et al., 2020; Zhang et al., 2014). Surprisingly, while 100 % conversion of anisole was seen in 2 hours for the single model compound, a very low anisole conversion of 23.1% was recorded in 6 hours from the mixed bio-oil model compounds. With the increase in reaction temperature to 320 ℃, anisole conversion only improved to 35.4% and then decreased slightly to 34.1% at 340 ℃. The lower conversion of anisole could be attributed to the competitive adsorption of the reactants at the catalyst's active sites, indicating benzoic acid dominating the available sites.

It should be noted here that; different functional groups have distinct chemical properties that influence their interaction with the surface (Wang et al., 2023). For example, polar functional groups such as hydroxyl (-OH) or carboxyl (-COOH) tend to form hydrogen bonds with the surface, enhancing their adsorption. On the other hand, nonpolar functional groups like alkyl ($-CH_3$) or aromatic rings have weaker interactions and are less likely to be adsorbed (Ghampson et al., 2016; Wang et al., 2023). Surface properties of the catalyst are one of the major factors that influence the competition between different functional groups in the reacting mixture. If the surface is acidic, it will favour the adsorption of -COOH groups due to their ability to donate protons. Conversely, if the surface is basic, it will preferentially adsorb -OH groups because they can accept protons (Si et al., 2017). Hence, this probably justified the higher surface coverage of the catalyst surface by the benzoic acid.

During the HDO of eugenol over Ni/SB-ZM-R catalyst, conversion was nearly 100% (Chen et al., 2020). However, adding furfural as a second reactant greatly decreased the eugenol conversion and effected product distribution. In Section 6.3, it was shown that increase in HDO temperature favours the formation of benzene during the HDO of benzoic acid. This means intermediate products such as benzaldehyde and benzyl alcohol, and totally deoxygenated products like toluene are re-adsorbed onto the catalyst's active sites for further transformation (hydrogenation, deoxygenation, and demethylation). In other words, the formation of more benzene means an increase in the conversion of the intermediate products like benzaldehyde and benzyl alcohol, which have high affinity to the catalyst active sites compare to anisole. Hence, this might explain the observed decrease in anisole conversion, as the reaction temperature increased from 320 to 340 ℃. Unlike the anisole, an increase in the benzoic acid conversion was observed at all the studied temperatures. However, compared to what was seen when the model compound was treated singly (Section 6.2)

where conversion was 76.7% (320 ℃) and 97.9% (340 ℃), lower benzoic acid conversion was seen (55.8% at 320 ℃ and 75.5% at 340 ℃) for the mixed bio-oil model compounds. This observation supports the earlier prediction of the competitive and strong adsorption of benzoic acid onto most of the active sites on the catalyst during the HDO of the mixed bio-oil model compounds. This implies that anisole was only able to access limited number of active sites on the hie-Ni/ZSM-5 catalyst, thus very low conversion of anisole was recorded.

7.3 Effect of Reaction Temperature on Product Distribution During Mixed Bio-oil HDO

It is evident from the results in Section 7.2 that benzoic acid would have more interactions with the hie-Ni/ZSM-5 catalyst than anisole. It is worth investigating the product distribution to validate the observation as well as examine the possibility of product-reactant interactions. Figure 7.2 presents the product distribution and total yield of liquid product as a function of reaction temperature at a constant hydrogen partial pressure of 60 bar. When the HDO was carried out at 300 ℃ for 6 hours, the products obtained were benzaldehyde, toluene, and cyclohexane, with selectivity of 65.8%, 31.5%, and 2.9%, respectively. An increase in the reaction temperature to 320 ℃ changed the product distribution with the emergence of benzene and a decrease in benzaldehyde selectivity. The selectivity was 57.3% benzaldehyde, 25.7% toluene, 12.6% benzene, and 4.4% cyclohexane. A further increase in the reaction temperature to 340 ℃ caused a decrease in benzaldehyde selectivity to 41.2% from 57.3% at 320 ℃. An increase in the selectivity of toluene, 26.2%, and benzene, 19.3%, and the appearance of 9.6% benzyl alcohol was observed. It is worth noting the decrease in cyclohexane selectivity at 340 ℃ (3.7%), which is consistent with the observed trend on the effect of temperature on anisole conversion in the binary mixture of bio-oil model compounds (Section 7.2).

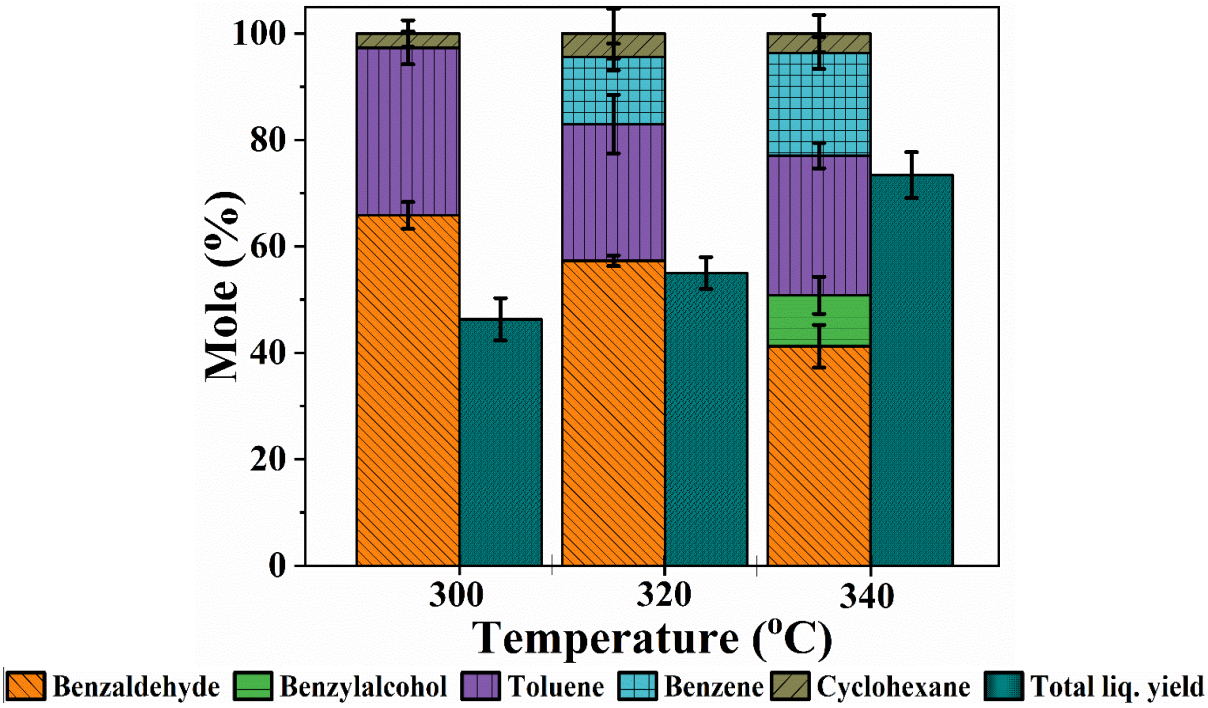

Figure 7.2: *Product distribution and total yield of liquid product as a function of temperature during the HDO reaction of the mixed bio-oil model compound (benzoic acid and anisole) hie-Ni/ZSM-5. Catalyst loading; 100 mg, solvent; tetralin, bio-oil initial concentration; benzoic acid 0.1 M, anisole 0.14 M, reaction time; 6 hours.*

In general, total yield of liquid product increased with increase in the reaction temperature from 46.7% (300 °C), 52.6% (320 °C), to 70.7% (340 °C) respectively. Although both benzaldehyde and benzyl alcohol are major intermediate products, it should be emphasised here that their presence in the final product is undesirable, given that one of the primary goals of HDO is to maximise the removal of oxygenates. Based on the observed product distribution a simplified reaction scheme is proposed and presented in Figure 7.3. Although it is obvious that competitive absorption onto the active sites of the hie-Ni/ZSM-5 catalyst and cross-reactivity of the mixed bio-oil components affects the rate of reaction, it was assumed that anisole transformation occurred via direct deoxygenation-hydrogenation pathway (Ghampson et al., 2018; Li, et al., 2020; Sankaranarayanan et al., 2015). For benzoic acid, transformation was through deoxygenation, decarboxylation, hydrogenation,

and demethylation (Chen, 2019; Kong et al., 2022; de Lange et al., 2002; Shinde and Deshpande, 2017; Tang et al., 2017; Xu et al., 2014).

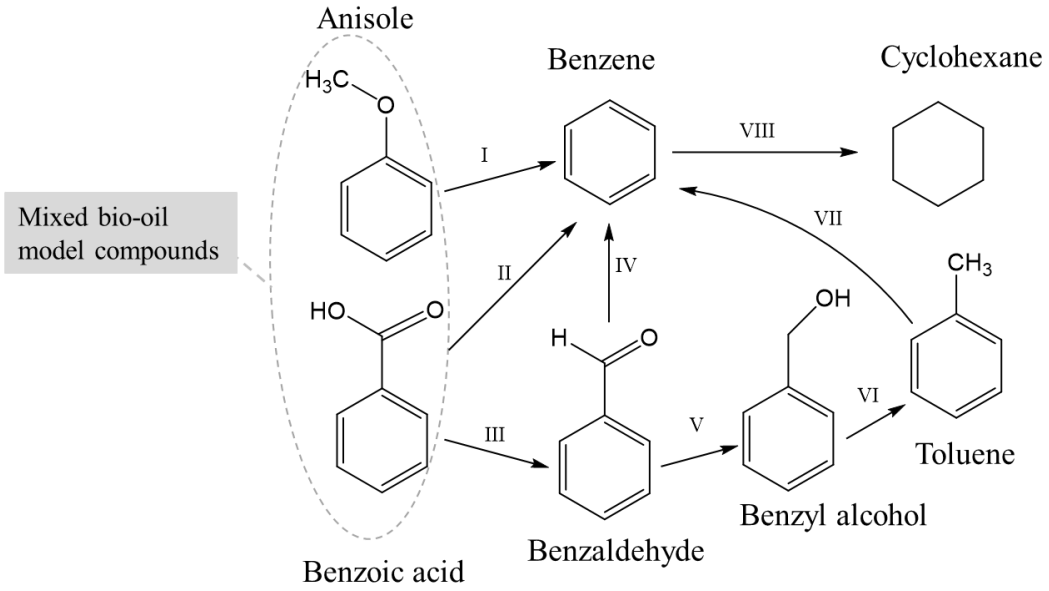

Figure 7.3: *Reaction scheme for the HDO of the mixed bio-oil model compound over the 5 wt.% nickel-based hie-Ni/ZSM-5 catalyst: I-demethoxylation; II-decarboxylation; III-deoxygenation; IV- decarboxylation; V-hydrogenation; VI-deoxygenation; VII-demethylation; VIII-hydrogenation.*

Anisole HDO over a Co/SBA-15 catalyst via a direct deoxygenation-hydrogenation pathway has been reported in the literature (Sankaranarayanan et al., 2015). That is achieved by breaking down the methoxy-phenyl bond to form benzene. Thereafter, the benzene is hydrogenated to cyclohexane. With benzoic acid, a conducive environment for surface reactions is achieved at a high reaction temperature, which creates a high concentration of oxygen vacancies (de Lange et al., 2002). At this point, benzoic acid is deoxygenated to benzaldehyde and thereafter to benzyl alcohol via hydrogenation. The benzyl alcohol is further deoxygenated into toluene and, subsequently, benzene via demethylation (Chen, 2019). Notably, the literature has also reported on the potential for benzene to be produced directly from benzoic acid and benzaldehyde by decarboxylation (Tang et al., 2017).

Figure 7.3 was derived by combining the proposed reaction pathways for the HDO of the single bio-oil model compounds in Figure 5.3 (anisole) and Figure 6.2 (benzoic acid), taking into consideration the product distribution recorded during the HDO of the mixture of the two model compounds. It can be recalled that the only liquid product seen for the HDO of anisole over hie/Ni/ZSM-5 catalyst was cyclohexane, with a selectivity of 92.5% and a yield of 27.2% at 150 ℃ (Section 5.4). With an increase in reaction temperature to 200 ℃, there was a decrease in cyclohexane selectivity to 89.6% and an increase in yield to 82.5%. However, during the HDO of benzoic acid over the same catalyst (Section 6.3), the two major products at 320 ℃ were benzene (26.6%) and toluene (42.6%). Intermediate products were benzaldehyde (13.6%) and benzyl alcohol (17.3%). The total liquid yield for this reaction was 73.9%. Thus, an increase in the reaction temperature to 340 ℃ increased the total liquid yield to 94.7% and changed the product distribution. The selectivity was 42.1% benzene, 25.0% toluene, 12.8% benzaldehyde, and 20.1% benzyl alcohol. Comparing these results with the product distribution from HDO of the mixed bio-oil model compound, there was a decrease in both selectivity (12.6% benzene, 25.7% toluene at 320 ℃, and 19.3% benzene, 26.2% toluene at 340 ℃) and total liquid yield (52.6 % at 320 ℃ and 70.7% at 340 ℃). In addition, higher amounts of benzaldehyde and cyclohexane (57.3% and 4.4%) were recorded at 320 ℃ compared to the amounts obtained at 340 ℃ (41.2% and 3.7%).

In summary, during the HDO of anisole over the hie-Ni/ZSM-5 in a single model compound system, the only liquid product observed was cyclohexane. There were no other intermediates products seen at any point during the reaction. Based on the proposed reaction scheme (Figure 5.3), the reaction medium is less competitive; therefore, benzene was transformed quickly to cyclohexane. This reaction was promoted by the acid sites on the catalyst via hydrodearomatisation (Pawelec et al., 2020). However, in the HDO of binary

mixture, where benzoic acid (-COOH functional group) dominated most of the active sites, the overall kinetics was very slow. In addition, the selectivity to cyclohexane was very low. One possible reason for this is the presence of highly reactive oxygenate intermediates (benzaldehyde and benzyl alcohol) that compete for the acid sites with both the anisole, toluene, and benzene.

7.4 HDO of a Real Bio-oil Derived from Thermo-Catalytic Reforming

In the Chapters 5 and 6, the single HDO of anisole and benzoic acid was reported. The effects of temperature, pressure, catalyst loading, reaction time, and solvent on conversion and product distribution during the HDO have been discussed. The reaction mechanism and kinetics have been formulated and analysed. Further to the results presented earlier in this chapter for a binary mixture of model compounds, the HDO of a real bio-oil was tested experimentally to gain more insight on the effect of the presence of multiple compounds on the catalytic activity during the HDO. It was also important to evaluate the effectiveness of the developed catalysts in catalysing the upgrading of bio-oil itself. This is because for single and double model compounds studies the developed catalyst hie-Ni/ZSM-5 catalyst has demonstrated superior activity and selectivity based on its mesoporosity. This allows access to active sites while minimising mass transport limitations. It would be worthwhile to test its performance in deoxygenating an actual bio-oil through HDO, given these characteristics. A bio-oil derived from the thermo-catalytic reforming of sewage sludge, which is a sustainable and easily available source of bio-oil (Ding et al., 2017), was used. For the sake of comparison, the catalysts employed for the upgrading were nickel-based hie-ZSM-5, SiO_2, and a bimetallic nickel/molybdenum-based γ-Al_2O_3 catalysts (i.e., a commercially used HDO catalyst). The NiMo supported on alumina (TK-341) is a commercial HDO catalyst supplied by Haldor Topsøe, which is used as a benchmark in evaluating the catalyst developed in this

study. The reaction was carried out in a 0.1 L high-pressure batch reactor at 350 °C and 60 bar hydrogen partial pressure for 3 hours. The studies were done at the Tyseley Energy Park in collaboration. The reactor and procedure are described in Section 3.6 of the experimental chapter.

7.5 HDO of Sewage Sludge Oil Over TK-341, hie-Ni/ZSM-5, and Ni/SiO_2 Catalysts

Firstly, sewage sludge oil obtained from the University of Birmingham's pilot-scale TCR unit was analysed to determine its composition. From the GC-MS analysis, some of the major oxygenates, nitrogen, and sulpur containing compounds in the oil were identified and presented in Figure 7.4.

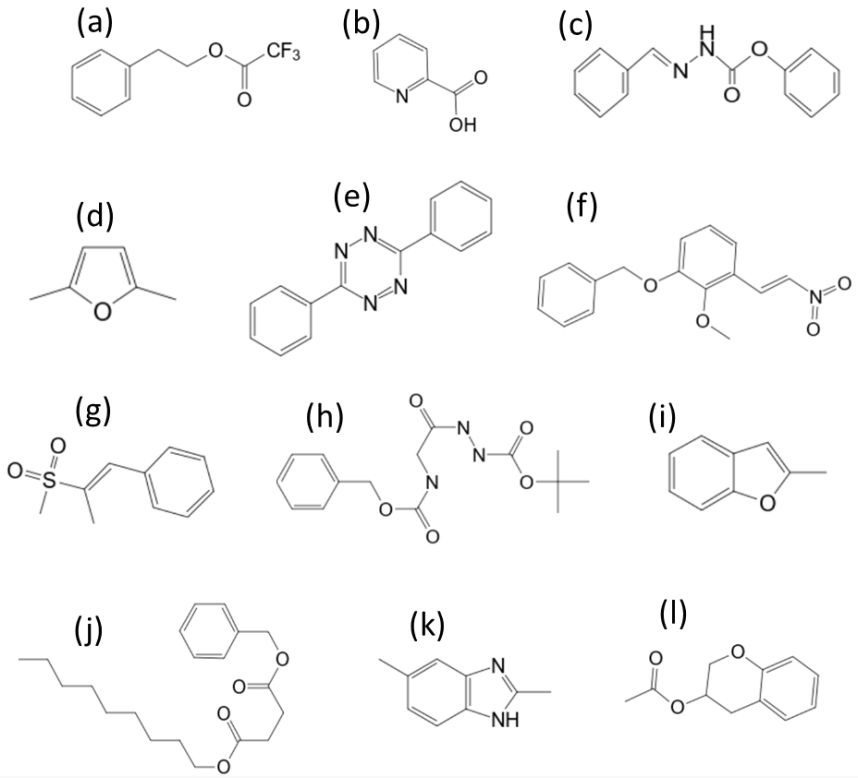

Figure 7.4: *Some of the major oxygen, nitrogen, and sulphur-containing compounds in the raw sewage sludge oil: trifluoroacetic acid, phenethyl ester (a), 2-pyridinecarboxylic acid (b), benzaldehyde phenoxycarbonylhydrazone (c), 2,5-Dimethylfuran (d), 3,6-diphenyl-1,2,4,5-tetraazine (e), benzene, 2-methoxy-1-(2-nitroethenyl)-3-(phenylmethoxy)- (f), benzene, [2-(methylsulfonyl)-1-propenyl]- (g), acethydrazide, 2-benzyloxycarbonylamino-N2-tert-butoxycarbonyl- (h), 2,5-dimethylbenzimidazole (i), 1-benzyl 4-nonyl succinate (j), 2-methylbenzofuran (k), and 1- 2H-1-Benzopyran-3-ol, 3,4-dihydro-, acetate (l).*

As can be seen, the bio-oil consists of a range of monocyclic and bicyclic aromatics, which is consistent to what was reported by Bashir et al. (2022). The proportion of oxygen and nitrogen containing compounds are higher in the oil compared to the sulphur containing compounds. Bio-oil often has a relatively low concentration of sulfur (Chang et al., 2013). The high concentration of nitrogen compounds in sludge justified why land application for agricultural value is common in areas where environmental restriction and regulations are lax (Adhikari et al., 2018).

Prior to the reaction, the catalyst was activated *in-situ* at 350 ℃ and 60 bar hydrogen for 3 hours. Table 7.1 presents the elemental composition of the bio-oil before and after upgrading determined from the GC-MS analysis. As expected, carbon has the highest proportion followed by hydrogen, oxygen and nitrogen with a trace of sulphur. The amount of carbon and hydrogen in the untreated bio-oil was 79.8% and 10.3% respectively, while oxygen, nitrogen, and sulfur was determined as 4.9%, 4.4%, and 0.3% respectively.

It is evident from the results (Table 7.1) that there were changes in the percentage composition of these elements after the 3-hour HDO reaction. Generally, there was a decrease in oxygen, nitrogen, and sulfur content in the treated oil over all the catalysts compared to the raw bio-oil. While the oxygen content of the bio-oil decreased to 2.6%, 2.5%, and 2.6% over the TK-341, Ni/SiO_2, and hie-Ni/ZSM-5 catalysts, the nitrogen content decreased to 1.4%, 2.1%, and 1.8%, respectively. Notably, the developed hie-Ni/ZSM-5 catalyst demonstrated comparable performance to the commercial catalyst in terms of deoxygenation. However, hie-Ni/ZSM-5 catalyst produced an upgraded oil with higher carbon content than that of TK-341 and Ni/SiO_2. The lower hydrogen content in the upgraded bio-oil using hie-Ni/ZSM-5 compared to TK-341 and Ni/SiO_2 catalysts, suggests

that the produced upgraded oil with hie-Ni/ZSM-5 catalyst contains more aromatic compounds. Although the amount of sulphur was very low in the raw oil, some trace was still seen in the bio-oil treated with Ni/SiO_2 catalyst, suggesting incomplete desulphurization.

Table 7.1: Elemental composition of the raw and treated sewage sludge oil: Oil to catalyst ratio: 10:1, reaction temperature: 350 °C, reaction pressure: 60 bar H_2, reaction time: 3 hours.

		Treated sewage sludge oil		
Composition	**Feed**	**TK-341**	**Ni/SiO_2**	**hie-Ni/ZSM-5**
C (wt.%)	79.8 ± 1.4	83.8 ± 2.1	83.3 ± 1.8	84.0 ± 1.6
H (wt.%)	10.3 ± 1.1	12.3 ± 1.8	12.0 ± 0.9	11.6 ± 1.2
O (wt.%)	4.9 ± 0.5	2.6 ± 0.3	2.5 ± 0.5	2.6 ± 0.3
N (wt.%)	4.4 ± 0.6	1.4 ± 1.0	2.1 ± 0.4	1.8 ± 0.3
S (wt.%)	0.3 ± 0.1	0.0 ± 0.0	< 0.1 ± 0.0	0.0 ± 0.0
H/C molar ratio	1.50 ± 0.2	1.74 ± 0.1	1.72 ± 0.5	1.66 ± 0.2

Additionally, it can be observed that the H/C molar ratio in the treated oil is increased. While only 1.503 was recorded for the raw oil, 1.74, 1.72, and 1.66 were obtained from the oil treated over TK-341, Ni/SiO_2, and hie-Ni/ZSM-5 catalysts, respectively. Since the primary purpose of catalytic hydrotreatment of bio-oil is to minimise the oxygen concentration and thereby raising the bio-oil's H/C ratio (Auersvald et al., 2017; Kadarwati et al., 2017), the HDO of sewage sludge oil has been successfully achieved.

Similar to what is recorded herein, Auersvald et al. (2017) reported the HDO of bio-oil obtained from the ablative pyrolysis of straw over a commercial NiMo-based catalyst. When the reaction was carried out at 360℃, the carbon and hydrogen contents increased from

71.9% and 7.1% in the feed to 83.9% and 10.8% in the treated oil, respectively. In addition, the oxygen and nitrogen content decreased from 20.1% and 0.8% to 4.5% and 0.8%, respectively.

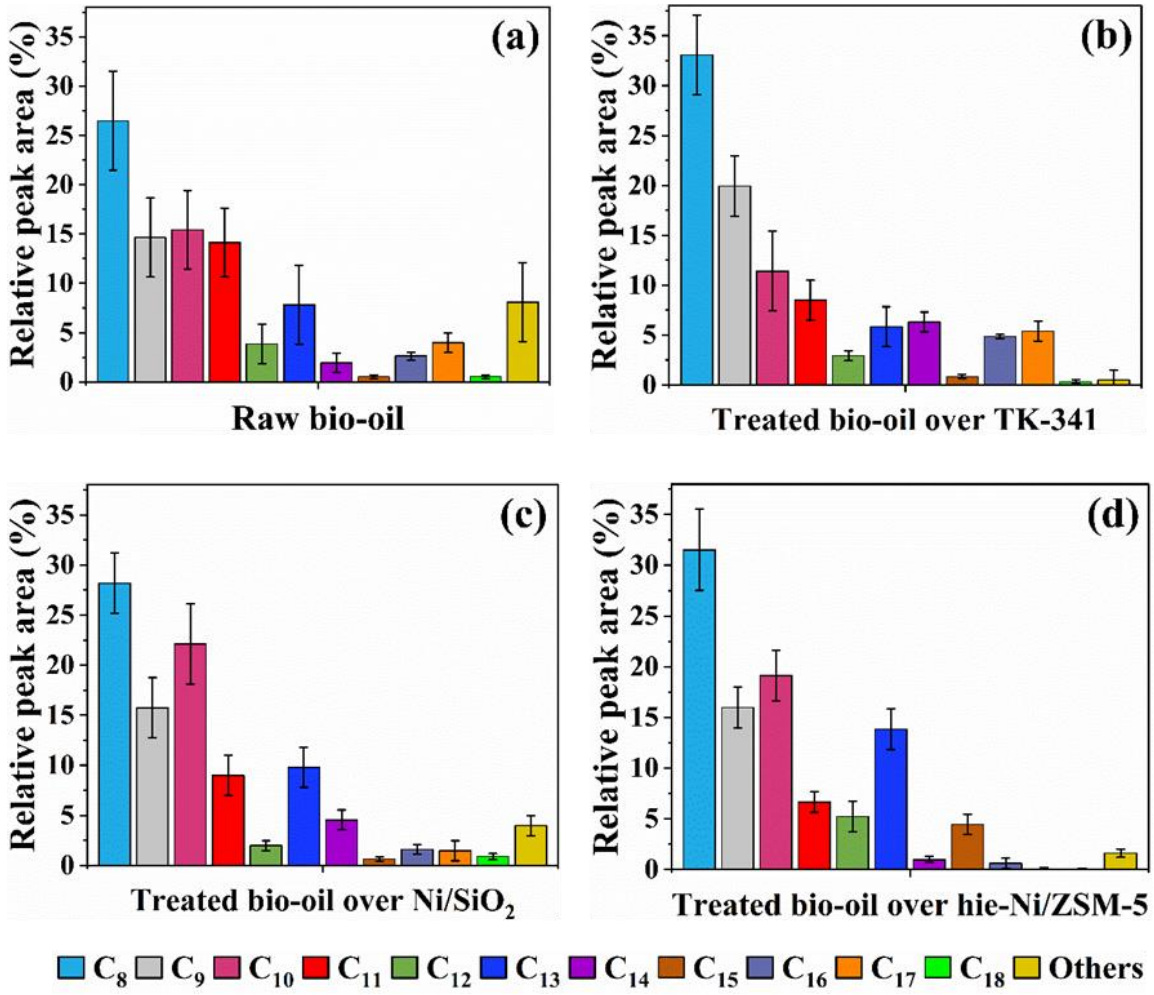

Figure 7.5: *Distribution of carbon compounds in the raw bio-oil (a) and treated bio-oil over non-sulfided catalysts: TK-341 (b), Ni/SiO_2 (c), and hie-Ni/ZSM-5 (d). Oil to catalyst ratio: 10:1, reaction temperature: 350 °C, reaction pressure: 60 bar H_2, reaction time: 3 hours.*

In a related study, Bashir et al. (2022) reported an increase in carbon (78.9% to 86.3%) and hydrogen (10.3% to 11.0%), and a decrease in oxygen (4.2% to 0.7%), nitrogen (4.5% to 2.0%), and sulphur (2.1% to less than 0.1%) contents during the HDO of a sewage sludge oil. The reaction was carried out over a $NiMo/Al_2O_3$ catalyst in a high-pressure batch reactor at

350 °C and 60 bar H_2 for 4 hours. However, contrary to what was seen herein, the H/C molar ratio decreased from 1.56 to 1.53. Figure 7.5 presents the distribution of carbon in the feed oil and in the HDO product. According to Figure 7.5a, the feed contains more monocyclic aromatic compounds than bicyclic aromatic compounds.

The total composition of C_8, C_9, C_{10}, and C_{11} is about 70%, with C_8 having the highest proportion of 26.5%. Following treatment, an increase in the proportion of the monocyclic, or rather lighter, components increased on both catalysts (Figure 7.5b–d). A total of 72.9%, 75.1%, and 73.3% were recorded for TK-341, Ni/SiO_2, and hie-Ni/ZSM-5 catalysts, respectively. The corresponding increases in C_8 for the three catalysts were 33.1% (TK-341), 28.2% (Ni/SiO_2), and 31.5% (hie-Ni/ZSM-5), respectively. The lower proportion of C_8 from the Ni/SiO_2 catalyst could be linked to the low acid site concentration of the support (as shown by the NH_3-TPD result in Section 4.6), making it have a low affinity for C-C cracking.

7.6 HDO of Sewage Sludge Oil over Sulfided TK-341, hie-Ni/ZSM-5, and Ni/SiO_2 Catalysts

Due to their traditional industrial application in the hydrodesulphurization of petroleum hydrocarbons, sulfided catalysts such as CoMo and NiMo on Al_2O_3 support have been widely researched for HDO (Heracleous et al., 2022; Loricera et al., 2011; Rahimpour et al., 2016; Saleheen et al., 2019). Sulfiding helps to convert catalyst metal oxide into metal sulphides, which is the most active state of the hydrotreating catalysts. It is also shown to reduce the tendency for quick deactivation by preventing coking (Cheah et al., 2023; Loricera et al., 2011). Therefore, the TK-341, hie-Ni/ZSM-5, and Ni/SiO_2 catalysts were sulfided and activated *in-situ* with 1 mL DMDS per gram of catalyst and 60 H_2 at 350 °C prior to the reaction.

Table 7.2: Elemental composition of the sewage sludge oil treated using sulfided catalysts: Oil to catalyst ratio: 10:1, reaction temperature: 350 °C, reaction pressure: 60 bar H_2, reaction time: 3 hours.

Composition	Feed	Treated sewage sludge oil		
		s-TK-341	s-Ni/SiO_2	s-hie-Ni/ZSM-5
C (wt.%)	79.8 ± 1.7	84.2 ± 2.0	83.4 ± 1.9	83.6 ± 2.2
H (wt.%)	10.3 ± 1.5	12.6 ± 1.7	12.1 ± 1.1	11.8 ± 1.3
O (wt.%)	4.9 ± 0.4	2.1 ± 0.2	2.7 ± 0.4	3.2 ± 0.1
N (wt.%)	4.4 ± 0.9	1.1 ± 0.3	1.7 ± 0.2	1.4 ± 0.1
S (wt.%)	0.3 ± 0.1	0.0 ± 0.0	< 0.1 ± 0.0	0.0 ± 0.0
H/C molar ratio	1.50 ± 0.1	1.79 ± 0.2	1.73 ± 0.5	1.70 ± 0.2

s-: stands for sulfided

Based on GC-MS analysis, Table 7.2 shows the elemental composition of the bio-oil before and after upgrading. It can be noticed that the percentages by weight of carbon (79.8%), hydrogen (10.3%), oxygen (4.9%), nitrogen (4.4%), and sulphur (0.3%), respectively, in the untreated bio-oil. Following the 3 hours reaction, there was an increase in carbon and hydrogen content in the treated oil. The carbon was 84.2%, 83.4%, and 83.6%, while the hydrogen was 12.6%, 12.1, and 11.8%, respectively, over the s-TK-341, s-Ni/SiO_2, and s-hie-Ni/ZSM-5. However, the oxygen, nitrogen, and sulphur content of the treated oil decreased as compared to the raw bio-oil across all catalysts. While the oxygen concentration of the bio-oil was reduced to 2.1%, 2.7%, and 3.2% over the s-TK-341, s-Ni/SiO_2, and s-hie-Ni/ZSM-5 catalysts, respectively, the nitrogen content decreased to 1.1%, 1.7%, and 1.4%. Noticeably, total desulphurization was achieved with all the catalysts except s-Ni/SiO_2. The percentage composition of the constituent elements seen here is relatively similar to those recorded for the non-sulfided catalysts (Table 7.1), although the s-TK-341 catalyst showed some improvement in all aspect of the upgrading. A greater decrease in the proportion of

nitrogen was observed in s-Ni/SiO_2 and s-hie-Ni/ZSM-5 compared to their non-sulfided counterparts.

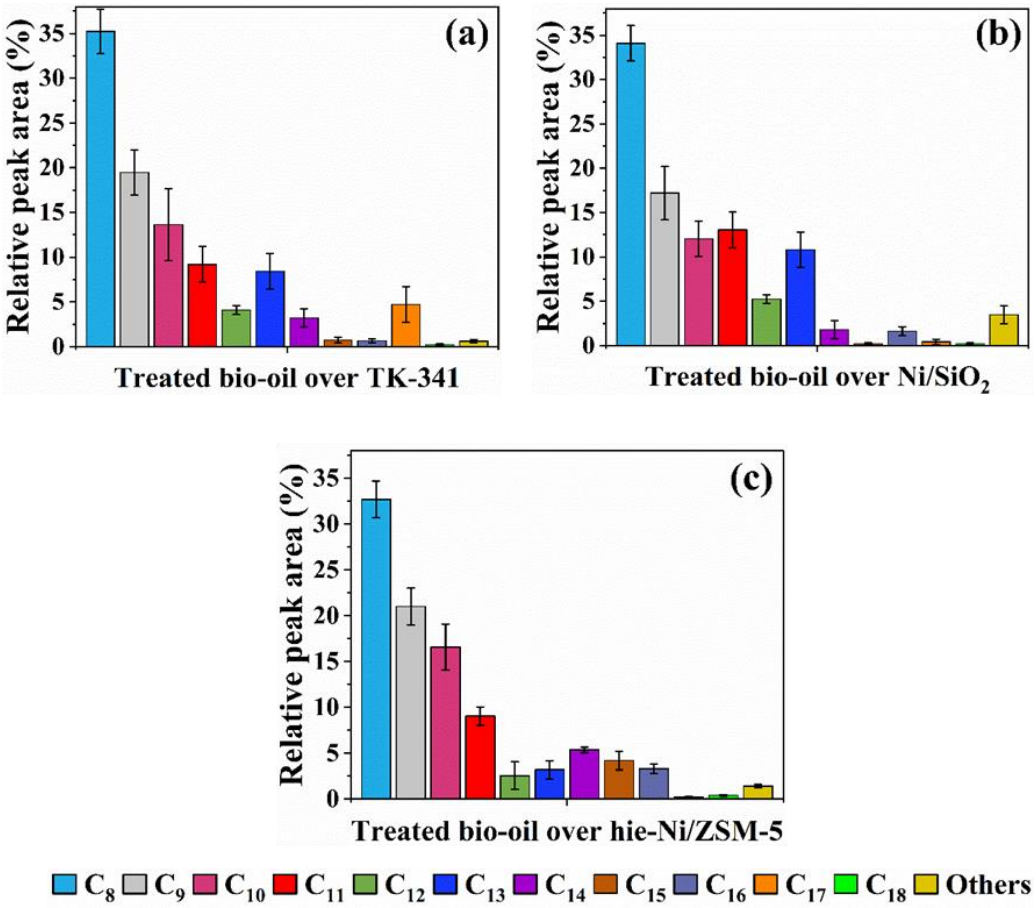

Figure 7.6: *Distribution of carbon compounds in the treated bio-oil over sulfided catalysts: TK-341 (a), Ni/SiO_2 (b), and hie-Ni/ZSM-5 (c). Oil to catalyst ratio: 10:1, reaction temperature: 350 °C, reaction pressure: 60 bar H_2, reaction time: 3 hours.*

Product distribution from the sulfided catalysts shows higher selectivity for monocyclic aromatics than that obtained from the non-sulfided catalysts. As shown in Figure 7.6, the total C_8, C_9, C_{10}, and C_{11} were s-TK-341 (77.6%), s-Ni/SiO_2 (76.5%), and s-hie-Ni/ZSM-5 (79.4%). This high activity may be due to the nickel sulfide species on the catalyst surface. High deoxygenation and hydrolysis during the HDO of a methyl stearate over a sulfided NiMo-Al_2O_3 catalyst were attributed to the activity of the evolved metal sulfide (Cheah et al., 2023).

7.7 Degree of Hydrodeoxygenation, Hydrodenitrogenation, and Hydrodesulphurization of the Sewage Sludge Oil

Bio-oil is usually a dark brown, highly viscous liquid with a unique smokey odour (Auersvald et al., 2017; Zhang et al., 2013). Effective upgrading treatment will, following the removal of oxygen, nitrogen, and sulphur in the bio-oil, improve the colour and decrease the viscosity of the oil (Roy et al., 2023; Sakka et al., 2023; Zhang et al., 2014). A visual comparison between raw bio-oil and catalytically upgraded bio-oil is shown in Figure 7.7. There is a noticeable change in colour from dark brown to light brown depending on the catalyst and experimental conditions used. The raw bio-oil feedstock is black or dark brown in colour as can be seen in Figure 7.7a, which changes to a lighter one due to catalytic HDO upgrading for 3 h.

Figure 7.7: *Sewage sludge oil samples: (a) raw bio-oil; treated oil over catalysts, (b) TK-341, (c) s-TK-341, (d) hie-Ni/ZSM-5, (e) s-hie-Ni/ZSM-5, (f) Ni/SiO_2, and (g) s-Ni/SiO_2 treated oil: Oil to catalyst ratio*: 10:1, reaction temperature: 350 °C, reaction pressure: 60 bar H_2, reaction time: 3 hours.

This is an indication of deoxygenation following catalytic HDO upgrading. Similarly, the brightening of the colour of the bio-oil from dark to light suggests a decrease in viscosity. Bio-oil quality can also be determined by its viscosity, which measures a liquid's resistance to flow. In addition to deoxygenation, the decrease observed in the viscosity of bio-oil treated

over both the sulfided and non-sulfided catalysts, may be associated with the increase in the light fractions recorded (Table 7.1 and 7.2).

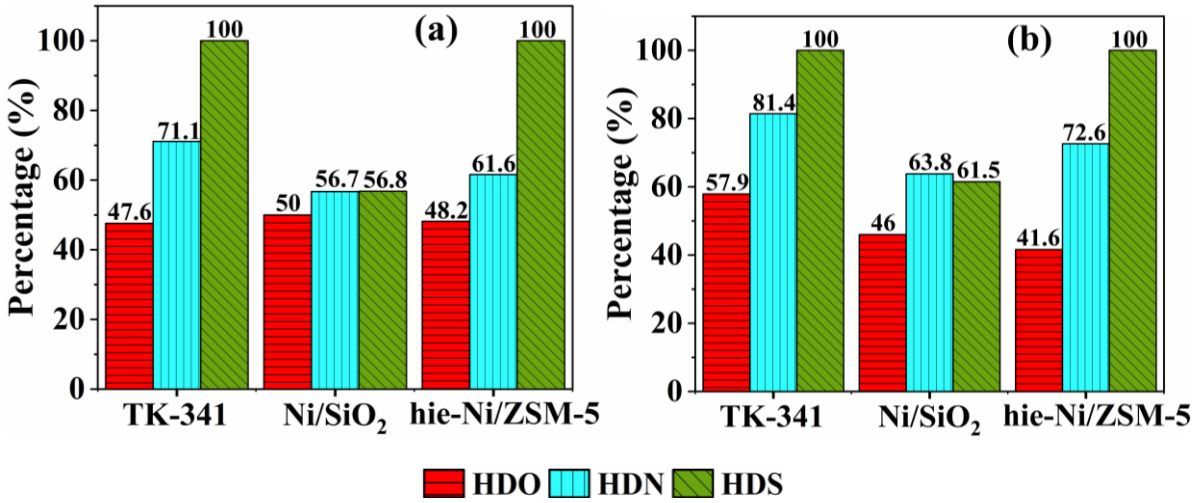

Figure 7.8: *Degree of hydrodeoxygenation, hydrodenitragenation, and hydrodesulphurization of the sewage sludge bio-oil over the TK-341, Ni/SiO₂ and hie-Ni/ZSM-5 non-sulfided (a), and sulfided (b) catalysts: Oil to catalyst ratio: 10:1, reaction temperature: 350 °C, reaction pressure: 60 bar H_2, reaction time: 3 hours.*

The degree of hydrodeoxygenation (X_{HDO}), hydrodenitrogenation (X_{HDN}), and hydrodesulphurization (X_{HDS}) in the bio-oil using both the non-sulfided and sulfided catalysts is shown in Figure 7.8 a and b. Figure 7.8a reveals that the Ni/SiO_2 has the highest degree of HDO (50.0%), followed by hie-Ni/ZSM-5 (48.1%) and TK-341 (47.3%). However, the extent of HDN was 71.1%, 61.6%, and 56.7% for TK-431, hie-Ni/ZSM-5, and Ni/SiO_2, respectively. In addition, total HDS was recorded on TK-341 and hie-Ni/ZSM-5 catalysts, while 56.8% was observed on Ni/SiO_2. Noteworthy is the high activity of the Ni/SiO_2 catalyst which is attributed to the synergic effects between mesoporosity and good metal site distribution. The nature of the SiO_2 support, as seen from the BET results in Chapter 4 (Section 4.3), allows bulky molecules to easily access the available active sites for reactions. This is consistent with the observation during the HDO of benzoic acid as a bio-oil model compound (Chapter 6, Section 6.2). Comparing the unsulfided with the sulfided

catalysts (Figure 7.8b), there was an increase in HDN for all the sulfided catalysts. However, HDO only increased from 47.6 to 57.9% for TK-341), but decreased from 50.0 to 46.0% for Ni/SiO_2, and 48.2 to 41.6% hie-Ni/ZSM-5 catalysts.

In a similar study, Heracleous et al. (2022) reported the HDO of sewage sludge oil using a sulfided catalyst (bi-metallic NiMo support on alumina). The reaction was in two stages involving stabilization (250 ℃ for 4 hours) and the main reaction (350 ℃ for 4 hours). The degrees of HDO, HDN, and HDS were 72.9%, 3.3%, and 74.7%, respectively. Despite the fact that a high degree of HDO could be achieved from the sulfide NiMo and CoMo catalysts and their low cost, the catalysts stability remains an issue (Yin et al., 2017). Furthermore, sulfided catalyst systems are criticised since they negate the benefit of bio-oil, which contains no or low sulphur inherently (Cheah et al., 2023). Hence, with the remarkable bio-oil upgrading achieved from the mesoporous Ni/SiO_2 and hie-Ni/ZSM-5, they are regarded as potential candidates for further development.

7.8 Summary of the Chapter

The HDO of a mixture of some selected model compounds composed of phenolic ether (anisole) and carboxylic acid (benzoic acid) as a blend yielded some essential understanding of the reaction mechanisms. The effects of temperature on competitive adsorption and cross-reactivity on conversion and product distribution during the HDO have been demonstrated. Furthermore, HDO of sewage sludge oil has been successfully carried out. The levels of oxygen, nitrogen, and sulphur in the real bio-oil were noticeably reduced following treatment with the hie-Ni/ZSM-5, Ni/SiO_2, and commercial TK-341 catalysts. Upon sulfidation, an increase in the degree of HDN was observed in all three catalysts. However, the extent of HDO only increased with the commercial TK-341 catalyst. Conclusively, mesoporous, Ni-

based, and unsulfided catalysts might be viable options for the HDO of real bio-oil with more testing on stability and reusability. The next chapter (Chapter 8) presents a general conclusion of the entire research work. The chapter also makes some recommendations for future work.

CHAPTER 8

Conclusions and Recommendations for Future Work

8.1 Conclusions

A set of catalysts, including mic-Ni/ZSM-5 (5 wt.% Ni), hie-Ni/ZSM-5 (5 wt.% Ni), Zn/ZSM-5, bimetallic mic-NiZn/ZSM-5 (3 wt.% Ni and 2 wt.% Zn), and Ni/SiO_2, were successfully prepared and characterised using a wide range of techniques. The catalysts were tested for the HDO of bio-oil model compounds (anisole and benzoic acid) and a real bio-oil obtained from the thermo-chemical reforming of sewage sludge. The activity test was performed in a Parr reactor at a range of temperatures (160–350 °C) and hydrogen pressure (20–60 bar). The influences of catalyst support, active metal, and reaction solvent on the extent of anisole and benzoic acid HDO were investigated. Furthermore, a successful kinetic analysis was carried out and kinetic parameters evaluated. Finally, the prepared catalysts were compared with a commercial NiMo-based (TK-341) counterpart in the HDO of the sewage sludge oil. Based on the research objectives and the major findings of the work, the following conclusions have been drawn:

8.1.1 Catalyst characterisation

The prepared catalysts were successfully characterised using XRD, BET, SEM-EDX, TEM, NH_3-TPD, H_2-TPR, and TGA techniques. The parent zeolite support (mic-ZSM-5) retained all the characteristic diffraction peaks after the it was treated with 0.2 M NaOH without any noticeable destruction of its framework. However, there was a decrease in crystallinity owing to the NaOH treatment and the addition of nickel to produce the catalysts. The BET analysis showed an increase in the quantity of adsorbed N_2 and a shift from Type I (in mic-ZSM-5) to Type II (in hie-ZSM-5) isotherms. The hie-ZSM-5 shows a hysteresis loop (Type

H4) at higher relative pressures, indicating the presence of mesopores. The SiO_2 and Ni/SiO_2 exhibit marked uptake of Type IV isotherm with H2 type hysteresis loop at $p/p_0 > 0.75$, showing mesoporous characteristics. While the hie-ZSM-5 support showed an improved surface area, loading of the nickel caused an evident decrease in the surface area and total pore volume for all the supports, suggesting that nickel was effectively deposited. Similarly, a decrease in the total pore volume attributed to partial blockage of pores due to the metal loading was seen. Interestingly, the targeted metal loading of 5 wt.% was approximately achieved (± 0.51 mean deviation). EDX elemental mapping demonstrated the uniform distribution of Ni and, by extension, confirms the successful deposition of Ni on the supports. It is evident from the TEM result that a high degree of metal dispersion was achieved, particularly in mic-Ni/ZSM-5 and hie-Ni/ZSM-5. Similarly, an increase in the acid site concentration in the hie-ZSM-5 compared to the mic-ZSM-5 was observed. While SiO_2 was almost neutral, there were changes in the acid sites concentration and distribution after the metal impregnation on the supports. However, compared to the nickel-based catalysts, the zinc-based catalysts showed a reduced total acid sites concentration.

8.1.2 HDO of anisole

Anisole HDO was performed in a 0.1 L high-pressure batch reactor using the prepared catalysts. The test was done over a range of temperature (150-280 ℃), hydrogen pressure (20-60 bar), a catalyst loading of 100 mg, and decahydronaphthalene (decalin) and n-decane as the solvents. Catalysts were activated *ex-situ* in a tubular furnace at 500 ℃ for 3 hours prior to the reaction. During the catalytic test, variation seen in conversion and product distribution showed the influence of the support properties, particularly, the porosity and acidity. Acidity of the support in combination with the active metal sites demonstrated a synergetic effect that favours the hydrodeoxygenation reaction of anisole. The catalytic

activity increased with rising reaction temperature and hydrogen partial pressure to the optimum at 200 ℃ and 60 bar. Changing the reaction solvent from decalin to n-decane did not show any noticeable difference in term of anisole conversion and product distribution. Similarly, introducing Zn as the second metal on the catalyst did not show desirable outcome as the catalytic activity and selectivity to liquid products decreased. The order of catalytic activity decrease as follows; hie-Ni/ZSM-5 > mic-Ni/ZSM-5 > Ni/SiO_2 > mic-NiZn/ZSM-5 > mic-Zn/ZSM-5, with the highest anisole conversion of 100% in 120 minutes over the hie-Ni/ZSM-5 catalyst. A simplified reaction scheme proposed shows the transformation of anisole proceeds via either direct deoxygenation-hydrogenation or isomerization-direct deoxygenation route, with total hydrodeoxygenation on all the catalysts and complete hydrodearomatisation on hie-Ni/ZSM-5, but only 84.6% over Ni/SiO_2. The dominant product on mic-Ni/ZSM-5 and hie-Ni/ZSM-5 catalysts was cyclohexane, whereas toluene was the major product from Ni/SiO_2 catalyst. Notably, the catalyst reusability test revealed improved catalytic activity and very good stability in terms of liquid product selectivity over the hie-Ni/ZSM-5 catalyst. Hence, compared with the mic-ZSM-5 and SiO_2 supports, the 0.2 M NaOH-treated sample proved to be the best solid-support candidate for anisole HDO. Subsequently, a kinetic analysis was carried out over the hie-Ni/ZSM-5 catalyst. The reaction order, activation energy, enthalpy, and entropy of adsorption were determined. The Langmuir adsorption isotherm and pseudo-first-order kinetic models were the best that described the HDO of anisole over the hie-Ni/ZSM-5 catalyst.

8.1.3 HDO of benzoic acid

The hydrodeoxygenation of benzoic acid as a typical bio-oil model compound has been reported. The study was carried out in a 0.1 L high-pressure batch reactor at a temperature of 310–340 ℃, a pressure of 20–60 bar hydrogen with tetralin as solvent. The effects of

reaction temperature, pressure, and initial concentration of benzoic acid on conversion and product distribution were investigated over mic-Ni/ZSM-5, hie-Ni/ZSM-5 and Ni/SiO_2 catalysts. The highest conversion of benzoic acid, 97%, was recorded from the hie-Ni/ZSM-5 catalyst with the largest number of acid sites and better metal dispersion. The mesoporous Ni/SiO_2 which is nearly neutral compared to the ZSM-5-based catalysts, shows a higher benzoic acid conversion (91.5%) than the microporous nickel-zeolite catalyst, mic-Ni/ZSM-5 (84.3%). It is obvious that although acid sites are important in the reaction, a synergy between the support acidity and the metal site is crucial. It is believed that the high mesoporous nature of the SiO_2 supports easy access for the reacting molecule (bulk benzoic acid) to the available catalytic active sites. For all the catalysts investigated herein, conversion increased with an increase in reaction temperature and pressure. The products were benzaldehyde, benzyl alcohol, toluene, and benzene on mic-Ni/ZSM-5 and SiO_2 catalysts. Cyclohexane was observed in addition to the aforementioned products during the HDO of benzoic acid over the hie-Ni/ZSM-5 catalyst. It is proposed from these products that benzoic acid HDO on the studied catalysts proceeds through deoxygenation to benzaldehyde, hydrogenation to benzyl alcohol, deoxygenation to toluene, demethylation to benzene, and finally hydrogenation of benzene to cyclohexane. Additionally, the formation of benzene could be via a radical mechanism leading to the direct decarboxylation of benzoic acid to benzene over the highly acidic zeolite-based catalysts. Alternatively, the formation of cyclohexane on the hie-Ni/ZSM-5 catalyst may likely occur via total hydrogenation of benzoic acid to cyclohexane-carboxylic acid, which subsequently decarboxylates to cyclohexane. In general, a high degree of HDO (X_{HDO} > 70%) was seen on all the catalysts, while hydrodearomatisation was only observed on the hie-ZSM-5 catalyst. On the other hand, a kinetic study of benzoic acid HDO over a hie-Ni/ZSM-5 catalyst was covered. The rate of benzoic acid disappearance on the hie-Ni/ZSM-5 was found to be non-linear with a

fractional order 0.21 – 0.55. Furthermore, a kinetic model was developed using the LHHW approach. A mechanism assuming dual-site adsorption of dissociatively adsorbed hydrogen was shown to be the most accurate representation (coefficient of determination, R^2 > 99%) of the three-phase benzoic acid HDO carried out with the 5 wt.% hie-Ni/ZSM-5 catalyst. The observed activation energy from the model was 137.2 kJ mol^{-1}.

8.1.4 HDO of mixed bio-oil model compounds

The study of some selected model compounds composed of phenolic ether (anisole) and carboxylic acid (benzoic acid) as a blend yielded some essential understanding of the reaction mechanisms. The reaction was carried out in a 0.1 L high-pressure batch reactor at 300–340 ℃ and 60 bar hydrogen partial pressure. The effects of temperature on the competitive adsorption and cross-reactivity on conversion and product distribution during the HDO have been demonstrated. Higher conversion of benzoic acid compared to anisole was recorded, which increased with an increase in the reaction temperature. This was attributed to the strong adsorption, leading to the occupation of most of the available active sites on the hie-Ni/ZSM-5 catalyst, by the benzoic acid. Products identified were benzaldehyde, benzyl alcohol, toluene, benzene, and cyclohexane. Transformation proceeded via deoxygenation, decarboxylation, hydrogenation, and demethylation of benzoic acid and direct deoxygenation-hydrogenation pathway for anisole. A decrease in the selectivity of the undesirable and intermediate product, benzaldehyde, was observed with the increase in the reaction temperature from 300 to 340 ℃. However, while the selectivity of benzene increased with temperature, a trace amount of undesired benzyl alcohol intermediate appeared at 340 ℃.

8.1.5 HDO of sewage sludge oil

Hydrodeoxygenation of sewage sludge oil (real bio-oil) have been successfully carried out in a 0.1 L high-pressure batch reactor at 350 ℃ and 60 bar hydrogen. The levels of oxygen, nitrogen, and sulphur in the bio-oil were noticeably reduced following treatment with the hie-Ni/ZSM-5, Ni/SiO_2, and the commercial TK-341 catalysts. The highest degree of HDO was obtained from Ni/SiO_2 (unsulfided) catalysts. Upon sulfidation, an increase in the degree of HDN was observed in all the three catalysts. However, the extent of HDO only increased over the commercial TK-341 catalyst. The constituents of the liquid products were mostly monocyclic (about 70%) and bicyclic aromatics. Since sulphur is one of the components aimed at eliminating, employing a sulfided catalyst has a significant risk of introducing more sulphur into the end product. With further testing on stability and reusability, the mesoporous, Ni-based, and unsulfided catalysts could be promising choices for the HDO of real bio-oil.

8.2 Recommendations

Due to limitations, a number of experiments and analyses could not be completed within the confines of this study. As a result, the following recommendations are made for future work:

- This study should be repeated using a continuous flow reactor, catalytic activity and kinetic parameters should also be compared.
- With a clear evidence of the effect of mesoporosity, there is need to explore other mesoporous supports for the catalyst preparation.
- Best catalytic activity was seen on the 5 wt.% nickel catalyst, which decreased with decreasing nickel loading to 3 wt.% and the addition of 2 wt.% zinc. There is need to investigate more Ni/Zn ratios.

- Previous research has demonstrated the effects of Co and Mo in the bio-oil upgrading application, hence combination of either of these metals with Ni on SiO_2 or hie-Ni/ZSM-5 support should be explored.
- More studies are needed for the real bio-oil. There is need to investigate the effect of temperature, hydrogen pressure, and the addition of solvent during the upgrading operation.
- The catalysts developed and used herein for real bio-oil upgrading (Ni/SiO_2 and hie-Ni/ZSM-5) should be utilize for a different bio-oil and compare the results with the one obtained in this study.
- Having extensively studied the individual model compounds of the major functional groups in bio-oil, there is a need for more research on the blends of model compounds. This will provide a better understanding of how bio-oil model compounds behave singly and in mixtures during HDO. In addition, a crucial piece of information on how the process can be efficiently carried out and catalysts effective developed will be generated.
- For the HDO of real bio-oil, a reactor with higher maximum operating conditions compared to the one deployed herein should be used. This is to enable reaction at higher temperature (400 – 600 ℃) and a high temperature catalyst activation. This is because the H_2-TPR analysis revealed that temperature higher than 350 ℃ is needed for complete reduction of the Ni-based catalyst.
- Sulfided catalyst have been extensively tested and the catalyst stability appears to be an issue despite the fact that complete HDO could be achieved. There is need for further studies on the mesoporous SiO_2 and ZSM-5 supports with respect to the stability and reusability. With comparable degree of HDO, HDN, and HDS to the

commercial NiMo/Al_2O_3 catalyst, addition of 2nd metal could also be considered for further investigation.

- Finally, based on the understanding of the different chemistries in the complex system, a rational design of the HDO catalysts, comprising of a support with optimum mesoporosity, appropriate acid sites, and a right combination of active metal(s), is highly recommended.

REFERENCES

Abdelsayed, V., Smith, M. W., and Shekhawat, D. (2015). Investigation of the stability of Zn-based HZSM-5 catalysts for methane dehydroaromatization. *Applied Catalysis A: General*, *505*, 365–374. https://doi.org/10.1016/j.apcata.2015.08.017

Abdulhamid, Z., and Muhammad, A. I. (2022). Adsorption Kinetics and Isotherm Models : A Review. *Caliphate Journal of Science and Technology (CaJoST). 3121*, 20–26. https://dx.doi.org/10.4314/cajost.v4i1.3

Adhikari, S., Nam, H., and Chakraborty, J. P. (2018). Conversion of solid wastes to fuels and chemicals through pyrolysis. In *Waste Biorefinery: Potential and Perspectives*. Elsevier B.V. https://doi.org/10.1016/B978-0-444-63992-9.00008-2

Al Soubaihi, R. M., Saoud, K. M., Ye, F., Zar Myint, M. T., Saeed, S., and Dutta, J. (2020). Synthesis of hierarchically porous silica aerogel supported Palladium catalyst for low-temperature CO oxidation under ignition/extinction conditions. *Microporous and Mesoporous Materials*, *292*(September 2019), 109758. https://doi.org/10.1016/j.micromeso.2019.109758

Alalwan, H. A., Alminshid, A. H., and Aljaafari, H. A. S. (2019). Promising evolution of biofuel generations. Subject review. *Renewable Energy Focus*, *28*(March 2019), 127–139. https://doi.org/10.1016/j.ref.2018.12.006

Albero, J., and García, H. (2016). Metal Organic Frameworks as Catalysts for Organic Reactions. In New Materials for Catalytic Applications. Elsevier B.V. https://doi.org/10.1016/B978-0-444-63587-7.00002-0

Alghamdi, A. A., Al-Odayni, A. B., Abduh, N. A. Y., Alramadhan, S. A., Aljboar, M. T., and Saeed, W. S. (2021). Adsorptive Performance of Polypyrrole-Based KOH-Activated Carbon for the Cationic Dye Crystal Violet: Kinetic and Equilibrium Studies. *Adsorption Science and Technology*, *2021*. https://doi.org/10.1155/2021/5527594

Alhanash, A. M., Atran, A. A., Eissa, M., Benaissa, M., and Hamdy, M. S. (2019). Liquid phase hydrogenation of MIBK over M/CsPW (M = Ag, Ru, Pt, and Pd). *Catalysts*, *9*(1), 1–10. https://doi.org/10.3390/catal9010047

Aliu, E., Hart, A., and Wood, J. (2019). Kinetics of Vanillin Hydrodeoxygenation Reaction in an Organic Solvent Using a Pd/C Catalyst [Research-article]. *Industrial and Engineering Chemistry Research*, *58*(33), 15162–15172. https://doi.org/10.1021/acs.iecr.9b02907

Amutova, F., Jurjanz, S., Akhmetsadykov, N., Kazankapova, M., Razafitianamaharavo, A., Renard, A., Nurseitova, M., Konuspayeva, G., & Delannoy, M. (2023). Adsorption of organochlorinated pesticides: Adsorption kinetic and adsorption isotherm study. *Results in Engineering*, *17*(October 2022). https://doi.org/10.1016/j.rineng.2022.100823

Anderson, J. R. (1975). Structure of metallic catalysts. *Academic Press, Lodon*, *55*, 86. https://api.semanticscholar.org/CorpusID:92070093

April, M., Kowanga, K. D., Gatebe, E., Mauti, G. O., and Mauti, E. M. (2016). Kinetic , sorption isotherms , pseudo-first-order model and pseudo-second-order model studies of Cu (II) and Pb (II) using defatted Moringa oleifera seed powder. *The Journal of*

Phytopharmacology, *5*(2), 71–78. doi:10.31254/phyto.2016.5206

Aqsha, A., Katta, L., Tijani, M. M., de Oliveira, C. F., and Mahinpey, N. (2021). Investigation of catalytic hydrodeoxygenation of anisole as bio-oil model compound over Ni-Mo/TiO2 and Ni-V/TiO2 catalysts: Synthesis, kinetic, and reaction pathways studies. *Canadian Journal of Chemical Engineering*, *99*(5), 1094–1106. https://doi.org/10.1002/cjce.23912

Armenante, P. M., Nagamine, E. U., and Susanto, J. (1998). Determination of correlations to predict the minimum agitation speed for complete solid suspension in agitated vessels. *Canadian Journal of Chemical Engineering*, *76*(3), 413–419. https://doi.org/10.1002/cjce.5450760310

Arora, P., Grennfelt, E. L., Olsson, L., and Creaser, D. (2019). Kinetic study of hydrodeoxygenation of stearic acid as model compound for renewable oils. *Chemical Engineering Journal*, *364*(October 2018), 376–389. https://doi.org/10.1016/j.cej.2019.01.134

Auersvald, M., Straka, P., Shumeiko, B., and Staš, M. (2017). Study of catalytic hydrotreatment of pyrolysis bio-oil. In *2nd International Conference on Companion Technology (ICCT 2017), Ulm, Germany*

Baruwati, B. (2007). Studies on the synthesis, characterization, surface modification and application of nanocrystalline nickel ferrite. *India Institute of Chemical Technology Hyderabad*. https://www.researchgate.net/publication/49177963

Bashir, M. A., Lima, S., Jahangiri, H., Majewski, A. J., Hofmann, M., Hornung, A., and Ouadi, M. (2022). A step change towards sustainable aviation fuel from sewage sludge. *Journal of Analytical and Applied Pyrolysis*, *163*(September 2021), 105498. https://doi.org/10.1016/j.jaap.2022.105498

Basu, P. (2013). Production of Synthetic Fuels and Chemicals from Biomass. In *Biomass Gasification, Pyrolysis and Torrefaction*. Elsevier Inc. https://doi.org/10.1016/b978-0-12-396488-5.00011-3

Benaliouche, F., Boucheffa, Y., Ayrault, P., Mignard, S., and Magnoux, P. (2008). NH_3-TPD and FTIR spectroscopy of pyridine adsorption studies for characterization of Ag- and Cu-exchanged X zeolites. *Microporous and Mesoporous Materials*, *111*(1–3), 80–88. https://doi.org/10.1016/j.micromeso.2007.07.006

Berenguer, A., Bennett, J. A., Hunns, J., Moreno, I., Coronado, J. M., Lee, A. F., Pizarro, P., Wilson, K., and Serrano, D. P. (2018). Catalytic hydrodeoxygenation of m-cresol over Ni2P/hierarchical ZSM-5. *Catalysis Today*, *304*(July 2017), 72–79. https://doi.org/10.1016/j.cattod.2017.08.032

Berenguer, A., Gutiérrez-Rubio, S., Linares, M., Ochoa-Hernández, C., Moreno, I., García-Fierro, J. L., Coronado, J. M., Serrano, D. P., and Pizarro, P. (2019). On the Feasibility of Using Hierarchical ZSM-5 and Beta Zeolites as Supports of Metal Phosphides for Catalytic Hydrodeoxygenation of Phenol. *Energy Technology*, *7*(6), 1–13. https://doi.org/10.1002/ente.201900214

Bhoi, P. R., Ouedraogo, A. S., Soloiu, V., and Quirino, R. (2020). Recent advances on catalysts for improving hydrocarbon compounds in bio-oil of biomass catalytic pyrolysis. *Renewable and Sustainable Energy Reviews*, *121*(January), 109676. https://doi.org/10.1016/j.rser.2019.109676

Bullen, J., Saleesongsom, S., and Weiss, D. J. (2020). A revised pseudo-second order kinetic model for adsorption, sensitive to changes in sorbate and sorbent concentrations. *ChemRxiv*, 1–27. https://doi.org/10.26434/chemrxiv.12008799

Bykova, M. V., Zavarukhin, S. G., Trusov, L. I., and Yakovlev, V. A. (2013). Guaiacol hydrodeoxygenation kinetics with catalyst deactivation taken into consideration. *Kinetics and Catalysis*, *54*(1), 40–48. https://doi.org/10.1134/S0023158413010023

Caicedo-Realpe, R., and Pérez-Ramírez, J. (2010). Mesoporous ZSM-5 zeolites prepared by a two-step route comprising sodium aluminate and acid treatments. *Microporous and Mesoporous Materials*, *128*(1–3), 91–100. https://doi.org/10.1016/j.micromeso.2009.08.009

Čejka, J., and Vinu, A. (2009). Catalysis by Mesoporous Molecular Sieves. *Ordered Porous Solids*, 669–692. https://doi.org/10.1016/B978-0-444-53189-6.00025-1

Chaihad, N., Karnjanakom, S., Kurnia, I., Yoshida, A., Abudula, A., Reubroycharoen, P., and Guan, G. (2019). Catalytic upgrading of bio-oils over high alumina zeolites. *Renewable Energy*, *136*, 1304–1310. https://doi.org/10.1016/j.renene.2018.09.102

Chang, J., Danuthai, T., Dewiyanti, S., Wang, C., and Borgna, A. (2013). Hydrodeoxygenation of guaiacol over carbon-supported metal catalysts. *ChemCatChem*, *5*(10), 3041–3049. https://doi.org/10.1002/cctc.201300096

Che, Q., Yang, M., Wang, X., Yang, Q., Chen, Y., Chen, X., Chen, W., Hu, J., Zeng, K., Yang, H., and Chen, H. (2019). Preparation of mesoporous ZSM-5 catalysts using green templates and their performance in biomass catalytic pyrolysis. *Bioresource Technology*, *289*(June), 121729. https://doi.org/10.1016/j.biortech.2019.121729

Cheah, Y. W., Salam, M. A., Sebastian, J., Ghosh, S., Arora, P., Öhrman, O., Olsson, L., and Creaser, D. (2023). Upgrading of triglycerides, pyrolysis oil, and lignin over metal sulfide catalysts: A review on the reaction mechanism, kinetics, and catalyst deactivation. *Journal of Environmental Chemical Engineering*, *11*(3). https://doi.org/10.1016/j.jece.2023.109614

Chen, D., Cen, K., Jing, X., Gao, J., Li, C., and Ma, Z. (2017). An approach for upgrading biomass and pyrolysis product quality using a combination of aqueous phase bio-oil washing and torrefaction pretreatment. *Bioresource Technology*, *233*, 150–158. https://doi.org/10.1016/j.biortech.2017.02.120

Chen, G., Liu, J., Li, X., Zhang, J., Yin, H., and Su, Z. (2020). Investigation on catalytic hydrodeoxygenation of eugenol blend with light fraction in bio-oil over Ni-based catalysts. *Renewable Energy*, *157*, 456–465. https://doi.org/10.1016/j.renene.2020.05.040

Chen, J., Ma, Z., Qin, J., Chen, M., Dong, L., Mao, W., Zhou, X., Long, Y., and Ma, J. (2023). Highly efficient and selective hydrodeoxygenation of guaiacol to cyclohexanol over a rod-like CoNi-C catalyst. *Fuel*, *353*(May), 129216. https://doi.org/10.1016/j.fuel.2023.129216

Chen, M., Li, C., Li, G. R., Chen, Y. L., and Zhou, C. G. (2019). *In-situ* preparation of well-dispersed CuO nanocatalysts in heavy oil for catalytic aquathermolysis. *Petroleum Science*, *3*(0123456789). https://doi.org/10.1007/s12182-019-0300-3

Chen, X. (2019). Selective hydrogenation of unsaturated carboxylic acids. *The University of*

Manchester (United Kingdom).

Cheng, S., Wei, L., Zhao, X., and Julson, J. (2016). Application, deactivation, and regeneration of heterogeneous catalysts in bio-oil upgrading. *Catalysts*, *6*(12). https://doi.org/10.3390/catal6120195

Coker, A. (2001). Modeling of chemical kinetics and reactor design. In *Technology*. http://books.google.com/books?hl=enandlr=andid=pnNc496xxEMCandoi=fndandpg=PR13anddq=Modeling+of+Chemical+Kinetics+and+Reactor+Designandots=_aC2EGZ4LKandsig=9P2B8npQ46UldNxbKr9bJs9qLbQ

Da Silva, A. L. M., Den Breejen, J. P., Mattos, L. V., Bitter, J. H., De Jong, K. P., and Noronha, F. B. (2014). Cobalt particle size effects on catalytic performance for ethanol steam reforming - Smaller is better. *Journal of Catalysis*, *318*, 67–74. https://doi.org/10.1016/j.jcat.2014.07.020

Dahman, Y., Syed, K., Begum, S., Roy, P., and Mohtasebi, B. (2019). Biofuels: Their characteristics and analysis. In *Biomass, Biopolymer-Based Materials, and Bioenergy*. Elsevier Ltd. https://doi.org/10.1016/B978-0-08-102426-3.00014-X

Dauda, I. B., Yusuf, M., Gbadamasi, S., Bello, M., Atta, A. Y., Aderemi, B. O., and Jibril, B. Y. (2020). Highly Selective Hierarchical ZnO/ZSM-5 Catalysts for Propane Aromatization [Research-article]. *ACS Omega*, *5*, 2725–2733. https://doi.org/10.1021/acsomega.9b03343

De Lange, M. W., Van Ommen, J. G., and Lefferts, L. (2002). Deoxygenation of benzoic acid on metal oxides: 2. Formation of byproducts. *Applied catalysis A: general*, *231*(1-2), 17-26. https://doi.org/10.1016/S0926-860X(01)00702-5

Deshmukh, M. K. G., Sameeroddin, M., Abdul, D., and Abdul Sattar, M. (2023). Renewable energy in the 21st century: A review. *Materials Today: Proceedings*, *80*, 1756–1759. https://doi.org/10.1016/j.matpr.2021.05.501

Devarajulu, C., and Loganathan, M. (2016). Effect of impeller clearance and liquid level on critical impeller speed in an agitated vessel using different axial and radial impellers. *Journal of Applied Fluid Mechanics*, *9*(6), 2753–2761. https://doi.org/10.29252/jafm.09.06.24824

Díaz, M., Vega, A., and Coca, J. (1987). Correlation for the estimation of gas-liquid diffusivity. *Chemical Engineering Communications*, *52*(4-6), 271-281. https://doi.org/10.1080/00986448708911872

Ding, J., Wang, M., Peng, L., Xue, N., Wang, Y., and He, M. Y. (2015). Combined Desilication and phosphorus modification for high-silica ZSM-5 zeolite with related study of hydrocarbon cracking performance. *Applied Catalysis A: General*, *503*, 147–155. https://doi.org/10.1016/j.apcata.2015.07.011

Ding, X., Yuan, X., Leng, L., Huang, H., Wang, H., Shao, J., Jiang, L., Chen, X., and Zeng, G. (2017). Upgrading Sewage Sludge Liquefaction Bio-Oil by Microemulsification: The Effect of Ethanol as Polar Phase on Solubilization Performance and Fuel Properties. *Energy and Fuels*, *31*(2), 1574–1582. https://doi.org/10.1021/acs.energyfuels.6b02269

Ding, Y. L., Wang, H. Q., Xiang, M., Yu, P., Li, R. Q., and Ke, Q. P. (2020). The Effect of Ni-ZSM-5 Catalysts on Catalytic Pyrolysis and Hydro-Pyrolysis of Biomass. *Frontiers in Chemistry*, *8*(September), 1–11. https://doi.org/10.3389/fchem.2020.00790

Elahi, S. M., Ahmadi Khoshooei, M., Scott, C. E., Chen, Z., and Pereira-Almao, P. (2019). *In-situ* upgrading of heavy oil using nano-catalysts: A computational fluid dynamics study of hydrogen and vacuum residue injection. *Canadian Journal of Chemical Engineering*, *97*(S1), 1352–1360. https://doi.org/10.1002/cjce.23387

Elliott, D. C., Biller, P., Ross, A. B., Schmidt, A. J., and Jones, S. B. (2015). Hydrothermal liquefaction of biomass: Developments from batch to continuous process. *Bioresource Technology*, *178*, 147–156. https://doi.org/10.1016/j.biortech.2014.09.132

Ezeonu, L., Tang, Z., Qi, Y., Huo, F., Zheng, Y., Koel, B. E., and Podkolzin, S. G. (2023). Adsorption, surface reactions and hydrodeoxygenation of acetic acid on platinum and nickel catalysts. *Journal of Catalysis*, *418*, 190–202. https://doi.org/10.1016/j.jcat.2023.01.013

Falconer, J. L. (1998). X Kinetics and reaction engineering: General considerations in the rational design of chemical reactors. *Bullet Protocol for the Rational Design of Chemical Reactors*. https://www.studocu.com/in/document/anna-university/chemical-engineering/kinetics-and-reaction-engineering/5703221

Fan, S., Zhang, Y., Liu, T., Fu, W., and Li, B. (2022). Microwave-assisted pyrolysis of polystyrene for aviation oil production. *Journal of Analytical and Applied Pyrolysis*, *162*(December 2021), 105425. https://doi.org/10.1016/j.jaap.2021.105425

Fan, X. dong, Wu, Y. jian, Li, Z. yu, Sun, Y., Tu, R., Zhong, P. D., Jiang, E. chen, and Xu, X. wei. (2020). Benzene, toluene and xylene (BTX) from *in-situ* gas phase hydrodeoxygenation of guaiacol with liquid hydrogen donor over bifunctional non-noble-metal zeolite catalysts. *Renewable Energy*, *152*, 1391–1402. https://doi.org/10.1016/j.renene.2020.01.015

Feng, R., Yan, X., Hu, X., Wang, Y., Li, Z., Hou, K., and Lin, J. (2018). Hierarchical ZSM-5 zeolite designed by combining desilication and dealumination with related study of n-heptane cracking performance. *Journal of Porous Materials*, *25*(6), 1743–1756. https://doi.org/10.1007/s10934-018-0587-2

Fogler, H. S. (2004). Chemical reaction engineering. In *The Engineering Handbook, Second Edition*. https://doi.org/10.1201/9781420087567-13

Fogler, H. S. (2006). Elements of Chenzicn 1 Reaction Engineering. In *Bioprocess Engineering*.

Fogler, H. S. (2019). Elements of Chemical Reaction Engineering. In *Series in the Physical and Chemical Engineering Sciences*.

Freitas, I. C., Manfro, R. L., and Souza, M. M. V. M. (2018). Applied Catalysis B : Environmental Hydrogenolysis of glycerol to propylene glycol in continuous system without hydrogen addition over Cu-Ni catalysts. *"Applied Catalysis B, Environmental," 220*, 31–41. https://doi.org/10.1016/j.apcatb.2017.08.030

Fu, Y., Devred, F., Eloy, P., Haynes, T., Singleton, M. L., and Hermans, S. (2022). The effect of Ni particle size and carbon support on catalytic activity for glucose hydrogenation reaction. *Applied Catalysis A: General*, *644*(July), 118833. https://doi.org/10.1016/j.apcata.2022.118833

Gamliel, D. P., Baillie, B. P., Augustine, E., Hall, J., Bollas, G. M., and Valla, J. A. (2018). Nickel impregnated mesoporous USY zeolites for hydrodeoxygenation of anisole.

Microporous and Mesoporous Materials, *261*(October 2017), 18–28. https://doi.org/10.1016/j.micromeso.2017.10.027

Gao, D., Schweitzer, C., Hwang, H. T., and Varma, A. (2014). Conversion of guaiacol on noble metal catalysts: Reaction performance and deactivation studies. *Industrial and Engineering Chemistry Research*, *53*(49), 18658–18667. https://doi.org/10.1021/ie500495z

Garba, M. U., Musa, U., Olugbenga, A. G., Mohammad, Y. S., Yahaya, M., and Ibrahim, A. A. (2018). Catalytic upgrading of bio-oil from bagasse: Thermogravimetric analysis and fixed bed pyrolysis. *Beni-Suef University Journal of Basic and Applied Sciences*, *7*(4), 776–781. https://doi.org/10.1016/j.bjbas.2018.11.004

García, B., Moreno, J., Iglesias, J., Melero, J. A., and Morales, G. (2019). Transformation of Glucose into Sorbitol on Raney Nickel Catalysts in the Absence of Molecular Hydrogen: Sugar Disproportionation vs Catalytic Hydrogen Transfer. *Topics in Catalysis*, *62*(5–6), 570–578. https://doi.org/10.1007/s11244-019-01156-3

Garzon-Roman, A., Milosevic, O., and Rabanal, M. E. (2020). Morphological, structural, and functional properties of vertically aligned carbon nanotubes deposited on porous silicon layers by ultrasonic spray pyrolysis. *Microporous and Mesoporous Materials*, *292*(September 2019), 109738. https://doi.org/10.1016/j.micromeso.2019.109738

Gea, S., Hutapea, Y. A., Piliang, A. F. R., Pulungan, A. N., Rahayu, R., Layla, J., Tikoalu, A. D., Wijaya, K., and Saputri, W. D. (2023). A Comprehensive Review of Experimental Parameters in Bio-oil Upgrading from Pyrolysis of Biomass to Biofuel Through Catalytic Hydrodeoxygenation. *Bioenergy Research*, *16*(1), 325–347. https://doi.org/10.1007/s12155-022-10438-w

Ghampson, I. T., Sepúlveda, C., Dongil, A. B., Pecchi, G., García, R., Fierro, J. L. G., and Escalona, N. (2016). Phenol hydrodeoxygenation: Effect of support and Re promoter on the reactivity of Co catalysts. *Catalysis Science and Technology*, *6*(19), 7289–7306. https://doi.org/10.1039/c6cy01038e

Ghampson, I. Tyrone, Canales, R., and Escalona, N. (2018). A study of the hydrodeoxygenation of anisole over Re-MoOx/TiO2 catalyst. *Applied Catalysis A: General*, *549*(October 2017), 225–236. https://doi.org/10.1016/j.apcata.2017.10.009

Ghashghaee, M., Shirvani, S., Ghambarian, M., and Eidi, A. (2019). Two-stage thermocatalytic upgrading of fuel oil to olefins and fuels over a nanoporous hierarchical acidic catalyst. *Petroleum Science and Technology*, *37*(16), 1910–1916. https://doi.org/10.1080/10916466.2018.1463257

Goodarzi, F., Herrero, I. P., Kalantzopoulos, G. N., Svelle, S., Lazzarini, A., Beato, P., Olsbye, U., and Kegnæs, S. (2020). Synthesis of mesoporous ZSM-5 zeolite encapsulated in an ultrathin protective shell of silicalite-1 for MTH conversion. *Microporous and Mesoporous Materials*, *292*(September 2019), 109730. https://doi.org/10.1016/j.micromeso.2019.109730

Gorzin, F., and Yaripour, F. (2019). Production of light olefins from methanol over modified H-ZSM-5: effect of metal impregnation in high-silica zeolite on product distribution. *Research on Chemical Intermediates*, *45*(2), 261–285. https://doi.org/10.1007/s11164-018-3601-z

Guo, M., Kong, X., Li, C., and Yang, Q. (2021). Hydrogenation of benzoic acid derivatives

over Pt/TiO2 under mild conditions. *Communications Chemistry*, *4*(1), 1–10. https://doi.org/10.1038/s42004-021-00489-z

Gutiérrez-Rubio, S., Moreno, I., Serrano, D. P., and Coronado, J. M. (2019). Hydrotreating of Guaiacol and Acetic Acid Blends over Ni2P/ZSM-5 Catalysts: Elucidating Molecular Interactions during Bio-Oil Upgrading. *ACS Omega*, *4*(25), 21516–21528. https://doi.org/10.1021/acsomega.9b03221

Guvenc, C., Alan, E., Degirmencioglu, P., Celik Ozcan, M., Pekmezci Karaman, B., and Oktar, N. (2023). Catalytic upgrading of bio-oil model mixtures in the presence of microporous HZSM-5 and γ-Al2O3 based Ni, Ta and Zr catalysts. *Fuel*, *350*(June). https://doi.org/10.1016/j.fuel.2023.128870

Haghighat, M., Majidian, N., Hallajisani, A., and samipourgiri, M. (2020). Production of bio-oil from sewage sludge: A review on the thermal and catalytic conversion by pyrolysis. *Sustainable Energy Technologies and Assessments*, *42*(March). https://doi.org/10.1016/j.seta.2020.100870

Han, W., Jia, Y., Xiong, G., and Yang, W. (2007). Synthesis of hierarchical porous materials with ZSM-5 structures via template-free sol-gel method. *Science and Technology of Advanced Materials*, *8*(1–2), 101–105. https://doi.org/10.1016/j.stam.2006.11.015

Hansen, S., Mirkouei, A., and Diaz, L. A. (2020). A comprehensive state-of-technology review for upgrading bio-oil to renewable or blended hydrocarbon fuels. *Renewable and Sustainable Energy Reviews*, *118*(October 2019), 109548. https://doi.org/10.1016/j.rser.2019.109548

Haul, R., Gregg, J. S., and Sing, K. S. W. (1982). Adsorption, Surface Area and Porosity. 2. Auflage, Academic Press, London 1982. 303 Seiten, Preis: \$ 49.50. *Berichte Der Bunsengesellschaft Für Physikalische Chemie*, *86*(10), 957. https://doi.org/https://doi.org/10.1002/bbpc.19820861019

He, L., Xin, Z., Gao, W., Gu, J., and Meng, X. (2020). Highly efficient porous Ni/SiO_2 catalysts prepared by electrospinning method for CO methanation. *Huagong Xuebao/CIESC Journal*, *71*(11), 5007–5015. https://doi.org/10.11949/0438-1157.20200251

Heracleous, E., Vassou, M., Lappas, A. A., Rodriguez, J. K., Chiaberge, S., and Bianchi, D. (2022). Understanding the Upgrading of Sewage Sludge-Derived Hydrothermal Liquefaction Biocrude via Advanced Characterization. *Energy and Fuels*, *36*(19), 12010–12020. https://doi.org/10.1021/acs.energyfuels.2c01746

Hill, C. G. (2014). *An Introduction to Chemical Engineering Kinetics and Reactor Design*. John Wiley and Sons.

Holm, M. S., Taarning, E., Egeblad, K., and Christensen, C. H. (2011). Catalysis with hierarchical zeolites. *Catalysis Today*, *168*(1), 3–16. https://doi.org/10.1016/j.cattod.2011.01.007

Höök, M. (2009). Depletion and decline curve analysis in crude oil production. *Uppsala University*, *May*, 112. https://doi.org/10.1002/apj.212

Hosseinpour, M., Akizuki, M., Yoko, A., Oshima, Y., and Soltani, M. (2020). Novel synthesis and characterization of Fe-ZSM-5 nanocrystals in hot compressed water for selective catalytic reduction of NO with NH_3. *Microporous and Mesoporous Materials*,

292(September 2019), 109708. https://doi.org/10.1016/j.micromeso.2019.109708

Hu, X. Q., Liu, Z. K., Hou, Y. X., and Gao, Y. (2020). Single Electron Activation of Aryl Carboxylic Acids. *IScience*, *23*(7), 101266. https://doi.org/10.1016/j.isci.2020.101266

Hummelgård, M. (2009). *In-situ TEM Probing of Nanomaterials*. (Doctoral dissertation, Mid Sweden University). http://urn.kb.se/resolve?urn=urn:nbn:se:miun:diva-8998

Hunns, J. A., Arroyo, M., Lee, A. F., Escola, J. M., Serrano, D., and Wilson, K. (2016). Hierarchical mesoporous Pd/ZSM-5 for the selective catalytic hydrodeoxygenation of m-cresol to methylcyclohexane. *Catalysis Science and Technology*, *6*(8), 2560–2564. https://doi.org/10.1039/c5cy02072g

Ighalo, J. O., and Adeniyi, A. G. (2020). A comprehensive review of water quality monitoring and assessment in Nigeria. *Chemosphere*, *260*, 127569. https://doi.org/10.1016/j.chemosphere.2020.127569

Ivanova, I. I., Kuznetsov, A. S., Knyazeva, E. E., Fajula, F., Thibault-Starzyk, F., Fernandez, C., and Gilson, J. P. (2011). Design of hierarchically structured catalysts by mordenites recrystallization: Application in naphthalene alkylation. *Catalysis Today*, *168*(1), 133–139. https://doi.org/10.1016/j.cattod.2010.11.091

Jahromi, H., and Agblevor, F. (2017). Hydrodeoxygenation of acetic acid as a model compound for the aqueous phase catalytic pyrolysis oils. https://digitalcommons.usu.edu/bioeng_facpub/167/

Jia, Q., Teng, X., Yu, S., Si, Z., Li, G., Zhou, M., Cai, D., Qin, P., and Chen, B. (2019). Production of furfural from xylose and hemicelluloses using tin-loaded sulfonated diatomite as solid acid catalyst in biphasic system. *Bioresource Technology Reports*, *6*(January), 145–151. https://doi.org/10.1016/j.biteb.2019.03.001

Jia, Y., Wang, J., Zhang, K., Liu, S., Chen, G., Yang, Y., Ding, C., and Liu, P. (2017). Catalytic conversion of methanol to aromatics over nano-sized HZSM-5 zeolite modified by $ZnSiF6{\cdot}6H_2O$. *Catalysis Science and Technology*, *7*(8), 1776–1791. https://doi.org/10.1039/c7cy00143f

Jin, W., Pastor-Pérez, L., Shen, D. K., Sepúlveda-Escribano, A., Gu, S., and Ramirez Reina, T. (2019). Catalytic Upgrading of Biomass Model Compounds: Novel Approaches and Lessons Learnt from Traditional Hydrodeoxygenation – a Review. *ChemCatChem*, *11*(3), 924–960. https://doi.org/10.1002/cctc.201801722

Kadarwati, S., Hu, X., Gunawan, R., Westerhof, R., Gholizadeh, M., Hasan, M. D. M., and Li, C. Z. (2017). Coke formation during the hydrotreatment of bio-oil using NiMo and CoMo catalysts. *Fuel Processing Technology*, *155*, 261–268. https://doi.org/10.1016/j.fuproc.2016.08.021

Kathiraser, Y., Oemar, U., Saw, E. T., Li, Z., and Kawi, S. (2015). Kinetic and mechanistic aspects for CO2 reforming of methane over Ni based catalysts. *Chemical Engineering Journal*, *278*, 62–78. https://doi.org/10.1016/j.cej.2014.11.143

Kay Lup, A. N., Abnisa, F., Daud, W. M. A. W., and Aroua, M. K. (2017). A review on reaction mechanisms of metal-catalyzed deoxygenation process in bio-oil model compounds. *Applied Catalysis A: General*, *541*(May), 87–106. https://doi.org/10.1016/j.apcata.2017.05.002

Keav, S., Martin, A., Barbier, J., and Duprez, D. (2010). Deactivation and reactivation of

noble metal catalysts tested in the Catalytic Wet Air Oxidation of phenol. *Catalysis Today*, *151*(1–2), 143–147. https://doi.org/10.1016/j.cattod.2010.01.025

Kesavan, J. K., Luisetto, I., Tuti, S., Meneghini, C., Iucci, G., Battocchio, C., Mobilio, S., Casciardi, S., and Sisto, R. (2018). Nickel supported on YSZ: The effect of Ni particle size on the catalytic activity for CO2 methanation. *Journal of CO2 Utilization*, *23*(September 2017), 200–211. https://doi.org/10.1016/j.jcou.2017.11.015

Khitab, A., Ahmad, S., Khan, R. A., Arshad, M. T., Anwar, W., Tariq, J., Khan, A. S. R., Khan, R. B. N., Jalil, A., and Tariq, Z. (2021). Production of biochar and its potential application in cementitious composites. *Crystals*, *11*(5), 1–22. https://doi.org/10.3390/cryst11050527

Kim, H., Yang, S., Lim, Y. H., Ha, J. M., and Kim, D. H. (2022). Upgrading bio-oil model compound over bifunctional Ru/HZSM-5 catalysts in biphasic system: Complete hydrodeoxygenation of vanillin. *Journal of Hazardous Materials*, *423*(PA), 126525. https://doi.org/10.1016/j.jhazmat.2021.126525

Kim, J. H., Jung, J. M., Cho, S. H., Tsang, Y. F., Wang, C. H., Lee, J., and Kwon, E. E. (2019). Upgrading bio-heavy oil via esterification of fatty acids and glycerol. *Journal of Cleaner Production*, *217*, 633–638. https://doi.org/10.1016/j.jclepro.2019.01.289

Koekkoek, A. J. J., Tempelman, C. H. L., Degirmenci, V., Guo, M., Feng, Z., Li, C., and Hensen, E. J. M. (2011). Hierarchical zeolites prepared by organosilane templating: A study of the synthesis mechanism and catalytic activity. *Catalysis Today*, *168*(1), 96–111. https://doi.org/10.1016/j.cattod.2010.12.033

Kolvenbach, R., Al-Yassir, N., Al-Khattaf, S. S., Gobin, O. C., Ahn, J. H., Jentys, A., and Lercher, J. A. (2011). A comparative study of diffusion of benzene/p-xylene mixtures in MFI particles, pellets and grown membranes. *Catalysis Today*, *168*(1), 147–157. https://doi.org/10.1016/j.cattod.2011.01.037

Kong, A., Liu, M., Zhang, H., Cao, Z., Zhang, J., Li, W., Han, Y., and Fu, Y. (2022). Highly selective electrocatalytic hydrogenation of benzoic acid over Pt/C catalyst supported on carbon fiber. *Chemical Engineering Journal*, *445*(January), 136719. https://doi.org/10.1016/j.cej.2022.136719

Kristensen, T., Hulteberg, C., Blomberg, S., Tunå, P., and Abdelaziz, O. (2022). Parametric Analysis and Optimization of Vanillin Hydrodeoxygenation Over a Sulfided Ni-Mo/δ-Al2O3 Catalyst Under Continuous-Flow Conditions. *Topics in Catalysis*, *0123456789*. https://doi.org/10.1007/s11244-022-01762-8

Kumar, A., Kumar, A., Biswas, B., Kumar, J., Yenumala, S. R., and Bhaskar, T. (2019). Hydrodeoxygenation of m-Cresol over Ru based catalysts: Influence of catalyst support on m-Cresol conversion and methylcyclohexane selectivity. *Renewable Energy*, *xxxx*. https://doi.org/10.1016/j.renene.2019.11.076

Kumar, A., Kumar, A., Biswas, B., Kumar, J., Yenumala, S. R., and Bhaskar, T. (2020). Hydrodeoxygenation of m-Cresol over Ru based catalysts: Influence of catalyst support on m-Cresol conversion and methylcyclohexane selectivity. *Renewable Energy*, *151*, 687–697. https://doi.org/10.1016/j.renene.2019.11.076

Kumar, R., Strezov, V., Lovell, E., Kan, T., Weldekidan, H., He, J., Dastjerdi, B., and Scott, J. (2019). Bio-oil upgrading with catalytic pyrolysis of biomass using Copper/zeolite-Nickel/zeolite and Copper-Nickel/zeolite catalysts. *Bioresource Technology*,

279(January), 404–409. https://doi.org/10.1016/j.biortech.2019.01.067

Kumar, R., Strezov, V., Lovell, E., Kan, T., Weldekidan, H., He, J., Jahan, S., Dastjerdi, B., and Scott, J. (2019). Journal of Analytical and Applied Pyrolysis Enhanced bio-oil deoxygenation activity by Cu / zeolite and Ni / zeolite catalysts in combined *in-situ* and *ex-situ* biomass pyrolysis. *Journal of Analytical and Applied Pyrolysis*, *140*(February), 148–160.

Lawal, A. M., Hart, A., Daly, H., Hardacre, C., and Wood, J. (2019). Catalytic Hydrogenation of Short Chain Carboxylic Acids Typical of Model Compound Found in Bio-Oils. *Industrial and Engineering Chemistry Research*, *58*(19), 7998–8008. https://doi.org/10.1021/acs.iecr.9b01093

Lawan Muhammad, U. (2018). Biofuels as the Starring Substitute to Fossil Fuels. *Petroleum Science and Engineering*, *2*(1), 44. https://doi.org/10.11648/j.pse.20180201.17

Lee, H., Kim, H., Yu, M. J., Ko, C. H., Jeon, J. K., Jae, J., Park, S. H., Jung, S. C., and Park, Y. K. (2016). Catalytic Hydrodeoxygenation of Bio-oil Model Compounds over Pt/HY Catalyst. *Scientific Reports*, *6*, 1–8. https://doi.org/10.1038/srep28765

Lee, H., Kim, Y. M., Lee, I. G., Jeon, J. K., Jung, S. C., Chung, J. Do, Choi, W. G., and Park, Y. K. (2016). Recent advances in the catalytic hydrodeoxygenation of bio-oil. *Korean Journal of Chemical Engineering*, *33*(12), 3299–3315. https://doi.org/10.1007/s11814-016-0214-3

Lee, K., and Yoo, K. S. (2018). Kinetics and optimization of dimethyl carbonate synthesis by transesterification using design of experiment. *Korean Chemical Engineering Research*, *56*(3), 416–420. https://doi.org/10.9713/kcer.2018.56.3.416

Lestari, A. R., Suratmo, and Ulfa, S. M. (2019). Effect of Support on the Hydrodeoxygenation of Phenol using Ni-based Metal Catalysts: Ni/SiO_2, Ni/ZrO_2, and Ni/Al2O3. *IOP Conference Series: Materials Science and Engineering*, *546*(7). https://doi.org/10.1088/1757-899X/546/7/072004

Lewis, D. W. (2004). Template-host interaction and template design. *Computer Modelling of Microporous Materials*, 243–265. https://doi.org/10.1016/B978-012164137-5/50009-1

Li, C., Li, Y., Shao, Y., Zhang, L., Zhang, S., Wang, S., Li, B., Cui, Z., Tang, Y., and Hu, X. (2023). Activation of biomass with volatilized KOH. *Green Chemistry*, *25*(7), 2825–2839. https://doi.org/10.1039/d2gc04245b

Li, F. X., Wang, X. F., Zheng, Y., and Chen, J. X. (2018). Influence of metallic promoters on the performance of Ni/SiO_2 catalyst in the hydrodeoxygenation of anisole. *Ranliao Huaxue Xuebao/Journal of Fuel Chemistry and Technology*, *46*(1), 75–83. https://doi.org/10.1016/s1872-5813(18)30005-7

Li, K., Wang, R., and Chen, J. (2011). Hydrodeoxygenation of anisole over silica-supported Ni2P, MoP, and NiMoP catalysts. *Energy and Fuels*, *25*(3), 854–863. https://doi.org/10.1021/ef101258j

Li, M., Zhao, H., and Lu, Z. Y. (2020). Porphyrin-based porous organic polymer, Py-POP, as a multifunctional platform for efficient selective adsorption and photocatalytic degradation of cationic dyes. *Microporous and Mesoporous Materials*, *292*(September 2019), 109774. https://doi.org/10.1016/j.micromeso.2019.109774

Li, W., Li, F., Wang, H., Liao, M., Li, P., Zheng, J., Tu, C., and Li, R. (2020). Hierarchical

mesoporous ZSM-5 supported nickel catalyst for the catalytic hydrodeoxygenation of anisole to cyclohexane. *Molecular Catalysis*, *480*(September 2019), 110642. https://doi.org/10.1016/j.mcat.2019.110642

Li, W., Wang, H., Wu, X., Betancourt, L. E., Tu, C., Liao, M., Cui, X., Li, F., Zheng, J., and Li, R. (2020). Ni/hierarchical ZSM-5 zeolites as promising systems for phenolic bio-oil upgrading: Guaiacol hydrodeoxygenation. *Fuel*, *274*(March), 117859. https://doi.org/10.1016/j.fuel.2020.117859

Li, Xiangping, Chen, G., Liu, C., Ma, W., Yan, B., and Zhang, J. (2017). Hydrodeoxygenation of lignin-derived bio-oil using molecular sieves supported metal catalysts: A critical review. *Renewable and Sustainable Energy Reviews*, *71*(November 2016), 296–308. https://doi.org/10.1016/j.rser.2016.12.057

Li, Xiaohua, Zhang, X., Shao, S., Dong, L., Zhang, J., Hu, C., and Cai, Y. (2018). Catalytic upgrading of pyrolysis vapor from rape straw in a vacuum pyrolysis system over La/HZSM-5 with hierarchical structure. *Bioresource Technology*, *259*(March), 191–197. https://doi.org/10.1016/j.biortech.2018.03.046

Li, Z., Jiang, E., Xu, X., Sun, Y., and Tu, R. (2020). Hydrodeoxygenation of phenols, acids, and ketones as model bio-oil for hydrocarbon fuel over Ni-based catalysts modified by Al, La and Ga. *Renewable Energy*, *146*, 1991–2007. https://doi.org/10.1016/j.renene.2019.08.012

Liu, L. J., Liu, Y. G., Gao, X., Zhang, R. Q., and Zhai, Y. P. (2017). Hydrodeoxygenation of bio-oil model compounds over amorphous NiB/SiO_2-Al_2O_3 catalyst in oil-water biphasic system. *Ranliao Huaxue Xuebao/Journal of Fuel Chemistry and Technology*, *45*(8), 932–938. https://doi.org/10.1016/s1872-5813(17)30044-0

Liu, X., Yang, M., Deng, Z., Dasgupta, A., and Guo, Y. (2021). Hydrothermal hydrodeoxygenation of palmitic acid over Pt/C catalyst: Mechanism and kinetic modeling. *Chemical Engineering Journal*, *407*(May 2020), 126332. https://doi.org/10.1016/j.cej.2020.126332

Llewellyn, P. (2013). Adsorption by Ordered Mesoporous Materials. In *Adsorption by Powders and Porous Solids: Principles, Methodology and Applications: Second Edition* (2nd ed.). Elsevier Ltd. https://doi.org/10.1016/B978-0-08-097035-6.00013-9

Llewellyn, P., Maurin, G., and Rouquerol, J. (2013). Adsorption by Metal-Organic Frameworks. In *Adsorption by Powders and Porous Solids: Principles, Methodology and Applications: Second Edition* (2nd ed.). Elsevier Ltd. https://doi.org/10.1016/B978-0-08-097035-6.00014-0

Logar, N. Z., Tušar, N. N., Ristic, A., Mali, G., Mazaj, M., and Kaučič, V. (2009). Functionalisation and Structure Characterisation of Porous Silicates and Aluminophosphates. *Ordered Porous Solids*, 101–126. https://doi.org/10.1016/B978-0-444-53189-6.00005-6

Loricera, C. V., Pawelec, B., Infantes-Molina, A., Álvarez-Galván, M. C., Huirache-Acuña, R., Nava, R., and Fierro, J. L. G. (2011). Hydrogenolysis of anisole over mesoporous sulfided CoMoW/SBA-15(16) catalysts. *Catalysis Today*, *172*(1), 103–110. https://doi.org/10.1016/j.cattod.2011.02.037

Losch, P., Hoff, T. C., Kolb, J. F., Bernardon, C., Tessonnier, J. P., and Louis, B. (2017). Mesoporous ZSM-5 zeolites in acid catalysis: Top-down vs. bottom-up approach.

Catalysts, *7*(8). https://doi.org/10.3390/catal7080225

Lovell, E. C., Scott, J., and Amal, R. (2015). Ni-SiO_2 catalysts for the carbon dioxide reforming of methane: Varying support properties by flame spray pyrolysis. *Molecules*, *20*(3), 4594–4609. https://doi.org/10.3390/molecules20034594

Lu, Y., Wang, D., Song, Y., Yang, Q., Fu, M., Yu, D., and Fang, Y. (2015). *Synthesis of Hierarchical-Structured Zn / Mo-HZSM-5 and Its Application in Dimethy Ether Aromatization*. *Ap3er*, 123–126.

Luo, W., Cao, W., Bruijnincx, P. C. A., Lin, L., Wang, A., and Zhang, T. (2019). Zeolite-supported metal catalysts for selective hydrodeoxygenation of biomass-derived platform molecules. *Green Chemistry*, *21*(14), 3744–3768. https://doi.org/10.1039/c9gc01216h

Ma, H., Zhang, W., and Chen, D. (2023). Catalytic hydrodeoxygenation of phenolic compounds over Ru-MoFeP/Al2O3 catalyst. *Catalysis Today*, *408*(October 2022), 50–57. https://doi.org/10.1016/j.cattod.2022.10.001

Ma, Z., Wei, L., Zhou, W., Jia, L., Hou, B., Li, D., and Zhao, Y. (2019). Upgrading of fast pyrolysis bio-oil to drop-in fuel over Ru catalysts. *Journal of the Energy Institute*, *92*(4), 855–860. https://doi.org/10.1016/j.joei.2018.06.013

Madurai Elavarasan, R., Nadarajah, M., Pugazhendhi, R., Sinha, A., Gangatharan, S., Chiaramonti, D., and Abou Houran, M. (2023). The untold subtlety of energy consumption and its influence on policy drive towards Sustainable Development Goal 7. *Applied Energy*, *334*(October 2022), 120698. https://doi.org/10.1016/j.apenergy.2023.120698

Mak, A. T.-C. (1992). *Solid–liquid mixing In Mechanically Agitated Vessels*. (Thesis in Doctor of Philosophy, University of London, *June*, 248. http://onlinelibrary.wiley.com/doi/10.1002/0471451452.ch10/summary

McClure, S. M., Lundwall, M., Yang, F., Zhou, Z., and Goodman, D. W. (2009). Characterization of active sites on Rh/SiO_2 model catalysts. *Journal of Physics Condensed Matter*, *21*(47). https://doi.org/10.1088/0953-8984/21/47/474223

Mevawala, C., Bai, X., Hu, J., and Bhattacharyya, D. (2023). Plant-wide modeling and techno-economic analysis of a direct non-oxidative methane dehydroaromatization process via conventional and microwave-assisted catalysis. *Applied Energy*, *336*(February), 120795. https://doi.org/10.1016/j.apenergy.2023.120795

Moersidik, S. S., Nugroho, R., Handayani, M., Kamilawati, and Pratama, M. A. (2020). Optimization and reaction kinetics on the removal of Nickel and COD from wastewater from electroplating industry using Electrocoagulation and Advanced Oxidation Processes. *Heliyon*, *6*(2), e03319. https://doi.org/10.1016/j.heliyon.2020.e03319

Molina-Conde, L. H., Suárez-Méndez, A., Pérez-Estrada, D. E., and Klimova, T. E. (2023). Mesoporous Ni/Al-MCM-41 catalysts for highly active and selective hydrodeoxygenation of anisole to cyclohexane. *Applied Catalysis A: General*, *663*(June), 119313. https://doi.org/10.1016/j.apcata.2023.119313

Mortensen, P. M., Grunwaldt, J. D., Jensen, P. A., Knudsen, K. G., and Jensen, A. D. (2011). A review of catalytic upgrading of bio-oil to engine fuels. *Applied Catalysis A: General*, *407*(1–2), 1–19. https://doi.org/10.1016/j.apcata.2011.08.046

Mudi, I., Hart, A., Ingram, A., and Wood, J. (2023). Catalytic Hydrodeoxygenation of

Vanillin, a Bio-Oil Model Compound over Renewable Ni/Biochar Catalyst. *Catalysts*, *13*(1). https://doi.org/10.3390/catal13010171

Nada, M., Jayalath, S., Gillan, E. G., Grassian, V. H., and Larsen, S. C. (2019). Zeolites and Mesoporous Silica: From Greener Synthesis to Surface Chemistry of Environmental and Biological Interactions. In *Chemistry of Silica and Zeolite-Based Materials*. Elsevier Inc. https://doi.org/10.1016/b978-0-12-817813-3.00020-1

Nesterov, N. S., Smirnov, A. A., Pakharukova, V. P., Yakovlev, V. A., and Martyanov, O. N. (2021). Advanced green approaches for the synthesis of NiCu-containing catalysts for the hydrodeoxygenation of anisole. *Catalysis Today*, *379*(September 2020), 262–271. https://doi.org/10.1016/j.cattod.2020.09.006

Neto, J. M., Komesu, A., Martins, L. H. da S., Gonçalves, V. O. O., Oliveira, J. A. R. de, and Rai, M. (2019). Third generation biofuels: An overview. *Sustainable Bioenergy: Advances and Impacts*, 283–298. https://doi.org/10.1016/B978-0-12-817654-2.00010-1

Ni, Y., Sun, A., Wu, X., Hai, G., Hu, J., Li, T., and Li, G. (2011). Preparation of hierarchical mesoporous Zn/HZSM-5 catalyst and its application in MTG reaction. *Journal of Natural Gas Chemistry*, *20*(3), 237–242. https://doi.org/10.1016/S1003-9953(10)60184-3

Nie, L., and Resasco, D. E. (2014). Kinetics and mechanism of m-cresol hydrodeoxygenation on a Pt/SiO 2 catalyst. *Journal of Catalysis*, *317*, 22–29. https://doi.org/10.1016/j.jcat.2014.05.024

Nie, P., Liu, X., Zhang, P., Yuan, X., Li, X., Lin, S., Yin, Z., and Wang, Z. (2021). Quaternary ammonium cellulose promoted synthesis of hollow nano-sized ZSM-5 zeolite as stable catalyst for benzene alkylation with ethanol. *Journal of Materials Science*, *56*(14), 8461–8478. https://doi.org/10.1007/s10853-021-05856-8

Niu, X., Feng, F., Yuan, G., Zhang, X., and Wang, Q. (2019). Hollow MFI zeolite supported pt catalysts for highly selective and stable hydrodeoxygenation of guaiacol to cycloalkanes. *Nanomaterials*, *9*(3). https://doi.org/10.3390/nano9030362

Oasmaa, A., Elliott, D. C., and Korhonen, J. (2010). Acidity of biomass fast pyrolysis bio-oils. *Energy and Fuels*, *24*(12), 6548–6554. https://doi.org/10.1021/ef100935r

Oertel, T., Hutter, F., Helbig, U., and Sextl, G. (2014). Cement and Concrete Research Amorphous silica in ultra-high performance concrete : First hour of hydration. *Cement and Concrete Research*, *58*, 131–142. https://doi.org/10.1016/j.cemconres.2014.01.008

Ogunronbi, K. E., Al-Yassir, N., and Al-Khattaf, S. (2015). New insights into hierarchical metal-containing zeolites; synthesis and kinetic modelling of mesoporous gallium-containing ZSM-5 for propane aromatization. *Journal of Molecular Catalysis A: Chemical*, *406*, 1–18. https://doi.org/10.1016/j.molcata.2015.05.005

Oh, S., Ahn, S. H., and Choi, J. W. (2019). Effect of different zeolite supported bifunctional catalysts for hydrodeoxygenation of waste wood bio-oil. *Journal of the Korean Wood Science and Technology*, *47*(3), 344–359. https://doi.org/10.5658/WOOD.2019.47.3.344

Osatiashtiani, A., Puértolas, B., Oliveira, C. C. S., Manayil, J. C., Barbero, B., Isaacs, M., Michailof, C., Heracleous, E., Pérez-Ramírez, J., Lee, A. F., and Wilson, K. (2017). On the influence of Si:Al ratio and hierarchical porosity of FAU zeolites in solid acid catalysed esterification pretreatment of bio-oil. *Biomass Conversion and Biorefinery*,

7(3), 331–342. https://doi.org/10.1007/s13399-017-0254-x

Oyedun, A. O., Patel, M., Kumar, M., and Kumar, A. (2020). The Upgrading of Bio-Oil via Hydrodeoxygenation. *Chemical Catalysts for Biomass Upgrading*, 35–60. https://doi.org/10.1002/9783527814794.ch2

Pachauri, T., Singla, V., Satsangi, A., Lakhani, A., and Kumari, K. M. (2013). *SEM-EDX Characterization of Individual Coarse Particles in Agra , India*. 523–536. https://doi.org/10.4209/aaqr.2012.04.0095

Pattiya, A., and Suttibak, S. (2012). Production of bio-oil via fast pyrolysis of agricultural residues from cassava plantations in a fluidised-bed reactor with a hot vapour filtration unit. *Journal of Analytical and Applied Pyrolysis*, *95*, 227–235. https://doi.org/10.1016/j.jaap.2012.02.010

Pawelec, B., Loricera, C. V., Geantet, C., Mota, N., Fierro, J. L. G., and Navarro, R. M. (2020). Factors influencing selectivity in the liquid-phase phenol hydrodeoxygenation over ZSM-5 supported Pt/Ir and Pt+Ir catalysts. *Molecular Catalysis*, *482*(October 2019), 110669. https://doi.org/10.1016/j.mcat.2019.110669

Peng, H., Wang, A., He, P., Harrhy, J., Meng, S., and Song, H. (2019). Solvent-free catalytic conversion of xylose with methane to aromatics over Zn-Cr modified zeolite catalyst. *Fuel*, *253*(March), 988–996. https://doi.org/10.1016/j.fuel.2019.05.088

Perego, C., and Peratello, S. (1999). *Experimental methods in catalytic kinetics*. *52*, 133–145.

Petushkov, A., Yoon, S., and Larsen, S. C. (2011). Synthesis of hierarchical nanocrystalline ZSM-5 with controlled particle size and mesoporosity. *Microporous and Mesoporous Materials*, *137*(1–3), 92–100. https://doi.org/10.1016/j.micromeso.2010.09.001

Pierobon, F., Eastin, I. L., and Ganguly, I. (2018). Life cycle assessment of residual lignocellulosic biomass-based jet fuel with activated carbon and lignosulfonate as co-products. *Biotechnology for Biofuels*, *11*(1), 1–18. https://doi.org/10.1186/s13068-018-1141-9

Pintar, A., Berčič, G., and Levec, J. (1998). Catalytic liquid-phase nitrite reduction: kinetics and catalyst deactivation. *AIChE Journal*, *44*(10), 2280–2292. https://doi.org/10.1002/aic.690441017

Pocha, C. K. R., Chia, W. Y., Silvanir, Kurniawan, T. A., Khoo, K. S., and Chew, K. W. (2023). Thermochemical conversion of different biomass feedstocks into hydrogen for power plant electricity generation. *Fuel*, *340*(October 2022), 127472. https://doi.org/10.1016/j.fuel.2023.127472

Qin, Z., Shen, B., Gao, X., Lin, F., Wang, B., and Xu, C. (2011). Mesoporous y zeolite with homogeneous aluminum distribution obtained by sequential desilication-dealumination and its performance in the catalytic cracking of cumene and 1,3,5-triisopropylbenzene. *Journal of Catalysis*, *278*(2), 266–275. https://doi.org/10.1016/j.jcat.2010.12.013

Qu, L., Jiang, X., Zhang, Z., Zhang, X. G., Song, G. Y., Wang, H. L., Yuan, Y. P., and Chang, Y. L. (2021). A review of hydrodeoxygenation of bio-oil: Model compounds, catalysts, and equipment. *Green Chemistry*, *23*(23), 9348–9376. https://doi.org/10.1039/d1gc03183j

Rac, V., Rakíc, V., Miladinovíc, Z., Stošić, D., and Aurouxc, A. (2013). Influence of the desilication process on the acidity of HZSM-5 zeolite. *Thermochimica Acta*, *567*, 73–78.

https://doi.org/10.1016/j.tca.2013.01.008

Rades, S., Hodoroaba, V., Salge, T., and Wirth, T. (2014). *RSC Advances High-resolution imaging with SEM / T-SEM , EDX and morphological and elemental analyses of single*. 49577–49587. https://doi.org/10.1039/c4ra05092d

Raghav, S., and Kumar, D. (2018). *Adsorption Equilibrium , Kinetics , and Thermodynamic Studies of Fluoride Adsorbed by Tetrametallic Oxide Adsorbent*. https://doi.org/10.1021/acs.jced.8b00024

Rahimpour, H. R., Saidi, M., Rostami, P., Gates, B. C., and Rahimpour, M. R. (2016). Experimental Investigation on Upgrading of Lignin-Derived Bio-Oils: Kinetic Analysis of Anisole Conversion on Sulfided CoMo/Al2O3 Catalyst. *International Journal of Chemical Kinetics*, *48*(11), 702–713. https://doi.org/10.1002/kin.21026

Ramírez Bocanegra, N., Rivera De la Rosa, J., Lucio Ortiz, C. J., Cubillas González, P., Greenwell, H. C., Badillo Almaráz, V. E., Sandoval Rangel, L., Alcántar-Vázquez, B., Rodríguez-González, V., and De Haro Del Río, D. A. (2019). Catalytic conversion of 5-hydroxymethylfurfural (5-HMF) over Pd-Ru/FAU zeolite catalysts. *Catalysis Today*, *September*, 0–1. https://doi.org/10.1016/j.cattod.2019.11.032

Rao, N. S., and Rao, M. V. B. (2015). Structural and Optical Investigation of ZnO Nanopowders Synthesized from Zinc Chloride and Zinc Nitrate. *American Journal of Materials Science*, *5*(3), 66–68. https://doi.org/10.5923/j.materials.20150503.02

Ravanchi, M. T., and Sahebdelfar, S. (2019). Catalytic upgrading of bio-oil for production of drop-in fuels. *Handbook of Ecomaterials*, *3*, 1965–1966. https://doi.org/10.1007/978-3-319-68255-6_8

Regalbuto, J. R. (Ed.). (2007). *Catalyst preparation: science and engineering*. Taylor and Francis.

Rogers, K. A., and Zheng, Y. (2019). Decomposition of glucose with *in-situ* deoxygenation in a low H_2 pressure environment – Pt. II: Bimetallic catalysts. *Applied Catalysis A: General*, *578*(January), 10–19. https://doi.org/10.1016/j.apcata.2019.03.013

Romero, A., Nieto-Márquez, A., Essayem, N., Alonso, E., and Pinel, C. (2019). Improving conversion of D-Glucose into short-chain alkanes over RU/MCM-48 based catalysts. *Microporous and Mesoporous Materials*, *286*(March), 25–35. https://doi.org/10.1016/j.micromeso.2019.05.035

Rouquerol, F., Rouquerol, J., Sing, K. S. W., Maurin, G., and Llewellyn, P. (2014). Introduction. *Adsorption by Powders and Porous Solids: Principles, Methodology and Applications: Second Edition*, 1–24. https://doi.org/10.1016/B978-0-08-097035-6.00001-2

Roy, P., Jahromi, H., Rahman, T., Baltrusaitis, J., Hassan, E. B., Torbert, A., and Adhikari, S. (2023). Hydrotreatment of pyrolysis bio-oil with non-edible carinata oil and poultry fat for producing transportation fuels. *Fuel Processing Technology*, *245*(March), 107753. https://doi.org/10.1016/j.fuproc.2023.107753

Ruddy, D. A., Schaidle, J. A., Ferrell, J. R., Wang, J., Moens, L., and Hensley, J. E. (2014). Recent advances in heterogeneous catalysts for bio-oil upgrading via "*ex-situ* catalytic fast pyrolysis": Catalyst development through the study of model compounds. In *Green Chemistry* (Vol. 16, Issue 2). https://doi.org/10.1039/c3gc41354c

Gregg, S. J., and Sing, K. S. W. (1982). Adsorption, Surface Area and Porosity. 2. Auflage, Academic Press, London. 303 Seiten. *Berichte Der Bunsengesellschaft Für Physikalische Chemie*, *86*(10), 957. https://doi.org/https://doi.org/10.1002/bbpc.19820861019

Sadowska, K., Wach, A., Olejniczak, Z., Kuśtrowski, P., and Datka, J. (2013). Hierarchic zeolites: Zeolite ZSM-5 desilicated with NaOH and NaOH/tetrabutylamine hydroxide. *Microporous and Mesoporous Materials*, *167*, 82–88. https://doi.org/10.1016/j.micromeso.2012.03.045

Saidi, M., and Safaripour, M. (2022). Aqueous phase hydrodeoxygenation of anisole as a pyrolysis lignin-derived bio-oil by ether-functionalized ionic polymer-stabilized Ni-Mo nanocatalyst. *Sustainable Energy Technologies and Assessments*, *49*(November 2021), 101770. https://doi.org/10.1016/j.seta.2021.101770

Sakka, A., Putra, A. E. E., Amaliyah, N., and Mangkau, A. (2023). A review on catalytic upgrading of bio-oil produced from pyrolysis of biomass over the rice husk ash (RHA) and HZSM-5 catalyst. *AIP Conference Proceedings*, *2630*. https://doi.org/10.1063/5.0125962

Saleheen, M., Verma, A. M., Mamun, O., Lu, J., and Heyden, A. (2019). Investigation of solvent effects on the hydrodeoxygenation of guaiacol over Ru catalysts. *Catalysis Science and Technology*, *9*(22), 6253–6273. https://doi.org/10.1039/c9cy01763a

Salmi, H. M. (2023). *The impact of the traffic charge incentives on Sustainable Aviation Fuel (SAF).* (Master's thesis, Haaga-Helia University of Applied Sciences). Helsinki, Finland. https://www.theseus.fi/handle/10024/801112

Sangnikul, P., Phanpa, C., Xiao, R., Zhang, H., Reubroycharoen, P., Kuchonthara, P., Vitidsant, T., Pattiya, A., and Hinchiranan, N. (2019). Role of copper- or cerium-promoters on NiMo/Γ-Al2O3 catalysts in hydrodeoxygenation of guaiacol and bio-oil. *Applied Catalysis A: General*, *574*(February), 151–160. https://doi.org/10.1016/j.apcata.2019.02.004

Sankaranarayanan, T. M., Kreider, M., Berenguer, A., Gutiérrez-Rubio, S., Moreno, I., Pizarro, P., Coronado, J. M., and Serrano, D. P. (2018). Cross-reactivity of guaiacol and propionic acid blends during hydrodeoxygenation over Ni-supported catalysts. *Fuel*, *214*(February 2017), 187–195. https://doi.org/10.1016/j.fuel.2017.10.059

Sankaranarayanan, Thangaraju M., Berenguer, A., Ochoa-Hernández, C., Moreno, I., Jana, P., Coronado, J. M., Serrano, D. P., and Pizarro, P. (2015). Hydrodeoxygenation of anisole as bio-oil model compound over supported Ni and Co catalysts: Effect of metal and support properties. *Catalysis Today*, *243*(C), 163–172. https://doi.org/10.1016/j.cattod.2014.09.004

Sarkar, B., Tiwari, R., Singha, R. K., Suman, S., Ghosh, S., Acharyya, S. S., Mantri, K., Konathala, L. N. S., Pendem, C., and Bal, R. (2012). Reforming of methane with CO2 over Ni nanoparticle supported on mesoporous ZSM-5. *Catalysis Today*, *September*. https://doi.org/10.1016/j.cattod.2012.04.029

Sartipi, S., Makkee, M., Kapteijn, F., and Gascon, J. (2014). Catalysis engineering of bifunctional solids for the one-step synthesis of liquid fuels from syngas: A review. *Catalysis Science and Technology*, *4*(4), 893–907. https://doi.org/10.1039/c3cy01021j

Serrano, D. P., Aguado, J., Escola, J. M., Peral, A., Morales, G., and Abella, E. (2011).

Synthesis of hierarchical ZSM-5 by silanization and alkoxylation of protozeolitic units. *Catalysis Today*, *168*(1), 86–95. https://doi.org/10.1016/j.cattod.2010.12.040

Shafaghat, H., Rezaei, P. S., and Ashri Wan Daud, W. M. (2015). Effective parameters on selective catalytic hydrodeoxygenation of phenolic compounds of pyrolysis bio-oil to high-value hydrocarbons. *RSC Advances*, *5*(126), 103999–104042. https://doi.org/10.1039/c5ra22137d

Shafaghat, H., Sirous Rezaei, P., and Daud, W. M. A. W. (2015). Catalytic hydrogenation of phenol, cresol and guaiacol over physically mixed catalysts of Pd/C and zeolite solid acids. *RSC Advances*, *5*(43), 33990–33998. https://doi.org/10.1039/c5ra00367a

Shahbeik, H., Shafizadeh, A., Gupta, V. K., Lam, S. S., Rastegari, H., Peng, W., Pan, J., Tabatabaei, M., and Aghbashlo, M. (2023). Using nanocatalysts to upgrade pyrolysis bio-oil: A critical review. *Journal of Cleaner Production*, *413*(January). https://doi.org/10.1016/j.jclepro.2023.137473

Sharifzadeh, M., Sadeqzadeh, M., Guo, M., Borhani, T. N., Murthy Konda, N. V. S. N., Garcia, M. C., Wang, L., Hallett, J., and Shah, N. (2019). The multi-scale challenges of biomass fast pyrolysis and bio-oil upgrading: Review of the state of art and future research directions. *Progress in Energy and Combustion Science*, *71*, 1–80. https://doi.org/10.1016/j.pecs.2018.10.006

Shi, Y., Xing, E., Wu, K., Wang, J., Yang, M., and Wu, Y. (2017). Recent progress on upgrading of bio-oil to hydrocarbons over metal/zeolite bifunctional catalysts. *Catalysis Science and Technology*, *7*(12), 2385–2415. https://doi.org/10.1039/c7cy00574a

Shinde, S. B., and Deshpande, R. M. (2017). Catalytic Hydrogenation of Benzoic Acid. *New Advances in Hydrogenation Processes - Fundamentals and Applications*, *667*. https://doi.org/10.5772/66428

Shinde, S. B., and Deshpande, R. M. (2022). Kinetic Study for Chemoselective Hydrogenation of Benzoic Acid to Benzyl Alcohol in a Batch Slurry Reactor using Ru-Sn/Al2O3 Catalyst. *Asian Journal of Chemistry*, *34*(10), 2538–2544. https://doi.org/10.14233/ajchem.2022.23817

Si, Z., Zhang, X., Wang, C., Ma, L., and Dong, R. (2017). An overview on catalytic hydrodeoxygenation of pyrolysis oil and its model compounds. *Catalysts*, *7*(6), 1–22. https://doi.org/10.3390/catal7060169

Siddiquee, M. N., Klerk, A. De, and Nazemifard, N. (2016). *SUPPLEMENTARY INFORMATION : Application of microfluidics to control product selectivity during non-catalytic oxidation of naphthenic-aromatic hydrocarbons*. 1–11.

Sing, K. S. W. (2013). Assessment of Surface Area by Gas Adsorption. In *Adsorption by Powders and Porous Solids: Principles, Methodology and Applications: Second Edition* (2nd ed.). Elsevier Ltd. https://doi.org/10.1016/B978-0-08-097035-6.00007-3

Singh, A., Kushwaha, A., Sen, S., Goswami, S., Katiyar, S., Kumar, A., Borah, S. N., Goswami, L., and Hussain, C. M. (2022). Recent advancement in microwave-assisted pyrolysis for biooil production. In *Waste-to-Energy Approaches Towards Zero Waste: Interdisciplinary Methods of Controlling Waste*. INC. https://doi.org/10.1016/B978-0-323-85387-3.00014-8

Singhvi, M. S., and Gokhale, D. V. (2019). Lignocellulosic biomass: Hurdles and challenges

in its valorization. *Applied Microbiology and Biotechnology*, *103*(23–24), 9305–9320. https://doi.org/10.1007/s00253-019-10212-7

Sirous-Rezaei, P., Jae, J., Cho, K., Ko, C. H., Jung, S. C., and Park, Y. K. (2019). Insight into the effect of metal and support for mild hydrodeoxygenation of lignin-derived phenolics to BTX aromatics. *Chemical Engineering Journal*, *377*(October 2018), 120121. https://doi.org/10.1016/j.cej.2018.10.058

Sompech, S., Dasri, T., and Thaomola, S. (2016). Preparation and Characterization of Amorphous Silica and Calcium Oxide from Agricultural Wastes. *An international Research Journal of Pure and Applied Chemistry*, *32*(4). http://dx.doi.org/10.13005/ojc/320418

Song, M., Zhong, Z., and Dai, J. (2010). Different solid acid catalysts influence on properties and chemical composition change of upgrading bio-oil. *Journal of Analytical and Applied Pyrolysis*, *89*(2), 166–170. https://doi.org/10.1016/j.jaap.2010.07.007

Souza, I. M. S., Sainz-Díaz, C. I., Viseras, C., and Pergher, S. B. C. (2020). Adsorption capacity evaluation of zeolites as carrier of isoniazid. *Microporous and Mesoporous Materials*, *292*(September 2019), 109733. https://doi.org/10.1016/j.micromeso.2019.109733

Sridevi, V., Surya, D. V., Reddy, B. R., Shah, M., Gautam, R., Kumar, T. H., Puppala, H., Pritam, K. S., and Basak, T. (2023). Challenges and opportunities in the production of sustainable hydrogen from lignocellulosic biomass using microwave-assisted pyrolysis: A review. *International Journal of Hydrogen Energy*, *xxxx*. https://doi.org/10.1016/j.ijhydene.2023.06.186

Srivastava, A., Jain, V. K., and Srivastava, A. (2009). *SEM-EDX analysis of various sizes aerosols in Delhi India*. *February 2008*, 405–416. https://doi.org/10.1007/s10661-008-0239-0

Srivastava, S. (2018). *Optimization and Reaction Kinetics Studies on Copper-Cobalt Catalyzed Liquid Phase Hydrogenation of 5-Hydroxymethylfurfural to Abstract :* 1–16. https://doi.org/10.1515/ijcre-2017-0197

Staš, M., Auersvald, M., Kejla, L., Vrtiška, D., Kroufek, J., and Kubička, D. (2020). Quantitative analysis of pyrolysis bio-oils: A review. *TrAC - Trends in Analytical Chemistry*, *126*(2020). https://doi.org/10.1016/j.trac.2020.115857

Sulejmanovic, D., Keiser, J. R., Su, Y. F., Kass, M. D., Ferrell, J. R., Olarte, M. V., Wade, J. E., and Jun, J. (2022). Effect of Carboxylic Acids on Corrosion of Type 410 Stainless Steel in Pyrolysis Bio-Oil. *Sustainability (Switzerland)*, *14*(18). https://doi.org/10.3390/su141811743

Suresh, S., and Sundaramoorthy, S. (2014). Green chemical engineering: An introduction to catalysis, kinetics, and chemical processes. In *Green Chemical Engineering: An Introduction to Catalysis, Kinetics, and Chemical Processes*. https://doi.org/10.1201/b17929

Szczyglewska, P., Feliczak-Guzik, A., and Nowak, I. (2020). A support effect on the hydrodeoxygenation reaction of anisole by ruthenium catalysts. *Microporous and Mesoporous Materials*, *293*. https://doi.org/10.1016/j.micromeso.2019.109771

Tang, M., Mao, S., Li, M., Wei, Z., Xu, F., Li, H., and Wang, Y. (2015). RuPd alloy

nanoparticles supported on N-doped carbon as an efficient and stable catalyst for benzoic acid hydrogenation. *ACS Catalysis*, *5*(5), 3100–3107. https://doi.org/10.1021/acscatal.5b00037

Tang, M., Mao, S., Li, X., Chen, C., Li, M., and Wang, Y. (2017). Highly effective Ir-based catalysts for benzoic acid hydrogenation: Experiment- and theory-guided catalyst rational design. *Green Chemistry*, *19*(7), 1766–1774. https://doi.org/10.1039/c7gc00387k

Tang, X., Ding, W., and Li, H. (2021). Improved hydrodeoxygenation of bio-oil model compounds with polymethylhydrosiloxane by Brønsted acidic zeolites. *Fuel*, *290*(November 2020). https://doi.org/10.1016/j.fuel.2020.119883

Taoukis, P. S., Tsironi, T. N., and Giannakourou, M. C. (2014). Reaction kinetics. *Food Engineering Handbook: Food Engineering Fundamentals*, 529–569. https://doi.org/10.1201/b17843

Tian, Z., Liang, X., Li, R., Wang, C., Liu, J., Lei, L., Shu, R., and Chen, Y. (2022). Hydrodeoxygenation of guaiacol as a model compound of pyrolysis lignin-oil over NiCo bimetallic catalyst: Reactivity and kinetic study. *Fuel*, *308*(September 2021), 122034. https://doi.org/10.1016/j.fuel.2021.122034

Tran, N., Uemura, Y., Chowdhury, S., and Ramli, A. (2014). A review of bio-oil upgrading by catalytic hydrodeoxygenation. *Applied Mechanics and Materials*, *625*, 255–258. https://doi.org/10.4028/www.scientific.net/AMM.625.255

Tu, C., Chen, J., Li, W., Wang, H., Deng, K., Vinokurov, V. A., and Huang, W. (2019). Hydrodeoxygenation of bio-derived anisole to cyclohexane over bi-functional IM-5 zeolite supported Ni catalysts. *Sustainable Energy and Fuels*, *3*(12), 3462–3472. https://doi.org/10.1039/c9se00554d

Tursi, A., and Olivito, F. (2021). Biomass conversion. In *Advances in Bioenergy and Microfluidic Applications*. Elsevier Inc. https://doi.org/10.1016/B978-0-12-821601-9.00001-7

van Hooff, J. H. C., and Roelofsen, J. W. (1991). Chapter 7 Techniques of Zeolite Characterization. *Studies in Surface Science and Catalysis*, *58*(C), 241–283. https://doi.org/10.1016/S0167-2991(08)63605-8

Vareda, J. P. (2023). On validity , physical meaning , mechanism insights and regression of adsorption kinetic models. *Journal of Molecular Liquids*, *376*, 121416. https://doi.org/10.1016/j.molliq.2023.121416

Venkatesan, K., Krishna, J. V. J., Anjana, S., Selvam, P., and Vinu, R. (2021). Hydrodeoxygenation kinetics of syringol, guaiacol and phenol over H-ZSM-5. *Catalysis Communications*, *148*(August 2020), 106164. https://doi.org/10.1016/j.catcom.2020.106164

Vennestrøm, P. N. R., Grill, M., Kustova, M., Egeblad, K., Lundegaard, L. F., Joensen, F., Christensen, C. H., and Beato, P. (2011). Hierarchical ZSM-5 prepared by guanidinium base treatment: Understanding microstructural characteristics and impact on MTG and NH_3-SCR catalytic reactions. *Catalysis Today*, *168*(1), 71–79. https://doi.org/10.1016/j.cattod.2011.03.045

Verykouki, E., and Nakas, C. T. (2023). Adaptations on the Use of p-Values for Statistical

Inference: An Interpretation of Messages from Recent Public Discussions. *Stats*, *6*(2), 539–551. https://doi.org/10.3390/stats6020035

Viswanadham, N., Muralidhar, G., and Rao, T. S. R. P. (2004). Cracking and aromatization properties of some metal modified ZSM-5 catalysts for light alkane conversions. *Journal of Molecular Catalysis A: Chemical*, *223*(1–2), 269–274. https://doi.org/10.1016/j.molcata.2003.11.045

Wang, A., Austin, D., Karmakar, A., Bernard, G. M., Michaelis, V. K., Yung, M. M., Zeng, H., and Song, H. (2017). Methane Upgrading of Acetic Acid as a Model Compound for a Biomass-Derived Liquid over a Modified Zeolite Catalyst. *ACS Catalysis*, *7*(5), 3681–3692. https://doi.org/10.1021/acscatal.7b00296

Wang, H., Feng, M., and Yang, B. (2017). Catalytic hydrodeoxygenation of anisole: An insight into the role of metals in transalkylation reactions in bio-oil upgrading. *Green Chemistry*, *19*(7), 1668–1673. https://doi.org/10.1039/c6gc03198f

Wang, J. G., Yang, L. Y., Liu, H., and Li, C. Y. (2005). Intrinsic kinetics of methane steam reforming over a Ni/α-Al2O3 catalyst. *Beijing Huagong Daxue Xuebao (Ziran Kexueban)/Journal of Beijing University of Chemical Technology (Natural Science Edition)*, *32*(1), 10–15

Wang, J., and Guo, X. (2020). Adsorption kinetic models: Physical meanings, applications, and solving methods. *Journal of Hazardous Materials*, *390*(January), 122156. https://doi.org/10.1016/j.jhazmat.2020.122156

Wang, W., Lin, J., Shao, S., Chen, H., Dai, J., and Yang, Y. (2023). Journal of Environmental Chemical Engineering Enhanced adsorption of benzo (a) pyrene in soil by porous biochar : Adsorption kinetics , thermodynamics , and mechanisms. *Journal of Environmental Chemical Engineering*, *11*(1), 109002. https://doi.org/10.1016/j.jece.2022.109002

Wang, Wanjun, Lin, J., Shao, S., Chen, H., Dai, J., and Yang, Y. (2023). Journal of Environmental Chemical Engineering Enhanced adsorption of benzo (a) pyrene in soil by porous biochar : Adsorption kinetics , thermodynamics , and mechanisms. *Journal of Environmental Chemical Engineering*, *11*(1), 109002. https://doi.org/10.1016/j.jece.2022.109002

Wang, Wenbo, Luo, Z., Li, S., Xue, S., and Yang, Y. (2019). Effects of the controllable mesostructure of nano-sized ZSM-5 on the co-cracking of phenolic bio-oil model compounds and ethanol. *Catalysis Science and Technology*, *9*(13), 3525–3536. https://doi.org/10.1039/c9cy00576e

Wilke, C. R., and Chang, P. (1955). Correlation of diffusion coefficients in dilute solutions. *AIChE journal*, *1*(2), 264-270.

Witsuthammakul, A., and Sooknoi, T. (2015). Selective hydrodeoxygenation of bio-oil derived products: Ketones to olefins. *Catalysis Science and Technology*, *5*(7), 3639–3648. https://doi.org/10.1039/c5cy00367a

Wu, X., Sun, Q., Wang, H., Han, J., Ge, Q., and Zhu, X. (2019). Effect of acid-metal balance of bifunctional Pt/Beta catalysts on vapor phase hydrodeoxygenation of m-cresol. *Catalysis Today*, *March*, 0–1. https://doi.org/10.1016/j.cattod.2019.04.039

Xekoukoulotakis, N. P., Xinidis, N., Chroni, M., Mantzavinos, D., Venieri, D., Hapeshi, E.,

and Fatta-Kassinos, D. (2010). UV-A/TiO2 photocatalytic decomposition of erythromycin in water: Factors affecting mineralization and antibiotic activity. *Catalysis Today*, *151*(1–2), 29–33. https://doi.org/10.1016/j.cattod.2010.01.040

Xu, D., Lv, H., and Liu, B. (2018). Encapsulation of metal nanoparticle catalysts within mesoporous zeolites and their enhanced catalytic performances: A review. *Frontiers in Chemistry*, *6*(NOV), 1–14. https://doi.org/10.3389/fchem.2018.00550

Xu, Q., Feng, P., Huang, K., Xin, S., Wei, T., Liao, L., and Yan, Y. (2019). Research of the combined reforming of bio-oil model compound for hydrogen production. *Environmental Progress and Sustainable Energy*, *June*, 1–9. https://doi.org/10.1002/ep.13320

Xu, Xiwei, Jiang, E., Lima, R. W. S., Hewer, T. L. R., Schmal, M., KADEJAH, Lan, X., Hensen, E. J. M., Weber, T., Hellinger, M., Baier, S., Mortensen, P., Kleist, W., Jensen, A., Grunwaldt, J.-D., Liu, K., Liu, K., Peters, J. E., Carpenter, J. R., … Song, W. (2015). Catalytic Hydrodeoxygenation of Bio-oil and Model Compounds. *Energy and Fuels*, *550*(3), 1472–1483. http://www.mdpi.com/2073-4344/5/3/1152

Xu, Xuan, Tang, M., Li, M., Li, H., and Wang, Y. (2014). Hydrogenation of benzoic acid and derivatives over Pd nanoparticles supported on N-doped carbon derived from glucosamine hydrochloride. *ACS Catalysis*, *4*(9), 3132–3135. https://doi.org/10.1021/cs500859n

Yan, P., Kennedy, E., and Stockenhuber, M. (2021). Natural zeolite supported Ni catalysts for hydrodeoxygenation of anisole. *Green Chemistry*, *23*(13), 4673–4684. https://doi.org/10.1039/d0gc04377j

Yan, P., Tian, X., Kennedy, E. M., and Stockenhuber, M. (2022). The role of Ni sites located in mesopores in the selectivity of anisole hydrodeoxygenation. *Catalysis Science and Technology*, *12*(7), 2184–2196. https://doi.org/10.1039/d1cy02132j

Yang, W., Wang, Z., Song, S., Chen, H., Wang, X., Cheng, J., Sun, R., and Han, J. (2019). Understanding catalytic mechanisms of HZSM-5 in hydrothermal liquefaction of algae through model components: Glucose and glutamic acid. *Biomass and Bioenergy*, *130*(March), 105356. https://doi.org/10.1016/j.biombioe.2019.105356

Yang, Yanfan, Xu, X., He, H., Huo, D., Li, X., Dai, L., and Si, C. (2023). The catalytic hydrodeoxygenation of bio-oil for upgradation from lignocellulosic biomass. *International Journal of Biological Macromolecules*, *242*(P1), 124773. https://doi.org/10.1016/j.ijbiomac.2023.124773

Yang, Yongxing, Qiao, L., Hao, J., Shi, H., and Lv, G. (2019). Hydrodeoxygenation upgrading of bio-oil on Ni-based catalysts with low Ni loading. *Chemical Engineering Science*, *208*. https://doi.org/10.1016/j.ces.2019.08.012

Yao, T., Qiao, L., and Du, K. (2020). High tough and highly porous graphene/carbon nanotubes hybrid beads enhanced by carbonized polyacrylonitrile for efficient dyes adsorption. *Microporous and Mesoporous Materials*, *292*(24), 109716. https://doi.org/10.1016/j.micromeso.2019.109716

Yin, W., Venderbosch, R. H., He, S., Bykova, M. V., Khromova, S. A., Yakovlev, V. A., and Heeres, H. J. (2017). Mono-, bi-, and tri-metallic Ni-based catalysts for the catalytic hydrotreatment of pyrolysis liquids. *Biomass Conversion and Biorefinery*, *7*(3), 361–376. https://doi.org/10.1007/s13399-017-0267-5

You, S. J., and Park, E. D. (2014). Effects of dealumination and desilication of H-ZSM-5 on xylose dehydration. *Microporous and Mesoporous Materials*, *186*, 121–129. https://doi.org/10.1016/j.micromeso.2013.11.042

Yusuf, M., Leeke, G., and Wood, J. (2022). Anisole Hydrodeoxygenation over Nickel-Based Catalysts: Influences of Solvent and Support Properties. *Energy and Fuels*. https://doi.org/10.1021/acs.energyfuels.2c03734

Yu, Z., Yao, K., Wang, Y., Yao, Y., Sun, Z., Liu, Y., Shi, C., Wang, W., and Wang, A. (2021). Kinetic investigation of phenol hydrodeoxygenation over unsupported nickel phosphides. *Catalysis Today*, *371*(May 2020), 179–188. https://doi.org/10.1016/j.cattod.2020.06.006

Zaarour, M., Dong, B., Naydenova, I., Retoux, R., and Mintova, S. (2014). Progress in zeolite synthesis promotes advanced applications. *Microporous and Mesoporous Materials*, *189*, 11–21. https://doi.org/10.1016/j.micromeso.2013.08.014

Zhang, Le, Liu, R., Yin, R., and Mei, Y. (2013). Upgrading of bio-oil from biomass fast pyrolysis in China: A review. *Renewable and Sustainable Energy Reviews*, *24*, 66–72. https://doi.org/10.1016/j.rser.2013.03.027

Zhang, Luxin, Xi, G., Chen, Z., Jiang, D., Yu, H., and Wang, X. (2017). Highly selective conversion of glucose into furfural over modified zeolites. *Chemical Engineering Journal*, *307*, 868–876. https://doi.org/10.1016/j.cej.2016.09.001

Zhang, Mingyuan, Wang, H., Han, X., Zeng, Y., and Xu, C. C. (2023). Catalytic HDO of pyrolysis oil in supercritical ethanol with CoMoP and CoMoW catalysts supported on different carbon materials using formic acid as *in-situ* hydrogen sources. *Biomass and Bioenergy*, *174*(April), 106814. https://doi.org/10.1016/j.biombioe.2023.106814

Zhang, Minhua, Du, J., and Chen, Y. (2023). Hydrodeoxygenation of acetic acid over Ni-promoted Cu-based catalysts: a theoretical mechanism and kinetic study. *Catalysis Science and Technology*, 1345–1357. https://doi.org/10.1039/d2cy02097a

Zhang, X., Long, J., Kong, W., Zhang, Q., Chen, L., Wang, T., Ma, L., and Li, Y. (2014). Catalytic upgrading of bio-oil over ni-based catalysts supported on mixed oxides. *Energy and Fuels*, *28*(4), 2562–2570. https://doi.org/10.1021/ef402421j

Zhang, Y. Q., Li, L., Sadiq, M., and Chien, F. S. (2023). The impact of non-renewable energy production and energy usage on carbon emissions: Evidence from China. *Energy and Environment*. https://doi.org/10.1177/0958305X221150432

Zhang, Y., Wu, S., Xu, X., and Jiang, H. (2020). Ethane aromatization and evolution of carbon deposits over nanosized and microsized Zn/ZSM-5 catalysts. *Catalysis Science and Technology*, *10*(3), 835–843. https://doi.org/10.1039/c9cy01903k

Zhao, C., Hong, C., Hu, J., Xing, Y., Ling, W., Zhang, B., Wang, Y., and Feng, L. (2023). Upgrading technologies and catalytic mechanisms for heteroatomic compounds from bio-oil – A review. *Fuel*, *333*(P2), 126388. https://doi.org/10.1016/j.fuel.2022.126388

Zhao, H., Hu, X., Hao, J., Li, N., Zhi, K., He, R., Wang, Y., Zhou, H., and Liu, Q. (2020). An efficient bifunctional Ru-NbOPO4 catalyst for the hydrodeoxygenation of aromatic ethers, phenols and real bio-oil. *Applied Catalysis A: General*, *591*(September 2019). https://doi.org/10.1016/j.apcata.2019.117378

Zhao, T., Wang, Y., Sun, C., Zhao, A., Wang, C., Zhang, X., Zhao, J., Wang, Z., Lu, J., Wu,

S., and Liu, W. (2020). Direct synthesis of hierarchical binder-free ZSM-5 and catalytic properties for MTP. *Microporous and Mesoporous Materials*, *292*(September 2019), 109731. https://doi.org/10.1016/j.micromeso.2019.109731

Zheng, J., Zeng, Q., Yi, Y., Wang, Y., Ma, J., Qin, B., Zhang, X., Sun, W., and Li, R. (2011). The hierarchical effects of zeolite composites in catalysis. *Catalysis Today*, *168*(1), 124–132. https://doi.org/10.1016/j.cattod.2011.01.006

Zhou, Y., and Hu, C. (2020). Catalytic thermochemical conversion of algae and upgrading of algal oil for the production of high-grade liquid fuel: A review. *Catalysts*, *10*(2), 1–25. https://doi.org/10.3390/catal10020145

Zhu, J., Meng, X., and Xiao, F. (2013). Mesoporous zeolites as efficient catalysts for oil refining and natural gas conversion. *Frontiers of Chemical Science and Engineering*, *7*(2), 233–248. https://doi.org/10.1007/s11705-013-1329-2

Zuliani, A., Chelazzi, D., Mastrangelo, R., Giorgi, R., and Baglioni, P. (2023). Journal of Colloid and Interface Science Adsorption kinetics of acetic acid into ZnO / castor oil-derived polyurethanes. *Journal of Colloid and Interface Science*, *632*, 74–86. https://doi.org/10.1016/j.jcis.2022.11.049

Appendix A: EDX Elemental Mapping Result of the Fresh and Used Catalysts

Table A1: EDX elemental mapping of the fresh and used mic-Ni/ZSM-5, hie-Ni/ZSM-5, and Ni/SiO_2 catalysts (HDO of anisole).

Element (%)	**Mic-Ni/ZSM-5 catalyst**		**hie-Ni/ZSM-5 catalyst**		**Ni/SiO_2 catalyst**	
	Fresh	Used	Fresh	Used	Fresh	Used
O	50.52	47.26	50.43	46.91	50.24	48.07
Si	28.68	30.19	28.27	30.34	35.23	31.62
Al	1.81	1.91	1.75	1.90	0.00	0.00
Ni	4.26	4.71	4.60	5.40	5.44	5.46
C	14.78	15.82	13.70	15.44	9.09	13.94
Others	-	0.11	-	-	-	0.91
Total (%)	**100**	**100**	**100**	**100**	**100**	**100**

Appendix B: Anisole HDO over 0.2 M NaOH Treated and Untreated ZSM-5 Supports

Table B1: Conversion and product distribution for the HDO of anisole over hie-ZSM-5 and mic-ZSM5 supports at 200 ℃, 50 bar H_2, decalin as solvent, and 100 mg catalyst loading.

Catalyst support	**hie-ZSM-5**	**Mic-ZSM-5**
Conversion (%)	3.7	1.8
Cyclohexane Selectivity (%)	ND	ND
Toluene Selectivity (%)	ND	ND

ND = Not detected

Appendix C: Effect of Hydrogen Pressure on its Solubility in Tetralin During Benzoic Acid HDO

Table C1: Concentration of dissolved hydrogen in tetralin at different hydrogen pressure.

Temp. (°C)	Pressure (bar)	C_{H_2} (mM)
330	20	39.84
330	40	59.76
330	60	67.94

Appendix D: Production Distribution for the HDO of 0.16 M Benzoic Acid over hie-Ni/ZSM-5 Catalyst at Different Temperature

Table D1: Product distribution as a function of temperature during the HDO of benzoic acid over 5 wt.% nickel-based hie-Ni/ZSM-5: Catalyst loading; 100 mg, solvent; tetralin, benzoic acid initial concentration; 0.16 M, reaction time; 6 hours.

Temp. (℃)	**320**	**330**	**340**
Conversion (%)	83.8	95.2	99.6
	Product distribution (%)		
Benzene	19.1	23.7	27.6
Toluene	45.2	38.1	36.9
Cyclohexane	1.9	3.7	1.4
Benzaldehyde	20.2	15.5	17.3
Benzyl alcohol	13.6	19.1	16.8

Appendix E: Calculation of Critical Impeller Speed Using Zwietering Empirical Correlation

The Zwietering correlation is given as (eq. 6.1);

$$N_{js} = S_Z \left(\frac{g(\rho_{cat} - \rho_s)}{\rho_s} \right)^{0.45} \frac{X_w{}^{0.13} d_p^{0.2} v^{0.1}}{D_{imp}{}^{0.85}}$$

where N_{js} is the just suspended speed (rpm), S represents the Zwietering correlation parameter, v is the kinematic viscosity of the solvent (tetralin, $m^2\ s^{-1}$), d_p represents the particle size (m), g is the gravitational constant (9.81 $m\ s^{-2}$), ρ_{cat} and ρ_s is the densities of the catalyst and the solvent, respectively (kg m^{-3}), X_w is the weight percent of the solid (solid loading, g g^{-1} ×100), and D_{imp} is the impeller diameter (m).

The Zwietering correlation parameter S_Z, which is a function of reactor geometry, is given by Devarajulu and Loganathan, (2016) as;

$$S_Z = 13.98 \left(\frac{C_c}{Td} \right)^{0.639} \left(\frac{H}{Td} \right)^{-0.055}$$

where C_c is the impeller clearance, Td is the reactor diameter, and H is the liquid level in the reactor.

$X_w = 2.10 \times 10^{-1}$

$D_{imp} = 2.06 \times 10^{-2}$ m

$\rho_s = 9.7 \times 10^2$ kg m^{-3}

ρ_{cat} = 2.14×10^{3} kg m^{-3}

g = 9.81 m s^{-2}

v = 2.08×10^{-6} m^{2} s^{-1}

But to determine N_{js}, S_Z has to be calculated first, hence these were determined from the reactor geometry;

C_c = 1.13×10^{-2} m

T_d = 3.30×10^{-2} m

H = 6.38×10^{-2} m

Therefore, **S = 6.7761**

For three ranges of catalyst particle sizes (d_p);

8.25×10^{-5} m, ***Njs* = 1.88 $\times10^{1}$** rpm

1.05×10^{-4} m, ***Njs* = 1.97$\times10^{1}$** rpm

1.30×10^{-4} m, ***Njs* = 2.06$\times10^{1}$** rpm

Appendix F: Calculation of Hydrogen Concentration Using Fogg and Gerrard Correlations

The equations below (eq. 6.5 and 6.6) present Fogg and Gerrard correlations used to determine the value of hydrogen concentration in mg L^{-1} Pintar et al., 1998; Srivastava, 2018);

$$C_{H_2} = y_{H_2} \times \frac{P_{total}}{P_{total=1bar}} \times \frac{x_{H_2}}{1-x_{H_2}} \times \rho_s \frac{M_{H_2}}{M_s} \times 1000 \qquad 6.5$$

$$x_{H_2} = \exp\left(-125.939 + \frac{5528.45}{T} + 16.8893 \times ln(T)\right) \qquad 6.6$$

where C_{H2} is the concentration of hydrogen, y_{H_2} is the mole fraction of hydrogen in the gas phase, x_{H_2} is the mole fraction of hydrogen in the liquid phase, ρ_s is the density of solvent in g L^{-1}, is the molar mass of hydrogen in g mol^{-1}, M_s is the molar mass of solvent in g mol^{-1}, and T is the reaction temperature in Kelvin.

Given the following constants;

P_{Total} = 60 bar

ρ_s = 973 g L^{-1}

M_{H_2} = 2.016 g mol^{-1}

Ms =132.2 g mol^{-1}

While values for x_{H_2} were determined from equation 6.6 at different temperatures shown in Table F1**,** values for y_{H_2} at the corresponding temperatures were obtained from solubility data for the tetralin-hydrogen system available in solubility data series volume 5/6 (International Union of Pure and Applied Chemistry).

Table F1: Hydrogen concentration in tetralin solvent at different reaction temperature.

Temp. ℃	**Temp. K**	y_{H_2}	x_{H_2}	C_{H_2} **(mol L^{-1})**
310	583	0.8195	0.000136114	0.049265728
320	593	0.7949	0.000154597	0.054276824
330	603	0.7702	0.000175678	0.059762649
340	613	0.7456	0.000199713	0.06577049

Appendix G: Calculation of Diffusion Coefficient (D_{ei}) and the Observable Modulus ($\eta\varphi^2$)

Diffusivities in liquid can be calculated from different correlations that are available. Díaz et al. (1987) is one of the most widely used correlation to calculate the diffusivity of gases in liquid over wide temperature range. For accuracy, this correlation considered diffusivity at both 25 °C and the actual reaction temperature as states by equation 3.12 and 3.13 This is applied here to determine the coefficient of hydrogen and benzoic acid in tetralin;

$$(D_{ei})_T = 4.996 \times 10^3 \times [(D_{ei})_{T=25}] \times e^{-2539/T}$$

$$(D_{ei})_{T=25\,°C} = 6.02 \times 10^{-5} \frac{V_A^{0.36}}{\mu_A^{0.61} V_i^{0.64}}$$

where $(D_{ei})_T$ is the diffusion coefficient of reactant *i* (hydrogen and benzoic acid) in solvent *A* (tetralin)(at a given temperature *T* in $cm^2\ s^{-1}$, $(D_{ei})_{T=25\,°C}$ is the diffusion coefficient at 25 °C in $cm^2\ s^{-1}$, *T* is absolute temperature in Kelvin, μ_A is the viscosity of tetralin in cP, V_i is the molar volume of reactant at the normal boiling point temperature in $cm^3\ gmol^{-1}$, and V_A is the molar volume of tetralin at normal boiling temperature in $cm^3\ gmol^{-1}$.

Hence

V_{H_2} = 23.8 $cm^3\ gmol^{-1}$

V_{BA} = 92.5 $cm^3\ gmol^{-1}$

V_A = 135.7 $cm^3\ gmol^{-1}$

μ_A = 2.02 cP

Therefore,

$(D_{eH2})_{T=25\,°C}$ = 2.67 × 10^{-9} $m^2\ s^{-1}$

$(D_{eBA})_{T=25\,°C}$ = 1.27 × 10^{-9} $m^2\ s^{-1}$

Table G1 gives values of effective diffusivities of hydrogen and benzoic acid in tetralin at different temperatures.

Table G1: Diffusivity coefficients of hydrogen and benzoic acid in tetralin at different temperatures.

Temp. (K)	$(D_{eH2})_T$ **m^2 s^{-1}**	$(D_{eBA})_T$ **m^2 s^{-1}**
583	1.70×10^{-7}	8.13×10^{-8}
593	1.80×10^{-7}	8.75×10^{-8}
603	2.01×10^{-7}	9.39×10^{-8}
613	2.10×10^{-7}	10.1×10^{-8}

Weisz and Prater (1954) criteria (eq. 6.3) were deployed to calculate the observable modulus ($\eta\varphi^2$). The following parameters were used for the calculation;

$L = 1.63 \times 10^{-5}$ m where $L = \frac{D}{6}$ for D = 75 µm - 120µm

$\omega = 2$ kg m^{-3} $C_{BA} = 0.24$ mol L^{-1}

Therefore, Table G2 presents the details of the calculations at different reaction temperatures.

Table G2: Calculation for the observable modulus.

Temp.	C_{H_2}	$r_0 \times 10^{-6}$	$(D_{eH2})_T \times 10^{-7}$	$(D_{eBA})_T \times 10^{-8}$	$\eta\varphi^2{}_{H_2}$	$\eta\varphi^2{}_{BA}$
K	**mM**	**kmol kg$^{-1}_{cat}$ s^{-1}**	**m^2 s^{-1}**	**m^2 s^{-1}**	**$\times 10^{-7}$**	**$\times 10^{-7}$**
583	49	5.77	1.70	8.13	3.60	1.56
593	54	7.03	1.80	8.75	3.71	1.77
603	60	8.92	2.01	9.39	3.98	2.09
613	66	12.00	2.10	10.10	4.54	2.63